EPFL

Thèse n° 7504

Morphology and morphodynamics of braided rivers: an experimental investigation

Présentée le 13 octobre 2020

à la Faculté de l'environnement naturel, architectural et construit
Laboratoire d'hydraulique environnementale
Programme doctoral en mécanique

pour l'obtention du grade de Docteur ès Sciences

par

Daniel Vito PAPA

Acceptée sur proposition du jury

Prof. F. Gallaire, président du jury
Prof. C. Ancey, directeur de thèse
Prof. M. G. Kleinhans, rapporteur
Dr P. Bohórquez Rodríguez de Medina, rapporteur
Dr G. De Cesare, rapporteur

École
polytechnique
fédérale
de Lausanne

2020

Be realistic, demand the impossible!
— Herbert Marcuse

Alea jiacta est
— Caius Iulius Caesar

Remerciements

Par où commencer la partie, probablement la plus difficile, d'une thèse ? Qui remercier en premier ? En dernier ? Ai-je oublié quelqu'un ? Va-t-il/elle se fâcher si je ne le/la mentionne pas ? Est-ce trop long ? Est-ce trop court ? Est-ce bien écrit ?

Bon, pour ne pas rater ce dernier grand moment de science, je vais commencer par le début, à savoir par El Jefe. Merci Christophe de m'avoir donné l'opportunité de réaliser cette thèse. Je ne sais pas trop où tu avais la tête en m'engageant, mais au final ça s'est plutôt bien terminé. On aura au moins pu discuter de pleins de sujets qui n'avaient pas grand-chose à voir avec ma thèse (et c'est tant mieux d'ailleurs), tu m'auras fait découvrir pleins de livres et d'auteurs que je n'aurais jamais connu sans toi. Et moi, ben on va dire que j'ai rafraîchi ton espagnol.

Que dire ensuite du LHE ? Sacré laboratoire que ce LHE, bastion des graveleux. Une mention toute spéciale à Blaise, premier graveleux et fondateur d'une dynastie qui atteignit son apogée avec Gauthier avant de décliner inexorablement, comme toute dynastie, avec moi. J'espère que Bob gardera la flamme du LHE bien au chaud et la fera revivre, comme il fait vivre tout le laboratoire. Désolé Christophe, mais le vrai chef c'est bien lui. Finalement, on n'a pas réussi à collaborer scientifiquement, et peut être même qu'un jour on la fera notre fameuse publication des graveleux. Mais en attendant, on aura quand même bien rigolé entre l'île d'Oleron, l'AGU et autres joyeuseries du monde académique. Merci beaucoup les gars, sans vous je n'aurais rien réussi !

Je n'ai pas oublié le reste du labo, en particulier sa touche féminine. Une pensée à notre chère camarade du Parti Communiste Chinois, Zhenzhu, rentrée en Chine, et ses innombrables virées en montagne ainsi que ses anecdotes de voyages qui coloraient nos réunions du lundi après le fameux «lunch time guys ». Merci à Barbara, sans qui toutes les vacances, heu..., les conférences et autres déplacements seraient impossibles. Compañero latinoamericano Tomás TT, gracias por traer un poco de nuestro querido y maltratado continente acá en las Europasy al laboratorio. Ivan il terribile, grazie per essere stato conquistato dalla piu grande generale che la storia umana abbia visto, ho nombrato Giulia Cesare. *Morituri te salutant!* (anche se veramente, qua il *morituri* sei tu di fronte a lei).

Le LMS... que dire de ce laboratoire, repère de roches et de créatures étranges allant de l'escogriffe au professore, le tout en passant par Mykonos. Je parle évidemment d'Etienne, Alessandro et Dimitrios. Je n'oublie pas non plus Severin, collègue du laboratoire « frère »(LCH) avec qui on aura partagé la halle hydraulique et les innombrables apéros GC sur la terrasse. Ces apéros (et autres festivitées en tous genres) n'auraient pas été les mêmes sans la présence de Darko, Steffen, Luca, Andrea, Arnaud, et j'en oublie sûrement bien d'autres. Toute une sacrée bande de thésards sans qui le chemin du doctorat serait moins long, mais autrement moins amusant. Petite mention quand même à Bertil, ex-civiliste devenu thésard à son tour, pour la quantité d'objets oubliés dans tout l'EPFL et

pour m'avoir aidé à construire mon expérience. Bonne chance pour ce qu'il te reste de thèse à parcourir.

Les copains non thésards, vous avez aussi contribué à me faire trainer des pieds et à me retarder dans mon oeuvre. Je pense à Bernard, qui partagea mon bureau sans même faire parti du labo et qui a réussi l'exploit de se faire passer pour un post-doc. Mes collocs, Bastian et Johann, qui devront me prendre au sérieux maintenant et m'appeler docteur, à leur grand regret. À Eve et Hugo, qui ont dû me supporter pendant le confinement et faire semblant de s'intéresser aux bêtises que je racontais. À ceux qui n'apparaissaient qu'une fois par an, quand il s'agissait d'aller à un festival (Samuel, tu t'es reconnu). À Merve qui n'a toujours pas compris que la salsa c'est dépassé et que la vraie danse, et bien c'est le tango. À ce propos, une mention toute spéciale à ArchiTango, dont j'ai été voté contre mon gré président, qui m'a fait découvrir à moi, moitié argentin, le tango en Suisse ! Je ne compte plus les heures de labo (oups, Christophe tu ne devrais pas lire ça) que j'ai consacré à répondre aux mails kilométriques de Joël et organiser des milongas plutôt que de faire avancer la science. Mais ça en aura valu la peine car, *la vida es una milonga y hay que saberla bailar!*

Enfin, *last but not least* comme disent les anglais et surtout pour que mes parents anglophones comprennent quelque chose, je voudrais remercier tout particulièrement ma famille. Merci maman, merci papa, je ne sais pas si vous avez contribué en quoi que ce soit, à part peut-être m'avoir élevé, éduqué, nourri (ça c'était dur et coûteux), enfin des broutilles quoi. Les trois autres par contre, qui à part s'allier contre moi à Super Smash Bros ne m'ont rien apporté, je ne sais pas quoi leur dire. Enfin si, je sais quoi vous dire: que vous êtes nuls au foot, à Smash et au piano. Et que ce n'est pas pour rien que je suis votre Grand frère à tout jamais.

Les dedico un pensamiento muy grande a mi queridísima Nona Fina y a mi querido padrino Gramática. Espero que allá desde el cielo puedan leer estas lineas.

Lausanne, le 5 Octobre 2020 Daniel Vito Papa

Abstract

Braided rivers form some of the most fascinating fluvial patterns found on Earth. They are identifiable by their unique morphology of complex networks of intertwined channels that spread across wide floodplains. Detailed knowledge of their dynamics is needed to define proper river management strategies that can address both human needs (*e.g.* protection against floods, bank migration, *etc.*) and natural needs (*e.g.* the preservation of fauna and flora, river restoration, *etc.*).

Recently, the study of braided rivers has undergone significant progress. Developments in the areas of laboratory experiments, monitoring techniques and field surveys, in addition to new paradigms in the field of geosciences and mathematical modelling have greatly improved our understanding of braided rivers. However, many questions remain unanswered. Is it possible to predict the long-term evolution of a braided river under steady flow conditions? More fundamentally, where do the braided pattern emerge from? Does it grow out of an intrinsic flow instability? And, if this is the case, which one? The present work aims to fill two specific gaps in the current state of knowledge: the dynamics of braided river networks and the development of a morphodynamic model that uses a non-equilibrium bedload formula that can predict bedforms that ultimately produce braiding.

This thesis studied the dynamics of the braided networks experimentally. Two laboratory-scale experiments were performed from which we extracted and investigated the braided network's temporal evolution. A set of variables describing the network was determined –namely the number of nodes, the number of links and the network's total link length. These variables were shown to relate to the flow conditions. Moreover, the evolution of the braided network was described by identifying similar network configurations as modes. The modes' evolution was well captured by their probability. Using a Markov process, we were ultimately able to reproduce the probability of occurrence of those modes.

A morphodynamic model based on the shallow-water equations and a stochastic-based bedload transport formula was developed. Applying linear stability theory, we were able to obtain marginal stability curves that predicted the development of bedforms. Two types of bedforms were identified: two-dimensional bedforms (antidunes and dunes) and three-dimensional bedforms (bars). The results agreed well with the literature. The present work was the first morphodynamical model to predict the development of both dunes and bars within the same framework using shallow-water equations. Moreover, we were able to show, albeit qualitatively, the influence of particle diffusion–present in the bedload transport equation– in the development of bedforms.

Keywords: *braided rivers*, *laboratory modelling*, *morphodynamics*, *bedload transport*, *linear stability theory*

Contents

Remerciements v

Abstract vii

List of figures xii

List of tables xiv

Nomenclature xvii

1 Introduction 1

1.1 Why braiding matters? . . . 1
1.2 What is braiding? . . . 2
1.2.1 Experimental approach to braided dynamics . . . 3
1.2.2 Morphodynamical approach . . . 4
1.3 Points requiring clarification . . . 6
1.3.1 Open questions about the braided dynamics . . . 6
1.3.2 Open questions about bedload and morphodynamics . . . 7
1.4 Thesis' goals and objectives . . . 9
1.4.1 Thesis' goals . . . 9
1.4.2 Thesis's objectives . . . 9
1.5 Thesis' organisation . . . 11

2 Material & Methods 13

2.1 Experimental flume . . . 13
2.1.1 Experimental flume . . . 13
2.1.2 Flumes in the literature . . . 14
2.2 Similarity theory and setup's design . . . 15
2.2.1 Dimensional analysis . . . 15
2.2.2 Similarity theory . . . 16
2.2.3 Similarity in hydraulic models . . . 18
2.2.4 Hydraulic model design . . . 19
2.3 Measurement devices . . . 20

2.3.1 Bed elevation & Structure from Motion . . . 20
2.3.2 Bedload time-series . . . 22
2.4 Methods . . . 22
2.4.1 Edge detection . . . 22
2.4.2 Modified Hausdorff distance and DBSCAN clustering . . . 23
2.4.3 Fréchet distance . . . 25
2.4.4 Low Path method . . . 25
2.5 Markov process . . . 27

3 Results **31**
3.1 Preliminary considerations . . . 31
3.2 Bedload time-series . . . 32
3.3 Bed morphological evolution . . . 34
3.3.1 Bed morphological variables . . . 34
3.3.2 Results . . . 36
3.4 Braided network . . . 39
3.4.1 Low Path method . . . 39
3.4.2 Results . . . 40
3.5 Modal analysis . . . 41
3.5.1 Edge dataset . . . 41
3.5.2 Network dataset . . . 43
3.6 Results summary . . . 46
3.6.1 Bedload . . . 46
3.6.2 Bed morphology . . . 46
3.6.3 Braided network . . . 47
3.6.4 Modal analysis . . . 48
3.6.5 Take home message . . . 48

4 Discussion **51**
4.1 Similarity measures . . . 51
4.1.1 Morphological indicators . . . 51
4.1.2 Concluding remarks . . . 54
4.2 Modal analysis . . . 55
4.2.1 Parameters determination . . . 55
4.2.2 Modes temporal evolution . . . 58
4.2.3 Modes probabilities . . . 63
4.2.4 Markov simulations . . . 65
4.2.5 Concluding remarks . . . 67
4.3 Dimensionless numbers and network variables . . . 68
4.3.1 Dimensionless numbers . . . 68
4.3.2 Network dimensionless numbers . . . 70
4.3.3 Concluding remarks . . . 71
4.4 Limitations . . . 71

4.5 Take home message . . . 72

5 Morphodynamical model **73**
5.1 Preliminary considerations . . . 73
5.2 Hydrodynamics . . . 74
5.2.1 Flow equations . . . 74
5.2.2 Boundary conditions and closure relations . . . 75
5.3 Exner equation . . . 76
5.4 Bedload transport . . . 78
5.4.1 Microstructural model . . . 78
5.4.2 Two-dimensional extension . . . 81
5.4.3 Steady-state solution . . . 83
5.5 Linear stability . . . 84
5.5.1 Linear stability theory . . . 84
5.5.2 Non-dimensionalisation and controlling parameters . . . 86
5.5.3 Linearisations . . . 90
5.6 Eigenvalue problem . . . 91
5.6.1 Normal-mode expansion . . . 91
5.6.2 Numerical resolution . . . 92
5.7 Results . . . 93
5.7.1 Experimental observations . . . 93
5.7.2 Bars marginal stability curves . . . 96
5.8 Discussion . . . 98
5.8.1 Two-dimensional formulation . . . 98
5.8.2 Influence of diffusion . . . 101
5.8.3 Limitations . . . 105
5.9 Take home message . . . 106

6 Conclusion and perspectives **107**
Conclusions . . . 107
Perspectives . . . 108

A Experimental setup and experimental methods **111**
A.1 Experiments . . . 111
A.1.1 Bedload influx . . . 111
A.1.2 Bed monitoring . . . 112
A.2 Markov process' algorithm . . . 115
A.2.1 Algorithm structure . . . 115
A.2.2 Algorithm implementation . . . 116
A.3 Modified Hausdorf distance . . . 117
A.4 Frechet distance . . . 120
A.5 Bed morphological variables . . . 122
A.5.1 Bed morphological variables . . . 122

A.5.2 Bed Relief Index . . . 123
A.5.3 Morphologically Active Length . . . 124
A.5.4 Bed convexity . . . 125
A.5.5 Area above average . . . 125
A.5.6 Hydraulic power . . . 126

B Mathematical developments **127**
B.1 Exner equation . . . 127
B.2 Non dimensionalisation . . . 128

C Eigenvalue problem **131**
C.1 Linearisations . . . 131
C.2 Eigenvalue problem . . . 134
C.3 Matematica notebook for the resolution . . . 135

Bibliography **151**

Curriculum Vitae **153**

List of Figures

1.1 Waimakariri braided river . . . 2
1.2 Fluvial patterns found in nature . . . 3
1.3 Schematic definition of bedload transport . . . 5
1.4 Organization of the thesis. . . . 12

2.1 Schematic representation of the flume . . . 13
2.2 GCPs and markers of the fume for SfM . . . 21
2.3 Edges detection . . . 23
2.4 DBSCAN cluster model . . . 24
2.5 Example of bed elevation field with its corresponding braided network. . . . 26
2.6 Graphical representation of a Markov process. . . . 28

3.1 Temporal evolution of the bedload transport rate in run 1 and 2 . . . 33
3.2 Temporal evolution of the bed variables . . . 36
3.3 Temporal evolution of the bed dynamical variables . . . 37
3.4 Example of bed elevation field with its corresponding braided network. . . . 39
3.5 Dynamics of the links and nodes of the braided network . . . 40
3.6 Clusters of modes from the edges dataset . . . 42
3.7 Time evolution of modes detected through the modal analysis of the edge dataset . . . 43
3.8 Clusters of modes from network graph dataset . . . 44
3.9 Time evolution of modes detected through the modal analysis of the network dataset . . . 45

4.1 Parameter determination of the DBSCAN algorithm of run 1 . . . 55
4.2 Parameter determination of the DBSCAN algorithm of run 2 . . . 57
4.3 Temporal evolution of mode in run 1 and run 2 . . . 59
4.4 Temporal evolution of modes in run 1 plotted alongside morphological variables . . . 61
4.5 Temporal evolution of modes in run 2 plotted alongside morphological variables . . . 62
4.6 Graphic representation of the set of all graphs identified as modes for run 1 . . . 64
4.7 Graphic representation of the set of all graphs identified as modes for run 2 . . . 65
4.8 Markov simulations from transition probabilities matrices of run 1 and 2 . . . 67

5.1 Sketch of the problem . . . 74
5.2 Morphodynamical feedback loop . . . 77

5.3 Bedload transport in a control volume . . . 78
5.4 Steps of the linear stability analysis . . . 86
5.5 Bedforms in function of the transverse wavenumber for bar mode of order m . . . 94
5.6 Bedform dataset from flume and field experiments. . . . 95
5.7 Marginal stability curves in the $k_x - k_y$ plane. . . . 96
5.8 Marginal stability curve and celerity of antidunes in the $k_x - k_y$ plane. . . . 98
5.9 Marginal stability curve and celerity of bars in the $k_x - k_y$ plane. . . . 99
5.10 Comparison of the marginal stability curves obtain form the two and three dimensional model 100
5.11 Marginal stability curve of antidunes/dunes in the $k_x - k_y$ with varying c_d and Sc . . . 102
5.12 Marginal stability curve of bars in the $k_x - k_y$ with varying c_d and Sc . . . 104
5.13 Marginal stability curve in the $k_x - \beta$ plane . . . 105
5.14 Marginal stability curve in the $k_x - \beta$ plane . . . 106

A.1 Bedload Recking . . . 111
A.2 Marginal stability curve of the initially straight channel . . . 114
A.3 Intial development of alternate bars, $t = 0$ min . . . 114
A.4 Intial development of alternate bars, $t = 30$ min . . . 115
A.5 Markov process' algorithm . . . 116
A.6 Example of Hausdorff distance . . . 118
A.7 Analysis of the sensitivity of δ_{mhd} to noise. Plot (a) refers to noise 1; plot (b) refers to noise 2; plot (c) refers to noise 3; plot (d) refers to noise 4. . . . 119
A.8 δ_{Fr} and δ_{mhd} distances . . . 121
A.9 δ_{Fr} and δ_{mhd} distances with noise . . . 122
A.10 Example of convex function. . . . 125

List of Tables

1 Variables xvii

1.1 Morphodynamic models classified in function of the flow model and the bedload model 8

2.1 Flume dimensions 13
2.2 Experimental investigations on braided rivers 14
2.3 Experimental parameters of the flume 20

3.1 Experimental conditions 32
3.2 Bed morphological variables and their utilisation 35
3.3 Summary of bedload variables. 46
3.4 Summary of morphological variables. 47
3.5 Summary of braided network variables. 48
3.6 Summary of the modal analysis. 48

4.1 Measure of similarity criteria 52
4.2 Bedload similarity measure 52
4.3 Bed variables similarity measure 52
4.4 Bed dynamic variables similarity measure 53
4.5 Network variables similarity measure 54
4.6 DBSCAN algorithm parameters for the edges database 58
4.7 DBSCAN algorithm parameters for the graph network database 58
4.8 Modes probabilities 63
4.9 Dimensional and dimensionless hydraulic parameters 70

Nomenclature

Table 1: Variables

variable	*description*
a	mode covered area rate (chapter 4)
$\mathbf{A}$	matrix equation of the eigenvalue problem (chapter 5)
A_a	area above average (chapters 3 and 4)
B	bed relief index (chapters 3 and 4)
B	channel half width (chapter 5)
B_l	longitudinal bed relief index (chapters 3 and 4)
β	width-to-depth ratio (chapter 5)
c	longitudinal velocity (celerity) of the perturbation (chapter 5)
C	bed convexity (chapters 3 and 4)
c_d	empirical coefficient related to the deposition rate (chapter 5)
c_e	empirical coefficient related to the entrainment rate (chapter 5)

variable	*description*
$d(x, Y)$	Euclidian distance between a point x and a set Y (chapter 2)
$d(X, Y)$	Euclidian distance between a set X and a set Y (chapter 2)
d_s	median sediment diameter (chapters 2, 3, 4 and 5)
D	deposition rate (chapter 5)
D_p	particle diffusivity (chapter 5)
$\mathscr{D}$	particle diffusion number (chapter 5)
δ	relative roughness (chapter 5)
δ_H	Hausdorff distance (chapter 2)
δ_{mhd}	modified Hausdorff distance (chapters 2, 3 and 4)
ϵ	radius of inquiry for DBSCAN (chapters 2 and 4)
ε	small amplitude factor in the linear decomposition (chapter 5)
η	bed elevation (chapter 5)
E	entrainment rate (chapter 5)
f	Darcy-Weisbach friction factor (chapter 5)
Fr	Froude number (chapter 2 and 5)
g	gravitational acceleration
γ	particle activity (chapter 5)
γ_{ss}	steady-state particle activity (chapter 5)
h	water depth (chapter 5)
H_0	water depth of the base flow (chapter 5)
$\boldsymbol{k}$	wavelength vector (chapter 5)
k_x	longitudinal wavelength of the perturbation (chapter 5)
$\hat{k}_x$	dimensional longitudinal wavelength of the bedform (chapter 5)
k_y	transverse wavelength of the perturbation (chapter 5)
$\hat{k}_y$	dimensional transverse wavelength of the bedform (chapter 5)
κ	deposition rate when $\mu = 0$ (chapter 5)
κ_{eta}	entrainment number (chapter 5)
κ_γ	deposition number (chapter 5)
l	characteristic length in similarity analysis (chapter 2)
ℓ_i	link/edge i of the braided graph (chapters 2, 3 and 4)
l_ℓ	total links length of a braided network per unit area (chapters 2, 3 and 4)
L	flume length (chapters 2, 3 and 4)
L_{ell_i}	length of link/edge i (chapters 2, 3 and 4)
L_ℓ	total links length of a braided network (chapters 2, 3 and 4)
L_{ma}	morphologically active length (chapters 3 and 4)
λ	individual entrainment rate (chapter 5)
λ_x	scaling ratio of a variable x (chapter 2)
Λ_x	longitudinal wavelength of the perturbation (chapter 5)
Λ_y	transverse wavelength of the perturbation (chapter 5)
$m(q_s)$	cumulative mass (chapter 2)
m_i^j	mode i of run j (chapters 3 and 4)
μ	water dynamic viscosity (chapter 2)
μ	collective entrainment rate (chapter 5)

variable	*description*
n_ℓ	number of links of a braided network per unit area (chapter 4)
n_{neigh}	minimum number of neighbours for DBSCAN (chapters 3 and 4)
N_ℓ	number of links of a braided network (chapters 3 and 4)
N_n	number of nodes of a braided network (chapters 3 and 4)
ν	water kinematic viscosity (chapter 2)
ν	eddy viscosity (chapter 5)
ν_d	inverse Reynolds number (chapter 5)
ν_t	dimensionless parameter of the eddy viscosity (chapter 5)
ω	dimensionless stream power (chapter 4)
ω	complex angular frequency of the perturbation (chapter 5)
ω_i	imaginary part of the angular frequency (chapter 5)
ω_r	real part of the angular frequency (chapter 5)
p_{ij}	probability of switching from state i to j (2)
p_{ij}^k	transition probability from mode i to j in run k (chapters 3 and 4)
p_i^j	probability of mode i in run j (chapters 3 and 4)
Π	dimensionless variable/similarity criteria (chapters 2 and 4)
Φ_x	dimensionless function of the variable x (chapters 2 and 4)
q	dimensionless discharge (chapter 4)
$\boldsymbol{q_s}$	bedload flux vector (chapter 5)
$q_{s,in}$	inlet sediment discharge (chapter 2)
$q_{s,out}$	outlet sediment discharge (chapter 2)
$\bar{q}_s$	mean outlet sediment discharge (chapter 2)
Q	flume inlet water discharge (chapter 2)
r	Pearson's correlation coefficient (chapters 3 and 4)
ϱ	water density (chapters 2, 3, 4 and 5)
ϱ_s	sediment density (chapters 2, 3, 4 and 5)
Re	Reynolds number (chapters 2 and 5)
s	relative sediment density (chapter 5)
s_x	local bed slope (chapters 3 and 4)
S_0	steady state bed slope (chapter 5)
σ	deposition rate (chapter 5)
σ_z	bed elevation standard deviation (chapters 3 and 4)
Sc	Schmidt number (chapter 5)
t	time
τ_b	bed shear stress
τ_{cr}	critical bed shear stress
ϑ	flume slope
θ	Shields number
θ_{cr}	critical Shields number
$\bar{\boldsymbol{u}}$	depth-averaged velocity vector
$\bar{u}, u$	depth-averaged longitunal velocity
$\bar{v}, v$	depth-averaged transverse velocity
v_*	shear velocity
v_e	total eroded volume
V_e	cumulative eroded volume
V_p	particle volume

variable	*description*
x	longitudinal coordinate
y	transverse coordiante
z_m	mean bed elevation
ζ_b	bed (sand) porosity

1 Introduction

1.1 Why braiding matters?

Braiding is a fluvial pattern characterised by a complex dynamic where multiple channels join and split continuously along their floodplain (see Figure 1.1). It is one of Earth's most dynamic surface processes, and it belongs to the continuum of river channel patterns [Kleinhans, 2010]. Braiding rivers are not commonly found in nature, and this is due to the particular combination of conditions that is needed for them to form: a laterally active bed and the presence of bars, a quite particular type of fluvial bedform [Kleinhans and van den Berg, 2011]. These forming conditions are met in mountainous regions (like the Swiss Alps), in Piedmont plain environments or in wide river deltas. Moreover, the presence of bars in the middle of these webs of channels renders braiding an ecological niche [Tockner et al., 2009]. The combination of all these elements makes braiding a fascinating, highly complex, dynamic system [Ashmore, 2013].

River management has long been an issue for humankind. Indeed, rivers are simultaneously a source of life and death. One the one and, they carry the water essential to the development of agriculture and human life. On the other hand, floods are a permanent danger looming over the people living on river banks. This is why populations have always tried to control rivers and bring out the best in them. Ancient civilizations, such as the Egyptians or the Chinese, were characterised by their mastery of hydraulics. Their management of the Nile and the Yellow River, respectively, was necessary for their very survival and one of the main reasons why they flourished. Without going so far back in time, the Netherlands is a notable example of a country that has had to control its rivers for the safety of its inhabitants. However, there is a limit to the extent to which humankind can manage rivers. The floods that affected Europe in October–November 2018 showed once again that nature's behaviour is difficult to predict, even in the twenty-first century. In part, this limitation comes from the unpredictable nature of river floods, but it also comes from our incomplete understanding of hydraulics.

Braided rivers are not an exception in our partial knowledge of river mechanics. For hundreds of years, human activity has resulted in changes in sediment supply and transport regimes that have caused the braiding intensity of many European braided rivers to diminish. This, in turn, has provoked the unwanted destruction of ecological niches [Gurnell et al., 2009, Belletti et al., 2015]. Moreover, in the context of global warming and biodiversity loss, river restoration and the rebuilding of natural habitats for fauna is of particular importance today. Braided rivers can become significant parts of these restoration programs [Wohl et al., 2005, Dufour and Piégay, 2009]. However, for them to be fully efficient and avoid causing unwanted damage in the long run requires a solid

understanding of their dynamics. That understanding is currently lacking, unfortunately (or fortunately, for a PhD student).

1.2 What is braiding?

Braiding emerges from an intertwining of mechanisms acting at various scales, ranging from the particle-scale (microscopic-scale) up to the catchment-scale (macroscopic-scale).

- *at the microscopic scale:* Hydrodynamics and sediment transport describe the mechanisms acting at the particle-scale and explain how fluvial patterns develop from an instability;
- *at the macroscopic scale:* Field studies, experimental studies and numerical modelling describe the overall braided network via its macroscopic constituents.

Combining hydrodynamics and sediment transport into a coherent model, a so-called morphodynamic model, allows us to study the development of fluvial patterns through the governing equations. This approach, also called physics-based approach, relies on the precision and physical well-foundedness of the governing equations. This is true for the hydrodynamic equation, but not quite so for sediment transport models. Because of the inherent difficulty in solving the complete system of equations, the literature on morphodynamics shows that the study of fluvial patterns has relied predominantly upon the use of linear stability analysis (see Figure 1.2) [Engelund and Skovgaard, 1973, Parker, 1976, Blondeaux and Seminara, 1985, Colombini et al., 1987, Tubino, 1991, Devauchelle et al., 2010, Andreotti et al., 2012, Colombini and Stocchino, 2012, Bohorquez and Ancey, 2015]. These models can predict the early development of bedforms (at the linear stage of development), but they fail to describe the dynamics of an already developed braided system (non-linear system).

Figure 1.1: Waimakariri is a braided river in the Southern Alps in the hinterland, Canterbury, New Zealand (from Te Ara). This picture captures the very essence of a braided river: a wide, unconfined valley covered with a complex network of channels joining and splitting across the floodplain and forming this beautiful pattern.

We can develop a good understanding of the evolution of braided systems as a whole by combining numerical models with field and experimental investigation, since these approaches are able to describe the macroscopic structures (such as bars, bifurcations, *etc.*) which control the braiding mechanism [Bolla Pittaluga et al., 2003, Bertoldi and Tubino, 2007, Bertoldi, 2012, Kleinhans et al., 2013]. Numerical models generally solve the full, non-linear, morphodynamical system. They therefore go beyond the linear stage of bedform development and can thus simulate a complete fluvial pattern. Field investigation remains, to this day, the only means with which to obtain quantitative data about real braided rivers. By reducing the scale of the problem to laboratory scale and by operating in controlled environment, experimental investigation facilitates a thorough examination of specific aspects of the problem in a reliable and reproducible way, as well as the collection of high-quality data.

Each approach has its particular flaw: complex to management (field studies), potential oversimplification of reality (experimental studies and morphodynamics) and computational too expense (numerical modelling). Since I will follow an experimental and morphodynamic approach, I will highlight their respective strengths and explanatory powers.

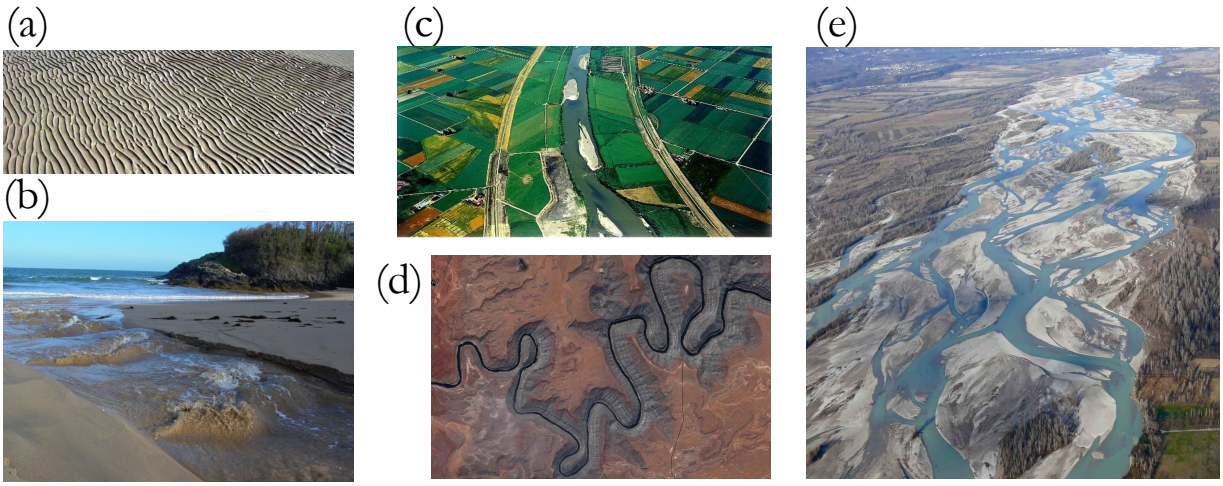

Figure 1.2: Fluvial patterns found in nature. (a) sand ripples (from MIT); (b) migrating antidunes in Belle Île, Port Andro (from Pierre-Yves Lagrée); (c) alternate bars in Japan (from Deltares); (d) meandering river in Goosenecks State Park (from NASA Earth Observatory); (e) Tagliamento braided river in Veneto (from Pinterest).

1.2.1 Experimental approach to braided dynamics

The processes occurring in braided rivers can be studied under closely monitored and controlled experimental conditions by using reduced-scale models. The main idea behind the experimental approach to braided rivers is to describing and relating the evolution of the braided network to the hydraulic conditions. Mosley [1983] conducted a series of field studies to investigate the influence of slope and water discharge on the complexity of braided networks. He associated an increasing trend in network's complexity with an increase in the river's longitudinal slope and water discharge. Ashmore [1991b] confirmed these results by means of laboratory experiments instead of field study. He highlighted the product of discharge and gradient (the stream power) as a potential key parameter controlling network's complexity. More recently, Egozi and Ashmore [2009] emphasised the tendency of braided systems to adapt to changes in water discharge and to reach new steady-state configurations. They mentioned

an increase in braiding intensity at higher discharges. Bertoldi et al. [2009b] individuated two dimensionless parameters controlling braided systems at steady state, the dimensionless discharge and dimensionless stream power. The common attribute of these works was to show a deep relationship between hydraulic conditions and the braided network of the river. Nonetheless, these investigations failed to answer the question of how to properly quantify the braided network, or at the very least, they failed to address it fully.

When modelling braided rivers, Howard et al. [1970] and Webb [1995] emphasized their network-like nature. In particular, they identified a set of topological and geometrical properties characterising the braided network. They demonstrated the possibility of describing braided rivers abstractly and opened the door to new insights. Using a similar approach, Foufoula-Georgiou and Sapozhnikov [2001] showed that multi-channel geometry was self-affine over a range of spatial scales and this self-affinity implied a statistical scale invariance. More recently, Redolfi et al. [2016] showed that the cross-sections of experimental braided rivers were statistically equivalent to a single channel whose section satisfied a power-law function. They went on to calculate the bedload transport rate in this synthetic channel and their estimation agreed well with experimental results. Although they appear different in nature and goal, these works both highlighted two important aspects: the use of statistical methods to study the braided rivers and the ability to precisely describe braided networks.

1.2.2 Morphodynamical approach

Morphodynamics is the technical term referring to the branch of science devoted to the understanding of the erosional processes that shape the Earth's surface [Seminara, 2010, Blondeaux et al., 2017]. Its main goal is to describe and predict the development of bedforms that ultimately lead to fully developed fluvial patterns, in our case, braided rivers. Morphodynamic models are based on equations, usually obtained from physics, therefore based on well-established science. They rely on the Navier-Stokes or Saint-Venant equations for hydrodynamics and the Exner equation for river-bed mass conservation [Paola and Voller, 2005]. To account for sediment transport processes, morphodynamic models are completed by sediment transport models, which are generally obtained empirically. They thus depend heavily on the sediment transport equation used. Even today, after more than a century of research, sediment transport (and bedload transport in particular) is not completely understood. Let us briefly introduce the subject.

Bedload transport is a particular form of sediment transport where the granular material is eroded and advected by the flow. It occurs in the near vicinity of the river bed, in the so-called bedload layer, and it is mainly composed of three modes of transportation: rolling, sliding and saltating (see Figure 1.3). Bedload transport was originally developed as a subfield of civil engineering and geomorphology before gaining considerable attractiveness to other branches of science because of its multi-disciplinary nature. Indeed, bedload transport embraces fields as varied as granular physics and fluid mechanics Ancey [2020a]. Since the pioneering work of du Boys [1879], a vast number of bedload transport models have been proposed, ranging from purely empirical formulations [Meyer-Peter and Müller, 1948] to models inspired from kinetic theory of gases [Furbish et al., 2012b]. I will not attempt to make an exhaustive presentation of this vast subject, the interested reader may refer to Yalin [1972], Graf [1984], Julien [2010] for general books on the subject or to Gomez and Church [1989], Gomez [1991], Ancey [2020a,b] for extended review articles. I will limit myself to introducing the bedload transport model that is going to be used in this work and to putting that into context with respect to the other equations.

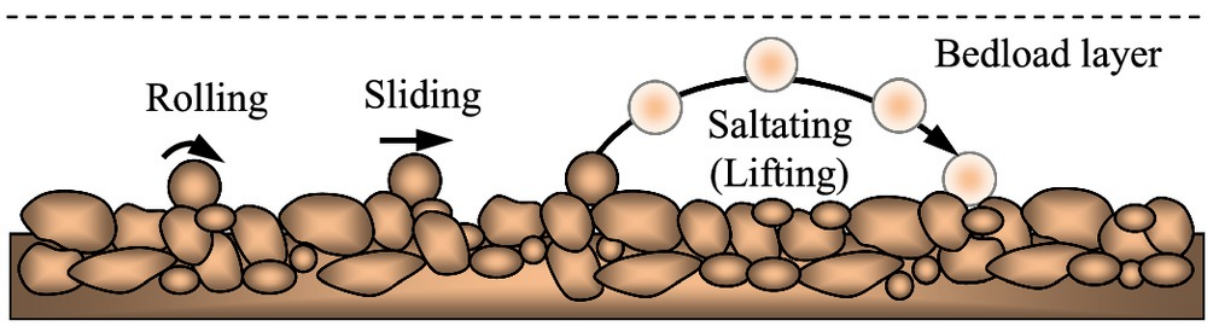

Figure 1.3: Schematic definition of bedload transport and bedload layer (from Dey [2014]).

There are two main approaches to examining bedload transport: the deterministic/mechanical approach and the statistical/stochastic approach. The deterministic approach is rooted in the early work of du Boys [1879]. He was the first to relate bedload transport to the shear stress exerted by the flow on the river bed, the bed shear stress. He pointed out that bedload transport started above a certain threshold, the critical shear stress. Later on, Shields formalised the concept of critical shear stress by introducing the dimensionless number that holds its name, the Shields number θ [Shields, 1936]. θ serves to define the critical Shields number, *i.e.* the threshold for incipient sediment motion. Parallel to du Boys' view on bedload transport, there was Bagnold's approach. He argued that bedload transport was not proportional to the excess shear stress but rather to the excess energy of the flow, the so-called stream power [Bagnold, 1956]. Ultimately, du Boys and Bagnold's approaches are quite similar in their foundations, they are both deterministic in the sense that bedload transport is directly proportional to the mechanical forces exerted on the bed.

Deterministic approaches are based on the key assumption that bedload transport is intimately linked to flow conditions; therefore every law is ultimately calibrated with laboratory or field data. This explains the success of deterministic approaches in the comparison of predictions with experimental data. However, despite these calibrations, they have has been shown to perform poorly when compared to field data [Gomez and Church, 1989, Gomez, 1991]. Moreover, deterministic approaches are unable to grasp the inherent fluctuations observed in bedload time-series from both the field and the laboratory. These fluctuations can reach up to 10 times the average bedload flux, even in laboratory experiments [Dhont and Ancey, 2018]. To improve bedload models predictions, researchers refined them by introducing more dependent variables into their equations, *e.g.* grain size distribution among others. The main idea was that the more parameters were used in the models, the more accurate their results should be [Wong and Parker, 2006, Recking, 2013]. A fundamentally different strategy was to improve understanding of the physical mechanisms underlying bedload transport. To account for the fluctuations of bedload time-series, which could not be explained by measurement errors alone, researchers had to follow a statistical approach to sediment transport.

The statistical approach originated with the work of Einstein [1950]. In his view, sediment transport is, by nature, a random process, as shown by the trajectory of eroded particles. Indeed, when looking at individual particles, he noted an erratic pattern; composed of moments of rest and moments of travel, with varying travel distances and travel speeds. In short, a random-walk-like movement. He noticed that, on average, the number of eroded

particles equalled the number of deposited particles. In the long run, the bed remained at the same altitude despite the erosional processes. He formulated that, at equilibrium and for steady state uniform flows, bedload transport should match the entrainment and deposition of particles from the bed. He then identified the relationship between bedload transport and the exchange of particles between the river bed and the flow. This formulation opened the door to a discrete, probabilistic description of the problem, relating the entrainment and deposition rates to probabilities of being entrained or deposited respectively. Although Einstein was credited as the father of stochastic models of bedload transport, this was not exactly true. His model, despite using probabilities, is deterministic and does not derive from a purely stochastic process. Nonetheless, he surely paved the way for the introduction of stochastic methods that researcher subsequently used. I will briefly present the stochastic framework that will be used in the morphodynamic model, namely Ancey et al. [2008]'s microstructural model.

The microstructural model uses a Markovian framework to determine the bedload flux. Consider the following situation: a particle is sheared off the bed by the flow and advected, either by rolling, sliding or, on occasion, saltating (this situation corresponds to entrainment); from time to time it collides with other resting particles, entraining them in turn (this situation corresponds to collective entrainment); eventually, after a given time, it comes back to rest on the bed (this situation corresponds to deposition). Making an analogy with population dynamics –deposition being similar to death, entrainment to birth and displacement to migration– it is possible to use the framework of jump Markov processes to model bedload [Ancey et al., 2008, Ancey and Heyman, 2014, Ancey et al., 2015]. Using this approach, they were able to obtain bedload time-series that exhibited the large non-Gaussian fluctuations observed in experiments. Even though the model had been developed at the grain scale, they were able to define average quantities, such as the mean bedload flux, and to determine a governing equation for the average number of moving particles. Interestingly, this equation took the form of an advection-diffusion equation. Strictly speaking the model is not stochastic, but it is the result of averaging the stochastic model. It thus originates from a purely stochastic framework, namely the birth-death Markov processes.

1.3 Points requiring clarification

1.3.1 Open questions about the braided dynamics

Recent technological progress has given researchers access to a wide range of affordable, reliable image-based and computer-vision-based techniques (Structure from Motion, LIDAR scanning, *etc.*). There has ensued an explosion of available data, and their abundance has paved the way towards statistical methods which have created staggering advances in the field of geosciences. Indeed, the abundance of data has led to data-driven approaches (*e.g.* machine-learning) and new statistical methods across science in general, *e.g.* the works of Mariethoz et al. [2010], Pirot et al. [2014]. They were able to simulate the evolution of braided rivers from a set of training images using a method based on multiple-point statistics. These works are by no means isolated and are part of a more general trend emphasising the use of statistical techniques [Mariethoz and Caers, 2015].

Parallel to the development of statistical techniques, graph theory has also made its apparition in the field of geomorphology. A constantly growing proportion of researchers are now drawing attention to the concept of connectivity and its importance in understanding how geomorphological systems behave [Heckmann et al., 2015, Phillips et al., 2015, Wohl et al., 2017, Turnbull et al., 2018, Connor-Streich et al., 2018, Wohl et al., 2019]. Graph

theory is the branch of mathematics concerned with the quantitative analysis of networks [Harary, 1969, Newman, 2003, 2010]. Braided rivers, with their network-like patterns, naturally suggest following a graph theory-based approach. The application of graph theory to braided rivers is not new, going back as far as Howard et al. [1970] and Webb [1995]. They used network-based metrics (inspired by graph theory) to describe the topology of braided rivers. Lehotský et al. [2018] took a graph theory approach to quantify sediment connectivity between bars in a wandering-braided river. Marra et al. [2014] have combined satellite images with graph theory to analyse braided channel network structures using connectivity metrics. Kleinhans et al. [2017] very recently proposed a method, the Low Path algorithm, for extracting a braided system's network in the form of a graph from bed elevation data. This method was used by Hiatt et al. [2020] to study the topology of estuaries and braided rivers.

Although successful when used on their own, I suspect that the statistical approach and the connectivity approach have not yet been employed to their full potential. Their joint utilisation within a unified framework coupled with experimental data could bring new insights to the study of braided rivers. As mentioned above, the Low Path method is in its infancy and, besides Hiatt et al. [2020]'s work, it has not been applied anywhere else, to the best of my knowledge. However, it shows very promising potential in the investigation of braided rivers' dynamics as a whole. Indeed, no other method can provide such a detailed, precise description of the braided network in the form of a graph. Moreover, that description is obtained from the bed elevation, which is the most reliable and easily obtained data on braided rivers (via image-based techniques, as mentioned above). It thus single-handedly answers the long standing problem of how to quantify braided systems and, at the same time, opens up the possibility of a more mathematical analysis of those systems. Equipped with this powerful tool and within the current context of statistical and connectivity approaches, I believe that I can address the following questions:

- *What is the appropriate metric of the braided network?*
- *Is it possible to relate the braided network's evolution to hydraulic conditions?*
- *Given a braided system, is it possible to simulate, in a statistical sense, its dynamics?*

1.3.2 Open questions about bedload and morphodynamics

The formulation of the fluid mass and momentum conservation equations is a fundamental component of any morphodynamic model. In their most general form, they are the Navier–Stokes equations. In fluvial environments, where the flow depth is generally several orders of magnitude smaller than the flow width, the Navier-Stokes equations can be reduced to the Saint-Venant equation, alternatively called the depth-averaged equations. They present the advantage of having one less component: the vertical one. They are therefore easier to solve both analytically and numerically and are often used. Morphodynamic models that include the depth-averaged equations have been successfully used to describe the formation of alternate bars and higher-order bar modes [Callander, 1969, Parker, 1976, Blondeaux and Seminara, 1985, Colombini et al., 1987, Tubino et al., 1999]. The use of shallow-water equations to describe the formation of dunes and antidunes is, however, not common in the literature. Indeed, the first attempts to do so were unsuccessful and concluded that depth-averaged models damped two-dimensional bedforms for $\mathrm{Fr} < 2$ in an unphysical manner [Reynolds, 1965, Gradowczyk, 1968, Balmforth and Provenzale, 2001]. Further, they concluded that only fully three-dimensional flow equations

which considered the vertical structure of the flow were capable of capturing the development of bedforms. Indeed, researchers have managed to explain the development of both bars and dunes, within the same theoretical framework, for both turbulent flows [Andreotti et al., 2012, Colombini and Stocchino, 2012] and laminar flows [Devauchelle et al., 2010]. A non-exhaustive summary is presented in table 1.1. On the other hand, to the best of my knowledge, there is as yet no unified framework using the shallow-water equations that is able to predict the development of both dunes and bars does not exist.

Table 1.1: Morphodynamic models classified in function of the flow model and the bedload model

	Shallow-Water	Navier–Stokes
MPM	Parker [1976] Blondeaux and Seminara [1985] Colombini et al. [1987]	Tubino [1991] Colombini and Stocchino [2012]
Non MPM	Bohorquez and Ancey [2015, 2016] Vesipa et al. [2012]	Devauchelle et al. [2010] Andreotti et al. [2012]

In an attempt to explain the failure of shallow-water-based morphodynamic models to predict the development of dunes and antidunes, the emphasis was put on the failure of the flow model and not on the sediment transport equation used. However, sediment transport plays an important, if not crucial, role in the bedform development process. Indeed, many of the aforementioned studies used empirical sediment transport equations, such as the classic MPM formula [Meyer-Peter and Müller, 1948], even though it has proven to be too simplistic to describe the full extent of bedload transport. This is demonstrated by the fact that MPM formula may over-estimates sediment transport rates by several orders of magnitude [Recking, 2012, 2013] and is unable to reproduce the fluctuations observed in bedload time-series from experiments or field measurements.

Using more refined bedload transport models, researchers have been able to capture the development of two-dimensional bedforms using depth-averaged equations [Vesipa et al., 2012, Bohorquez and Ancey, 2015, Bohorquez et al., 2019]. One of the reasons explaining the success of these models (often called non-equilibrium models) is that they break the one-to-one relationship between bedload transport and the flow conditions. In other words, classical equilibrium formulations such as the MPM equation are a direct function of flow conditions of the form $q_s = q_s(h, u)$ (with h and u representing the flow conditions). A diffusion mechanism, for instance, breaks this relationship by introducing a second order differential term into the bedload equation (as in Ancey et al. [2008]'s microstructural model). The relationship is also broken when the bedload transport is derived from a differential equation (as in Charru et al. [2004]'s model). These non-equilibrium equations have been shown to outperform equilibrium equations both at the laboratory scale and in numerical simulations [Bohorquez et al., 2019].

The presence of diffusion in the bedload model seems to be the key element in the development of bedforms in shallow-water-based morphodyamical models. The diffusive term provides a more complete and complex physical description of the bedload process, even if its origin is not purely physical [Ancey et al., 2015]. Particle diffusion's influence on the development of bedforms should not be underestimated. Recently, several authors have highlighted particle diffusion as one of the potential driving mechanisms behind the determination of the width of alluvial rivers [Seizilles et al., 2013, 2014]. The recent work of Abramian et al. [2019] has even shown that particle diffusion is the main mechanism driving the development of bedload streaks [Colombini and Parker, 1995] that may be ultimately responsible of the early development of braided rivers.

In the light of these recent developments, I believe that by coupling the microstructural bedload transport model to the shallow-water equations, I can address the following questions:

- *Is a morphodynamic model based on shallow-water equations combined with a non-equilibrium bedload transport model, able to predict the development of bars and dunes/antidunes within the same framework?*
- *What is particle diffusion's influence on the development of bars and dunes/antidunes?*

1.4 Thesis' goals and objectives

1.4.1 Thesis' goals

Recent developments in research into braided rivers have highlighted that although there has been a tremendous increase in our understanding of them, many gaps remain. In particular, long-term predictions of their evolution are still elusive. This could be inherent to the fact that they are complex, unpredictable systems (just as chaotic systems are inherently unpredictable in the long run). Nevertheless, given the current state of research, I propose to:

Use a graph-theory-based method to develop a statistical framework with which to investigate the dynamic temporal evolution of an experimental, laboratory-scale, braided river network.

Linear stability analysis has been the favoured method with which to study the development of fluvial patterns such as braided rivers. However, the morphodynamic models on which that analysis was applied often used bedload transport equations that lacked physical depth. Recent years have seen the development of stochastic bedload transport models that introduce diffusion into the overall process. Simultaneously, diffusion has been proposed as a mechanism which might explain the early development of braided rivers. Therefore, I propose to:

Build a morphodynamic model that uses the shallow-water equations, coupled with an advection-diffusion model for bedload transport, to predict the development of the three-dimensional bedforms (bars) that are ultimately responsible for the development of braided rivers.

1.4.2 Thesis's objectives

To achieve these goals, I have broken them down into a list of questions to be addressed by the present thesis. First, the questions related to the braided river dynamics are:

(i) *What are the appropriate variables with which to quantify braided river dynamics?*

(ii) *What is the temporal evolution of a braided network under given hydraulic conditions?*

(iii) *How does the braided network relates to hydraulics conditions?*

(iv) *Can I implement a statistical framework to reproduce the network's evolution?*

These questions will be tackled in the following manner:

- *flume experiment:* I will design and build a flume in which to carry out the experiments.
- *braided morphology:* I will use the recently developed Low Path method to extract the networks of experimental braided rivers [Kleinhans et al., 2017]. From this dataset, I will define a set of variables that characterises the braided network and study its temporal evolution. I will compare that set to a set of variables characterising the hydraulic conditions and the bed morphology.
- *stochastic modelling:* I will apply a recently developed methodology that will allow me to identify the particular modes/states of my braided system [Scheidt et al., 2016, Hoffimann et al., 2019]. The resulting statistical distribution of these modes will be used within a Markov framework (the whole process is called *modal analysis*). The novelty lies in the joint use of the Low Path method and stochastic modelling.
- *perspectives:* Once the results have been obtained, I will propose a new perspective on the dynamics of braided rivers. Comparing results from the three different angles of bed morphology, braided network and modal analysis, I will observe and describe the difference in the system's behaviour and argue that this difference has to be taken into account in future investigations.

The questions addressed by my morphodynamic model are:

(i) *Is the morphodynamic model linearly unstable? That is, can it develop both bars and dunes/antidunes?*

(ii) *Do the predicted bedforms fit the experimental data?*

(iii) *Can diffusion's influence on the development of both bars and dunes/antidunes be quantified?*

These questions will be tackled in the following manner:

- *morphodynamic model:* I will develop a morphodynamic model coupling the microstructural model of bedload transport and the Shallow-water equations. Applying linear stability, I will demonstrate its ability to predict the development of bars and dunes/antidunes within the same framework (which is the model's novelty).
- *comparison with the experimental dataset:* I will assess my morphodynamical model's validity by comparing its predictions with experimental datasets obtained from the literature.
- *particle diffusivity:* I will highlight, even if qualitatively, particle diffusion's influence on the development of both bars and dunes/antidunes.

1.5 Thesis' organisation

The overall structure of the thesis is presented in Figure 1.4. The general content of each chapter is described below:

- *Chapter 2* introduces the experimental setup, its design, the measurement devices and measurement techniques, and the methods used to analyse the obtained data. The first section presents my flume and proposes a non-exhaustive summary of the literature on experimental braided rivers. The second section describes the design of the flume: the theory of similarity is introduced and applied to determine the experimental setup. The third section presents the measurement devices and measurement techniques. The fourth section is devoted to the various methods that I will apply in the Results and Discussion chapters. Finally, the fifth section is a brief introduction to Markov processes.

- *Chapter 3* presents the results obtained from the experiments. The first section starts with brief preliminary considerations on the experimental runs. The second section introduces the bedload time-series. The third section presents the results of the river bed's morphological evolution. The fourth section is dedicated to the braided network's evolution. The fifth section presents the results of the modal analysis. Finally, the sixth section is a concise summary of all the results, with a take-home message at the end.

- *Chapter 4* discusses the results in more details. The first section analyses the similitude of the time-series of network and morphological variables. Second two enters into greater detail about the modal analysis: its parameter determination, the time evolution of modes, the probabilities of modes and the Markov process. The end of this section presents some concluding remarks on the modal analysis. Section three discusses a methodology, based on the similarity theory (of Chapter 2) to extend my results on network variables. Section four discusses my approach's limitations. The chapter ends with a conclusion to the discussion.

- *Chapter 5* is entirely devoted to the morphodynamic model. Section one briefly introduces the chapter. Section two presents the flow equations, the boundary conditions and the closure relations. The third section introduces the Exner equation. Section four is a thorough presentation of the bedload transport model: I start by introducing it in details and then extend it in order to use it in my morphodynamic model. Finally, I present a steady-state solution which is used later on. Section five briefly presents linear stability theory, introduces its fundamental steps and presents the linearised governing equations. Section six is a brief presentation of the resolution procedure. Section seven introduces the main results of my model, *i.e.* the marginal stability curves. These curves are compared with experimental datasets of bedforms from the literature. Section eight explore the model's novelties: its two-dimensional limit and the influence of particle diffusion. Moreover, I discuss the model's shortcoming. The chapter closes with ninth section with including the main conclusions and the contributions of the morphodynamic model.

- *Chapter 6* summarises the main results of this thesis, reflects on its contributions and ends with some perspectives opened up by the work.

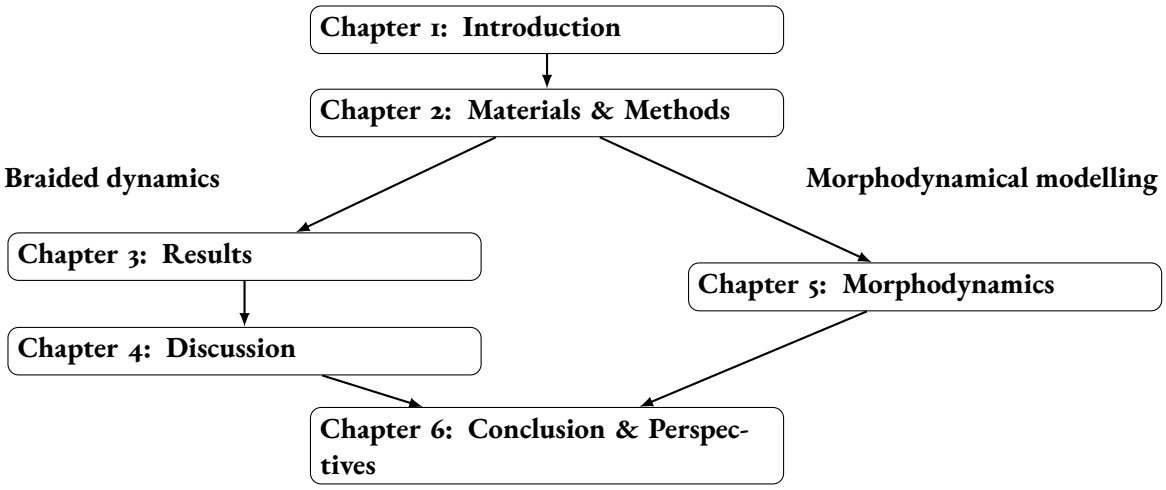

Figure 1.4: Organization of the thesis.

2 Material and methods

2.1 Experimental flume

2.1.1 Experimental flume

The experiments were realized in the hydraulic facilities. They are equipped with high discharge pumps that feed a network of flumes. The experiment was designed from a flume that was previously used for experiments that did not involved braided rivers. A sketch of the flume is shown in Figure2.1. At the upper end of the flume are found the water inlet and the sediment feeder. The water inlet is preceded of a small retention basin connected to one of the high discharge pump. This retention basin serves to break the pressure with which the water enters the flume. The flow is forced to pass through a honeycomb structure to soften its entrance. The sediment feeder is located right after the retention basin, above the water inlet and feeds the flume with dry sediment. It is composed of a hopper containing dry sediment and connected to a vibrating device. The sediment inflow is directly proportional to the vibration intensity. A mobile cart equipped with a camera is mounted on rails above the flume. Using this mobile cart, it was possible to shot the flume at regularly spaced intervals. The pictures are then used to reconstruct the topography with Structure from Motion (SfM, see section 2.3.1). A sediment collector is located at the lower end of the flume and collects the outgoing sediment. This collector is connected to a weight and measures the bedload transport rate (see section 2.3.2).

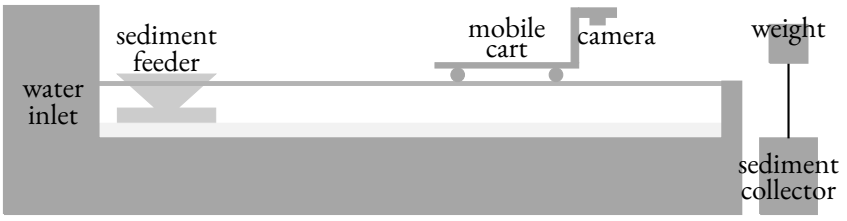

Figure 2.1: Schematic representation of the flume.

The general dimensions of the flume are found on table 2.1.

Table 2.1: Flume dimensions

length L	width W	slope ϑ	discharge Q
12.5 m	2.2 m	0.015	1–100 l/s

2.1.2 Flumes in the literature

There is a large amount of experimental studies on braided rivers in the literature. On table 2.2 a non-exhaustive list of experiments with their main characteristics is presented: the flume dimension, the sediment mean diameter and the water discharge.

Table 2.2: List of experimental investigations on braided rivers

Reference	Flume dimensions $L \times W$	Sediment diameter d_s	Water discharge Q	Bed slope ϑ
Ashmore [1982]	9×1.3 m	1.20 mm	1.2–3 l/s	0.013
Ashmore [1988]	10×2 m	1.16 mm	1.2–3 l/s	0.015
Ashmore [1991a]	10×2 m	1.16 mm	1.2–3 l/s	0.010–0.015
Ashmworth et al. [2007]	5.5×3.6 m	–	1.8 l/s	0.007–0.017
Bertoldi and Tubino [2005]	12×0.6 m	0.50–1.30 mm	0.2–0.5 l/s	0.010–0.020
Bertoldi et al. [2009a]	25×2.9 m	0.63 mm	0.7–1.5 l/s	0.0067–0.016
Davies and Lee [1988]	2×2 m	0.50 mm	1.43 l/s	0.01
Egozi and Ashmore [2008]	20×3 m	1.17 mm	1.4–2.8 l/s	0.040
Egozi and Ashmore [2009]	18×3.3 m	1.20 mm	1.0–3.0 l/s	0.040
Germanoski and Schumm [1993]	18.8×1.8 m	0.87–2.20 mm	2.4 l/s	0.015–0.038
Germanoski and Harvey [1993]	18.8×1.8 m	0.87 mm	2.4 l/s	0.015–0.038
Hoey [1996]	14.2×3 m	0.57 mm	1.9 l/s	0.010
Ikeda [1984]	25×2.9 m	1.00 mm	1.5–2.5 l/s	0.010
Garcia Lugo et al. [2015]	25×2.9 m	1.00 mm	1.5–2.5 l/s	0.010
Métivier and Meunier [2003]	1×0.5 m	500 µm	0.016–0.041 l/s	0.033–0.093
Paola [2001]	11×1 m	2.23 mm	1.8–4.5 l/s	0.016
Pryor et al. [2011]	12×0.8 m	1.00 mm	1.1 l/s	0.030
Tubino [1991][1]	19×0.6 m	1.10 mm	4.9–6.4 l/s	0.007
Warburton and Davies [1994]	20×3 m	0.50 mm	1.4 l/s	0.011
Warburton [1996]	25×3 m	0.50 mm	1.4 l/s	0.011–0.012
Young and Davies [1991]	20×3 m	0.30 mm	0.9–1.4 l/s	0.007–0.011

There is a wide range of possibility in the design of experiments. The dimensions of the flume vary over one order of magnitude for both the length and the width of the flume, from 1×0.5 m to 25×3 m. The sediment diameter is always of the order ot the millimetre, exception made of Métivier and Meunier [2003] where the authors specifically used very small glass beads. Water discharge is in general of the order of the litre per second (exception made again for Métivier and Meunier [2003]). Flume slopes are more variables but are generally found in the range of 0.01. When designing the experiment I faced the following problem: given the experimental facility, how to determine the proper hydraulic conditions to reproduce a braided river experimentally? The answer lies in the similarity theory and is presented in the next section.

2.2 Similarity theory and setup's design

The design of the experimental setup is of the utmost importance in our investigation and in hydraulic engineering in general. In order to investigate experimentally the properties of braided rivers, the experiment actually has to reproduce its dynamics. To do so, the reduced-scale rivers must be similar to the full-scale river: similar in the geometric, kinematic and dynamic sense. This is the fundamental idea behind the principle of similarity. The same principle is used with small-scale plane tested in wind tunnels, where the real plane is scaled down while keeping the same aspect ratio as the real plane and the air flow is adapted to represent the same flying condition. I followed the cardinal works of Yalin [1971], Warburton and Davies [1994], Young and Warburton [1996] to design the hydraulic reduced-scale model. The reader interested in the theoretical aspects of the scaling laws can refer to Barenblatt [2003].

2.2.1 Dimensional analysis

The cardinal concept behind similarity theory is dimensional analysis, *i.e.* the analysis of the relationships between different physical variables by identifying their base quantities (length, mass, time, and electric charge for instance) and units of measure (kilometres, kilograms second and volt). Paraphrasing [Barenblatt, 2003] 'Despite the seemingly simple aspect of dimensional analysis researchers have been able to obtain remarkably deep results that have sometimes changed entire branches of science'. The idea on which it is based is indeed very simple and can be stated on a single phrase understandable by the layman: physical laws do not depend on arbitrarily chosen basic units of measure. An important conclusion can be drawn from this fundamental idea: the functions that express physical laws must possess a certain property, which in mathematics is called generalized homogeneity or symmetry. With this property, the number of arguments in these functions can be reduced, thereby making them simpler to obtain by computation or through experiments. This is the core of dimensional analysis.

The so-called Π-theorem may be stated in the following form: *A physical relationship between some dimensional (generally speaking) quantity and several dimensional governing parameters can be rewritten as a relationship between some dimensionless parameter and several dimensionless products of the governing parameters; the number of dimensionless products is equal to the total number of governing parameters minus the number of governing parameters with independent dimensions* [Barenblatt, 2003]. The Π-theorem incorporates the fact that physical laws are independent of the arbitrary choice of units. A dimensionless relationship of the form has the following advantages:

(i) it is a correct version of a natural law;

(ii) it is a function of a reduced number of variables;

(iii) its numerical value does not depend on the system of units:

(iv) the variable Π_i are the *criteria of similarity* of the phenomenon.

2.2.2 Similarity theory

Principle of similarity

The concept of physical similarity is a generalization of the concept of similarity in geometry. Take two triangles for instance, they are said to be similar if they differ only in the numerical values of the dimensional parameters (*i.e.* the lengths of their sides) while the dimensionless parameters (*i.e.* the angles at the vertices) remain identical. Analogously, two physical phenomenon are similar if the numerical values of their dimensional parameters $x_1, \ldots, x_n$ differs while their corresponding dimensionless parameters $\Pi_1, \ldots, \Pi_m$ remain identical (recall that $n = m + k$ with k the number of basic quantities describing the problem at hand). The quantities $\Pi_1, \ldots, \Pi_m$ are called the similarity parameters. Lets do some nomenclature. The system that is going to be studied is called prototype (for instance the real river) and the parameters related to it are noted with the superscript ^{P}. The reduced-scale model (or simply model) is the system that is going to be designed (for instance the experimental flume) and the related parameters are noted with the superscript ^{M}. The scaling ratio λ_x is defined as the ratio between the model and the prototype for any variable or parameter x, *i.e.*

$$\frac{x^M}{x^P} = \lambda_x. \tag{2.1}$$

Lets consider the example of a hydraulic model representing a real river. If in the model water is used to represent the real stream, then the scaling ratios for the viscosity and density read $\lambda_\mu = \mu^M/\mu^P = 1$ and $\lambda_\varrho = \varrho^M/\varrho^P = 1$ respectively.

Geometric similarity is obtained when the length scaling ratio, namely $\lambda_l = l^M/l^P$ where l is a characteristic dimension, is respected for all the lengths of the model and in all the directions of the model. For instance if one reduces (or increases) the dimensions of a cube by a factor λ_l for two ou of the three sides one does not obtained a geometrically similar cube. This full geometric similarity implies that areas and volumes are scaled by a factor λ_l^2 and λ_l^3 respectively.

Kinematic similarity is obtained when the velocity of the model is a fraction λ_u of the prototype velocity and is in the same direction as in the prototype. An important property of kinematic similarity is that it directly involves geometric similarity. Indeed the velocity u can be viewed as the ration between l and a characteristic time t, so in definitive $\lambda_u = l^M t^P/(t^M l^P) = \lambda_l/\lambda_t$. It means that if, for instance, one wants to build a 1:50 reduced scale model (meaning $\lambda_l = 1/50$) and decide to run the experiment two times faster than in reality (meaning $\lambda_t = 2$) then the ratio of velocities should be $\lambda_u = (1/50)/2 = 1/100$, *i.e.* the velocity in the model should be a hundred times slower than in the prototype.

Dynamic similarity is obtained when the dynamics of the model is similar to the dynamics of the prototype. By virtue of Newton's second law $F = ma$ dynamic similarity also involves massic properties of the system. In a fluid massic properties relate to the density ϱ, the viscosity μ and the surface tension γ. The idea of dynamics similarity is that the model has to reproduce the force ratios of the prototype. Let's illustrate the concept of force ratio with the following example: when an aircraft flies, if the thrust is two times greater (in amplitude) than

the drag, then when building a reduced-scale model this force ratio should be maintained. In fluid mechanics there are two types of forces: body forces such as the weight under a gravitational field and surface forces such as viscous forces, pressure gradients or surface tension forces. In hydraulics surface tensions effects are in general negligible as long as the model is large enough, for very small model surface tension effects start to appear (see Métivier and Meunier [2003] in table 2.2 for instance). Gravity is the driving force of free surface flows while viscous forces are the driving forces of sediment transport. In order to respect dynamic similarity between a real river and a laboratory river, the ratio between these two forces have to be maintained in the reduced-scale model.

With the Buckingham−Π theorem, it is possible to determine the dimensionless numbers that govern the flow and also the similarity criteria. In hydraulics flows, two numbers are of particular importance, the Reynolds number and the Froude number:

$$\mathsf{Re} = \frac{\varrho u l}{\mu}, \quad \mathsf{Fr} = \frac{u}{\sqrt{g l}}. \tag{2.2}$$

They represent the importance of viscous effects and gravitational effect respectively. To be more precise they represent the relative importance of inertial forces over viscous forces for Re and the relative importance of the kinetic energy of the flow over the potential energy (hence the gravitational energy) for Fr. In a sense they are the dynamic similarity criterion that any hydraulic model has to respect, *i.e.* $\lambda_{\mathsf{Re}} = \lambda_{\mathsf{Fr}} = 1$. By definition of both number the dynamic similarity criterion implies that

$$\frac{\lambda_\varrho \lambda_u \lambda_l}{\lambda_\mu} = \frac{\lambda_u}{\sqrt{\lambda_g \lambda_l}}. \tag{2.3}$$

If in both the model and the prototype water is used and the gravitational acceleration g is kept the same, then dynamic similarity implies $\lambda_l = \lambda_u = 1$, *i.e.* the only way to achieve perfect dynamic similarity is to use a full scale model!

To overcome this limitation the only way to proceed is to determine which of the forces acting on the hydraulic system are the most relevant. In open channel flows the gravitational force is predominant since it is the main driver of the flow. It is thus fundamental to respect the Fr similarity between the prototype and the model. Viscous forces can be neglected provided some precautions are taken. In particular as long as Re is sufficiently high one can consider that viscous forces dominate over inertial forces and thus the dynamic similarity of viscous forces between the prototype and the model is respected. This is true because in general the flow resistance does not depend on the viscosity (like in the Chézy law or Manning law) when $\mathsf{Re} > 100$.

To conclude, when water is used in a reduced-scale hydraulic model full dynamic similarity is impossible. To overcome this difficulty, the dynamic similarity is restricted to the Froude number only, *i.e.* $\lambda_{\mathsf{Fr}} = 1$. By partially satisfying similarity in the Reynolds number,*i.e.* by respecting $\mathsf{Re}^M > 100$, it is ensured that at least the ratio of inertial to gravitational forces is respected in the model and that viscous forces are negligible in the model (perhaps not as negligible as in reality but at least they are to some extent). This is the whole idea behind Froude similarity and is at the core of model design. It will be used to its full extent when modelling a river with sediment

transport in it.

2.2.3 Similarity in hydraulic models

General case

As showed in the previous section, using water and the same gravitational acceleration in the model hinders dynamic similarity and forces to use a partial similarity criterion. However the selection of the scaling ratio was not discussed, especially of how many of them and how they are chosen.

Hydraulic systems are a subsets of mechanical systems, and therefore three fundamental units are at play in those systems. Only three dimensionally independent variables are needed to express any dimension of the system. It means that provided that there are three scaling ratio, say λ_a, λ_b and λ_c of three dimensionally independent variables a, b and c, then those ratio uniquely define the scaling ratio of the system. In other words, one needs to choose only three scaling ratio.

In our particular case both λ_μ, λ_ϱ and λ_g are determined by water and gravity. Yet g and ϱ (or g and μ) are dimensionally independent variables. It means that there is only one free scaling ratio to design the experiment. The last dimensionally independent variable relevant to hydraulics is the length of the model, *i.e.* the scaling ratio which in turn defines the geometric similarity. In other words when using water, the scaling ratio λ_l is the only free choice when building the hydraulic model. Once λ_l is chosen, the rest of the scaling ratios are automatically determined by the similarity principles. How this scaling ratio is chosen will be answered in the next section.

Up until now the attention was focused on Fr and Re, which are the most important dimensionless numbers but not the only ones. The Buckingham$-\Pi$ theorem will now be used to determine all the relevant dimensionless numbers to model a hydraulic system with sediment transport.

A fluvial system coupled with sediment transport is a particular case of a mechanical system without thermal or electromagnetic interactions. It is then completely described by 3 fundamental units, they are generally chosen to be length L, mass M and time T. Therefore the number of independent variables in a fluvial system is always at most $k = 3$. The governing parameters are directly related the problem and a good understanding of the underlying physics is needed to enumerate the relevant ones. Sparing the details (they are found in Yalin [1971] for instance) the governing parameters are classified into three categories:

1. the physical properties of the fluid: its density ϱ of dimension ML^{-3} and its viscosity μ of dimension $ML^{-1}T^{-1}$;
2. the physical properties of the sediment: its density ϱ_s of dimension ML^{-3} and its characteristic length d_s of dimension L;
3. the base flow, or uniform flow over an flat inclined bed: in this case the governing equation of motion reduce to the simple expression $\tau_b = \varrho g h \sin\theta$. Are considered as governing parameters: the gravitational acceleration g of dimension LT^{-2}, the flow depth h of dimension L and the bed slope of dimension 1 or $[-]$ (dimensionless).

Following Yalin [1971] the shear velocity is used $v_* = \sqrt{gh\sin\theta}$ to relate both the slope and the gravitational acceleration and the specific weight of grains in fluid $\gamma_s = (\varrho_s - \varrho)g$. There is a total of 7 governing parameters from which three are chosen and form the set of independent parameters. d_s, v_* and ϱ are chosen. The Buckingham-Π theorem thus states that four dimensionless parameters completely characterize the flow. They are

$$\Pi_1 = \frac{\varrho_s}{\varrho}, \quad \Pi_2 = \frac{v_* d_s}{\nu}, \quad \Pi_3 = \frac{h}{d_s}, \quad \Pi_4 = \frac{\varrho v_*^2}{\gamma_s d_s}, \tag{2.4}$$

where $\nu = \mu/\varrho$ is the kinematic viscosity. Π_2 is nothing more than the Reynolds number and Π_4 is the Shields number θ. The Shields number is the ratio between viscous forces and the buoyant weight of particles and is the critical number describing the sediment transport phenomenon. In particular one should ensure that in both the prototype and the model θ is kept constant in order to have dynamic similarity in the bedload transport process. In practice it is sufficient to ensure that in the model θ is sufficiently above the critical shear stress, *i.e.* $\theta^M > \theta_{cr}$.

Perfect dynamic similarity between the hydraulic model and the prototype (the real river) is impossible, as demonstrated earlier. However, provided that some conditions are respected,a partial dynamic similarity called Froude similarity is achieved. These conditions are the following:

- $\mathsf{Fr}^M = \mathsf{Fr}^P$: there must be Froude similarity (the most important condition to be respected);
- $\mathsf{Re}^M > 100$: the flow has to be hydraulically rough;
- $\theta^M > \theta_{cr}$: the Shields number should be above the critical Shields number.

Once these conditions are met, it is possible to relate the scaling ratios of all the dependent variables of the problem to the three scaling ratios defined by the set of independent variables used, *i.e.* λ_l, λ_ϱ and λ_g. These ratio are

$$\lambda_{d_s} = \lambda_l, \quad \lambda_\vartheta = 1, \quad \lambda_Q = \lambda_l^{5/2}. \tag{2.5}$$

In other words once the scaling ratio λ_l is chosen, then the sediment size, the slope of the flume and the discharge are automatically defined. The last remaining question to be solved is how is this scaling ratio chosen.

2.2.4 Hydraulic model design

The only free scaling ratio is λ_l, *i.e.* the length scaling ratio. In theory, the model should be based on a real braided river reach and λ_l chosen according to the dimensions of the flume. For instance having a flume of 12.5×2.2 m, a reach of say 20×5 km with a length scaling ratio of approximately $\lambda_l = 6.25\ 10^{-4}$ could be modelled. In practice I proceeded otherwise. Ashmore [1988] among others have designed its experiments based on a braided reach of the Sunwapta River in Alberta, Canada. They used the geometric scale of $\lambda_l = 1/20$ to design their model (see table 2.2). Their flume is very similar to mine, 10×2 m long in their case compared to 12.5×2.2 m

in mine. Their setup was used as the prototype and my setup as the model to define the geometric scaling ratio λ_l. Because their flume is a little bit smaller than ours, it turned out to be an upscaling rather than a downscaling of the prototype.

Both flume's lengths were used to define λ_l, *i.e.* $l^P = 10$ and $l^M = 12.5$. It yields a geometric scale of $\lambda_l = l^M/l^P = 1.25$. Following equations (2.5) the corresponding sediment diameter, slope and water discharge is computed:

$$d_s^M = \lambda_l d_s^P = 1.45\,\text{mm}, \quad S^M = 1 \cdot S^P = 0.015, \quad Q^M = \lambda_l^{5/2} Q^P = 2.1 - 5.25\,\text{l/s}. \tag{2.6}$$

The choice of the sediment was mostly constrained by economic as well as practical reason. Quartz sand of 1.1 mm median diameter had to be bought, which is close to the sand used in Ashmore [1988]. The water discharge, although being determined theoretically, serves as the adjustment variable to ensures that our setup did produced braided rivers. The discharge was tested to ensure that the system was indeed braiding even with these sediments.

It is of primordial importance for the Froude number to be in a range close to unity, as braided rivers naturally occur for transitional flows at the limit between super and sub critical flows [Warburton and Davies, 1994]. Ashmore [1988] model was based on a reach of the Sunwapta river where Fr was found in the range 0.41–1.08. The Shields number is notoriously difficulty to be measure especially in braided rivers. It is quite hard to evaluate properly the shear stress and it is not self-evident to measure it (by the mere existence of several channels in braided rivers). Fr, Re and θ were estimated theoretically by considering an initial straight channel under the flow conditions presented in equation (2.6). The results, as well as the main characteristics of the flume are summarized on table 2.3 below.

Table 2.3: Experimental parameters of the flume.

L	W	S	Q	d_s	Fr	Re	θ
12.5 m	2.2 m	0.015	2 l/s	1.1 mm	0.8–1.5	250	0.5
$\boldsymbol{\lambda_l}$	$\boldsymbol{\lambda_l}$	$\boldsymbol{\lambda_S}$	$\boldsymbol{\lambda_Q}$	$\boldsymbol{\lambda_l}$	λ_{Fr}	λ_{Re}	λ_θ
1.25	1.25	1	1.75	1.25	1	1	1

2.3 Measurement devices

2.3.1 Bed elevation and Structure from Motion

Structure-from-Motion (SfM) is a technique that reconstructs three-dimensional structures from a sequence of images. It belongs to the broader field of photogrammetry, which is defined by the American Society for Photogrammetry and Remote Sensing (ASPRS) as: 'Photogrammetry is the art, science, and technology of obtaining reliable information about physical objects and the environment, through processes of recording, measuring, and interpreting images and patterns of electromagnetic radiant energy and other phenomena.'

SfM works on the principles of stereoscopic photogrammetry: a series of overlapping picture is used to recreate

the three dimensionality of the studied object. The characteristic property of SfM lies in its ability to solve automatically the location and orientation of the camera without any a priori knowledge of its position. It is solved automatically by a highly redundant, iterative bundle adjustment algorithm based on features detected in the set of pictures (see Snavely et al. [2008] for more details on the method). This approach is thus ideal for highly overlapping pictures of a given scene such as our experimental setup. To determine the real dimensions of the scanned scene, SfM requires the precise location of some control points, the Ground Control Points (GCP). They can be set manually (thus defining a local frame of reference) or using points with precisely known GPS coordinates. GPS coordinates are better suited for field work whereas local GCPs are better suited for experimental works.

In addition to its technical specification SfM posses several practical aspects. It require little to no installation equipment. In theory the picture can be taken from anywhere provided that the GCPs remain fixed. In practice however, a mobile system like a moving cart (see in Figure2.1) is ideal for an automated acquisition. Any camera will work provided that the pictures taken cover the area of interest with an appropriate overlap. The greater the camera resolution, the higher the precision of SfM. That being said any non-blurred set of picture is in principle sufficient. The constant increase in computational power has also helped overcome one of the main drawbacks of SfM, namely the processing time and power needed to make it work. Today any regular computer is good enough to process a set of pictures at a reasonable time (of the order of 30 minutes per set). For all these reasons I decided to go for SfM to determine the bed elevation.

We used a Nikon D7000 mounted on a mobile chariot to scan the flume. Each picture is taken at a distance of approximately 1.5 m of the bed, meaning that they have a resolution of $\approx$ 0.3 mm/pix. The flume is scan by shooting the river bed every 20 cm on a total distance of $\approx$ 11 m for a total of 53 pictures per scan. On the left and right sides of flume are installed the GCPs. They are regularly spaced on a rectangular grid to maximize the performance of the SfM algorithm, and they are tagged by uniquely identifiable markers that are detected automatically by the SfM software. The disposition of the GCP is shown in Figure and an example of marker is shown in Figure 2.2.

Figure 2.2: GCPs and markers of the fume for SfM

There is a large choice of SfM softwares, and the vast majority of them offer academic licences at an affordable price. The software Pix4D was used. It is a professional SfM software that also offers academic license. After processing the images Pix4D returns the bed elevation in the form of a geo tiff image. It is basically a greyscale image where the shade of grey encodes the altitude information. The geo tiff is ultimately imported and treated as arrays (matrices) of bed elevation with Python.

2.3.2 Bedload time-series

The bedload is measured by weighting the outgoing sediment collected in the basket located at the downstream end of the flume (see figures 2.1). I originally planned to also measure the bedload optically by particle tracking velocimetry (PTV), *i.e.* tracking the individual sediment particle and measuring their velocity. This method requires a complex installation: a white board where it is possible to film the passing sediments; high speed camera to track them; proper lighting; a large computational power and large memory to treat the data and store it. The method was working but with a considerable amount of drawbacks; especially the data storage and computations which required too much memory to store the data in addition to the processing time (the idea was to compute the bedload with a precision of the order of the second). All things considered, a simple yet precise weighting of the sediments was used to measure the mass balance and from it extrapolate to have an averaged bedload measurement.

2.4 Methods

2.4.1 Edge detection

I developed a procedure to quantify the braided pattern from the bed elevation to have an alternative measurement in order to assess the results obtained by the Low Path method. The idea is to extract a 'footprint' of a given braided pattern consisting of only binary information. In other words, a black and white image containing the relevant information about the pattern. Scheidt et al. [2016] and Hoffimann et al. [2019] used a similar approach. In their experiments, they dyed the water in blue and with an appropriate algorithm were able to extract the channel network as a black and white image. In our case, a similar technique was not a viable option since the water is shared with other experiments.

The idea behind the method, called Edge Detection, is the following: to convert the topographic data into a greyscale image, the shades of grey representing the bed elevation, and from the greyscale image extract features representing the braided pattern. The most distinctive features of the braided pattern such as banks, scour holes, bends etc appear quite distinctively on a greyscale image by the sharpness of the intensity gradient, which reflects the elevation gradient. The sharper the gradient, the higher the contrast on the greyscale. Combining the Canny edge detection method [Canny, 1986] with a preprocessing filter (Gaussian blur), it is possible to build an image containing only the most salient edges for a given bed elevation. An example is shown in Figure2.3 where the detected edges are depicted in green.

Only the most relevant morphological features are detected. Regions with low elevation variations do not exhibit strong colour gradients and consequently are not detected by the Edge Detection algorithm. The method can be fine tuned to exhibit longer edges. However there is a point where noise starts to appear. The parameters of the algorithm were optimized (mostly by visual inspection) to detect the important features while minimizing the noise. The data obtained is a black and white image where the white pixels are the points corresponding the edges. This image is transformed into a matrix of points whose coordinates correspond to the real location of the edges. The matrix forms a set of point in a metric space that can be analysed with the Hausdorff distance presented in the next section.

Figure 2.3: Edges detection algorithm

2.4.2 Modified Hausdorff distance and DBSCAN clustering

To quantify the variation of the braided pattern in time, a robust tool is needed to properly measure and identify its evolution. Following Scheidt et al. [2016], Hoffimann et al. [2019], a metrics based on the Hausdorff distance was used to measure the similitude (in our case the dissimilitude) between patterns and thus quantify their evolution in time. The Hausdorff distance is a measure of the distance between two subsets of a metric space (V, d) where d is the Euclidean distance. It is widely used in computer vision in object matching algorithms [Dubuisson and Jain, 1994]. By definition, object matching aims at minimizing the distance separating two objects. In our case matching patterns is not exactly the goal. The goal is to gather patterns that look similar and identify them as modes/states of the braided river (both terms will be used indistinctively). To achieve it, a combination of the Hausdorff distance with a clustering algorithm will be used. Again, this idea is inspired by Scheidt et al. [2016], Hoffimann et al. [2019].

Mathematically the Hausdorff distance is a measures how far two subsets X and Y of a metric space (V, d) are from each other. It is defined as

$$\delta_H(X, Y) = \max\left(\sup_{x\in X}\inf_{y\in Y} d(x, y), \sup_{y\in Y}\inf_{x\in X} d(x, y)\right), \tag{2.7}$$

where inf is the infimunm and sup the supremum and X and Y are the two sets whose distance is being measured. In this thesis, a modified version of δ_H is used. It is simply called Modified Hausdorff Distance (MHD) and noted δ_{mhd} [Dubuisson and Jain, 1994]. It works in the following manner:

(i) it evaluates the distance between X and Y and the distance between Y and X (which can differ);

(ii) the maximum of these two distances is taken as δ_{mhd}.

The distance between a point x and a set Y is noted $d(x, Y)$. It is defined as the distance of x to the closest point $y \in Y$

$$d(x, Y) = \min_{y\in Y} \|x - y\| . \tag{2.8}$$

The distance $d(X, Y)$ between two sets X and Y is the average of those distances

$$d(X, Y) = \frac{1}{N_x} \sum_{x \in X}^{N_x} d(x, Y). \tag{2.9}$$

In order to respect the fundamental property of a distance, namely that $d(X, Y) = d(Y, X)$ which by definition of (2.9) is not always the case, δ_{mhd} is defined as the maximum distance between X and Y

$$\delta_{mhd}(X, Y) = \max(d(X, Y), d(Y, X)). \tag{2.10}$$

δ_{mhd} can be used to measure the distance between curves as well. Indeed, a curve is a set of points. The important prerequisite to use δ_{mhd} is that the sets upon which it is applied must be subsets of a metric space. In general the Euclidean distance is used to measure distances, provided that the coordinates of each points in the subsets are properly defined. In our case, when measuring the distances of patterns obtained from the Edge Detection method (see in Figure2.3 in section 2.4.1) each points have the real world coordinates of the braided pattern (which belongs to the Euclidean space). When comparing two curves representing the time variations of a given variable, say the temporal evolution of the bedload q_s in two different experiments for instance, each points of the curve have a coordinate $(t_i, q_{s,i})$ in the plane (space) $t - q_s$ which is not a metric space strictly speaking. To overcome this difficulty, these curves are rendered dimensionless in order to have a collection of points in the plane $[0, 1] - [0, 1]$. More detail is found on appendix A.3.

The DBSCAN (density-based spatial clustering applications with noise) clustering algorithm was used to detect potential clusters of morphological patterns. Clustering algorithms are a class of algorithm used in knowledge discovery in database (KDD) processes with the particularity that they are able to identify clusters, *i.e.* grouping of objects closely related according to some particular requirement Ester et al. [1996]. DBSCAN algorithms use a minimum density level estimation to detect clusters, the density being based on the minimum number of neighbours n_{neigh} within a given radius ε. Points with more than n_{neigh} neighbours (including the query point) within the radius of inquiry ε are considered core points. All points within a radius ε of a core point are considered to be part of the cluster of points. If a point is in the cluster but does not have enough neighbours then it is considered to be a border point of the cluster. A point which is not reachable to any core point is considered to be noise and do not belong to any cluster.

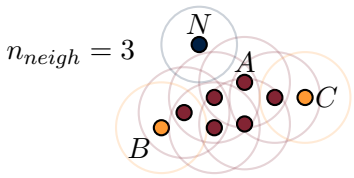

Figure 2.4: Illustration of the DBSCAN cluster model. The radius ε is depicted as the coloured circle around the points. Red points (A) are the core points, yellow points (B and C) are the border points and the blue point is noise (N). The figure is taken from Schubert et al. [2017].

in Figure2.4 illustrates the working principles of DBSCAN. A is a core point (and all subsequent red points); observe that each of them possess at least two neighbours, the radius of inquiry being the red circle around each points. B and C are border points, since they belong to the cluster (they have at least on neighbour inside the cluster) but they do not fulfil the number of neighbours condition (in this case three neighbours). N is a noise point since it has no core point within the radius of inquiry. For simplicity no distinction will be made between border points and core points, both being identified as core points. Only noise points will be differentiated from core points.

2.4.3 Fréchet distance

The Fréchet distance is a measure of the similarity between two curve in a metric space. It can be viewed intuitively as follows: a man walks a dog on a leash, both the man and the dog move on different paths. Each path represents the two curves whose similarity is measured. The man and the dog can move on each respective path varying their speed but are not allowed to backtrack. The Fréchet distance is basically the answer to the following question: what is the length of the shortest leash that is sufficient fo traversing both curves? By definition the Fréchet distance takes into account the ordering of the curves, in other words and reusing the man and dog metaphor, the Fréchet distance takes into account the direction of travel along the curves. It is more sensitive than the Hausdorff distance to the shape of curves, and more specifically to the variations of the shape. Its formal mathematical definition is given in appendix A.4.

The Fréchet distance, noted δ_{Fr}, will be used as a tool to compare the temporal evolution of the morphological variables (see section 4.1). However, similarly to the Hausdorff distance, δ_{Fr} is defined on a metric space. The compared variables thus need to be expressed in a metric space in order to measure their similarity properly. WThe same non-dimensionalization procedure mentioned in section 2.4.2 will be used. Again more detail is found on appendix A.4

2.4.4 Low Path method

Kleinhans et al. [2017] developed an algorithm that extracts the braided network from the DEM of a braided river. The braided network is represented in the form of a graph, where by graph is intended a series of edges/links and nodes connected together (the mathematical definition of a graph found in Harary [1969]). This algorithm, named Low Path, has been developed especially to reconstruct the complex network of channels exhibited in braided rivers. An example of graph generated by the Low Path algorithm from a bed elevation is shown in Figure2.5.

The Low Path algorithm was developed to extract the network-like structure of braided rivers from bed elevation data only and to represent it in terms of nodes and edges, *i.e.* in the form of a graph. The edges represent the channels of the braided pattern while the nodes represent confluences. These channels are intimately linked to the notion of thalweg, *i.e.* the path corresponding to the lowest points on a given topography. Indeed, rivers generally flow along the path of steepest descent. In braided rivers however it is not always the case since channels can split and merge, hence they dot not always following the path of steepest descent but several local paths of steepest descents. This notion of thalweg is the core concept behind the Low Path algorithm.

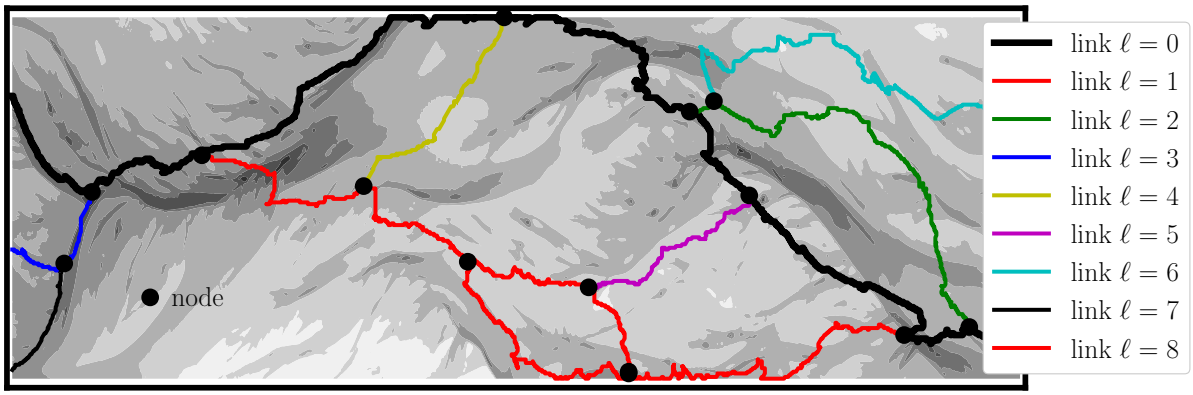

Figure 2.5: Example of bed elevation field with its corresponding braided network. The shades of grey represent the altitudes of the bed elevation, with darker shades corresponding to lower points in altitude and vice-versa. In thick black line is depicted ℓ_0, while others links ℓ_i are depicted in coloured thinner lines. The black circles represent the nodes (junctions between two edges) of the network.

The starting point of the modelization of braided river is the bed elevation data. The authors defined the lowest paths followed by braided channels as 'the paths that do not go higher than they need to go to connect the endpoints' [Kleinhans et al., 2017], where the endpoints are the two ends points of the bed elevation. To find such paths the author use a descending quasi Morse-Smale complex algorithm (for more details see the original work of Kleinhans et al. [2017] and the references therein). This method computes a great number of channels that are not physically meaningful. To discriminate between them the authors introduced a differentiation criterion, the so-called sand function. Paraphrasing again Kleinhans et al. [2017] for the clarity of their explanation, its definition reads: '[the sand function] relates to the volume of sediment the river has to move before the two channels become one. More volume needs more time to be removed. A bar of very small volume separating two channels requires insignificant time to be removed, so the channels are not significantly different. However a large bar with a large volume may require multiple floods to be shaved off or cut through by a new channel, meaning that the two channels separated by this bar are significantly different.

in Figure2.5 shows the bed elevation in greyscale, the computed links of the graph in coloured lines and the nodes of the graph in black points. Darker shades of grey correspond to deeper regions of the bed elevation. Each link ℓ_i is noted with the subscript i corresponding to the rank of the link. The numbering starts from 0 which is the rank of the main link, the one representing the global thalweg. Each link have a characteristic parameter called significance s. It relates to the rank of each link ℓ_i, with link ℓ_0 having the higher significance $s_0 = \infty$. By definition $s_i > s_{i+1}\ \forall i \geq 1$. The higher the rank of a link the lower its significance. It is possible to generate a graph with a given number of links or in functions of their significance.

Each link posses a length noted L_{ℓ_i} and is made of a collection of points of coordinates (x_k, y_k). Each node is defined by its position in coordinates (x_n, y_n) and is rank r, where r corresponds to the highest rank of the junction. For instance if a node is at the junction of a rank 1 and rank 2 link, then the node is of rank 1.

There are two ways to generate a graph such as the one displayed in Figure2.5, choosing the number of links (in this case there are 9 links) or choosing the links above a certain significance threshold. This second procedure

ensures that the graph have a certain physical reality. Indeed the lower s the higher the number of links, but there is a point were the Low Path algorithm generates artificial links. The author recommended (by personal communication) to check manually the proper significance value in order to generate graphs that represent the actual braided river. The graph displayed in Figure2.5 is computed with $s_{thr} = 0.047$. The rest of the graphs are computed with the same s_{thr}. It has been chosen because it correspond to the significance that most closely relates the graph to the actually observed river network. I stress out the fact that even though s_{thr} have been carefully chosen to best represent the actual river network in some cases it fails. In some bed elevations links and nodes are artificially generated and do not correspond to the exact braided stream. Nevertheless this situation was the exception rather than the norm. On average and over the whole set of experimental data the error relative to false positive links and nodes is relatively small.

2.5 Markov process

A Markov processes is a stochastic process describing a sequence of possible events in which the probability of each event depends only on the state attained in the previous event [Gagniuc, 2017]. It has the property of being memoryless, meaning that the next step only depends only on the current state. In other words, knowing the present of a system is the only relevant information to derive its future.

Markov processes possess interesting properties that have facilitated their usage in many areas of science. The reader may refer to Gardiner [1985] for a more insightful list of examples. One in particular have captured our attention, it is an investigation on mathematical information theory made by Shannon [1948]. In his seminal paper, the author investigated the possibility to generate words and sentence from the statistical distribution of letters and words obtained from literature. Using an algorithm based on Markov processes, he was able to generate sentences. In other words, the Markov process was able to reproduce (in a certain sense) the grammar without knowledge of the rules a priori. This property attracted our interest: to the present day, the mechanisms governing the braided dynamics are unknown but they could be grasped by means of a Markov process.

Hoffimann et al. [2019] recently used a combination of stochastic methods (among which a Markov process) to generate synthetic images of a braided delta. They obtained, from a set of experiments, a statistical distribution of modes/states of the braided delta and derived probability of transitioning between the modes. From experiments, it was possible for the authors to obtain informations about the evolution of the braided system, in a statistical sense, that was then used by a Markov chain to simulate the braided dynamics (regardless of their understanding of the physics behind). It is analogous with Shannon [1948]'s model where he was able to reproduce grammatically correct phrases from statistics obtained from literature. With these examples in mind, I will develop a Markovian framework to study the braided dynamics with results obtained from our experiments.

First, lets briefly introduce Markov processes, or the kind of Markov processes that are going to be used. A simple discrete Markov process can be seen as a collection of discrete states $S_1, S_2, \ldots, S_n$. In addition there exist a set of transition probabilities p_{ij} that correspond to the probability of transitioning from S_i to S_j. This probabilities must respect certain conditions, the most important being $\sum_j p_{ij} = 1$. It simply means that whenever the system is in state S_i there is certainty the it will evolve to another state S_j. A graphical representation of a Markov process with 3 states is shown in Figure2.6.

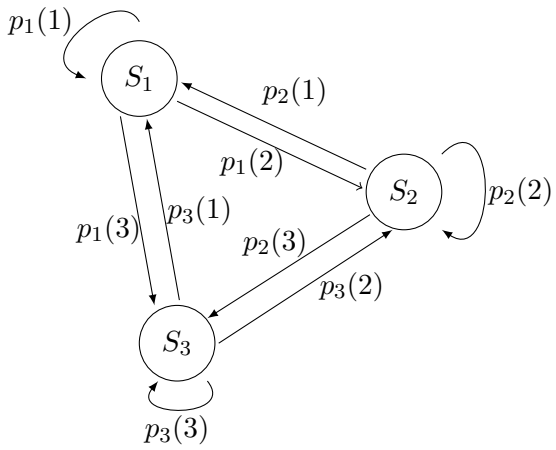

Figure 2.6: Graphical representation of a Markov process. The transition probabilities p_{ij} are the arrows, their direction indicates the transition towards the corresponding state.

In Figure2.6, each circle represents a state and each arrow represents a transition probability. Each state can transition to any of the existing states, thus implying 3^2 probabilities (in the general case it would be n^2 probabilities for n states). Each of these transition probabilities are collected in a transition matrix written as follows

$$p_{ij} = \begin{pmatrix} p_{11} & p_{12} & p_{13} \\ p_{21} & p_{22} & p_{23} \\ p_{31} & p_{32} & p_{33} \end{pmatrix}, \quad i, j = 1, 2, 3 \tag{2.11}$$

where each row i corresponds to transition from state S_i to any state S_j (recall the property $\sum_j p_{ij} = 1$). The transition probability matrix is then written, in the most general form for n states and $n \times n$ transitions probabilities

$$p_{ij} = \begin{pmatrix} p_{11} & p_{12} & \cdots & p_{1n} \\ p_{21} & p_{22} & \cdots & p_{2n} \\ \vdots & & \ddots & \vdots \\ p_{n1} & p_{n2} & \cdots & p_{nn} \end{pmatrix}, \quad i, j = 1, 2, \ldots, n. \tag{2.12}$$

Suppose that, for any reason, we are able to identify states that accurately represent the braided river. Suppose that we are able to provide a probability of occurrence to theses states, in other words, to the frequency with which theses states appear. Let us note $\mathscr{S}_m = \{S_1, S_2, \ldots, S_m\}$ the collection of m states and $\mathscr{P}_m = \{p_1, p_2, \ldots, p_m\}$ their respective probabilities. Supposing that, when the braided river is in a given state s_i, it has a certain probability $p_{i,j}$ to switch to another mode s_j (with $i, j = 1, 2, \ldots m$) and that this probability only depends on the current state s_i, then a Markov process is the natural candidate to simulate such system.

The issues are twofold:

1. are we able to identify hypothetical states S_i of the braided river?
2. are we able to obtain the probabilities p_i of these states, and their transition probabilities p_{ij}?

The combination of Low Path, DBSCAN and δ_{mhd} will provide us a method, called *modal analysis*, whose goal is to identified states. A detailed description of the *modal analysis* will be provided in Chapter 3. Summarising briefly its working principles, it consists in the three following steps:

- Low Path applied to DEM provides the braided network in the form of a graph;
- δ_{mhd} measures the difference between these graphs;
- DBSCAN regroups together similar graphs and identifies them as modes (the states mentioned earlier).

Applying the *modal analysis* to our experimental results, we are then able to obtain the modes' probabilities, both p_i and p_{ij}. Once obtained, we will be able to use them in simulations. The algorithm used for our Markov process is presented in appendix A.2.

3 Results

3.1 Preliminary considerations

In section 2.2, dimensional analysis and similarity theory were used to design the experiments. However, some practical issues remain. Feeding the flow with an appropriate sediment flux is crucial if one wants to maintain the river bed at a constant level on average, *i.e.* neither eroding nor aggrading (no net increase or decrease of the river bed slope on average either). A proper timescale to scan the river bed is needed if one wants to capture the relevant morphological changes. Continuous data acquisition is not possible for several reasons:

- it has a prohibitive data cost and processing time cost: each scanning of the bed weights more than 10 GB in raw data. Additional memory is also needed during the post-process for a final result of approximately 400 MB/scan in geotiff images and each processing last about 30 minutes;
- it is expensive: a continuous scanning technique would require an automated system which we did not have funds for, in addition the experimental flume was not particularly adapted to bear the equipments needed and would have required lengthy and costly works to be fully prepared;
- it lacks scientific value: as shown by Vesipa et al. [2017] a continuous monitoring of a braided river does not necessarily highlight the braiding dynamics which acts on a relatively large time-scale.

A detailed discussion about how these two issues were treated is found on appendix A.1. Here, the main results are summarized:

- the sediment influx $q_{s,in}$ is first estimate by mean of Recking's bedload formula [Recking et al., 2009] for the first hours of both experimental runs and afterwards the outgoing sediment is recirculated in the flume to ensure sediment mass balance;
- $q_{s,out}$ is measured every $\Delta t = 60$ min at the flume outlet by weighting the outgoing sediments;
- the bed topography is measured every $\Delta t = 60$ min to ensure that all the relevant morphological changes are captured and to avoid stopping the experiment too often.

Lets recall the goal of the experiments: to study and quantify the evolution of a braided river's network experimentally and relate it to the hydraulic conditions. To do so, the attention is focused on two stages of the development of a braided river. In the first experiment (called run 1), the emphasis is put on the evolution of a straight channel into a fully braided river. In the second experiment (called run 2), the evolution of a fully developed braided river with the same hydraulic conditions as in run 1 is monitored. By comparing both runs, I want to properly characterize the equilibrium state in contrast to the transition state, especially to assess the braided network in both stages. In table 3.1 below are recalled the main hydraulic conditions of both runs.

Table 3.1: Experimental conditions

run	duration	water discharge	sediment diameter	slope	braided regime
1	35 h	2 l/s	1 mm	1.5 %	transitory
2	100 h	2 l/s	1 mm	1.5 %	developed

3.2 Bedload time-series

In this section, the attention is focused on the outgoing bedload, $\bar{q}_{s,out}$. Recall that it is measured by weighting every $\Delta t = 60$ min the mass of sediment that leaves the flume. It thus writes

$$\bar{q}_{s,out} = \frac{\Delta m}{\Delta t} \tag{3.1}$$

where Δm is the weighted mass. From now on, the bedload outgoing flux is simply written as $\bar{q}_s$ instead of the more cumbersome $\bar{q}_{s,out}$.

The bedload time-series and the other relevant variables are presented in Figure 3.1. The red curves correspond to run 1 whereas the yellow curves correspond to run 2. To simplify the comparisons between both experiments the time is plotted in two different axis, the lower x–axis corresponding to run 1 and the upper x–axis corresponding to run 2. Figure 3.1 (a) shows the time-series of bedload in run 1 and 2. Figure 3.1 (b) shows the cumulative mass of the outgoing bedload transport and the theoretical cumulative mass obtain by integrating the average bedload $\bar{q}_s$. Figure 3.1 (c) shows the temporal evolution of the total eroded volume of the river bed v_e. Figure 3.1 (d) shows the temporal evolution of the cumulative eroded volume V_e. In plots (a), (c) and (d) are depicted for clarity the moving average $\mathrm{mov}()$ of q_s, v_e and V_e. The moving average is computed over the two neighbours of the point at hand, namely

$$\mathrm{mov}(x_i) = \frac{1}{5} \sum_{j=i-2}^{i+2} x_j. \tag{3.2}$$

The general trend of $q_s(t)$ in run 1 is to globally increase until reaching an equilibrium so to speak (see Figure 3.1 (a)). This trend is more clearly observed on the moving average curve (red dashed line). Notice that in both runs $\bar{q}_s$ is virtually equal (less than 2.5 % maximum relative difference between the two). Unlike in run 1, q_s fluctuates around its mean during the entire duration of run 2. Looking carefully at $\mathrm{mov}(q_s)$ (yellow dashed line) two

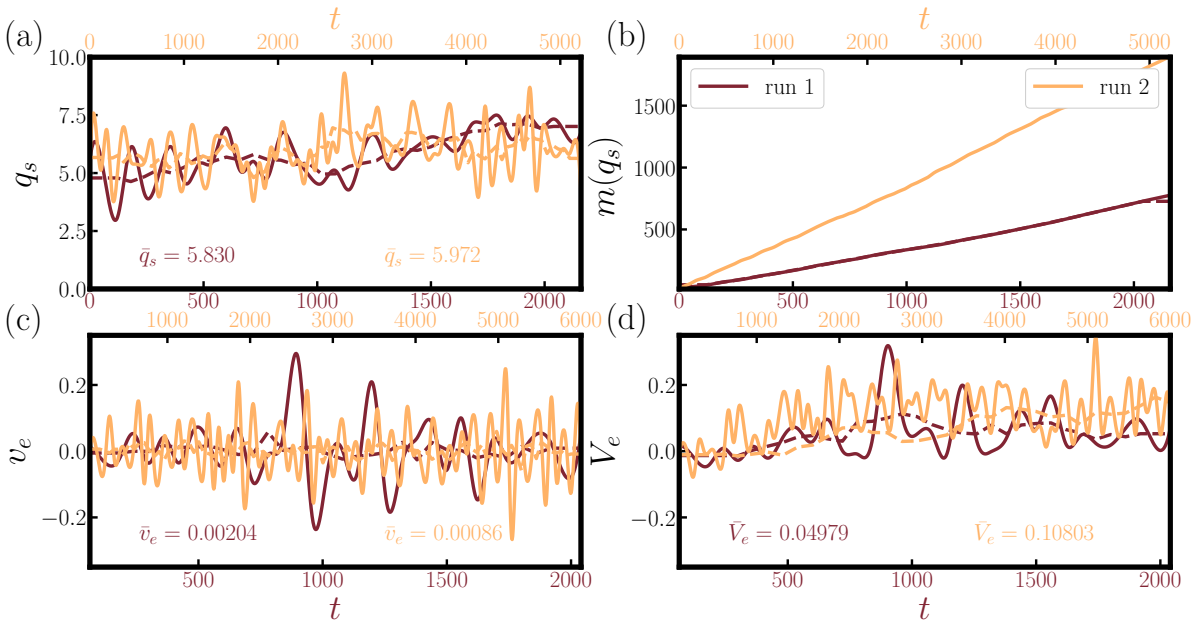

Figure 3.1: Temporal evolution of the bedload transport rate in run 1 and 2. Plot (a) displays the temporal evolution of q_s; plot (b) displays the cumulative sum of bedload transport rate q_s; plot (c) displays the temporal evolution of the eroded volume v_e; plot (d) displays the cumulative sum V_e of the eroded volume v_e. In all four plots run 1 is depicted in red and run 2 is depicted in yellow. The lower $x-$axis is used to plot the time-series of run 1 and the upper $x-$axis is used to plot the time-series of run 2. The dashed lines in plots (a), (c) and (d) represent the moving averages of q_s, v_e and V_e respectively.

slightly distinct regimes are observed: in the first half of run 2 where $q_s < \bar{q}_s$ and one where $q_s \approx \bar{q}_s$. In both case q_s is fluctuating in a similar fashion. The river is thus slightly aggrading in the first half of run 2 before finally settling around its mean.

The cumulative mass is defined as

$$m(q_s) = \int_{t_i}^{t_f} q_s \, \mathrm{d}t \tag{3.3}$$

where t_i and t_f are the initial and final times respectively. It is simply the total sum in time of the outgoing sediment, *i.e.* the total weigh. Comparing it with the cumulative mass of the average bedload gives an estimation of the overall sedimentary state of the river. If $m(q_s) < m(\bar{q}_s)$ (or $m(q_s) < m(q_{s,in})$), then the river is globally aggrading. Conversely, if $m(q_s) > m(\bar{q}_s)$ then the river is globally eroding. The behaviour of $m(q_s)$ confirms the general trend of q_s during run 1, that it is globally aggrading. Indeed, $m(q_s)$ is always below $m(\bar{q}_s)$ but slowly tends towards $m(\bar{q}_s)$ and reaches it at the very end of run 1. It is coherent with the regime of run 1, since the initially rectangular channel turns into a fully braided river. This process involves an intense morphological activity which is reflected on both q_s and $m(q_s)$. In this case, the river is aggrading and accumulating sediment to establish the braided system. During run 2, $m(q_s)$ reaches $m(\bar{q}_s)$ around half of the run. It means that for

slightly more than half of the duration of the experiment the sediment activity fluctuates around its mean. Once again, $m(q_s)(t)$ confirms the trends observed in Figure 3.1 (b). Up until $t = 3300$ $m(q_s)(t)$ lies below $m(\bar{q}_s)(t)$.

The eroded volume is defined as follows: let $z(x, y, t)$ be the river bed elevation at a given time and $z(x, y, t+\Delta t)$ be the river bed elevation at the following time (recall that in our experiments $\Delta t = 1$ h). The elementary eroded volume for a variation of z in time is defined as $\Delta z = z(x, y, t + \Delta t) - z(x, y, t)\mathrm{d}x\mathrm{d}y$. The total eroded volume is thus

$$v_e = \int_L \int_W \Delta z \, \mathrm{d}x\mathrm{d}y. \tag{3.4}$$

The total eroded volume can be seen as a proxy of the outgoing sediment transport rate, since by conservation of mass any change in the bed volume is related to the flux of sediment within this volume. As with the cumulative mass, it is possible to define the cumulative eroded volume V_e. It is the cumulative sum of v_e, *i.e.*

$$V_e = \int_{t_i}^{t_f} v_e \, \mathrm{d}t. \tag{3.5}$$

Figure 3.1 (c) shows the temporal evolution of v_e in run 1 and run 2. In both runs, v_e fluctuate around their average, which are both close to 0 ($\bar{v}_{e,1} = 0.0020$ and $\bar{v}_{e,2} = 0.0009$). Their fluctuations also look similar, even though they are more intense in run 1. However, the difference is not staggering. It is not possible to conclude on any particular erosional activity. However, by the shape of both curves, it is possible to infer that the erosional activity is similar in both runs.

Figure 3.1 (c) shows the temporal evolution of V_e in run 1 and run 2. In both runs, an increase of V_e is observed until finally stabilizing around their average. This behaviour is better seen when looking at the moving averages (the dashed curves). By definition of V_e, this means that the system is accumulating sediment in the initial stages of both runs, which means that there is a slight aggradation.

3.3 Bed morphological evolution

A video of the bed temporal evolution can be found on the YouTube webpage of the laboratory using the following link: https://www.youtube.com/channel/UCoA_xWkxSxU3UQLAk1HYpbg/videos.

3.3.1 Bed morphological variables

From the bed elevation it is possible to define several variables that characterize the bed dynamics. Following Leduc [2013], the variables used are the following:

- the bed slope s_x;

- the mean bed elevation z_m;
- the bed elevation standard deviation σ_z;
- the Bed Relief Index B;
- the longitudinal Bed Relief Index B_l;
- the Morphologically Active Length L_{ma};
- the bed convexity C;
- the bed area above average A_a;
- the hydraulic power Ω.

Table 3.2: Bed morphological variables and their utilisation

variable	utility
s_x	measures the general erosional pattern: an increasing s_x means aggradation and a decreasing s_x means erosion
z_m	measures the average bed elevation: an increasing z_m means aggradation and a decreasing z_m means erosion
σ_z	measures the (lateral) extent of braided: an increasing σ_z means a widening braiding channel and a decreasing σ_z means a narrowing braiding channel
B	measures the average transverse cross-section variability (with respect to z_m): an increasing B means erosion and a decreasing B means aggradation
B_l	measures the average longitudinal cross-section variability (with respect to z_m): an increasing B_l means erosion and a decreasing B_l means aggradation
L_{ma}	measures the average proportion of the bed morphologically active (eroding or aggrading): 1 means a fully active bed and 0 means an inactive bed
C	measures the average bed convexity with respect to z_m: an increasing C means aggradation, a decreasing C means erosion; $C > 0$ means a concave bed profile, $C < 0$ means a convex bed profile
A_a	measures the average proportion of the bed above z_m: an increasing A_a means erosion and a decreasing A_a means aggradation
Ω	measures the stream power, by definition it is a proxy of s_x: $\Omega = \varrho g Q s_x$

The are thoroughly defined in appendix A.5. Their main characteristics/properties are presented in table 3.2. In the rest of the thesis, they are separated and organized into two categories, the variable describing the state of the bed at a given time and the variables describing the erosional dynamics of the bed at a given time:

- the bed variables: s_x, z_m and σ_z;

– the bed dynamic variables: B, B_l, L_{ma}, C, A_a and Ω.

This dichotomy is arbitrary and do not ensue from a particular physical consideration, but it is considered relevant to clarify the presentation of the results.

3.3.2 Results

Before going into the results, it is important to mention that there was a problem with the bed elevation data of run 1 for the time $t = 900$ min. Therefore, almost all the time-series presented below show an unusual behaviour at this instant. Despite many attempts to correct the raw data, it was impossible to do so. I chose to keep the dataset as it is even if it may induce errors in some analysis and display an unusual behaviour.

Bed variables

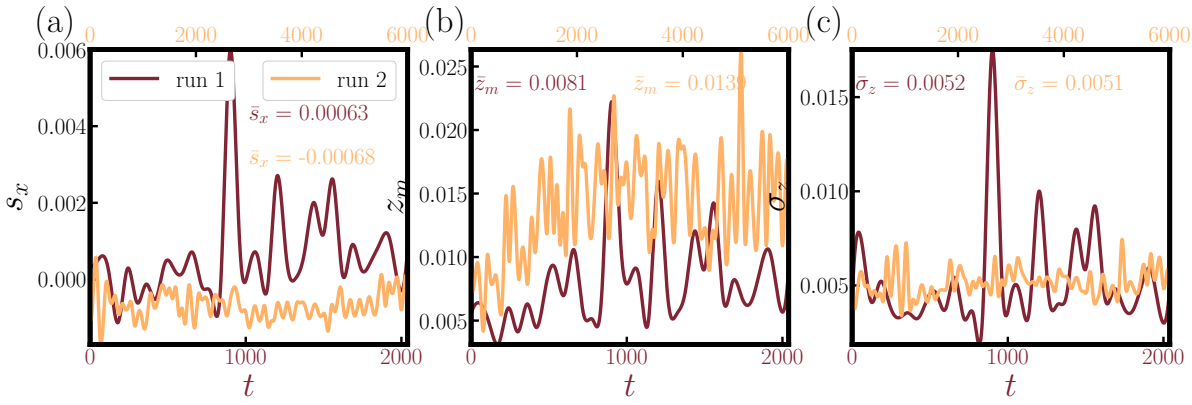

Figure 3.2: Temporal evolution of the bed variables s_x, z_m and σ_z for run 1 (red line) and run 2 (yellow line).

Figure 3.2 (a) shows the temporal evolution of slope in run 1 and 2 in red and yellow respectively. Two distinct behaviours are observed. In run 1 s_x starts around 0, because the bed is initially flat and there is no slope and gradually increases. The increase however is not monotonous since s_x rise from $t = 0$ to $t = 1000$ before progressively settling and fluctuating around the average $\bar{s}_x = 6.31 \cdot 10^{-4}$. On the other hand, run 2 does not exhibit a clear trend, neither increasing nor decreasing but fluctuating smoothly around $\bar{s}_x$. The slight but constant increase of s_x in run 1 indicates that the system is globally aggrading (following the lane balance principle). The reason lies with the fact that in run 1 the river evolves from a straight channel to a fully braided river. A braided river is characterized by the presence of multiple channels separated by bars and the presence of confluences and zones. The formation of these bars from a straight channel imply that at some point much of the bed material must be mobilised. This is coherent with the global increase in s_x. Nevertheless, this aggradation phase is not continuous, and at some point (around $t = 1000$ min) s_x tends to stabilize. On the other hand, once the system have reached a certain equilibrium (in run 2) the slope fluctuates mildly. It means that globally the system does not erodes nor aggrades, it undergoes erosional activity but not so intense as to fundamentally change s_x.

Figure 3.2 (b) shows the temporal evolution of z_m in run 1 and 2. In both runs, the same behaviour is observed: an increase in z_m in the initial stage of the run before a stabilization around the average. $\bar{z}_m$ is higher in run 2 than in run 1, testifying the constant accumulation of sediment by the braided river. This behaviour is interpreted as follows: the system accumulates sediment in the initial stage of each run (roughly half of their duration) to finally stabilize. Once it stabilizes, the dynamics of z_m is similar in both cases.

Figure 3.2 (c) shows the temporal evolution of the standard deviation of the bed elevation. In contrast with z_m, σ_z is virtually similar in both runs ($\bar{\sigma}_{z,1} \sim \bar{\sigma}_{z,2}$). They are also similar in shape, even though the fluctuations are wider in run 1. The similar behaviour of both runs strongly suggests that despite the difference in the average elevation of both river beds, they undergo the same erosional processes. This could come as a contradiction with the conclusion that was drawn from the evolution of z_m and other variables, *i.e.* that the river bed is undergoing a slight aggradation. For the moment, not enough evidence are gathered to make a definitive conclusion. It will be discussed it in more detail in chapter 4.

Bed dynamics

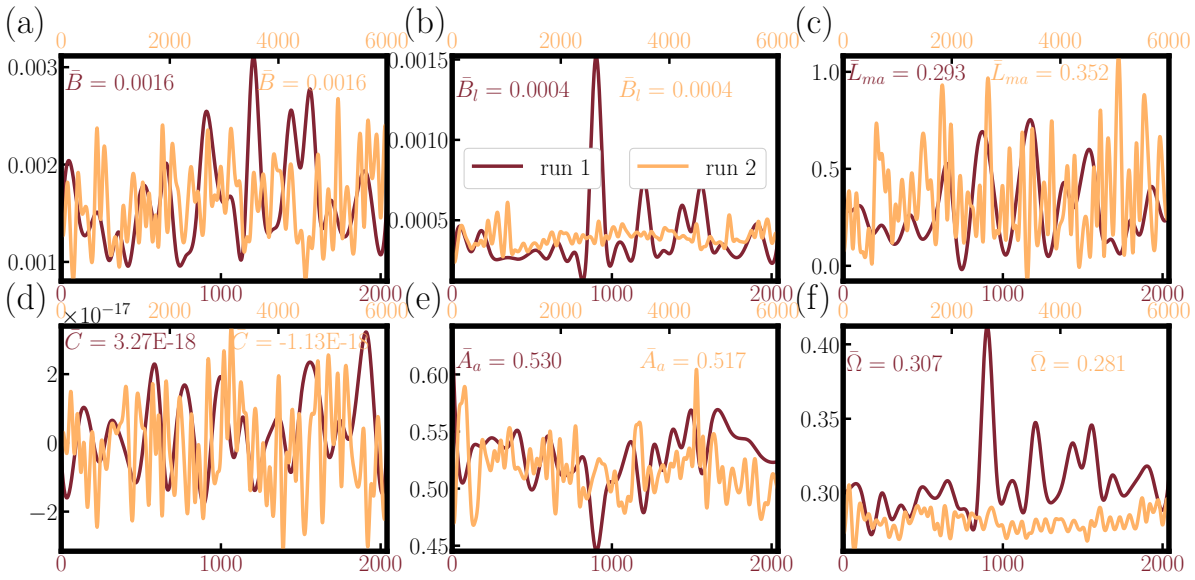

Figure 3.3: Temporal evolution of the bed dynamical variables B, B_l, L_{ma}, C, A_a and Ω for run 1 (red line) and run 2 (yellow line).

Figure 3.3 (a) shows the temporal evolution of B in run 1 and 2. In both runs, B fluctuates in a narrow range, and both runs have virtually the same average $\bar{B}_1 = \bar{B}_2 = 0.0016$. Even their trends are similar. B is an indicator of the erosional activity of the cross-section. B do not exhibit neither erosion nor aggradation, or at least B is not able to capture any clear tendency. It appears, however, that both runs display a very similar erosional behaviour (at the level of their cross-sections).

Figure 3.3 (b) shows the temporal evolution of B_l in run 1 and 2. In both run, B_l is virtually constant. This is especially true for run 2 where all the data lies very close to the average, whereas in run 1 the fluctuations are

slightly wider. In both runs, $\bar{B}_l$ are virtually similar. B_l measures the variability of a longitudinal cross section. Since B_l is similar in value and trend in the two experiments, it is again inferred that the erosional activity of the bed is similar.

Figure 3.3 (c) shows the temporal evolution of L_{ma} in run 1 and 2. L_{ma} exhibits wide fluctuations in both runs with no particularly identifiable trend. $\bar{L}_{ma,1}$ and $\bar{L}_{ma,2}$ are close but not quite so ($\bar{L}_{ma,1} = 0.293$ while $\bar{L}_{ma,2} = 0.352$). Run 2 displays more dispersion than run 1. L_{ma} measures the spatial extent of the erosional activity. On average, run 1 has a narrower erosional activity than run 2. This could be explained by the fact that in run 1 there is a transition from a narrow straight channel to a braided channel, and thus the extent of L_{ma} is automatically constrained by the initial channel width. However, a braided pattern appears very rapidly, around 2 to 3 h after the beginning of the run. It thus represent roughly $10\,\%$ of the total duration of the experiment. It seems unlikely that this short period could explain the overall difference. Moreover, L_{ma} shows a decreasing trend in the first 5 to 6 hours of experiment. Aside from the difference in their value, both curves fluctuate similarly. Run 2 have a wider (in space) morphological activity than run 1, but the dynamics of this morphological activity is similar.

Figure 3.3 (d) shows the the temporal evolution of C in run 1 and 2. In both runs C is virtually null. Indeed, $\bar{C}_1 = 3.2 \cdot 10^{-18}$ while $\bar{C}_2 = -1.1 \cdot 10^{-18}$. In spite of several verifications, no mistakes or were found in the algorithm used to compute C. However, it is not possible to entirely discard the fact that C might be meaningless (10^{-18} is indeed extremely low!). The obtained results are going to be considered nonetheless and put in perspective with the rest of the variables. In both runs, C fluctuates around 0. Run 1 do however exhibit a growth tendency. Run 2 on the other hand does not exhibit such behaviour. An increasing convexity is generally associated with an overall aggrading system. Run 1 is thus aggrading on average. This is coherent with the results of s_x where the evolution of the bed slope in run 1 suggested a slightly aggrading system. Run 2 does not exhibit a particular behaviour, which is again coherent with results observed in section 3.3. Despite the ridiculously low C, its behaviour seems to confirm its validity, especially when compared with the other variables.

Figure 3.3 (e) shows the the temporal evolution of A_a in run 1 and 2. In run 1, A_a decreases continuously until $t = 1000$ min, the moment when it starts growing until $t = 1400$ min to start decreasing again. In run 2, A_a simply fluctuates randomly around its mean. The fluctuations are quite narrow. The global trend of A_a in the initial stage of run 1 suggests that the system is globally aggrading, at least until $t = 1000$ min. After this period, run 1 seems to enter in the same dynamics as run 2, *i.e.* random fluctuations around its average. Once again this aggrading phase is consistent with trends observed for s_x and C.

Figure 3.3 (f) shows the temporal evolution of Ω in run 1 and 2. From its definition in table 3.2, Ω will have the exact same trend as s_x, *i.e.* Ω tend to increase during run 1, meaning a slight aggradation; Ω randomly fluctuates in run2, meaning no particular erosional state.

All the results are summarized at the end of this chapter (section 3.6) in tables 3.3, 3.4, 3.5 and 3.6.

3.4 Braided network

Again, video of the braided network temporal evolution can be found on the YouTube webpage of the laboratory using the following link: https://www.youtube.com/channel/UCoA_xWkxSxU3UQLAkıHYpbg/videos.

3.4.1 Low Path method

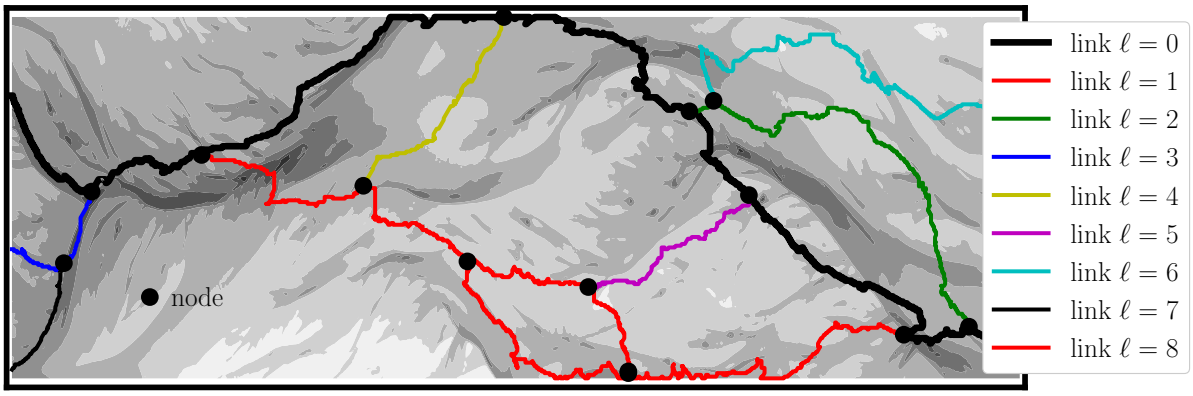

Figure 3.4: Example of bed elevation with its corresponding braided network (copy of Figure 2.5 from section 2.4.4).

To quantify the braided river network, the following set of variables are introduced:

- the number of links N_ℓ;
- the length of a link L_{ℓ_i};
- the total length of the braided network L_ℓ;
- the number of nodes N_n;

where ℓ_i is the i^{th} link of the network. Recall from graph theory that a link (or edge) is an entity that connects two nodes (vertices) of a graph, the graph being the mathematical representation of a network. In this case, the braided system is the network, the links represent the channels and the nodes represent the confluences (see Figure 3.4). Each link possess a length note L_{ℓ_i}. For sake of generality, it will be always referred to their dimensionless length, *i.e.* the dimensional length of a given link divided by the total length of the flume $L = 12.5$ m. The total length of the braided network is simply the sum of all the links' lengths in a given topography. It reads

$$L_\ell = \sum_{i=1}^{n_\ell} L_{\ell_i} \tag{3.6}$$

where n_ℓ is the number of links in the topography. Again for sake of generality, the dimensionless version L_ℓ / L

will always be used. The variables are separated into two groups, the links variables (N_ℓ, L_{ℓ_i} and L_ℓ/L) and the node variables (N_n).

3.4.2 Results

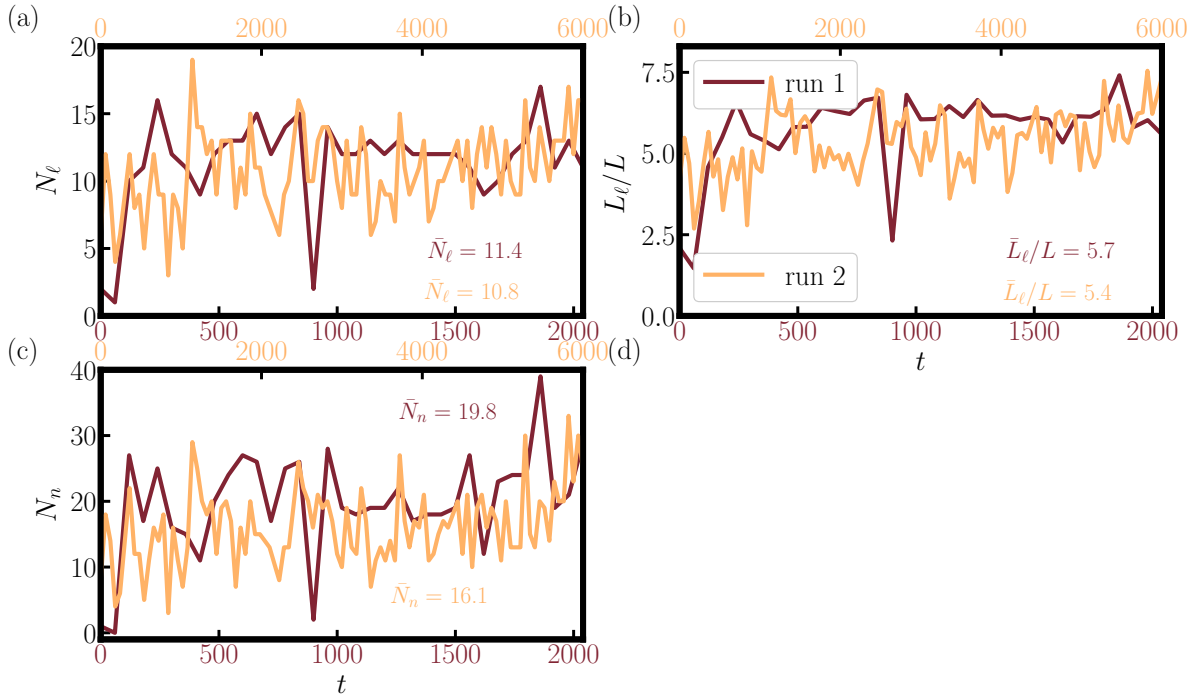

Figure 3.5: Dynamics of the links and nodes of the braided network. Plot (a) displays the temporal evolution of the number of links N_ℓ in run 1 (solid red line) and run 2 (solid yellow line). In dashed line is depicted their corresponding moving average. Plot (b) displays the temporal evolution of the total length of the braided network L_ℓ normalized by the channel length in run 1 (solid red line) and run 2 (solid yellow line). In dashed line is depicted their corresponding moving average. Plot (c) displays the temporal evolution of the number of nodes N_n in run 1 (solid red line) and run 2 (solid yellow line)

Figure 3.5 shows the temporal evolution of the network variables. In order to compare run 1 and run 2, each run respective time-series is displayed on the lower and upper x–axis for run 1 and 2 respectively (for plots (a) and (b)). Figure 3.5 (a) shows the time evolution of N_ℓ. At first glance, the behaviour of both runs is quite similar, as indicated by the closeness of $\bar{N}_\ell$. Indeed, the maximum relative difference of both $\bar{N}_\ell$ is 5.5 %.

Figure 3.5 (b) shows the time evolution of the L_ℓ/L. Again the general behaviour of run 1 and 2 is very similar. It is interesting to note that again the maximum relative difference of both $\bar{L}_\ell/L$ is 5.5 %.

Figure 3.5 (c) shows the time evolution of the number of nodes in both experiments. At first sight, the number of nodes is relatively similar in both runs but not as quite. Indeed, the maximum relative difference between both $\bar{N}_n$ is of the order of 22 %, *i.e.* almost 4 nodes. This is true even thought for run 1 $N_n = 0$ for the first two hours of the experiment, *i.e.* when the initial channel is still evolving into a fully braided river. In spite of the difference

in their mean, both curve of N_n do display a similar shape.

3.5 Modal analysis

By modal analysis is intended the identification of modes of the braided system and the analysis of their temporal evolution. The idea is based on Scheidt et al. [2016] and Hoffimann et al. [2019] work. The cornerstone of the modal analysis lies in the modes identification process. The idea is to use a measure of similarity (or disimilarity) between the braided networks to group together similar (or disimilar) clusters of networks. This similarity is measured by the modified Hausdorff distance δ_{mhd}. To find and identify the relevant modes, the DBSCAN clustering algorithm is used to regroup together the clusters of similar braided networks. These clusters are then identified as modes of the braided system (see section 2.4.2).

Two datasets representing the braided river are used: the set of points representing the salient edges of the bed elevation (see section 2.4.1) and the graph of the network (see section 2.4.4). They are called edge dataset and network dataset respectively. From them, similarity matrices based on δ_{mhd} between each networks of the respective datasets are computed. The clusters of similarly looking elements, which are ultimately identified as modes, are obtained from these matrices. Subsequently, we proceed to the modal analysis of run 1 and 2 for both datasets. Keep in mind that the main purpose is to use the network dataset, which correspond to the data obtained from the Low Path method. The edge dataset has been developed to have a point of comparison and to assess the validity of the network dataset. The results of the modal analysis are presented first for the edge dataset and then for the network dataset.

3.5.1 Edge dataset

Figure 3.6 shows the result the modal analysis applied to the edge dataset. Plot (a) and (b) show the identified modes of run 1 and plot (c) and (d) show the identified modes of run 2. In coloured circles are depicted the modes whereas black circles represent the noise points. The key parameters used by the DBSCAN method to identify the clusters are the number of neighbours n_{neigh} and the radius ϵ (see section 2.4.2 for more details on their meaning). A detailed discussion on the determination of these parameters will be presented in section 4.2. Plot (b) and (d) are simply a zoom on the region where the clusters of run 1 and 2 are found respectively.

In Figure 3.6 (a) and (b), only one mode has been identified, in addition to noise points (which do not belong to any cluster). It is coherent with the nature of run 1, where the system evolves from a straight channel towards braiding. Since the transition occurs quite rapidly (after 2–3 hours the system already exhibits a marked braided topography), it is clear that no cluster of mode corresponding to the flat bed could have been identified. Moreover, most of the noise points are found in the initial stage of the experiment, which is a clear sign of the lack of identification of a mode. The system then evolves towards braiding and a cluster of points corresponding to the braided system is found. This cluster remains stable in time with some noise points detected occasionally (they are mainly due to the corrupted data at $t = 900$ min). Figure 3.7 (a) shows the time evolution of modes in run 1 and confirms the transition from straight channel to braided channel (*i.e.* the transition from noise points to mode 1) with the sporadic detection of noise points after $t \approx 300$ min.

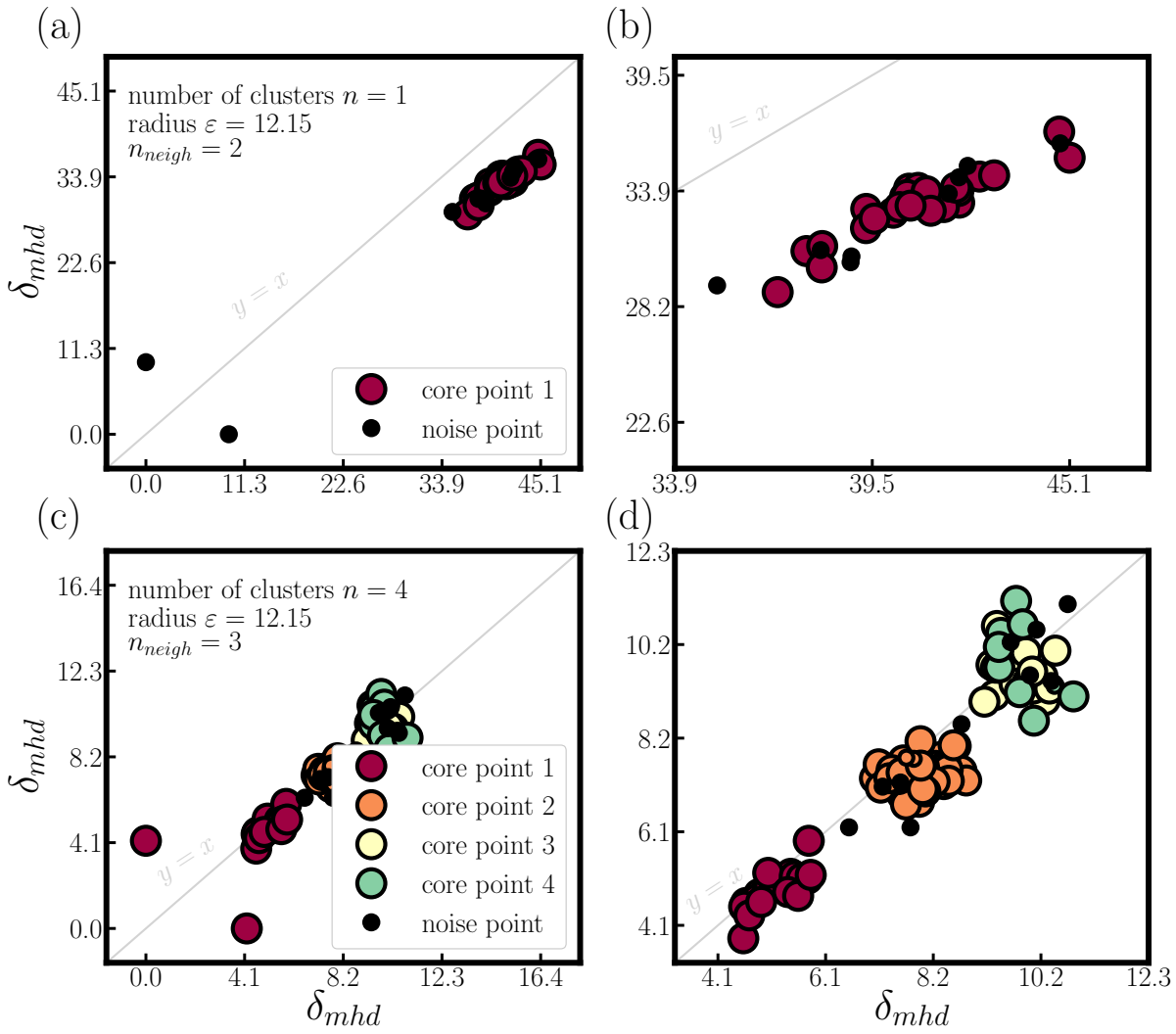

Figure 3.6: Clusters of modes computed from the δ_{mhd} matrix of the dataset of salient edges of the topography. Black points represent the noise points, coloured points represent point identified with a given mode. Plot (a) shows the complete collection of elements of run 1 (35 elements) and plot (b) show a zoom on the relevant zone of the clusters. Plot (c) shows the complete collection of elements of run 2 (100 elements) and plot (d) show a zoom on the relevant zone of the clusters.

In Figure 3.6 (c) and (d), four modes in addition to noise points are observed. Three clusters of points are clearly separated one from the other, except for mode 3 and 4. Run 2 starts with mode 1 already settled and it remains for the first 25 hours before switching to mode 2. In the vicinity of the mode switch, an increase of noise points is observed (with some occasional noise points detected as observed in Figure 3.7 (b)). The emergence of noise points between modes is kind of an early warning of a phase transition. Once mode 2 settles, it remains for approximately 50 hours before switching to mode 3, which is immediately followed by mode 4 for the next 3 hours before ultimately switching back to mode 3. This alternation between mode 3 and mode 4 lasts for about 20 hours before the systems settles back to mode 3 until the end of run 3. During this last part of run 2 (where

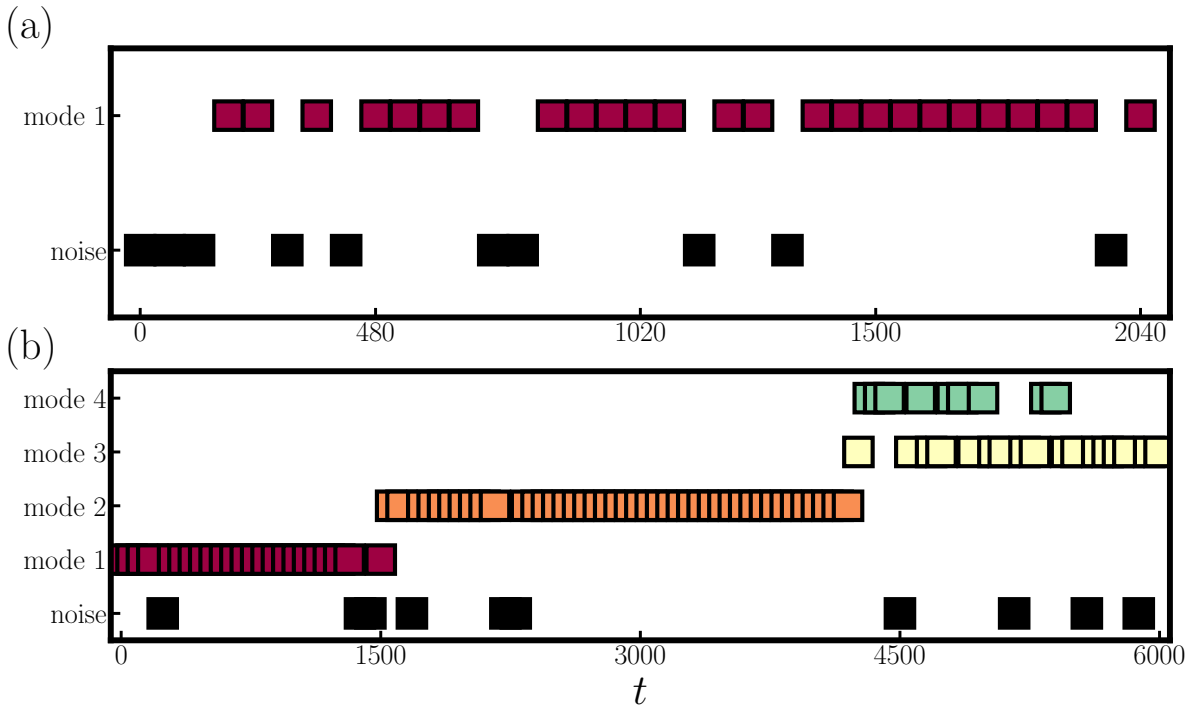

Figure 3.7: Time evolution of modes detected through the modal analysis of the edge dataset of run 1 (plot (a)) and run 2 (plot (b)).

the alternation occurs), some noise points are detected sporadically. Again this presence of noise points seems to announce the onset of mode transition.

This alternation of modes in run 2 is less obvious to interpret than in run 1 since the system is supposed to be at equilibrium, where by equilibrium is meant the morphodynamic definition of equilibrium presented in section 1.2 where the bedload transport rate is constant (to be precise, the sediment feeding rate balances exactly the sediment outgoing rate). Nevertheless, four different modes are observed, *i.e.* modes of the system that seem to be uncorrelated to the bed topographical and dynamical variations. A more detailed analysis will be presented in section 4.2.

3.5.2 Network dataset

Figure 3.8 shows the result of the modal analysis applied to the network dataset. Plot (a) and (b) show the identified modes of run 1 and plot (c) and (d) show the identified modes of run 2. As in section 3.5.1, the coloured circles show the modes whereas black circles represent the noise points identified by the DBSCAN clustering algorithm. Again a detailed discussion on the determination of DBSCAN parameters will be presented in section 4.2.

In Figure 3.8 (a) and (b), two modes are observed in addition to the noise points. There is an majority of points identified as mode 1, whereas noise points are being detected at the beginning of run 1 (again confirming

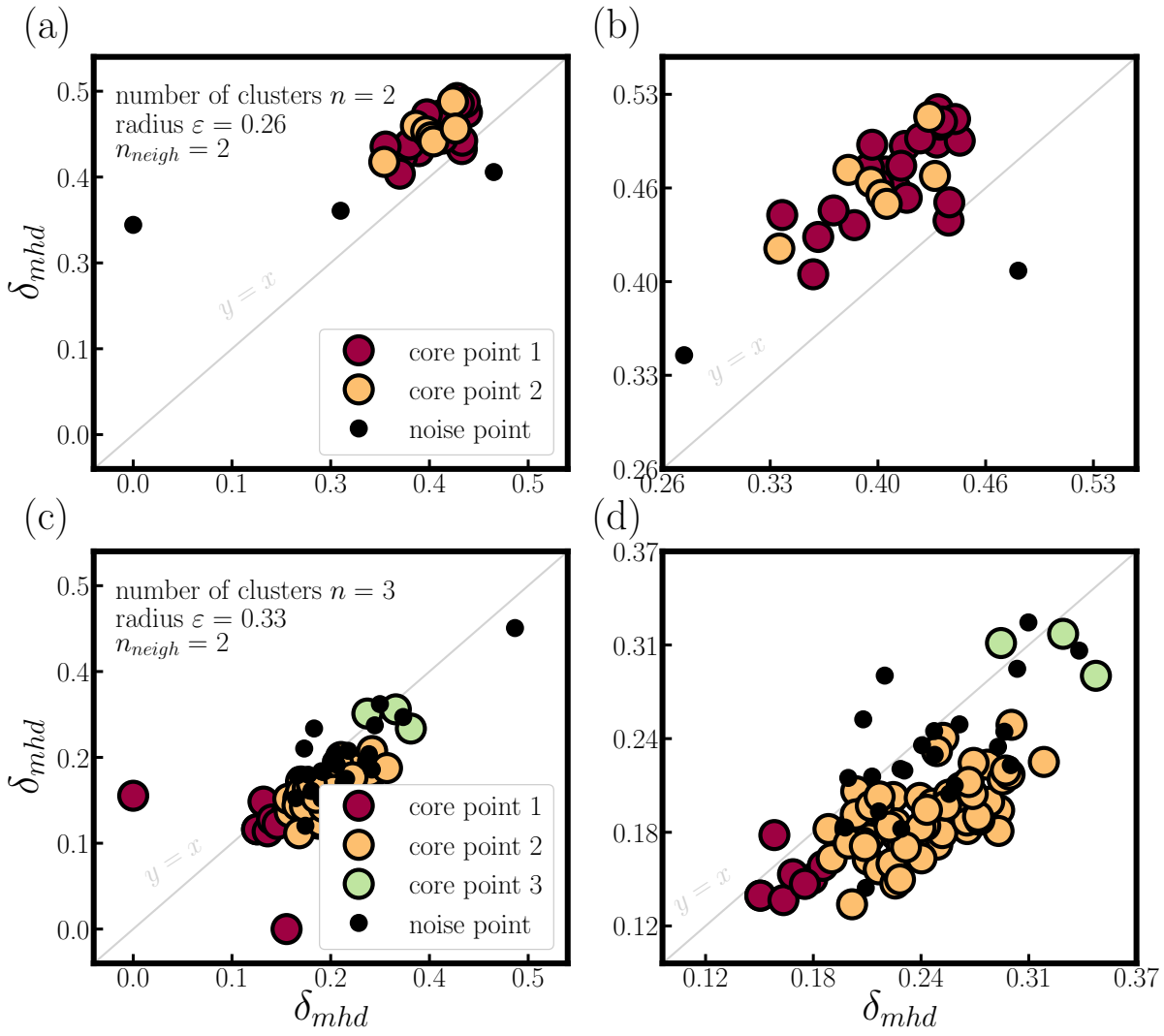

Figure 3.8: Clusters of modes computed from the δ_{mhd} matrix of the dataset of network graphs. Black points represent the noise points, coloured points represent point identified with a given mode. Plot (a) shows the complete collection of elements of run 1 (35) and plot (b) show a zoom on the relevant zone of the clusters. Plot (c) shows the complete collection of elements of run 2 (100) and plot (d) show a zoom on the relevant zone of the clusters.

the transition from straight to braided channel that occurs). In contrast with the state analysis based on edge detection, the apparition of a second mode during run 1 is observed, it develops in the early stage (around $t = 360 - -420$ min of experiment), it lasts until $t = 840$ min and finally switches back to mode 1 which lasts until the end of run 1. The time evolution of modes in run 1 is shown in Figure 3.9 (a).

In Figure 3.8 (c) and (d), three modes in addition to noise points are observed. We do not clearly observe three well defined clusters of points but rather a unique one with points relatively close one to another forming the core of mode 2. At the upper and lower ends of this cluster are found the points belonging to mode 1 and 3.

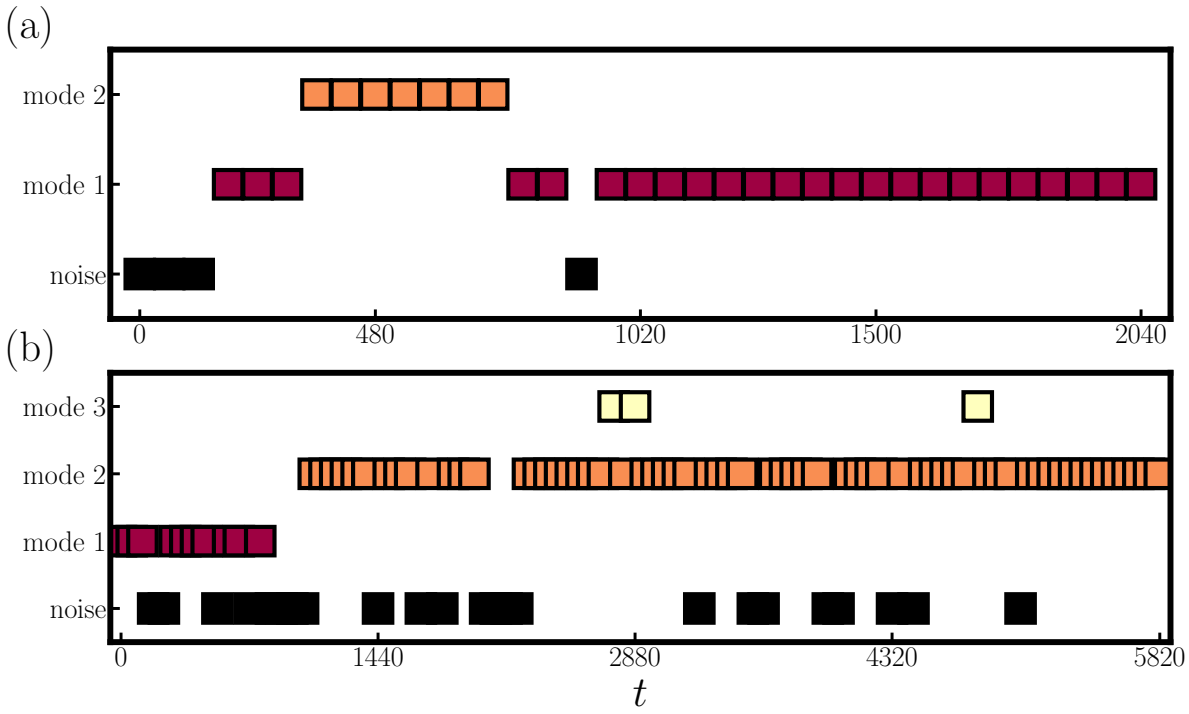

Figure 3.9: Time evolution of modes detected through the modal analysis of the network dataset of run 1 (plot (a)) and run 2 (plot (b)).

Run 2 starts with mode 1 already settled for the first 20 hours, albeit with some significant amounts of noise points detected. The transition to mode 2 occurs after a prolonged series of noise point (approximately 5 hours); again they appear as a warning sign of mode switching. Mode 2 is the dominant mode of run 2, lasting until the end of the run with spaced yet sporadic apparition of noise points and one very short transition to mode 3 (which lasts for only three hours). The temporal evolution of modes in run 2 is shown in Figure 3.9 (b).

We again observe an alternation of modes during run 2, only this time with one less mode and with a clearly dominant mode within the run (mode 2) with respect to the state analysis from edge detection. Mode 1 appears at the beginning for about the same amount of time as in the previous analysis (20 hours compared to 25) while mode 3 only appears for 3 hours before the system returns to mode 2. An explanation for this behaviour might lie in the nature of the cluster of points obtained from the distance matrix. Indeed, there is a unique cluster of points constituting mode 2, with mode 1 and 3 being located at the boundary of this cluster. Incidentally more noise points are observed in this analysis than in the previous one. A more detailed analysis will be presented in section 4.2.

The overall mode dynamics is broadly similar, whether the edge dataset is used or the network dataset. It means that independently of the quantification of the braided system, its dynamic is fairly constant (with respect to modal analysis). A proper quantitative argument will be given in chapter 4. It is interesting to note that run 2 is much more active than run 1. Regardless of the dataset used, run 2 always displays a higher number of modes than run 1. In a sense this result come as a surprise, since run 1 is characterized by a transition from single to

braided channel whereas run 2 is simply the braided channel at equilibrium. Therefore, new modes should not be detected. They are a clear indication that the braided network is evolving, rearranging its shape, in spite of the constant hydraulic conditions.

3.6 Results summary

A summary of this chapter is presented. First, the most relevant results of the analysis of the bed topography are recalled and finally the relevant results of the braided network dynamics are then summarized the relevant result of the Markov model are presented.

3.6.1 Bedload

Summary of the results of the analysis of the bedload time-series. All the variables are summarized in table 3.3.

Table 3.3: Summary of bedload variables. "—" means that there is no particular trend identified or the variables is not defined.

variable	run	average	std dev	global trend	system state
q_s	1	5.83	—	↗	aggrading
	2	5.97	—	—	fluctuating
$m(q_s)$	1	—	—	—	aggrading
	2	—	—	—	fluctuating
v_e	1	≈ 0	—	—	fluctuating
	2	≈ 0	—	—	fluctuating
V_e	1	0.052	—	↗	aggrading
	2	0.135	—	↗	aggrading

The main conclusions that we can draw are:

- run 1 is on average aggrading as testified by q_s, $m(q_s)$, and V_e;
- run 2 is neither aggarading nor eroding, except for V_e which shows aggradation;
- in both runs the dynamics of the erosional process is similar, as testified by v_e.

In general the bedload time-series suggests that run 1 and 2 are in different regimes, run 1 is slightly aggrading and run 2 is neither eroding nor aggrading, *i.e.* at equilibrium.

3.6.2 Bed morphology

Summary of the results of the analysis of the bed morphology. All the variables are summarized in table 3.4.

The main conclusions that we can draw are:

Table 3.4: Summary of morphological variables. "—" means that there is no particular trend identified or the variables is not defined.

variable	run	average	std dev	global trend	system state
s_x	1	$6.31 \cdot 10^{-4}$	$1.21 \cdot 10^{-3}$	↗	aggrading
	2	$-6.76 \cdot 10^{-4}$	$3.42 \cdot 10^{-3}$	—	fluctuating
B	1	$1.63 \cdot 10^{-3}$	$4.90 \cdot 10^{-4}$	—	fluctuating
	2	$1.61 \cdot 10^{-3}$	$3.80 \cdot 10^{-4}$	—	fluctuating
B_l	1	$3.88 \cdot 10^{-4}$	$2.30 \cdot 10^{-4}$	—	fluctuating
	2	$3.93 \cdot 10^{-4}$	$5.50 \cdot 10^{-5}$	—	fluctuating
L_{ma}	1	0.293	0.178	—	fluctuating
	2	0.352	0.233	—	fluctuating
C	1	$3.27 \cdot 10^{-17}$	$1.12 \cdot 10^{-17}$	↗	aggrading
	2	$6.31 \cdot 10^{-4}$	$1.21 \cdot 10^{-3}$	—	fluctuating
A_a	1	0.53	0.031	↘	aggrading
	2	0.517	0.024	—	fluctuating
Ω	1	0.307	0.026	↗	aggrading
	2	0.281	0.007	—	fluctuating
z_{mean}	1	$6.31 \cdot 10^{-4}$	$1.21 \cdot 10^{-3}$	↗	aggrading
	2	$6.31 \cdot 10^{-4}$	$1.21 \cdot 10^{-3}$	—	aggrading
$\sigma_{z_{mean}}$	1	$6.31 \cdot 10^{-4}$	$1.21 \cdot 10^{-3}$	↗	aggrading
	2	$6.31 \cdot 10^{-4}$	$1.21 \cdot 10^{-3}$	—	fluctuating

- run 1 is on average aggrading as testified by s_x, C, A_a, Ω, z_{mean} and $\sigma_{z_{mean}}$;
- run 2 is on average neither aggarading nor eroding, except for z_{mean};
- as a general rule, all variables representing the bed elevation (z_{mean}, $\sigma_{z_{mean}}$, s_x) shows that both runs are on average aggrading;
- some aspects of the erosional process are similar in both run, as testified by B, B_l and L_{ma}; others aspects clearly shows a distinction between run 1 and 2, as testified by C and A_a;
- the erosional processes are in general similar in both runs, they fluctuates and do not clearly represent one or the other erosional regime (namely erosion or aggradation).

The morphological variables suggest that run 1 and 2 are in different regimes, with run 1 being slightly aggrading and run 2 is neither eroding nor aggrading. This observation is much more nuanced than with the bedload time-series. Indeed, the morphological variables measuring erosional processes suggest that run 1 and 2 undergo the same dynamics. This has to be put in contrast with bed variables that suggest a clear distinction between both runs, *i.e.* run 1 is aggrading and run 2 is not (it is not eroding either).

3.6.3 Braided network

Summary of the results of the analysis of the braided network. All the variables are summarized in table 3.5.

Table 3.5: Summary of braided network variables. "—" means that there is no particular trend identified or the variables is not defined.

variable	run	average	std dev	global trend	system state
N_ℓ	1	11.4	—	—	—
	2	10.8	—	—	—
L_ℓ/L	1	5.7	—	—	—
	2	5.4	—	—	—
N_n	1	≈ 0	19.8	—	—
	2	≈ 0	16.1	—	—

The results of the network variables strongly suggests that there is no difference in the behaviour of both runs, as observed by the mean value and the shape of the curves of N_ℓ, L_ℓ/L and N_n. It suggest that despite the different regimes in which both runs are (run 1 being in aggradation and run 2 being at equilibrium), both runs have the same braided network.

3.6.4 Modal analysis

Summary of the results of the modal analysis. All the variables are summarized in table 3.6

Table 3.6: Summary of the modal analysis

variable	run	Edge dataset	Network dataset
States	1	1 + noise	2 + noise
	2	4 + noise	3 + noise
Noise points %	1	28.6	11.4
	2	10.0	23.5

The main result obtained from the modal is the following: run 2 have more modes than run 1 (with the edge dataset and with the network dataset). It is as if the braided system as a whole was more active in run 2 than in run 1 even though run 2 is supposed to be at morphodynamic equilibrium. It is counter-intuitive with the results obtained from the morphological variables. In any case, both runs exhibit a modal activity, suggesting that the network constantly evolves, and especially in run 2 (which is at equilibrium).

3.6.5 Take home message

As a general concluding remark, the following points are outlined:

- the morphological variables show that run 1 and run 2 have a similar erosional activity (shown by most of the dynamic variables) but are in slightly different regimes: run 1 is slightly aggrading whereas run 2 is at equilibrium. Nonetheless, this difference is mainly due to the transition from straight channel to braided system;
- network variables do not exhibit any difference between run 1 and run 2. The braided network is unaltered

throughout both runs;

– the modal analysis shows that both runs are active (by switching modes). More specifically, run 2 is more active than run 1.

The experimental results suggest that the braided system exhibit different behaviours depending on the perspective with which it is examined:

– from a hydraulic perspective, the system is at equilibrium (constant water discharge, constant sediment feeding rate);

– from morphological perspective, the system goes towards an equilibrium and reaches it;

– from a network perspective, the system is at equilibrium;

– from a mode perspective, the system is active.

4 Discussion

4.1 Similarity measures

When presenting the results in chapter 3, it was often mentioned that times-series of several variables were similar by visual inspection (when comparing say q_s in run 1 and run 2). In this section, these similarities are going to be discussed in a quantitative manner using the Hausdorff and Fréchet distances to compare the respective time-series.

As mentioned in section 2.4, both distances are defined in a metric space and require to be used within one. The time-series, as function of time, are defined in a space of the form $t \times f$ (where f is the function considered). They belong to a space similar to the phase space of functions in dynamical systems, and thus the distances measures are not properly defined and should not be used. To overcome this difficulty, the time-series are transformed into dimensionless curves defined on an interval ranging from 0 to 1 and whose image space is also define in the interval 0 to 1. The procedure is the following: consider the following parabolic function $f(x) = ax^2$ defined on the interval $[-b, b]$ where a and b are positive real numbers with its extrema on the interval $f_{max} = ab^2$ and $f_{min} = 0$. By applying the transformation $f' = (f - f_{min})/(f_{max} - f_{min})$ to both the function f and its original interval of definition, it is possible to redefine f into a function f' whose outputs lie in the interval $[0, 1]$ and defined on the interval $[0, 1]$ without altering the shape of the function. Once defined in the plane $[0, 1] \times [0, 1]$ which is a metric space by definition, the Hausdorff and Fréchet distances are used to compare this parabolic function f' with any other function g'.

By construction, the distances are bounded in the interval $[0, 1]$ for δ_{mhd}, where 0 implies no distance between the compared curves (identity) and 1 being the maximum difference (see appendix A.3). δ_{Fr} is bounded in the interval $[0, 2]$ where 0 implies no distance between the compared curves (identity) and 2 being the maximum difference (see appendix A.4). This procedure will be applied to all the time-series presented in section 4.1. The criteria of similitude are shown on table 4.1 below.

4.1.1 Morphological indicators

The similarity quantification of bedload variables is presented on table 4.2 below.

The following points are outlined:

Table 4.1: Measure of similarity criteria

similarity	δ_{mhd}	δ_{Fr}
very strong similarity	$0-0.2$	$0-0.4$
moderate similarity	$0.2-0.4$	$0.4-0.8$
no particular similarity	$0.4-0.6$	$0.8-1.2$
moderate dissimilarity	$0.6-0.8$	$1.2-1.6$
very strong dissimilarity	$0.8-1$	$1.6-2$

Table 4.2: Bedload similarity measure

variable	δ_{mhd}	δ_{Fr}	r
q_s	0.105	0.788	0.205
$m(q_s)$	0.018	0.035	0.999
v_e	0.042	0.348	0.138
V_e	0.060	0.417	0.261

- both time-series of q_s are similar in δ_{mhd} and slightly dissimilar in δ_{Fr};
- there is an almost perfect match between both $m(q_s)$ curves as shown by the low values of both δ_{mhd} and δ_{mhd};
- both time-series of v_e are very close in δ_{mhd} and δ_{Fr};
- both time-series of V_e are quite close in δ_{mhd} and δ_{Fr}.

As a concluding point, remark that time-series of bedload variables are, on the whole very similar in both shape, trend and values. However, q_s and V_e (the bedload flux and the cumulated eroded volume, its proxy) do exhibit trends of an aggrading channel. This is mainly due to the transition from a straight channel towards a fully braided system at equilibrium. Note, however, the following feature: a similar erosional activity is observed for both regimes.

The results of the similarity measure of bed variables are summarized in table 4.3 below.

Table 4.3: Bed variables similarity measure

variable	δ_{mhd}	δ_{Fr}	r
s_x	0.099	0.559	0.009
z_m	0.060	0.418	0.279
σ_z	0.082	0.544	-0.014

The following points are outlined:

- both time-series of s_x are close in δ_{mhd} but not as much in δ_{Fr};
- both time-series of z_m are close in both δ_{mhd} and δ_{Fr};

– both time-series of σ_z are close in δ_{mhd} but not as much in δ_{Fr}.

The similitude measures seem to suggest that in run 1 and 2 the bed variables exhibit similar fluctuations in general (as shown by the low δ_{mhd}) but not quite so in trends, except for z_m (as shown by the relatively low $\delta_{Fr} = 0.418$ compared to 0.559 and 0.544 for s_x and σ_z respectively). This result is interpreted as follow: the erosional processes of run 1 and 2 are similar in dynamics, as shown by the low δ_{mhd}; on the other hand they may follow slightly diverse trends, as shown by the relatively high δ_{Fr}, that is the consequence of the transient behaviour of run 1.

The results of the bed dynamic variables similarity measures are summarized in table 4.4 below.

Table 4.4: Bed dynamic variables similarity measure

variable	δ_{mhd}	δ_{Fr}	r
B	0.049	0.470	-0.029
B_l	0.096	0.465	0.053
L_{ma}	0.041	0.335	-0.067
C	0.033	0.382	-0.084
A_a	0.067	0.737	-0.067
Ω	0.099	0.559	0.009

The following points are outlined:

– both time-series of B are very close in both δ_{mhd} and δ_{Fr};

– both time-series of B_l are very close in both δ_{mhd} and δ_{Fr};

– both time-series of L_{ma} are very close in both δ_{mhd} and δ_{Fr};

– both time-series of C are very close in both δ_{mhd} and δ_{Fr};

– both time-series of A_a are very close in δ_{mhd} but not in δ_{Fr};

– both time-series of Ω are quite close in δ_{mhd} but not in δ_{Fr}.

As a general concluding point, remark that all bed dynamics variables display similar trends, thereby confirming that dynamically the bed undergoes comparable erosional activity. Apart from A_a and Ω whose δ_{Fr} is relatively high, it is quite difficult to say that run 1 and run 2 are in different bed regimes. A conclusion similar to that of morphological variables is drawn: both run have a similar erosional activity (recall from section 3.3 that $B, B_l L_{ma}, A_a, C, \Omega$ are all variables characterizing the bed erosional processes).

The results of the similarity measures of network variables are summarized in table 4.5 below.

The following points are outlined:

Table 4.5: Network variables similarity measure.

variable	δ_{mhd}	δ_{Fr}	r
N_ℓ	0.078	0.347	0.135
L_ℓ/L	0.082	0.371	0.178
N_n	0.067	0.336	0.124

- both time-series of N_ℓ are very close in δ_{mhd} and in δ_{Fr};
- that both time-series of L_ℓ/L are very close in in δ_{mhd} and in δ_{Fr};
- both time-series of N_n are are very close in in δ_{mhd} and in δ_{Fr}.

As general concluding point, remark that all three network variables are very similar in both run 1 and run 2. Aside from the early stage of run 1, both run 1 and 2 display a similar behaviour with respect to network variables N_ℓ, L_ℓ/L and N_n. This result suggests that the braided network is practically constant, regardless of the nature of the experiment and depends solely on the hydraulic conditions. A similar conclusion was drawn by Bertoldi et al. [2009b]. In their study, they related the main morphological indicator to the dimensionless discharge and the dimensionless stream power and showed that they were the only controlling parameters of the morphological activity of the bed. Here it is possible to go a step further and assert that the network structure of the braided system remains unchanged throughout both runs, even though run 1 is in a different regime (aggrading) than run 2 (equilibrium).

4.1.2 Concluding remarks

Generally speaking, all variables exhibit very similar trends in both runs, as testified by the low δ_{mhd}. The same general trend is observed for δ_{Fr}, albeit in a significantly less pronounced way. Higher δ_{Fr} are observed, in particular for q_s and A_a to other variables and especially in run 1. Network variables are, generally speaking, more homogeneous than the rest, both in δ_{mhd} and δ_{Fr}. This is even observed in their r coefficient, which are always positive and generally higher than for the rest of the variables.

Regardless of the variable focused on, there is always a high similarity between time-series, especially observed in δ_{mhd}. It is interpreted in the following manner: both runs are two distinct stages of a unique system, *i.e.* a braided river, thereby the relevant variables should display a similar dynamic on the whole. Consequently, it is expected that they behave similarly in time. In particular, their fluctuations, global trend and shape should somehow resemble. This is what is shown through δ_{Fr} and especially δ_{mhd}.

These results are interpreted as a confirmation of the concluding remarks of chapter 3, *i.e.*:

- the morphological variables shows that run 1 and run 2 have a similar erosional activity;
- network variables do not exhibit a significant difference between run 1 and run 2;
- the braided network depends on the hydraulic conditions of the flow.

4.2 Modal analysis

In this section, the results on the modal analysis presented in section 3.5 are going to be discussed in more details. First, the choice of the DBSCAN parameters will be detailed (a crucial step in the mode detection process). Then, the modes temporal evolution of both datasets (edges and network) are going to discussed, compared them and their respective differences, strengths and weaknesses assessed. Finally, this section will be closed with a direct application of the modal analysis to Markov processes and a discussion on its potential future utilization.

4.2.1 Parameters determination

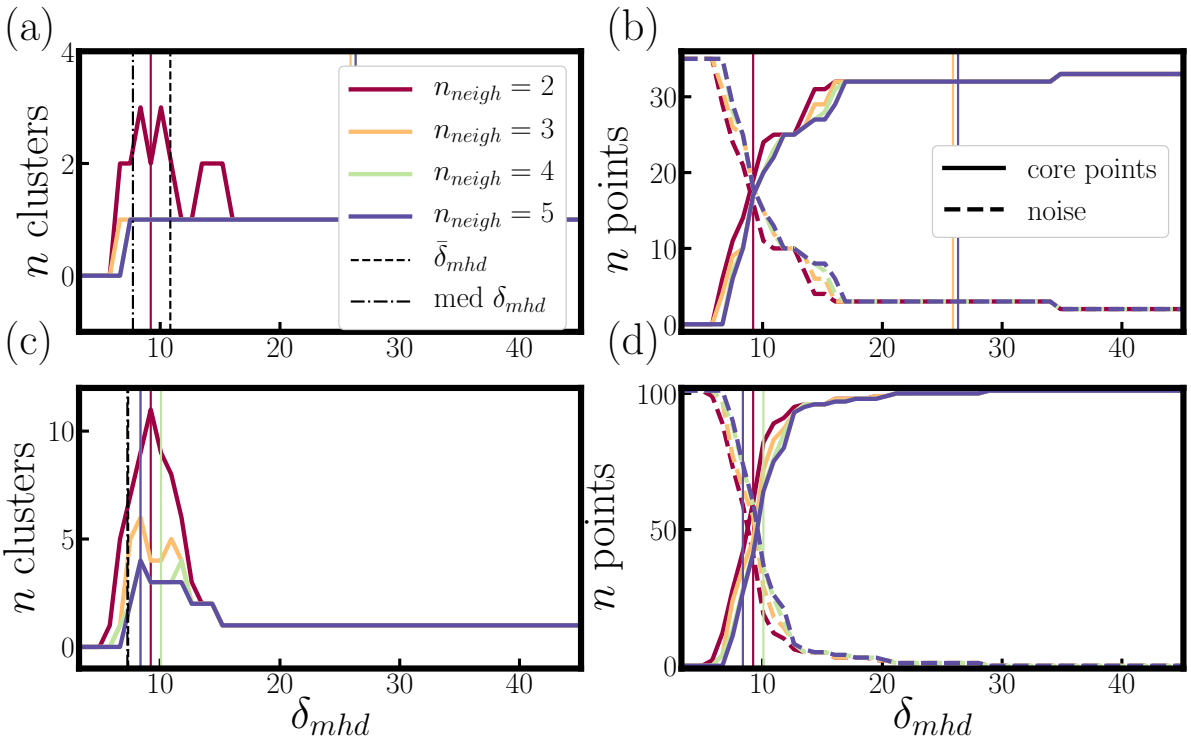

Figure 4.1: Parameters determination of the DBSCAN algorithm of run 1 for the edges dataset (plot (a) and (b)) and for the network dataset (plot (c) and (d)). Plots (a) and (c) show the number of detected clusters (*i.e.* modes) in function of ε measured in δ_{mhd} for $n_{neigh} = 2, 3, 4, 5$ displayed in red, orange, green and blue lines respectively. Plots (b) and (d) show the number of core points (*i.e.* points that belong to a mode) in function of ε measured in δ_{mhd} for $n_{neigh} = 2, 3, 4, 5$ displayed in red, orange, green and blue solid lines respectively; in coloured dashed lines are shown the noise points (*i.e.* points that do not belong to a mode). The vertical thin black dashed line represent the mean distance δ_{mhd} between points; the vertical thin black dotted-dashed line represent the median distance δ_{mhd} between points.

The DBSCAN algorithm mainly relies on two parameters: the radius of inquiry ε and the number of neighbours n_{neigh} (recall section 2.4). They fully determine the output of the clustering method and their selection has to meet some basic criteria. ε should not be too small, otherwise no points are located sufficiently close to others, and

therefore no cluster of points is detected. On the other hand if ε is too large, all points are close to each other and ultimately they tend to form a unique cluster. There are thus two theoretical limits to ε, $\lim_{\varepsilon \to 0} n_{clusters} = 0$ and $\lim_{\varepsilon \to \infty} n_{clusters} = 1$. In practice, ε is bounded by the minimum and maximum distances computed when analysing the datasets (δ_{min} and δ_{max}). If $\varepsilon = \delta_{min}$ is used, one cluster of 2 points at best is obtained while the rest of the points are identified as noise (for $n_{neigh} = 2$). On the other hand, using $\varepsilon = \delta_{max}$, the tendency is to obtain a unique cluster of points with some noise points scattered around (with the extreme case being on single cluster with no noise point, which is the theoretical limit if $\varepsilon \to \infty$). An upper limit of $\varepsilon_{max} = 2\delta_{max}/3$ and a lower limit of $\varepsilon_{min} = \delta_{min}$ was decided. The optimal ε should lie somewhere in between.

The other cardinal parameter is the minimum number of neighbours n_{neigh}. This is the minimum number of neighbouring points needed to form a cluster. Its lowest bound is 2 and its maximum is the total number of points. The higher its value, the harder for DBSCAN to detect a cluster. However, using its lowest bound or a low n_{neigh} value, there is a risk to consider any close gathering of points a threshold. A compromise has to be found.

For a given ε, different n_{neigh} could yield different number of clusters (in fact it is almost always the case). Consider the following hypothetical example: for $n_{neigh} = 2, 3, 4, 5$, $n_c = 30, 20, 15, 15$ are obtained. It is clear that $n_{neigh} = 2$ overestimates the number of clusters. In other words, non-relevant clusters are detected, non-significant. On the other hand, $n_{neigh} = 5$ is redundant in the sense that increasing n_{neigh} does not change the number of detected clusters. In fact increasing it further will ultimately decrease the number of clusters up to 1 (when the number of points needed to form a clusters equals the total number of points). The most significant n_{neigh} is loosely defined as the lowest value of n_{neigh} for which it is possible to detect of the same amount of clusters. In the previous example, $n_{neigh} = 4, 5$ yields $n_c = 15, 15$, the most significant (the lowest) number of minimum cluster in this case being $n_{neigh} = 4$. I want to emphasize that it is not an exact criterion but rather a guideline.

The algorithm discriminates between two kind of points, core points (which belong to a cluster) and noise points (which do not). The balance between these two points is important to assess the relevance of the clusters. The output of a couple of parameter (ε, n_{neigh}) is considered to be relevant if and only if the number of core points outgrows the number of noise points. It simply means that the majority of points belong to one of the detected clusters. Ideally, one should seek to minimize the number of noise points, but we will satisfy ourselves with just outgrowing them.

The final set of criteria used to select the DBSCAN parameters are summarized hereafter:

(i) the optimal ε has to be bound in the range: $\delta_{min} \leq \varepsilon \leq 2\delta_{max}/3$;

(ii) the optimal n_{neigh} as to be significant. By significant is intended that it has to be the lowest value for the same number of detected clusters;

(iii) for a given couple of parameters (ε, n_{neigh}) the number noise points has to be less than the number of core points.

First, the determination of the DBSCAN parameter with the edges distance database will be discussed (Figure 4.1)

and then the graph network distance database (Figure 4.2). The analysis is based on two graphs, the number of clusters in function of ε for different n_{neigh} and the number of core points in function of ε for different n_{neigh}. These two graphs are depicted for both run 1 and run 2 and from their analysis the optimal couple of parameters (ε, n_{neigh}) will be determined.

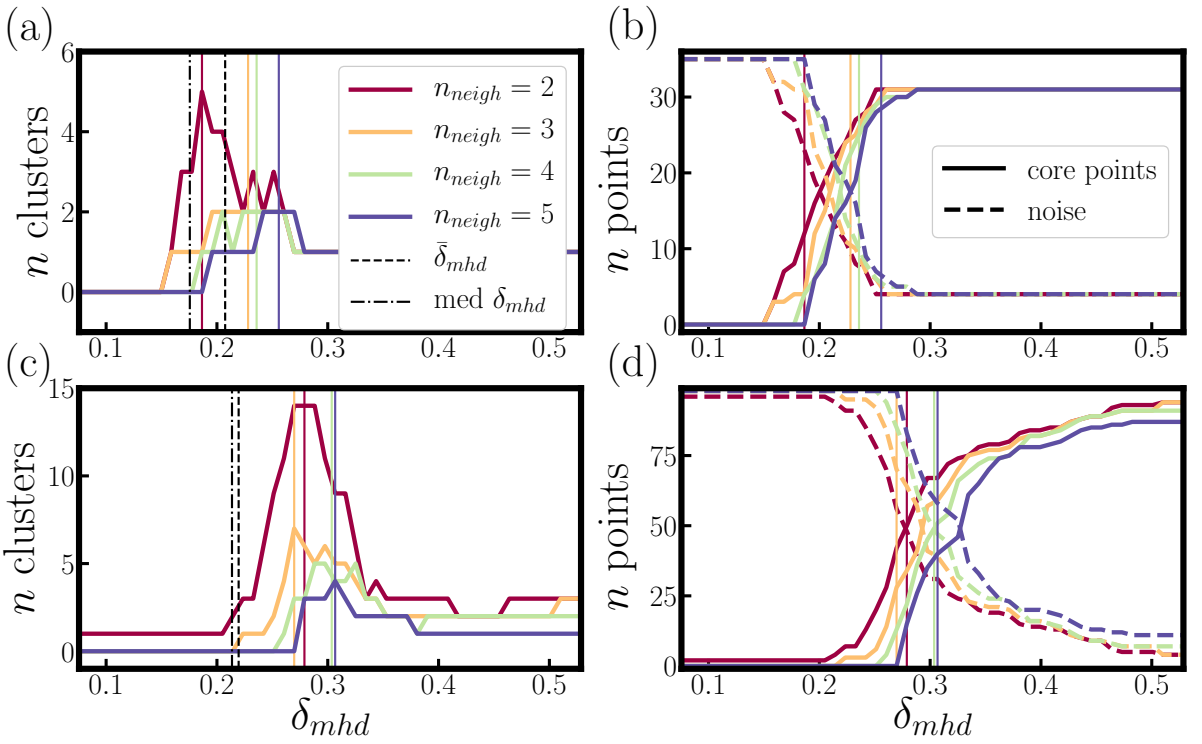

Figure 4.2: Parameters determination of the DBSCAN algorithm of run 2 for the edges dataset (plot (a) and (b)) and for the network dataset (plot (c) and (d)). Plots (a) and (c) show the number of detected clusters (*i.e.* modes) in function of ε measured in δ_{mhd} for $n_{neigh} = 2, 3, 4, 5$ displayed in red, orange, green and blue lines respectively. Plots (b) and (d) show the number of core points (*i.e.* points that belong to a modes) in function of ε measured in δ_{mhd} for $n_{neigh} = 2, 3, 4, 5$ displayed in red, orange, green and blue solid lines respectively; in coloured dashed lines are shown the noise points (*i.e.* points that do not belong to a mode). The vertical thin black dashed line represent the mean distance δ_{mhd} between points; the vertical thin black dotted-dashed line represent the median distance δ_{mhd} between points.

Figure 4.1 (a) and (c) show the number of clusters in function of ε (expressed in δ_{mhd} on the x axis) for four n_{neigh} (the four distinct colours) for run 1 (plot (a)) and run 2 (plot (c)) for the edge dataset. Plots (b) and (d) show the number of core points (solid lines) and the number of noise points (dashed lines) in function of ε for the same four n_{neigh} for run 1 (plot (b)) and run 2 (plot (d)). Criteria (iii) is met when the dashed and solid lines cross each other on plot (b) and (d) and that it determines the lower bound for ε. This crossing point is roughly similar for both runs and is located around 10. The upper bound being set by criteria (i) ($2\delta_{max}/3 \approx 30$), the range of possible values of ε is already determined (approximately 10 and 30 for both plots (b) and (d)). Criteria (ii) is met for $n_{neigh} = 3$ on plot (a) and $n_{neigh} = 4$ on plot (c). The final set of parameters is summarized on table 4.6 below.

Table 4.6: DBSCAN algorithm parameters for the edges database

	run 1	run 2
ε	12.5	12.5
n_{neigh}	3	4

Figure 4.2 (a) and (c) show the number of clusters in function of ε (expressed in δ_{mhd} on the x axis) for four n_{neigh} (the four distinct colours) for run 1 (plot (a)) and run 2 (plot (c)) with the networks graphs dataset. Following the previous analysis, criteria (iii) is met around 0.25 for run 1 and around 0.3 for run 2. The upper bound in both is the same, *i.e.* $\delta_{max} = 0.35$ (criteria (i)). Criteria (ii) is met when $n_{neigh} = 3$ for run 1. For run 2 the situation is more complex to properly assess since there is no unique number of cluster that is consistently detected when varying n_{neigh}. By trial and error and visually inspecting the results of DBSCAN, $n_{neigh} = 4$ was used. The final set of parameters is summarized on table 4.7 below.

Table 4.7: DBSCAN algorithm parameters for the graph network database

	run 1	run 2
ε	0.275	0.32
n_{neigh}	3	4

4.2.2 Modes temporal evolution

Lets recall the goal of the modal analysis: identify the modes of the braided system by a clustering method (DBSCAN). DBSCAN takes as an input the distance matrix m_{ij} where every element of the matrix represent the similarity (measured in δ_{mhd}) between two configurations i and j of the braided system. Provided that the parameters of DBSCAN are well determined, it is possible to proceed to the modal analysis of the braided system. The main results have been presented in section 3.5. Here, they will be discussed in greater details. The focus will be put first on the differences obtained when applying the DBSCAN method to both datasets, the edges dataset and the network dataset.

Both representations, the edge dataset and the network dataset, are a quantification of the braided system and should in theory yield the same results when applying modal analysis to them. As stated in section 3.5, it was not exactly the case even though the general dynamics remained fairly similar. Here, this similarity will be quantified and an explanation to these differences will be proposed.

In Figure 4.3 is shown the temporal evolution of modes computed from the edge dataset (red solid line) and from the network dataset (blue solid line) for run 1 (plot (a)) and run 2 (plot (b)). Lets briefly recall what was said in section 3.5:

- run 1: for both datasets the system starts from noise points (mode 0) to finally settle into a unique mode (mode 1) at the end of the run. From the network dataset (blue line in Figure 4.3 (a)) another mode (mode 2) is briefly explored by the system during the first half of the run before settling at mode 1;
- run 2: for both datasets the system starts from mode 1 (the mode is already settled) and for approximately

the same amount of time remains in this configuration. There is a switch towards mode 2 roughly simultaneously. From then on the behaviour is quite different according to the dataset used. For the edge dataset (red line in Figure 4.3 (b)) the system alternates between three different modes (mode 1, 3 and 4) whereas for the network dataset (blue line in Figure 4.3 (b)) the system only alternates between two modes (mode 1 and 3).

δ_{mhd}, δ_{Fr} and r was computed for time-series of run 1 and 2. Both the edges dataset and the network dataset (respectively the red and blue lines in Figure 4.3) are similar and positively correlated together, with $\delta_{mhd} = 0.206$ and $\delta_{mhd} = 0.115$ for run 1 and run 2 respectively and $r = 0.212$ and $r = 0.303$ for run 1 and run 2 respectively. On the other hand, they do not resemble much in the Fréchet sense, with $\delta_{Fr} = 1$ and $\delta_{Fr} = 2$. These results tend to corroborate the relative similarity in the mode dynamics despite the fact that different dataset were used. However, the high δ_{Fr} suggests that there are non negligible discrepancies. This is especially visible in the late stage of run 2. Overall, the mode dynamics is relatively similar, as testified by the positive correlation in both runs.

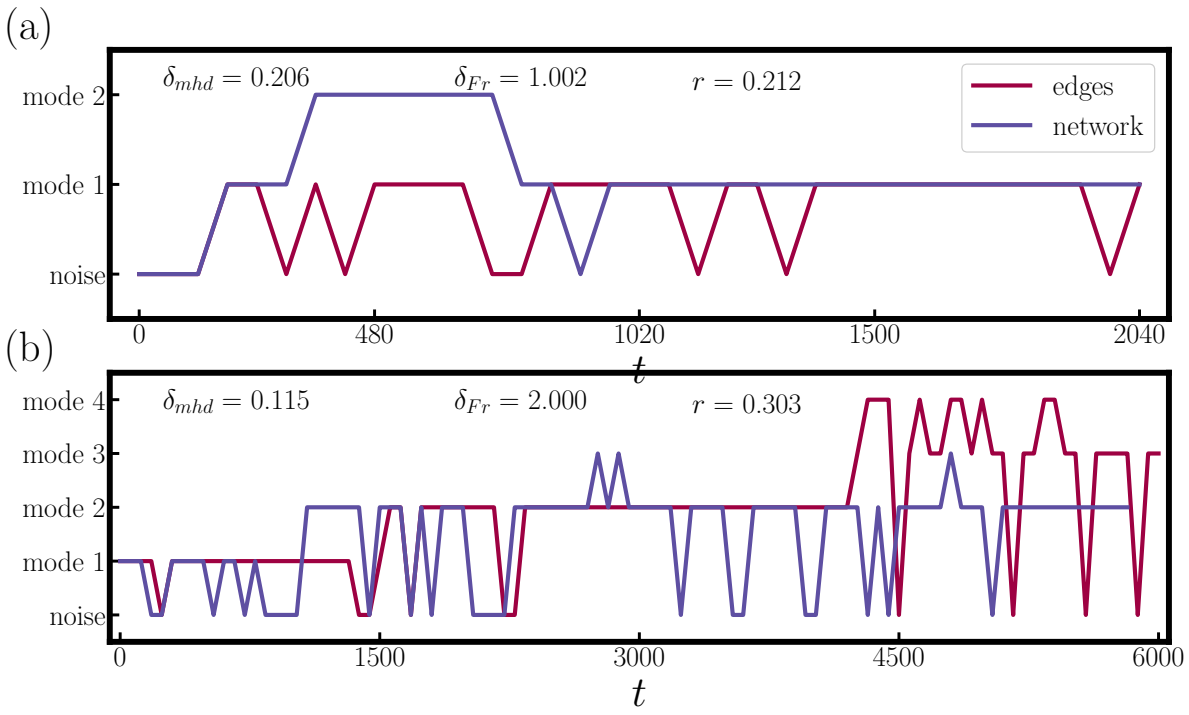

Figure 4.3: Temporal evolution of mode in run 1 (plot (a)) and run 2 (plot (b)) for the edge dataset (solid red line) and network dataset (solid blue line).

The difference observe in both modal analysis is mainly due to two factors:

- the internal structure of each dataset;
- the information contained by each dataset.

The edge dataset is composed of sparse points scattered around while the network dataset is composed of an dense alignment of points (forming the graph of the network). To give an idea of the difference between them, the point density of an edge dataset is typically in the range 0.04 and while the point density of a network dataset is typically in the range 0.1. The point density of each database is defined as the total number of element divided by the size of the array (the matrix containing the data in python). This difference is readily observed in the distance matrices, where for the edge datasets typical distances between each elements were of the order of $10 - 40$ whereas for the network datasets distances where of the order of $0.1 - 0.4$ (an order of magnitude lower). The higher density of the network dataset almost mechanically induces a higher precision in the measure of similarity between its elements and thus leads to a better determination of modes, at least in theory. Nevertheless, this it is not straightforwardly observed in the data, especially if one looks at the number of noise point detected. If one of the two method was more precise than the other, then it would have a significantly less amount of noise point than the other. This is not the case and in fact noise points are almost exactly in equal quantity in both method (with even a slight over-representation in the network dataset). It is interpreted as a sign of robustness of both method: they detect roughly the same number of noise points.

The edges dataset is an abstraction of the braided morphology that measures the location of the most salient edges, *i.e.* strong elevation gradients in the topography. This corresponds to banks, confluences, affluences, scour holes, etc., all elements constituting a braided river. By construction, it is a simplification of the information contained in the braided system through its most specific constituents, a kind of snapshot of the braided system. On the other hand, the network dataset is a straightforward representation of the braided network. Following the snapshot analogy, the network representation is more of a direct footprint of the system. It conveys much more information of the braided system than the edges dataset, even if both dataset are ultimately obtained from the same raw data, the bed elevation.

To conclude this discussion, the slight superiority of the network dataset over the edge dataset is highlighted. By its very nature, it is believed to be more directly linked to the physics of the braided system by representing its network-like structure, which is what one wants to quantify and study in the end. The edges dataset is supposed to follow any eventual morphological evolution of the braided river, but it is harder to ensure that it does. It is more likely to contain errors, or to misrepresent the braided pattern than the network dataset. Nonetheless, they are complementary and they could be used together. Indeed, both datasets were used to have a point of comparison, a calibration if one may, of the modal analysis.

Now that the validity of the modal analysis have been discussed, several question arise about the interpretation of the results obtained. Below are listed some of the questions raised:

- how to interpret the differences in the modes between run 1 and run 2?
- does the modal evolution relates to morphological variations?
- is it possible to relate the modes variations observed in Figure 4.3 to the morphological variables?

The focus will not be put on all the topographic variables but on four of them, namely the stream power Ω, the bedload transport rate q_s, the number of links N_ℓ and the number of nodes N_n. They are regrouped into two groups, the topographical variables and the network variables:

– morphological variables: Ω and q_s. Ω have been identified by Bertoldi et al. [2009b] as one the two main variables quantifying and controlling the evolution of a braided system, especially the topographical aspects. Following their approach, I want to confirm or not their insight on the modal evolution. The bedload flux q_s is chosen, as it is expected to be an excellent overall indicator of the erosional state of the river bed;

– network variables: N_ℓ and N_n. They were identified as the two most important characteristics variable quantifying the evolution of the the network, it thus seem coherent to compare their evolution with the modal analysis.

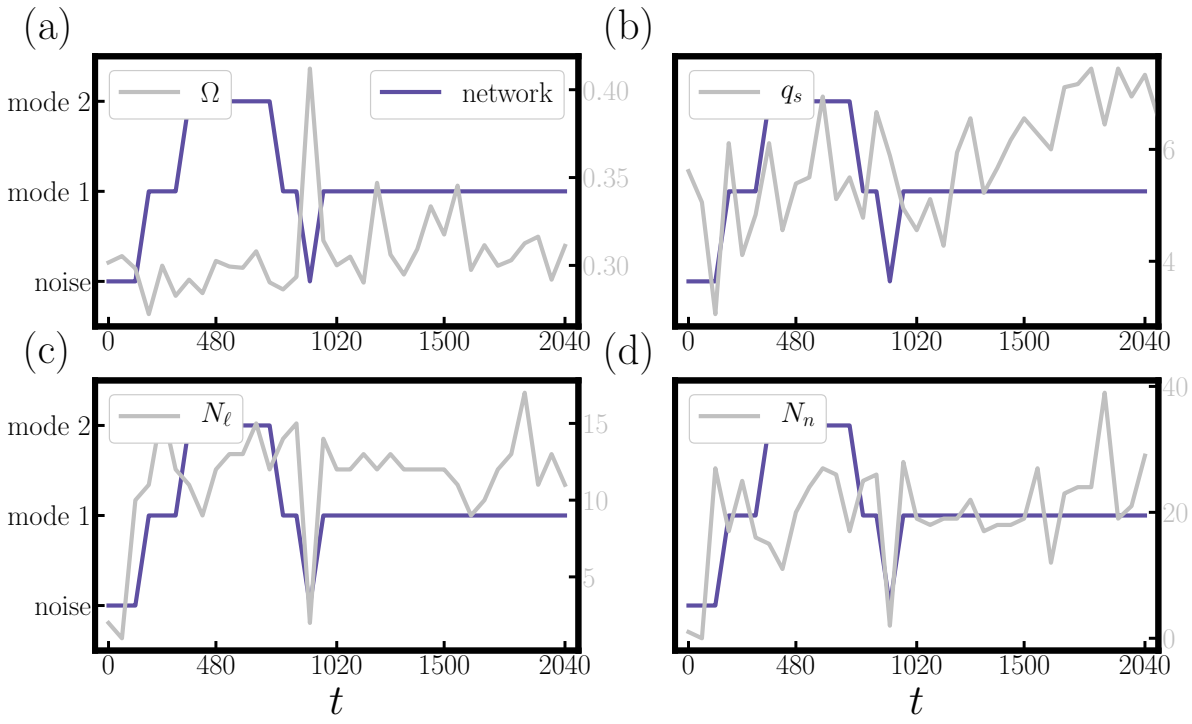

Figure 4.4: Temporal evolution of modes (blue line) in run 1 plotted alongside morphological variables (grey line): (a) the stream power Ω, (b) the bedload flux q_s, (c) the number of links N_ℓ, (d) the number of nodes N_n.

In Figure 4.4 are shown both the mode temporal evolution(blue line respectively) and the temporal evolution of Ω, q_s, N_ℓ and N_n (in grey line) on plot (a), (b), (c) and (d) respectively for run 1. The mode is displayed on the left y axis whereas Ω, q_s, N_ℓ and N_n are displayed on the right y axis (ticks are marked in grey). At first sight, none of the variables chosen seem to correlate with the mode evolution. More precisely, when a mode switch occur no particular behaviour in Ω, q_s, N_ℓ or N_n is observed. By particular behaviour is intended an inflexion point, a tendency shift, a step increase/decrease etc. Modes seem to be following a dynamics of their own, decoupled from both the hydraulics and the network's dynamics. Nonetheless, there seem to be a positive correlation with N_ℓ and N_n (respectively the number of links and nodes in the braided network). Indeed the rapid transition from straight channel to braided channel causes a rapid growth in both N_ℓ and N_n that do relates to the emergence of modes.

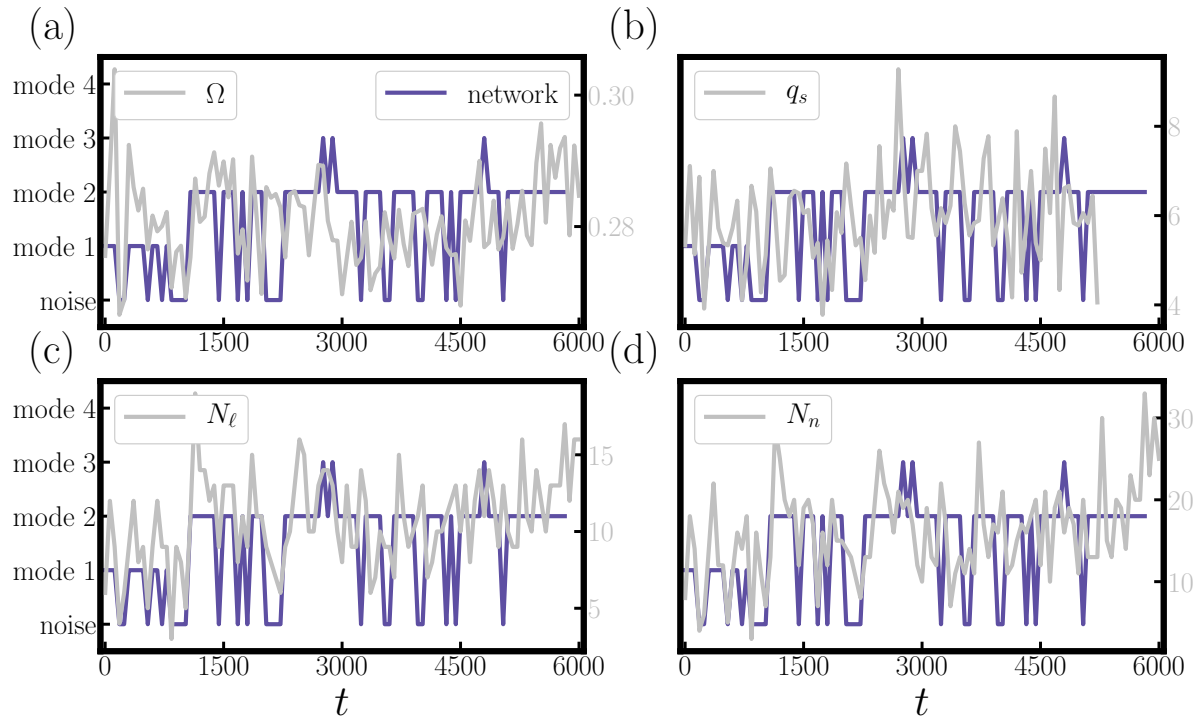

Figure 4.5: Temporal evolution of modes (blue line) in run 2 plotted alongside morphological variables (grey line): (a) the stream power Ω, (b) the bedload flux q_s, (c) the number of links N_ℓ, (d) the number of nodes N_n.

Figure 4.5 is the comparison of the mode temporal evolution for the edge and network datasets and the temporal evolution of Ω, q_s, N_ℓ and N_n for run 2. Again, a first observation of the curves does not show a particular correlation between modes evolution and variables evolution, nor there is a particular behaviour in Ω, q_s, N_ℓ or N_n that might explain the modes variations.

In their study of the dynamics of braided streams, Bertoldi et al. [2009b] observed that (paraphrasing them):

1. "two dimensionless parameters, the dimensionless discharge q^* and the dimensionless stream power ω^* (we use their notation) control and represent the braided system";
2. "braided streams reach a 'steady state' configuration, in terms of belt width, number of branches and nodes in a cross-section";
3. "Morphological parameters can be divided into two groups: (i) those characterizing the whole network that depend on the total discharge and (ii) those related to the instantaneous morphological activity that depend on the stream power".

These observations are confirmed, especially for morphological variables. Indeed, the experiments were carried at constant discharge, and no significant variations in N_ℓ, N_n or L_ℓ/L (the network variables) were observed. Moreover, most of the bed variables did not show any particular trends either (aside from some mild fluctuations,

see table 3.4). Some of them showed trends related to a slight aggradation of the system but only for run 1, which is the transition from straight channel to braided channel.

What is interesting to notice, nonetheless, is the braided system's 'activity' in terms of modes. It means that the braided network is evolving, rearranging, displacing itself (otherwise no modes could be detected) but keeping its core structure constant, *i.e.* keeping N_ℓ, N_n or L_ℓ/L constant. This process of rearrangement of the bed is undergoing regardless of the fact that hydraulic conditions are constants.

4.2.3 Modes probabilities

m_k^i is defined as the k^{th} mode of run i (with $k = 0, 1, \dots$ and $i = 1, 2$). Each mode m_k^i is composed of n_k^i elements, the total number of elements per run is N_i. The total number of modes per run is defined as N_m^i. The probability of occurrence of a mode m for the run i (again with $i = 1, 2$) is defined as

$$P(m_k^i) = p_k^i = \frac{n_k^i}{N_i}. \tag{4.1}$$

p_k^i of run 1 and 2 are noted in table 4.8 below

Table 4.8: Modes probabilities.

	run 1	run 2
p_k^i	$p_0^1 = 0.114$	$p_0^2 = 0.235$
	$p_1^1 = 0.686$	$p_1^2 = 0.102$
	$p_2^1 = 0.200$	$p_2^2 = 0.633$
		$p_3^2 = 0.031$

All the noise points are considered to form a mode of their own noted m_0^i. In addition to the mode probability, the occupation rate a of a given mode is defined. By occupation rate is intend the area covered by a given mode over the total area. Consider for instance Figure 4.6 (a): each coloured graph represent one of the elements of the mode m_0^1 ($n_0^1 = 4$ configurations over a total of $N_1 = 35$) and they cover a percentage $a = 0.044$ of the total area. The probability of being in mode m_0^1 is $p_0^1 = 4/35 = 0.114$. a gives an idea of the area covered by the mode, thus us quantifying the extent of its spatial spreading. The thickness of the graphs of Figure 4.6 have been amplified in order to appear clearly on the figure, they do not represent the actual covered area a.

Figure 4.6 shows all the graphs of the three modes of run 1. Mode 1 covers over a third of the area ($a = 0.387$) while mode 2 covers $a = 0.153$. Although mode 1 is more than three times more likely to appear than mode 2, it does not cover much more than two times its area ($a_1/a_2 = 2.53$ while $p_1/p_2 = 3.43$). Mode 1 on average occupies less space per graph than mode 2, its graphs are confined in a narrower space. In other words mode 1 is more static, less spread than mode 2. Each mode is composed of similarly looking graphs. This is not true for mode 0 (noise points) where it is clearly observed that each graph is very different one with the other.

Figure 4.7 shows all the networks of the identified modes of run 2. For mode 1 and mode 3, all the graphs looks similar. Mode 0 and mode 2 have less similar graphs, and this is shown by their higher occupation rate ($a = 0.339$

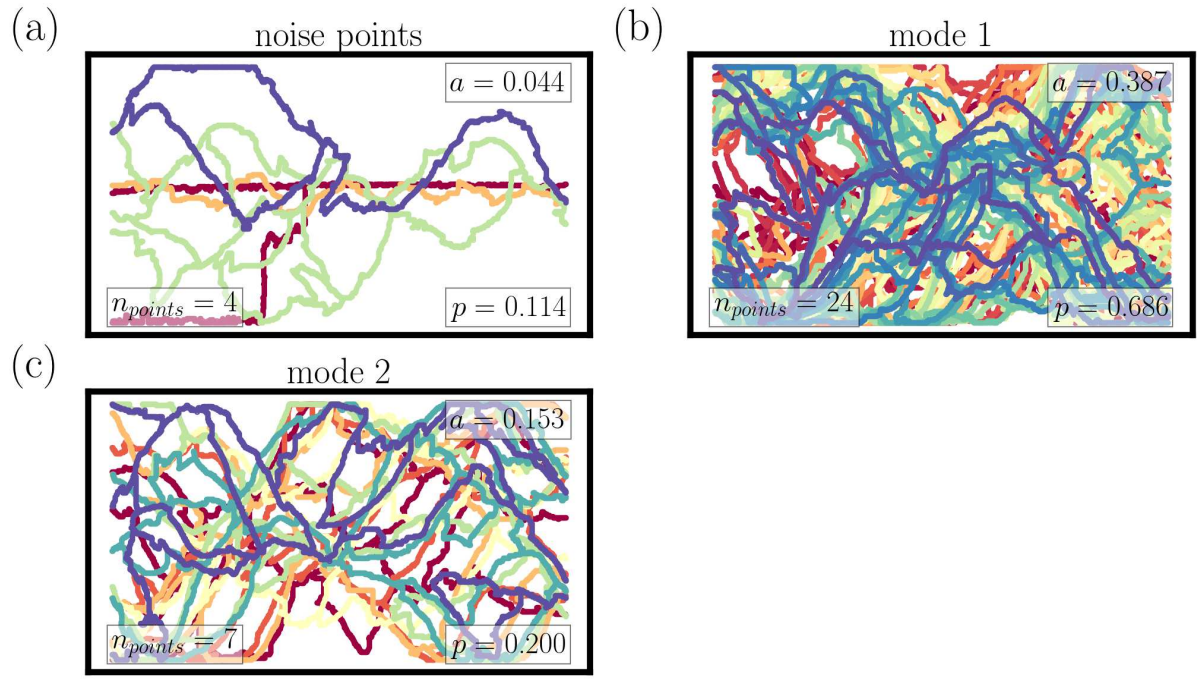

Figure 4.6: Graphic representation of the set of all graphs identified as modes for run 1. Plots (a), (b) and (c) correspond to mode 0 (noise points) mode 1 and mode 2 respectively and they are displayed with their corresponding probability p, occupation rate a and number of elements n.

and $a = 0.732$ respectively).

Observing the graphs of figures 4.6 and 4.7 helps to have an idea of the modes of the system and to verify a posteriori the accuracy of the DBSCAN method. Indeed, a visual inspection of mode 2 in run 1 (Figure 4.6 (c)) and more spectacularly modes 1 and 3 in run 2 (Figure 4.7 (b) and (d)) demonstrates that the graph of the networks are indeed quite similar, thus justifying the identification of these clusters as modes. Nonetheless, is less true for mode 1 in run 1 (m_1^1) and mode 2 in run 2 (m_2^2). Moreover, the graphs seem to cover the whole area, thus implying very diverse elements, hence their large a as mentioned above.

While interesting in their own right, the mode probabilities do not give a complete overview of the evolution of mode and of the evolution of the braided system in general. More precisely, they give a static image of the distribution of modes once the process have finished but they do not inform about the ongoing dynamics. To put it differently, we would like to have a movie of what is happening but we only have a picture. Instead of just knowing that after a long time T mode i is likely to be found with a probability p_i, it would be more interesting to know the following: given that at time t the system is in mode i, what is the probability of switching towards mode j? Even more interesting, provided that these probabilities are known, is it possible to simulate the process numerically? Does the simulation resembles reality? Could it be useful to study the braided network dynamics and anticipate its possible evolution in time? I propose to use a Markovian framework to address these questions in the following section.

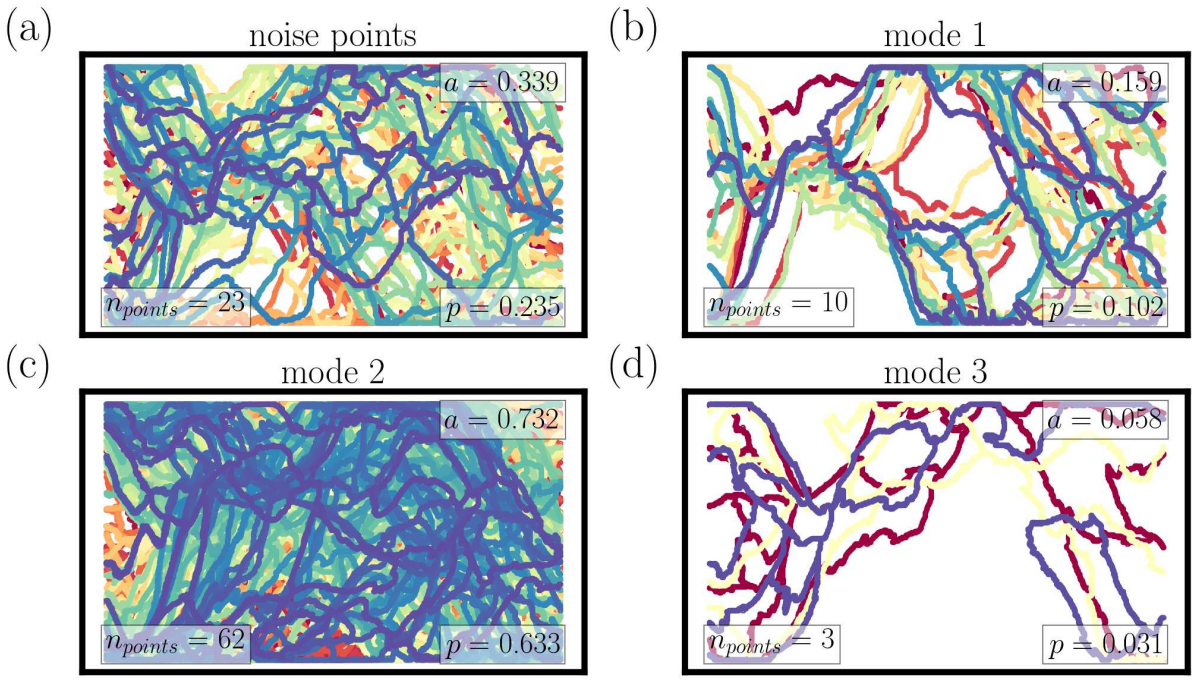

Figure 4.7: Graphic representation of the set of all graphs identified as modes for run 2. Plots (a), (b), (c) and (d) correspond to mode 0 (noise points) mode 1 mode 2 and mode 3 respectively and they are displayed with their corresponding probability p, occupation rate a and number of elements n.

4.2.4 Markov simulations

In section 2.5 Markov processes and their usage in the morphodynamic literature were briefly presented. Here, a Markovian process will be used to exploit the statistics obtained from run 1 and 2 on the mode evolution. For more details about its implementation, see appendix A.2. As a brief reminder, recall that a Markov process is a stochastic process where a finite number of events (states or modes in our terminology) have a certain probability of transitioning between them and where this probability of transition only depends on the current state. Observing the time-series of modes in Figure 4.3, it is tempting to think of their evolution as a paradigmatic example of Markov process. Indeed, why would not the transition from one mode to another be defined by a certain probability? That this probability depends on the physics/hydraulics of the problem at hand is a certainty, and this lack of knowledge is an obvious limitation in our understanding of braided systems (especially if one wants to study and predict their behaviour). On the other hand, and given the lack of precise knowledge about the dynamics of braided system, stochastic processes such as Markov processes seem to be a good way out. Indeed, probabilities are but a way to quantify what is not known in a useful manner. In the case of braided rivers: it is not known how and why the system evolves, but at least its frequency of change is known. As Poincaré stated so eloquently 'Le hasard n'est que la mesure de notre ignorance' (chance is but a measure of our ignorance). If this is true, then stochastic processes are the best tool at hand to take advantage of it.

The interesting aspect of the evolution of modes is not only their probability, interesting per se, but also the probability of transitioning from one mode to another. Let p_{ij}^k be the probability of transition from mode

i towards j in run k ($k = 1, 2$). This transition probability is measured from the time-series of modes (Figure 4.3 (b)). Basically the number of times mode i is followed by mode j is counted, dividing it by the total number of occurrences of mode i and the transition probability is obtained. The total information is stored in a transition probability matrix whose coefficients are p_{ij}^k with i the index of the row and j the index of the column. All elements in the row i thus represent the transition probabilities of mode i. Thus for instance $p_{01}^1 = 0.2$ is the probability that mode 0 switches to mode 1 in run 1 (recall that modes are numbered from 0, with 0 representing noise, to $N_m^i - 1$ with N_m^i the number of mode of run i). The transition probabilities of run 1 and 2 are presented hereafter

$$p_{ij}^1 = \begin{pmatrix} 0.5 & 0.5 & 0 \\ 0.04 & 0.92 & 0.04 \\ 0 & 0.14 & 0.86 \end{pmatrix}, \quad p_{ij}^2 = \begin{pmatrix} 0.39 & 0.13 & 0.48 & 0 \\ 0.4 & 0.6 & 0 & 0 \\ 0.16 & 0 & 0.79 & 0.05 \\ 0 & 0 & 1 & 0 \end{pmatrix}. \tag{4.2}$$

Depending on the mode the system is actually in, some transitions are impossible. For instance in run 1, transition form mode 2 to mode 0 (noise point) is impossible ($p_2^1(0) = 0$) as well as transition from mode 1 to mode 2 in run 2 is impossible. Indeed a quick examination at Figure 4.3 (a) and (b) confirms it, some transitions were not observed during the runs.

A Markov process with these transition matrices was ran and the final mode probabilities obtained from the simulations was compared with the probabilities measured from the experiments. The results are shown in Figure 4.8 (a) and (b). The Markov process is, on average, able to reproduce quite closely the modes probabilities measured from the experiments. This is true quite independently of the number of simulations used to compute them. Indeed p which fluctuates around its mean value regardless of the number of simulations used. This result tends to confirm the validity of the hypothesis made in proposing a Markov process to model the mode evolution, *i.e.*

- there is a finite number of modes;
- there is a probability that one mode i is followed by another mode j;
- the probability of transition towards mode j only depends on the actual mode i.

In contrast to Hoffimann et al. [2019], a full stochastic model that could actually generate numerically a full scale braided system's evolution was not developed. In their work, they proposed a complete model that generates synthetic time series of images. Using a criterion based on Bayesian inference, they were able to rejects images that do not reproduce the key morphodynamic statistics obtained from their experimental dataset. I wanted to apply the full extent of their model to our experimental dataset, but because of lack of time I was not able to develop the idea further. However, I think that this is a promising path in the investigation of the braided system since it provides an additional tool to study this complex phenomenon.

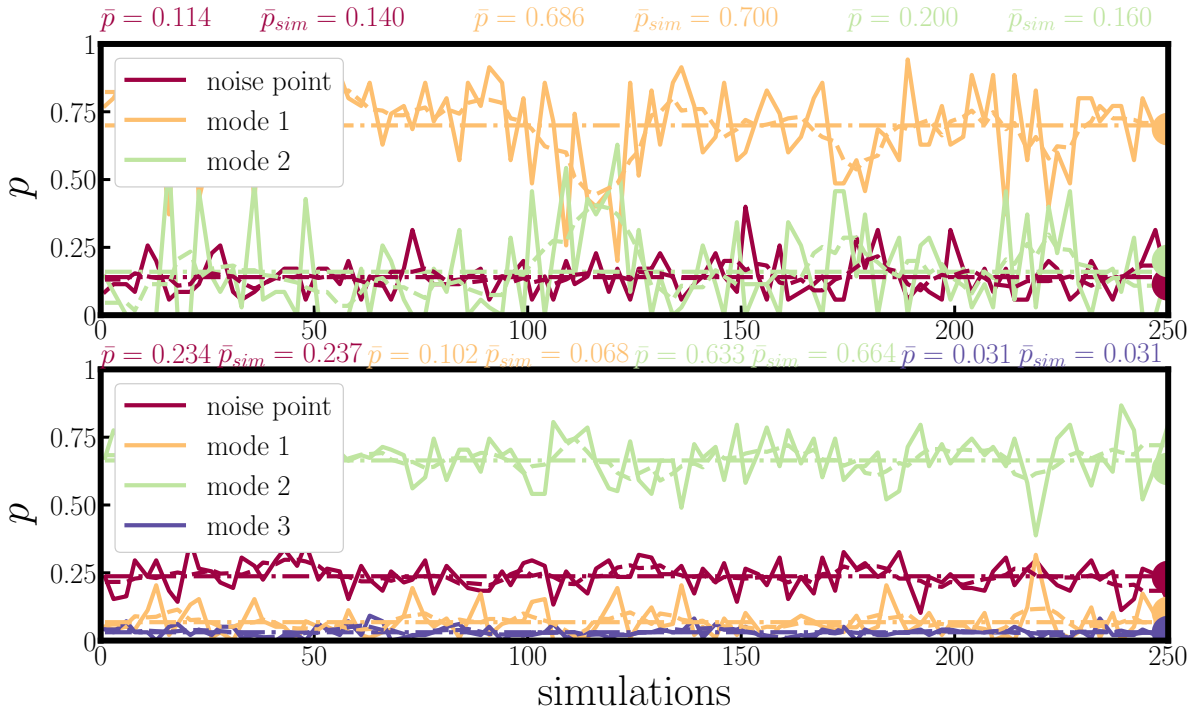

Figure 4.8: Markov simulations from transition probabilities matrices of run 1 and 2 (respectively plot (a) and (b)). On the y axis is shown the probability of each mode, represented by a specific colour. x axis represent the number of simulations used to compute the average mode probability p obtained from the simulation. Each simulation last 35 time steps and 100 time steps for run 1 and run 2 respectively (they last as long as the experimental runs, *i.e.* 35 and 100 hours respectively). $\bar{p}$ is the mode probability obtained from the experiments while $\bar{p}_{sim}$ is the mode probability obtained from the simulation. The solid coloured line represents p in function of the number of simulations, the dashed line represents the moving average of p, the dotted-dashed line represents $\bar{p}_{sim}$ and the bullet at the right end of the plot represents $\bar{p}$.

4.2.5 Concluding remarks

Lets briefly summarized the discussion on the modal analysis with the following key points:

- the DBSCAN algorithm can be combined with the graphs obtained by the Low Path method to identify clusters of similar graphs that form what are identified as modes/states of the braided system. The similarity is measured by a modified version of the Hausdorff distance, which is (mathematically) a measure of the distance between sets and which has been adapted to measure the distance between graphs;

- applying the procedure to the experiment results, three modes were identified for run 1 (two mode plus noise) and four modes for run 2 (three modes plus noise). Comparing the temporal evolution of these modes (here called modal analysis) with the topographic variables, it was observed that the system have two distinct behaviour whether one looks at it from the braided network point of view (through modal analysis) or from the hydraulics point of view (through topographic variables);

– following earlier works, it was shown that the results of the modal analysis are ideally suited for Markovian framework. The statistical distribution of modes after a given time is well reproduced by a Markov process, which suggest that a generalization of this process within a more complete stochastic simulation is not unrealistic. Due to lack of time, this path was not pursued but is highly recommended for future investigations.

A comment on the last point: to a very large extent, I was inspired by Scheidt et al. [2016], Hoffimann et al. [2019]'s work, especially for the mode detection. The main difference between the present work and theirs lies in the nature of the modes: while they used a set of digitalized images of a braided experiment, where each image represented the braided pattern (by dying the water), I took advantage of the Low Path method to work directly with the graph representing the braided pattern. Ultimately both method represent the braided system. I do think however that working directly with the graph is more relevant if one wants to study the dynamic of the braided network. Especially if the graphs are obtained directly from topographic data. Moreover, I believe that it offers broader opportunities to investigate the braided system with graph theory, opening the way to a more mathematical approach. Even better, it could also lead to a more physically based description of the braided network. Considering the vast literature on the statistical mechanics of networks of other types (see Strogatz [2001], Albert and Barabási [2002], Cimini et al. [2019] for instance), it is tempting to consider the possibility of describing the braided network in terms of statistical mechanics too, or to the very least apply concepts from statistical mechanics to the study of braided networks.

4.3 Dimensionless numbers and network variables

In this section a methodology to generalize the results obtained from application of the Low Path method to field data and to compare the results obtained from our experiment with the literature is proposed. Based on the similarity theory presented in section 2.2, a set of dimensionless groups and an appropriate adimensionalization of the main network variables are introduced, namely the number of nodes N_n, the number of links N_ℓ and the dimensionless total links length L_ℓ/L. Finally, a procedure to construct a database to obtain reliable and comparable information to rigorously study braided systems is proposed. I want to insist on the fact that this section is purely speculative, since more time than available was needed to apply the methodology proposed here. It should be viewed as a 'philosophical discussion', or a proposition of future work based on this investigation.

4.3.1 Dimensionless numbers

Dimensional analysis is a powerful theoretical tool to determine the dimensionless variables that characterize the phenomenon being studied [Barenblatt, 2003]. Fluvial system such as braided rivers are excellent candidate for dimensional analysis, since their dynamics remains unknown for the most part and is particularly hard to grasp. For instance, it is known that a braided river is an intertwinement of channels, but little is known about the physics governing their dynamics. Apart from the so-called bar theory, which mainly focuses on the linear stage of development of bedforms, no mathematical model has yet been proposed to explain the network dynamics.

The results obtained on the evolution of the braided network are interesting in their own right and allow to

already grasp some aspects about a given braided river. However, they are not particularly useful if one wants to generalize these findings to other systems or simply to compare braided rivers, be it in other experiments or even on the field. To do so would require to express them in the most general way. Here is where dimensional analysis come into play.

The Buckingham-Π theorem states that it is possible to build a set of 4 dimensionless parameters that completely characterizes a hydraulic system with sediment transport [Yalin, 1971]. They are

$$\Pi_1 = \frac{\varrho_s}{\varrho}, \quad \Pi_2 = \frac{v_* d_s}{\nu}, \quad \Pi_3 = \frac{h}{d_s}, \quad \Pi_4 = \frac{\varrho v_*^2}{\gamma_s d_s}, \tag{4.3}$$

where $\nu = \mu/\varrho$ is the kinematic viscosity. Π_2 is nothing more than the Reynolds number and Π_4 is the Shields number. The interesting part is that once the dimensionless variables are determined, it is possible to relate any other quantity of the problem in function of them. That is to say that for a dimensional quantity q it exist a function Φ such as

$$\Pi_q = \frac{q}{d_s^a v_*^b \varrho^c} = \Phi(\Pi_1, \Pi_2, \Pi_3, \Pi_4) \tag{4.4}$$

where a, b and c are real number chosen so as to render the ratio $\Pi_q = q/(d_s^a v_*^b \varrho_f^c)$ dimensionless. It is then possible to determine experimentally the function Φ relating the quantity q to the variables Π_i. In this case, the goal is to find a general relations between the hydraulics conditions and the network dynamics, in short find the relationship between Π_i and N_ℓ, N_n and L_ℓ. Three new parameters that characterize the network of the braided river were determined (in addition to the purely hydraulic parameters). They are the number of links N_ℓ which is dimensionless, the number of nodes N_n which is also dimensionless and the total link length L_ℓ whose dimension is L.

Some precisions must be made with respect to N_ℓ, N_n and L_ℓ. As they were presented in section 3.4, they do not give much information about the braided river. For instance the number of nodes or links of the river network without knowledge of the dimension of the whole braid plain does not say much about the magnitude of the braided dynamics. It is definitely more meaningful to express those three variables in function of the braided area $A = LW$. Therefore, the following new variables were defined

$$n_n = \frac{N_n}{A}, \quad n_\ell = \frac{N_\ell}{A}, \quad l_\ell = \frac{L_\ell}{A} \tag{4.5}$$

where their dimension are respectively L^{-2}, L^{-2} and L^{-1}. It is then possible to define their dimensionless counterparts and relate it to the governing dimensionless parameters

$$\Pi_{n_\ell} = n_\ell d_s^2 = \Phi_{n_\ell}(\Pi_1, \Pi_2, \Pi_3, \Pi_4), \tag{4.6}$$
$$\Pi_{n_n} = n_n d_s^2 = \Phi_{n_n}(\Pi_1, \Pi_2, \Pi_3, \Pi_4), \tag{4.7}$$
$$\Pi_{l_\ell} = l_\ell d_s = \Phi_{l_\ell}(\Pi_1, \Pi_2, \Pi_3, \Pi_4), \tag{4.8}$$
$$\tag{4.9}$$

where Φ_{n_ℓ}, Φ_{n_n} and Φ_{l_ℓ} are the function to be determined experimentally that relate the network properties of the braided river to the governing dimensionless number.

4.3.2 Network dimensionless numbers

To develop empirical laws relating the network variables to the hydraulic conditions, one should create a wide dataset of experiments with carefully controlled hydraulic conditions. The hydraulic conditions are contained in the dimensionless variables Π_i. By varying each of them while keeping the other three constant, one can map the space of hydraulic configurations and thus obtain a dataset from which it would be possible to obtain empirical formulae relating n_ℓ, n_n and l_ℓ to Π_i. In practice, however, it would not be so easy to vary each Π_i separately on from the other. Consider for instance $\Pi_3 = h/d_s$: to make it vary would imply to play with the discharge of the flow (since in this present case it is one of the few parameters controlled directly). However, by definition of $\Pi_2 = \mathsf{Re}$, varying the discharge would automatically mean varying Re through velocity. The solution is thus to simply vary the controlling parameters, in our case the flow discharge Q, measure n_ℓ, n_n and l_ℓ and Π_1, Π_2, Π_3 and Π_4 and proceed to analyse the results. On table4.9 below are gathered all the relevant parameters and variables of the problem.

Table 4.9: Dimensional and dimensionless hydraulic parameters

dimensional parameters							
ϱ	ϱ_s	μ	d_s	h	γ_s	v_*	$\sin\theta$
1000	2698	0.00005	0.001	0.0087	16658	0.036	0.015
flow dimensionless variables							
Π_1		Π_2		Π_3		Π_4	
2.69		717.00		8.74		0.077	
network dimensionless variables							
n_ℓ			n_n			l_ℓ	
11			12			15	

As Bertoldi et al. [2009b] pointed out, the dimensionless variables that controlled the dynamics of the braided network were:

- the dimensionless discharge q. In their work they defined it as: $q = Q/(L\sqrt{g\Delta d_s^3})$ with $L = Q^{2/5}/g^{1/5}$ a length scale and $\Delta = \varrho_s/\varrho$ the sediment relative density;
- the dimensionless stream power ω. In their work they defined it as: $\omega = QS/(L\sqrt{g\Delta d_s^3})$ with S the bed

slope.

It is indeed observed in the dataset that at constant hydraulic conditions n_ℓ, n_n and l_ℓ are virtually constant in both runs. It would thus be more interesting to express Π_{n_ℓ}, Π_{n_n} and Π_{l_ℓ} in function of q and ω rather than Π_i. Again, this is feasible by virtue of the similarity theory. Indeed, q and ω can be expressed as functions of $\Pi_1, \Pi_2, \Pi_3, \Pi_4$, and thus in turn express Π_{n_ℓ}, Π_{n_n} and Π_{l_ℓ} as a function of q and ω. That is

$$\Pi_{n_\ell} = \Phi_{n_\ell}(q(\Pi_1, \Pi_2, \Pi_3, \Pi_4), \omega(\Pi_1, \Pi_2, \Pi_3, \Pi_4)), \tag{4.10}$$
$$\Pi_{n_n} = \Phi_{n_n}(q(\Pi_1, \Pi_2, \Pi_3, \Pi_4), \omega(\Pi_1, \Pi_2, \Pi_3, \Pi_4)), \tag{4.11}$$
$$\Pi_{l_\ell} = \Phi_{l_\ell}(q(\Pi_1, \Pi_2, \Pi_3, \Pi_4), \omega(\Pi_1, \Pi_2, \Pi_3, \Pi_4)). \tag{4.12}$$
$$\tag{4.13}$$

4.3.3 Concluding remarks

The argument presented this section is purely speculative and apart from a set of dimensionless variables, does not present any results. Moreover, Π_i were already determined by Yalin [1971]. The idea is to convince the reader of a potential use of the network variables in general.

Indeed, these variables are relatively easy to define once the braided network is known. Moreover, the braided network is straightforwardly obtained from the bed elevation. As mentioned in the introduction, obtaining reliable bed elevation today is not a challenge, quite the contrary. Thereby, it is argued that developing empirical relation between the network variables and the flow condition is a potential goal of future research.

4.4 Limitations

We want to outline the following limitations of our approach:

- *experimental data:* only two experimental runs were performed and in the same hydraulic conditions, albeit in two different stages of the same system. Other runs in different hydraulic conditions would have been necessary.

- *Network variables:* as general as they are, they do not say much about the internal structure of the network (its spatial organization). For instance, there could be two networks with the same number of nodes N_n, but on having them all aligned on a straight line and the other having them scattered all over the place. This hypothetical example demonstrates that spatial information about the network is needed.

  In a sense, the modal analysis confirms that the spatial organization of the network changes while keeping constant its key constituents (statistically). If this was not true, then only a unique mode would be detected. Moreover, run 2 should be less active than run 1 since it is at equilibrium while run 1 is (in part) a transient

regime. All of this implies that a more profound analysis of the network is required, in particular to quantify its spatial distribution.

– *Markov process:* the current Markov process has actually very limited use. In fact, it has virtually no practical use at all. Moreover, the original aim was to develop it further within a more complete stochastic framework that would be able to simulate a real braided river. It nonetheless serves as a proof of concept of the modal analysis. Indeed, with the Markov process it was verified *a posteriori* that the transition probabilities obtain from the modal analysis are able to reproduce the mode probability distribution. It may seem like a circular argument, but apart from that there was no other mean to verify the validity of the modal analysis.

4.5 Take home message

To conclude the discussion, the following points are outlined:

– two experiments were conducted, namely run 1 and run 2: run 1 focused on the transition from a straight channel into a fully braiding channel; run 2 focused on the equilibrium stage of run 1, that is when the braided system has settled for a significant amount of time.

– both runs were quantified with two sets of variables, each focusing on a particular aspect of the braided system:

  - the morphological variables focusing more on hydraulic and morphological aspects of the braided system, with variables such as: the bedload transport rate q_s, the average bed elevation $\bar{z}$, the hydraulic power Ω etc.
  - the newly defined network variables focusing more on quantifying the braided network, with variables such as: the number of nodes N_n or the number of links N_ℓ.

– Morphological variables show that run 1 is on average aggrading as a signature of the transition from single channel to multiple channel, whereas run 2 is on average at equilibrium.

– analysis of the temporal evolution of network variables showed a diverse picture. Even though on average the number of nodes and links remains quite static, the spatial organization of the network was far from being at equilibrium, especially in run 2 (which was indeed at equilibrium). This was particularly noticeable through the modal analysis of the braided network.

– the statistics of modes evolution of the braided network is well captured and reproduced by a Markov process. At this stage of development, this Markov is only the first step for the development of a broader stochastic framework. The added value, however, comes from the utilisation of Low Path method to obtain a solid dataset quantifying the braided network's evolution.

5 Morphodynamical model

5.1 Preliminary introduction

Classic morphodynamical models often uses phenomenological equations such as the Meyer-Peter-Müller equation to express bedload transport. On top of the key issue that these models do not capture the wide fluctuations exhibited by sediment transport, they also underperform when used in numerical simulations and when predicting beforms formation. Seminara [2010] relates this failure to the lack of physical details in the bedload formulation. Previous work have highlighted the impact of diffusion on the development of bedforms in one-dimensional flow [Bohorquez and Ancey, 2016]. In their study, the authors coupled an advection-diffusion equation for the sediment balance with the classic Saint-Venant-Exner equations. They showed that particle diffusion plays a key role in bedload transport, thus ultimately influencing the development of bedforms (dunes and antidunes). Even better, benchmark analysis of numerical experiments tend to show that non-equilibrium bedload formulations (some of them including particle diffusion) perform better than classic phenomenological models [Bohorquez et al., 2019]. Several questions naturally arises:

- is an advection-diffusion bedload transport model couple with a shallow-water system able to predict the development of bedforms in a two dimensional flow?

- what is the influence diffusion on the development of bedforms?

We will address these questions in this chapter. First, I will introduce in detail the governing equations of the morphodynamical model (sections 5.2, 5.3 and 5.4). Then, I will present the linear stability analysis and apply it to the model (section 5.5). In section 5.6 I will introduce the numerical method used to solve the set of equations obtained from the linear stability analysis. In section 5.7 I will present the results obtained from the model and put it in perspective with the literature. In section 5.8 I will discuss these results and the limitations of the model. Finally I will conclude the chapter in section 5.9.

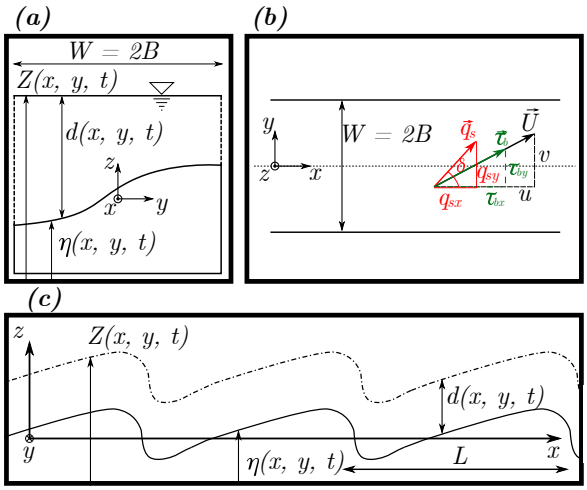

Figure 5.1: Sketch of the problem. Figure (a) shows the front view of the flow (water flowing towards the reader); Figure (b) shows the upper view of the flow (water flowing from left to right); Figure (c) shows the side view of the flow (water flowing from left to right).

5.2 Hydrodynamics

5.2.1 Flow equations

The mass and momentum conservation equation for a viscous fluid are the Navier-Stokes equations. In fluvial environments, where in general the flow depth is relatively small compared to the river width, the equations can be simplified by averaging along the vertical direction (the direction along the flow depth). Mathematically the procedure consists in integrating the Navier-Stokes along the vertical direction, from the bottom of the flow (the river bed interface or bed elevation) up to the flow free surface. The number of equations and terms is reduced and the problem is simplified. The resulting system of equations is commonly referred to as Saint-Venant equations or shallow-water equations. Both formulations will be used indistinctively. They are the foundational equations of practically every river engineering problem unless one specifically wants to study the vertical structure of the flow, in particular its turbulent structure. In my case I want to investigate the early stage formation of braided rivers, which are a paradigmatic case of shallow-water flow. Indeed, their width can be several orders of magnitude greater than their water depth, thus qualifying as shallow flows.

A proper derivation of shallow-water equation and can be found in numerous references books [Wu, 2007]. Here are simply presented the set of turbulent Shallow-Water equations that are going to be used in this study. They write, in compact form

$$\frac{\partial h}{\partial t} + \boldsymbol{\nabla} \cdot (h\bar{\boldsymbol{u}}) = 0, \tag{5.1}$$

$$\frac{\partial h\bar{\boldsymbol{u}}}{\partial t} + \boldsymbol{\nabla} \cdot (h\bar{\boldsymbol{u}}\bar{\boldsymbol{u}}) + \boldsymbol{\nabla}\left(\frac{gh^2}{2}\right) = -gh\boldsymbol{\nabla}\eta - \frac{\tau_b}{\varrho} + \boldsymbol{\nabla} \cdot (\boldsymbol{\nu}\boldsymbol{\nabla}\bar{\boldsymbol{u}}), \tag{5.2}$$

where t is time, x is the longitudinal coordinate, y is the transverse coordinate, z is the vertical coordinate, h is the water depth measured along the vertical coordinate, $\bar{\boldsymbol{u}}$ is the depth-averaged velocity vector, η is the bed altitude, g is the acceleration due to gravity and ν the turbulent viscosity tensor. $\boldsymbol{\nabla}$ is the gradient operator and $\boldsymbol{\nabla}\cdot$ is the divergence operator. The right hand side of equation (5.2) is composed of two source terms, the bed slope $\boldsymbol{\nabla}\eta = \tan\vartheta$ and the bottom shear stress $\boldsymbol{\tau_b}/\varrho$ where ϱ is the water density. The last term in the right hand side represents the depth-average Reynolds stress tensor where $\boldsymbol{\nu}$ is the viscosity tensor. In the rest of the study, the bar decoration used to express the longitudinal and transverse depth-averaged velocities will be discarded for clarity. Anytime the variable u will be written it will refer to its depth-averaged counterpart $\bar{u}$, the same for v and $\bar{v}$.

5.2.2 Boundary conditions and closure relations

Boundary conditions

The reference bed configuration, also called base state, is a straight rectangular channel of width W with rigid banks as shown in Figure 5.1. Rigid banks means vanishing flux of water and sediment on the banks, *i.e.* at $y = \pm B$ with $B = W/2$ the half width on the channel and $y = 0$ being at the centre of the channel (see Figure 5.1). They read

$$\bar{v} = q_{sy} = 0 \quad (y = \pm B) \tag{5.3}$$

Friction law

The bottom shear stress vector $\boldsymbol{\tau_b}$ is expressed in function of the Darcy-Weisbach friction factor f. It reads

$$\frac{\boldsymbol{\tau_b}}{\varrho} = \frac{f}{8}\boldsymbol{u}\left\|\boldsymbol{u}\right\|. \tag{5.4}$$

By setting the bed roughness to $4d_s$ and assuming a wide channel [Bohorquez and Ancey, 2015] it is possible to rewrite the friction factor as

$$\frac{1}{\sqrt{f}} = -2\log\left(\frac{d_s}{3.71h}\right) \tag{5.5}$$

where d_s is the sediment median diameter and h is the flow depth.

Viscous stress tensor

The eddy viscosity is usually neglected in ideal shallow water flows. In the seminal works on alternate bar development and meandering development, the authors have neglected it in their morphodynamical model [Blondeaux and Seminara, 1985, Colombini et al., 1987]. In spite of this omission, their model was able to predict

the formation of alternate bars. However, numerical simulations of free surface instabilities have shown that a non-negligible eddy viscosity is required to reproduce the non-linear steady-state shape of roll waves ([11],[15],[18],[64] in [Needham and Merkin, 1984, Balmforth and Vakil, 2012, Bohorquez and Ancey, 2015]) as well as to avoid the development of unphysical short wavelength instabilities. In Bohorquez and Ancey [2015], the main role of eddy viscosity was to prevent the development of discontinuities in the free surface of their morphodynamical model. All thing considered, the turbulent eddy viscosity was included for the completeness of the model. It was considered to be isotropic, meaning that the viscosity tensor $\boldsymbol{\nu}$ reduces to a scalar value ν. A rough estimation of the eddy viscosity is given by

$$\nu = \nu_t \sqrt{\frac{f}{8}} \tag{5.6}$$

where ν_t is a dimensionless parameter found in the range $4 \leq \nu_t \leq 18$ [Cao et al., 2015]. For simplicity, ν_t is considered $\nu_t = 1$ in the rest of the work.

5.3 Exner equation

The sediment continuity equation is the result of the balance of erosion and deposition of particles at the interface between the solid phase and the fluid phase. In morphodynamic literature it is called the Exner equation. Its derivation is found on appendix B.1. In two dimension it reads

$$(1 - \zeta_b)\frac{\partial \eta}{\partial t} = -\boldsymbol{\nabla} \cdot \boldsymbol{q_s} = D - E. \tag{5.7}$$

where ζ_b is the bed porosity, $\eta = \eta(x, y, t)$ is the bed elevation, $\boldsymbol{q_s}$ is the bedload flux vector, D and E are the deposition and entrainment respectively (they will be defined properly later on). It is generally admitted that morphological variations of the bed and variations in the fluid flow act on different timescales. Indeed, the fluid response time scales with the surface waves velocity $c = \sqrt{gH_0}$ for shallow water flow, with H_0 the characteristic flow depth. Given a characteristic length scale L_0 of the flow, the hydrodynamic time-scale is

$$T_H = \frac{L_0}{\sqrt{gH_0}}. \tag{5.8}$$

The morphological time scale is obtained from the Exner equation and writes

$$T_M = \frac{H_0 L_0}{Q_{s0}} \tag{5.9}$$

where $Q_{s0} = aU_0H_0$ is the characteristic sediment flux, U_0 is the characteristic fluid velocity and a is a coefficient.

In fluvial environments a is generally of the order 10^{-3} [Seminara, 2010]. Comparing both time scales,

$$\frac{T_H}{T_M} = \frac{L_0}{\sqrt{gH_0}} \frac{10^{-3}U_0}{L_0} = 10^{-3}\mathsf{Fr}_0 \tag{5.10}$$

Fr_0 being of order $O(1)$ the ratio $T_H/T_M \sim 10^{-3}$. The flow is supposed to adapt instantaneously to any change in the bed interface. This implies that the hydrodynamics may be decoupled from the bed dynamics, each system of equation being treated separately. When solving the full morphodynamical system, hydrodynamic equations can be considered at steady-state (no temporal terms in equations (5.1) and (5.2)).

The flow dynamics and the bed dynamics are related by the bedload transport mechanism through the term $\boldsymbol{\nabla} \cdot \boldsymbol{q_s}$, combined together they form the morphodynamical loop (see Figure 5.2 below). The bedload flux is driven by viscous forces that erode granular material from the bed; the particles are advected by the flow and finally settle back on the bed after a certain distance (or a certain time, depending on the particle velocity which depends on the flow conditions). Depending on the flow conditions, the entrainment and deposition of particles on the river bed can result in a whole range of morphological patterns such as dunes, antidunes, bars, chevrons etc. These bedforms alter the course of the fluid which adapts instantaneously to changes in the bed interface, induce a form drag that can mitigate or enhance the bottom shear stress. Changes in the bed shear stress alter the bedload flux which can increase or decrease, thus finally destroying or not the bedform, and the morphological loop starts again. If the conditions are such that the loop is stable, then the bedform will remain settled, otherwise no clear bedform can develop. In a nutshell, the linear stability analysis of the morphodynamical model determines the conditions for which a bedform of a given characteristics (dimension, celerity) can develop, at least at the linear level.

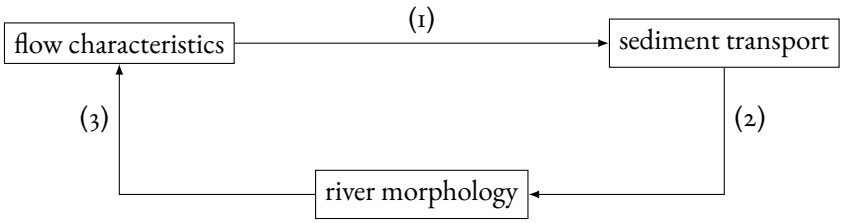

Figure 5.2: The morphodynamical feedback loop.

It is clear from Figure 5.2 that the sediment transport formulation plays a key role in the morphological feedback loop. Indeed, one could say that it plays a decisive role since it is the only physical mechanism that connects both the flow and the bed interface. Qualitatively speaking, one can readily imagine that the more physically precise the bedload formulation, the more realistic the prediction.

5.4 Bedload transport

5.4.1 Microstructural model

As stated in the introduction (section 1.1) there are numerous approaches for modelling bedload transport. Broadly speaking, they can be separated in two main families: deterministic approaches and stochastic approaches. Here only the latter is considered, and the main results and outcomes of this approach are briefly presented.

Classic bedload formulation commonly used in the literature provide decent prediction of bedload time series at sufficiently high Shields number and over long time-scales, but at the same time they can be inaccurate up to one order of magnitude [Recking, 2012]. These fluctuations occur both in natural streams and in experimental streams and to date no conclusive model have been able to grasp them. The microstructural approach to sediment transport developed by Ancey et al. [2008], Ancey [2010], Ancey and Heyman [2014] tackles the problem by taking into account the stochastic nature of the sediment transport phenomena. In particular it focuses on the microscopic interactions between grains. The framework of birth–death Markov processes offers a convenient theory to model the statistics of these exchanges.

Consider a control volume V like the one depicted in Figure 5.3. A particle may be in one the following states: resting on the bed or advected by the flow. Even without precise knowledge on the mechanics that erodes the resting particles, it is possible to assign probabilities of being entrained or deposited. Lets denote by λ the rate (probability) at which particles are being eroded from the bed and by σ the rate at which particles are being deposited back. In addition to the entrainment rate, consider that a particle may be entrained if there are already particles moving. This is called the collective entrainment μ. In V the total bedload is nothing more than the number of particles N that are moving (*i.e.* not resting) during a time interval dt, *i.e.* the sum of erosion and deposition events that occur during a time interval dt.

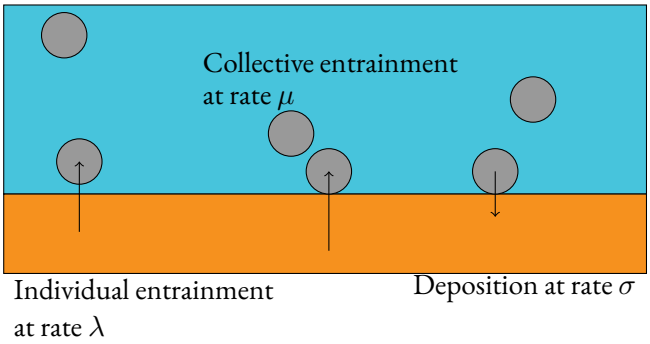

Figure 5.3: The mechanism of sediment transport in the control volume V (Figure from Ancey and Heyman [2014]). The number of moving particles observed within the window varies with time depending on the number of particles being entrained from/deposited on the stationary bed.

This formulation of the problem in terms of probabilities satisfies a probabilistic partial differential equation, called a *master equation* [Ancey et al., 2008]. When solving it, one determines the probability distribution of the number of moving particles N within the control volume V. This probability distribution follows a negative

binomial law:

$$P(N = n) = \frac{\Gamma(r+n)}{\Gamma(r)n!} p^r (1-p)^n, \tag{5.11}$$

with $r = \lambda/\mu$ and $p = 1 - \mu/(\mu + \sigma)$. The following step is to generalise the model from a discrete model to a continuous one. This is done through a technique called *Poisson representation*, which is a kind of Fourier transform that maps continuous and discrete probability spaces [Ancey and Heyman, 2014]. After ensemble-averaging the problem, bedload is expressed not in terms of moving particles N but in its continuous counterpart, the mean particle activity $\langle\gamma\rangle$, where $\langle\rangle$ stands for the ensemble average. γ denotes the number of moving particles per unit bed area. The master equation ultimately reduces, provided some approximations [Ancey et al., 2015], to an advection-diffusion equation for the activity, namely:

$$\frac{\partial\langle\gamma\rangle}{\partial t} + \frac{\partial(\bar{u}_p\langle\gamma\rangle)}{\partial x} - \frac{\partial^2(D_p\langle\gamma\rangle)}{\partial x^2} = \lambda - (\sigma - \mu)\langle\gamma\rangle = E - D \tag{5.12}$$

where $\bar{u}_p$ is the average particle velocity (taken to be constant), D_p is the particle diffusivity, $E = \lambda + \mu\langle\gamma\rangle$ is the total erosion and $D = \sigma\langle\gamma\rangle$ is the total deposition. Equation (5.12) is an advection-diffusion equation with a source terms that gives the ensemble average of the particle activity. Its interpretation is as follows: particle activity varies in time as a result of transport of particles by the water stream (advection), spreading (dispersion or diffusion due to particle velocity fluctuations), and mass transfer with the streambed (entrainment and deposition). Some comments must be made about its terms.

$\partial\langle\gamma\rangle/\partial t$ is the temporal variation of the particle activity. It simply relates the rate of change of $\langle\gamma\rangle$ with the other processes.

The advection term reads $\partial(\bar{u}_p\langle\gamma\rangle)/\partial x$. It represents the number of particles that are carried by the flow. One of the key assumptions is to consider that the particle average velocity $\bar{u}_p$ is independent of time and position but is dependent on flow conditions only. Several authors have proposed models to compute this velocity (see for instance Ancey et al. [2002], Lajeunesse et al. [2010], Furbish et al. [2012b]). $\bar{u}_p$ will be considered as the flow velocity mitigated only by a coefficient $\alpha \leq 1$, *i.e.* the particle velocity can only be lower or equal to flow velocity:

$$\bar{u}_p = \alpha u \tag{5.13}$$

The diffusive term reads $\partial^2(D_p\langle\gamma\rangle)/\partial x^2$. Some comments must be made about the nature of this term. Diffusion is a phenomenon that arises in a wide variety of physical problems such as thermal conduction or particle diffusion among many others. It appears in many areas of geophysics related to sediment transport such as landscape evolution, bedload transport or suspended transport. Despite its widespread presence in the geophysical science and in particular in the sediment transport process, no consensus exists on its physical origin. The stochastic approach of sediment transport Furbish et al. [2012a], Ancey and Heyman [2014] assimilates diffusion to the particles velocity fluctuations. Ancey et al. [2015] even highlights the importance of non-local effects of

these fluctuations in the diffusion coefficient. On the other hand, Lajeunesse et al. [2010], Seizilles et al. [2014], Abramian et al. [2019] emphasise the random-walk nature of particle displacement and therein lies the origin of diffusion. Here I will adopt a more pragmatic stance and treat diffusion as a second order term in equation (5.12) regardless of its physical origin.

The erosion term reads $E = \lambda + \mu\langle\gamma\rangle$. As a first approximation it is useful to consider that the collective entrainment term vanishes. Lets now focus in the details of the physical mechanisms governing λ. In a viscous flow, the particles are entrained by the viscous forces. The entrainment rate is thus expected to be proportional to viscous effects. In addition, a grain also feels its own weight (corrected by buoyancy). The ratio between these two forces is in essence the entrainment rate. When viscous forces dominate $\lambda \gg 0$ and erosion occurs, when the weight of the particles dominates $\lambda \to 0$. It is convenient to suppose that the entrainment rate is proportional to the excess shear stress, *i.e.* the amount of shear stress above the particle own weight. Even more convenient is to express this excess shear stress as an excess Shields number, *i.e.* the dimensionless version of the force ratio mentioned above. In definitive, it is possible to express the entrainment rate as

$$\lambda = \frac{c_e V_p}{\varrho d_s^3} \frac{\tau_b - \tau_c}{\sqrt{(s-1)g d_s}} \tag{5.14}$$

where V_p is the particle volume ($V_p = \pi d_s^3/6$), c_e is an empirical coefficient related to the deposition rate, $s = \varrho_s/\varrho$ is the relative sediment density, τ_b is the bottom shear stress corresponding the Shields number, τ_{cr} is the bottom shear stress corresponding the critical Shields number (the threshold of incipient motion) and g is the gravitational acceleration.

Lets now focus on the deposition rate. Once entrained, particles are advected over a certain distance (as identified by Einstein [1950]) at a given velocity. They travel for a certain amount of time depending on their velocity. The deposition rate is thus proportional to this time of travel, given that a particle is supposed to get deposited back on average after the travel time. The deposition rate is proportional to the weight of the particles and to the fluid in which the particle travel, the heavier the particle the shorter the travel time and vice-versa. In definitive, a deposition rate of the form of the Stokes settling time is determined

$$\sigma = c_d \sqrt{\frac{(s-1)g}{d_s}} \tag{5.15}$$

where c_d is an empirical coefficient determined from experiment. Lajeunesse et al. [2010] have evaluated this term as $c_d = 0.096 \pm 0.04$. For simplicity, I will consider $c_d = 0.1$ in the rest of the study unless stated otherwise.

Bedload flux

The bedload flux can be derived from the particle activity, even thought this derivation is not unique and poses certain problems [Furbish et al., 2012a]. Here Ancey and Heyman [2014] formulation will be followed, *i.e.* the sediment transport per unit width over a control volume V of length Δx and width B. The bedload flux then

reads

$$q_s(x,\, t) = \frac{\varpi_p}{\Delta x} \sum_{i=1}^{N} u_{p,i} = \frac{\gamma}{N} \sum_{i=1}^{N} u_{p,i} \tag{5.16}$$

with $\gamma = N\varpi_p/\Delta x$ the particle activity, $\varpi_p = 4\pi d_s^3/(24B)$ is the particle volume per unit width, N is the number of particle inside the control volume V, $u_{p,i}$ is the stream-wise component of the particle i and Δx is the width of the control volume. This definition of the bedload flux is valid inside the control volume V (see Figure 5.3). When ensemble-averaging equation (5.16) the mean bedload transport rate is obtained:

$$\langle q_s \rangle = \langle \gamma \rangle \bar{u}_p - \frac{\partial (D_p \langle \gamma \rangle)}{\partial x}. \tag{5.17}$$

Using equation (5.17) and replacing it in the advection-diffusion equation (5.12) and after some reformulations, the following equation is obtained:

$$\frac{\partial \langle q_s \rangle}{\partial x} = E - D - \frac{\partial \langle \gamma \rangle}{\partial t}. \tag{5.18}$$

If the term $\partial\langle\gamma\rangle/\partial t$ is small, then equation (5.18) reduces to the Exner equation (5.7). Recall that the Exner equation reads $(1 - \zeta_b)\partial\eta/\partial t = D - E$.

To compute the bedload flux, one must first solve equation (5.12), and provided that the fluid velocity is known (through solving the shallow-water equations), on can determine the intensity and direction of the bedload flux.

5.4.2 Two-dimensional extension

Equation (5.12) is one-dimensional. Equation (5.12) needs to be extended in two-dimensions in order to study the developments of bars, *i.e.* two dimensional bedforms. The proper way would require extending the stochastic microstructural model in two-dimensions and deriving the governing equation for the particle activity. However, this is out of the scope of this thesis. The model is going to be extended in two-dimension from purely qualitative considerations. This approach have already been used in the literature by Devauchelle et al. [2010] among others. In their work, the authors generalised the one-dimensional Erosion-Deposition model of Charru et al. [2004] in two-dimensions. This model is a particular case of the stochastic bedload model where the collective entrainment term μ is neglected and the diffusive term does not appear. Devauchelle et al. [2010] then managed to obtain a morphdynamical model that was able to capture, in its linear perturbed form and for laminar flows, the development of dunes, ripples and chevrons, and their transition towards bars (multi-dimensional chevrons as they called it). Therefore, if done properly, the extension of equation (5.12) in two-dimensions should yields similar results in the morphodynamical model.

To extend equation (5.12), each term is going to be analysed separately. The first thing to consider is that γ is now

a function of x, y and t, and not only of x and t. The first term of equation (5.12) thus remains the same, *i.e.*

$$\text{temporal term} = \frac{\partial \gamma}{\partial t}. \tag{5.19}$$

It remains unchanged with the only difference that γ is now a function of (x, y, t), *i.e.* $\gamma = \gamma(x, y, t)$. The bracket decoration $\langle\rangle$ for the particle activity γ and the mean bedload flux q_s is dropped for simplicity. This notation change is maintained for the rest of the thesis.

The second term of equation (5.12) is the advective term. It originates from the mass balance equation of moving particles passing through control volume as they are advected by the flow. The particle velocity should scale with the flow velocity. It is not known whether it scales with the shear velocity, hence $\|\boldsymbol{u_p}\| \propto \tau_b$, or with the flow velocity $\|\boldsymbol{u_p}\| \propto \|\boldsymbol{u}\|$. For simplicity, I decided to relate the particle velocity to the flow velocity. The flow velocity $\boldsymbol{u}$ is considered to be modulated by a coefficient $\alpha \leq 1$, so that particles cannot go faster than the flow. The particle velocity ultimately writes $\boldsymbol{u_p} = \alpha \boldsymbol{u}$. The advection term then writes

$$\boldsymbol{\nabla} \cdot (\boldsymbol{u_p} \gamma) = \alpha \left(\frac{\partial u \gamma}{\partial x} + \frac{\partial v \gamma}{\partial y} \right). \tag{5.20}$$

The third term of equation (5.12) is the diffusive term. Without a proper derivation of the advection-diffusion equation, it is not known whether diffusive effects act in two-dimensions or not, thus this possibility must be taken into account. Following Guazzelli et al. [2011], the diffusive term is expressed in the most general form

$$\boldsymbol{\nabla} \cdot (\boldsymbol{\mathcal{D}_p}(\boldsymbol{x}) \boldsymbol{\nabla} \gamma) \quad \text{with} \quad \boldsymbol{\mathcal{D}_p}(\boldsymbol{x}) = \begin{pmatrix} D_{xx}(\boldsymbol{x}) & D_{xy}(\boldsymbol{x}) \\ D_{yx}(\boldsymbol{x}) & D_{yy}(\boldsymbol{x}) \end{pmatrix} \tag{5.21}$$

where D_{ij} are the diffusion coefficients (with $i, j = x, y$) and $\boldsymbol{x}$ is the position along the bed. Unless there are anisotropic effects in the bedload transport process, the diffusion matrix $\boldsymbol{\mathcal{D}_p}(\boldsymbol{x})$ is symmetric ($D_{xy} = D_{yx}$). Here I must make some hypothesis to simplify its expression. In the most general case, the diffusion coefficient of $\boldsymbol{\mathcal{D}_p}$ may depend on the position along the bed. For instance the diffusion of a particle may be radically different if it is located on the crest or on the trough of a bedform. For simplicity, the diffusion process is considered to be isotropic and homogenous, meaning that the component $D_{ij}(\boldsymbol{x})$ do not depend on the position and on the orientation of the flow. An estimation the values of these components is now needed. Seizilles et al. [2014] studied diffusion in bedload transport and have estimated the cross-stream diffusion (that is the coefficient D_{yy}) as being proportional to the sediment diameter d_s and the particle settling velocity V_s (which also relates to a diffusion length that they have identified). They proposed random-walk as the mechanism responsible of diffusion. Indeed, when a particle is advected by the flow, the roughness of the bed or some flow fluctuation might induce a random lateral movement. However, as Ancey et al. [2015] showed, the diffusive term in their microstructural model was interpreted as a mathematical artefact due the averaging process used to extend their model from a discrete model to a continuous one. In other words, they argue that this diffusive term have a purely mathematical origin no physical basis. Without entering into the debate, I will consider the physical insights provided by Seizilles et al.

[2014] to simplify the diffusive terms of $\boldsymbol{\mathcal{D}_p}$. Seizilles et al. [2014] identified the mechanism originating diffusion as the difference in particle density. This gradient of density induces a Fickian flux of particle. This mechanism is has already been proposed to explain the stability of equilibrium channel [Seizilles et al., 2013, Métivier et al., 2017]. As a result the cross-stream diffusion is considered to have the same magnitude as the longitudinal diffusion, *i.e.* $D_{xx} = D_{yy} = D_p$. The last remaining terms are D_{xy} and D_{yx}. There is at the moment no clear estimation on their value nor on their physical meaning. For simplicity, they are discarded, *i.e.* $D_{xy} = 0$. The diffusive term then reduces to

$$\boldsymbol{\nabla} \cdot (\boldsymbol{\mathcal{D}_p} \boldsymbol{\nabla} \gamma) = D_p \left(\frac{\partial^2 \gamma}{\partial x^2} + \frac{\partial^2 \gamma}{\partial y^2} \right) \tag{5.22}$$

Finally the source terms, corresponding to E and D remain unchanged. The only difference here is that they now depend on x, y and t. They write

$$\lambda = \frac{c_e V_p}{\varrho d_s^3} \frac{\tau_b - \tau_c}{\sqrt{(s-1) g d_s}}, \tag{5.23}$$

$$\sigma = c_d \sqrt{\frac{(s-1)g}{d_s}}. \tag{5.24}$$

The advection-diffusion equation finally writes

$$\frac{\partial \gamma}{\partial t} + \alpha \left(\frac{\partial u \gamma}{\partial x} + \frac{\partial v \gamma}{\partial y} \right) - D_p \left(\frac{\partial^2 \gamma}{\partial x^2} + \frac{\partial^2 \gamma}{\partial y^2} \right) = \lambda - (\sigma - \mu)\gamma. \tag{5.25}$$

Recall that u and v are the longitudinal and transverse depth-averaged velocity component from the shallow-water equations (5.1)–(5.2) respectively.

5.4.3 Steady-state solution

Before going into the linear stability analysis, it is fundamental to consider the solution of equation (5.25) at steady-state. Its importance stems from the fact that rivers in general and braided river in particular exist at steady-state condition (constant water and sediment discharge at the boundaries). This implies that the resolution of the morphodynamical model should be at steady-state too. Consider the base flow described in Figure 5.1, namely a uniform flow over a flat inclined bed inside a rectangular channel, then u and v are constants. Even more specifically $v = 0$, the flow being unidirectional in the longitudinal direction. At base state on a flat bed, γ is also homogenous and time-independent. Equation (5.25) then writes

$$0 = \lambda - (\sigma - \mu)\gamma_{ss} \Rightarrow \gamma_{ss} = \frac{\lambda}{\sigma - \mu} = \frac{\lambda}{\kappa} \tag{5.26}$$

where γ_{ss} is the steady-state particle activity and $\kappa = \sigma - \mu$. For the rest of the study the collective entrainment will not be considered, *i.e.* $\mu = 0$ and thus $\kappa = \sigma$. From now on, κ will be used as the deposition rate instead of σ. Using equation (5.26), equation (5.25) then reduces to

$$\frac{\partial \gamma}{\partial t} + \alpha \left(\frac{\partial u\gamma}{\partial x} + \frac{\partial v\gamma}{\partial y} \right) - D_p \left(\frac{\partial^2 \gamma}{\partial x^2} + \frac{\partial^2 \gamma}{\partial y^2} \right) = \kappa(\gamma_{ss} - \gamma). \tag{5.27}$$

Using the new definition of γ_{ss} the Exner equation (5.7) reduces to

$$(1 - \zeta_b) \frac{\partial \eta}{\partial t} = \kappa(\gamma - \gamma_{ss}). \tag{5.28}$$

A small caveat has to be made here. γ_{ss} is the particle activity at steady state but it is not necessarily the activity at base state, which is noted γ_0 (the subscript $_0$ referring to any variable evaluated at base state). The base state is the reference flow that will be analysed and whose stability is studied in the linear stability theory (see section 5.5.1). Another way to see it is to say that the base state is the reference flow, and thus γ_0 is the reference particle activity. It is noted

$$\gamma_0 = \frac{\lambda_0}{\kappa} \tag{5.29}$$

with λ_0 the entrainment rate at base flow, *i.e.*

$$\lambda_0 = \frac{c_e V_p}{\varrho d_s^3} \frac{\tau_{b0} - \tau_c}{\sqrt{(s-1)g d_s}}, \tag{5.30}$$

with τ_{b0} the bottom shear stress at base state.

5.5 Linear stability problem

5.5.1 Linear stability theory

Fluid systems are often described and characterised by their stability. Perturbations of infinitesimal amplitude that grow in time when superimposed on an equilibrium state of the flow, the so-called base state, render the base flow unstable; conversely perturbations of infinitesimal amplitude that decay in time render the flow stable. In order to assess whether a given basic state is stable or unstable to an arbitrary small-amplitude perturbation, one needs to perform a direct numerical simulation of the full non-linear system, *i.e.* solving the complete morphodynamical model. It is computationally expensive as well as non-trivial. The clever way out of this involves linear stability theory (LST) [Juniper et al., 2014].

The instability of flows to small amplitude perturbations is analysed in the frequency domain through Fourier

transforms of the problem dependent variables after a proper linearisation of the governing equations. Given an operator describing the evolution of small perturbations, the temporal or spatial development of individual eigenmodes of that operator is considered. If the linearised set of equations possess at least one eigenvalue in the unstable half-plane (we shall see in the next section precisely what this means), an instability is deduced. The linear stability theory relies on the decomposition of any of the flow variable $\boldsymbol{v}$ into a steady part $\boldsymbol{v}_0$, usually called the base state or base flow, and an unsteady part $\boldsymbol{v}_1$. The decomposition reads

$$\boldsymbol{v}(\boldsymbol{x}, t) = \boldsymbol{v}_0(\boldsymbol{x}) + \epsilon \boldsymbol{v}_1(\boldsymbol{x}, t) \tag{5.31}$$

where $\boldsymbol{x}$ is the position vector, t is time and ϵ is a small amplitude factor. Substituting this perturbation into the governing equations and neglecting terms of order $\mathcal{O}(\epsilon^2)$, one obtains the set of linearised equations that are going to be solved. A key element of this procedure is the determination of the base state around which the perturbation is done. Once the base state is provided, the equations are expanded in normal modes, which are Fourier transforms of the dependent variables. The expansion writes, in the most general form

$$\boldsymbol{v}_1(\boldsymbol{x}, t) = \hat{\boldsymbol{v}}_1 \mathrm{e}^{i\Theta} \tag{5.32}$$

where $\hat{\boldsymbol{v}}_1$ is the complex amplitude and Θ is the phase. In general the phase is a function of both the wavelength(s) k of the problem and the frequency ω, *i.e.* $\Theta = \Theta(k, \omega)$. When one wants to study the growth or decay of the perturbation in time, the frequency ω is considered to be a complex number. When one wants to study the growth or decay of the perturbation in space, the wavelength k is considered to be a complex number. Once expanded, the system reduces to an eigenvalue problem expressed in the general matrix form

$$\mathbf{A}\hat{\boldsymbol{v}}_1 = \mathbf{0}. \tag{5.33}$$

The dispersion relation is obtained by setting the determinant of the stability matrix to zero, *i.e.*

$$\mathbb{D}(k, \omega) = 0 \tag{5.34}$$

where $\mathbb{D}$ is the determinant operator. The whole process is summarised in the following diagram.

The dispersion relation relates the frequency ω to the wavenumber k of the perturbation expansion. It is the pinnacle of the linear stability theory and answers the key questions of any stability problem:

1. for any value of the control parameter k, is the base state linearly stable or unstable, *i.e.* do the perturbations decay or grow in time?

2. what is the threshold value of k at which the base state becomes unstable?

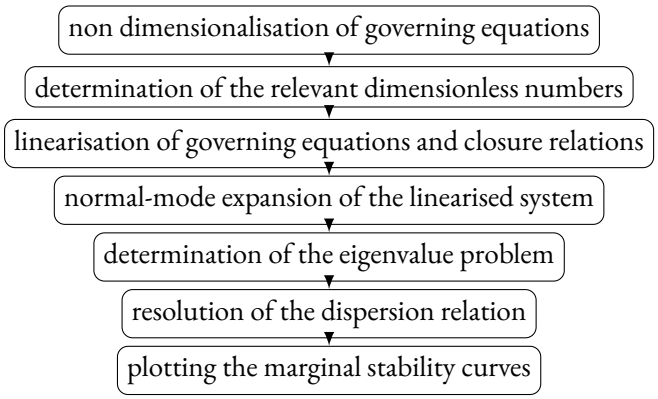

Figure 5.4: Steps of the linear stability analysis.

3. at the onset of instability, what is the spatial form of the unstable perturbations, and how fast do they grow?

Before continuing with the stability analysis of the morphodynamical problem, it is necessary to give a brief definition of stability. In general stability is viewed in the sense of Lyapunov. This definition is the following: $\boldsymbol{x}^e$ is a *stable equilibrium* if for every neighbourhood U of $\boldsymbol{x}^e$ there is a neighbourhood $V \subseteq U$ of $\boldsymbol{x}^e$ such that every solution $x(t)$ starting in $V(x(0) \in V)$ remains in U for all $t \geq 0$. Notice that $x(t)$ need not approach $\boldsymbol{x}^e$. If $\boldsymbol{x}^e$ is not stable, it is *unstable* (definition from Scholarpedia). In other words, a system is stable if after any perturbation applied on the system it returns to its initial state after waiting an infinite time. This definition of stability, based on an infinite time, is counter-intuitive to the observation of finite-time processes such as the developments of bedforms. For this reason, the concept of Lyapunov's stability will not be used. Instability is defined as the amplification of an initial perturbation, and stability as the damping of the perturbation.

5.5.2 Non-dimensionalisation and controlling parameters

In this section and in the rest of the chapter, the following notation will be used: dimensional variables will be noted with a hat ˆ decoration while dimensionless variables will not have any decoration (unless explicitly mentioned).

The following set of scales is used to non-dimensionalise the governing equations:

$$(\hat{x}, \hat{y}) = \hat{B}(x, y), \tag{5.35}$$

$$\hat{t} = \frac{\hat{B}}{\hat{U}_0} t, \tag{5.36}$$

$$\hat{\boldsymbol{u}} = \hat{U}_0 \boldsymbol{u}, \tag{5.37}$$

$$(\hat{h}, \hat{\eta}) = \hat{H}_0 (h, \eta), \tag{5.38}$$

$$\hat{\gamma} = \hat{\gamma}_0 \gamma, \tag{5.39}$$

$$\hat{\gamma}_{ss} = \hat{\gamma}_0 \gamma_{ss}, \tag{5.40}$$

$$\hat{\boldsymbol{\tau}}_{\boldsymbol{b}} = \frac{\hat{\varrho} f}{8} \hat{U}_0^2 \boldsymbol{u} \left\| \boldsymbol{u} \right\|, \tag{5.41}$$

where $\hat{U}_0$ and $\hat{D}_0$ are the velocity and flow depth of the uniform flow respectively. In our case the uniform flow is the flow down an inclined rectangular channel whose bed is at equilibrium (neither aggrading nor degrading).The uniform flow is the base state around which the system is perturbed. $\hat{B}$ is the half width of the channel, $\hat{\gamma}_0$ is the base flow particle activity (not to be confused with the steady-state particle activity $\hat{\gamma}_{ss}$), $\hat{\varrho}$ is the water density and f is the Darcy-Weisbach friction factor.

Using the aforementioned scales, equations (5.1), (5.2), (5.27) and (5.28) are rewritten in dimensionless form. They read:

$$\frac{\partial h}{\partial t} + \frac{\partial hu}{\partial x} + \frac{\partial hv}{\partial y} = 0, \tag{5.42}$$

$$\mathsf{Fr}^2 \left[\beta \frac{\partial hu}{\partial t} + \frac{\partial hu^2}{\partial x} + \frac{\partial huv}{\partial y} - \frac{\nu}{\beta} \left(\frac{\partial}{\partial x} \left(h \frac{\partial u}{\partial x} \right) + \frac{\partial}{\partial y} \left(h \frac{\partial u}{\partial y} \right) \right) \right] + h \frac{\partial (h + \eta)}{\partial x} = \beta S_0 h - \frac{\beta f \mathsf{Fr}^2}{8} u \left| \boldsymbol{u} \right|, \tag{5.43}$$

$$\mathsf{Fr}^2 \left[\beta \frac{\partial hv}{\partial t} + \frac{\partial huv}{\partial x} + \frac{\partial hv^2}{\partial y} - \frac{\nu}{\beta} \left(\frac{\partial}{\partial x} \left(h \frac{\partial v}{\partial x} \right) + \frac{\partial}{\partial y} \left(h \frac{\partial v}{\partial y} \right) \right) \right] + h \frac{\partial (h + \eta)}{\partial y} = - \frac{\beta f \mathsf{Fr}^2}{8} v \left| \boldsymbol{u} \right|, \tag{5.44}$$

$$\frac{\partial \eta}{\partial t} = \kappa_\eta \left(\gamma - \gamma_{ss} \right), \tag{5.45}$$

$$\frac{\partial \gamma}{\partial t} + \frac{\alpha}{\beta}\left(\frac{\partial u\gamma}{\partial x} + \frac{\partial v\gamma}{\partial y}\right) - \frac{\mathscr{D}}{\beta^2}\left(\frac{\partial^2 \gamma}{\partial x^2} + \frac{\partial^2 \gamma}{\partial y^2}\right) = \kappa_\gamma \left(\gamma_{ss} - \gamma\right), \tag{5.46}$$

where the dimensionless parameters are

$$\mathsf{Fr} = \frac{\hat{U}_0}{\sqrt{\hat{g}\hat{D}_0}} \text{ the Froude number,} \tag{5.47}$$

$$\nu_d = \frac{1}{\mathsf{Re}} = \frac{\hat{\nu}}{\hat{U}_0\hat{H}_0} \text{ the Reynolds number,} \tag{5.48}$$

$$\theta = \frac{\|\hat{\boldsymbol{\tau}}_{\boldsymbol{b}}\|}{\hat{\varrho}\,(s-1)\,\hat{g}\hat{d}_s} \text{ the Shields number,} \tag{5.49}$$

$$\beta = \frac{\hat{B}}{\hat{H}_0} \text{ the width-to-depth ratio,} \tag{5.50}$$

$$\delta = \frac{\hat{d}_s}{\hat{H}_0} \text{ relative sediment diameter,} \tag{5.51}$$

$$S = \frac{f\mathsf{Fr}}{8} \text{ the bed slope,} \tag{5.52}$$

$$\kappa_\eta = \frac{\hat{\kappa}\hat{H}_0}{\hat{U}_0} \text{ the entrainment,} \tag{5.53}$$

$$\kappa_\gamma = \frac{\hat{\kappa}\hat{\gamma}_0}{(1-\zeta_b)\hat{U}_0} \text{ the deposition number,} \tag{5.54}$$

$$\mathscr{D} = \frac{\hat{D}_p}{\hat{U}_0\hat{H}_0} \text{ the particle diffusion coefficient.} \tag{5.55}$$

A detailed computation of the non-dimensionalisation is found in appendix B.2. I will briefly introduce and discuss the nature and relevance of each dimensionless parameter for our problem.

The Froude number Fr is the ratio between the flow inertia and gravity acting on it. It is also a mean to characterise the relative importance between the flow velocity to surface wave velocity (gravity waves). The critical value $\mathsf{Fr}_c = 1$ is fundamental in the study of open channel flow since it characterises the nature of the flow, defined as supercritical if $\mathsf{Fr} > 1$ and subcritical if $\mathsf{Fr} < 1$. Both regimes are often referred to as upper flow regime for $\mathsf{Fr} > 1$ and lower flow regime for $\mathsf{Fr} < 1$. The distinction between both flow regime is important because in supercritical flows, information cannot propagate upstream since the flow velocity is greater than the surface wave velocity (the mean of propagation of information). Bedforms are also radically different in function of the flow regime and their behaviour is also profoundly affected by the flow regime.

The Reynolds number Re is the ratio between the flow inertial forces and the flow viscous forces. It is one of the most fundamental, if not the most fundamental dimensionless number of any hydrodynamical problem. Low values of Reynolds number correspond to a flow dominated by viscous forces, the flow thus tending to be laminar.

High Reynolds number correspond to a flow dominated by inertial forces, the flow being classified as turbulent. Laminar flows are generally smooths, reversible and time independent. Turbulent flows are generally chaotic, full of eddies, vortices, time dependent and displays large fluctuations in their variables (velocity fluctuations especially). Fluvial system are always turbulent. In this study, Re is written as the inverse of its generally accepted definition, *i.e.* $\nu_d = 1/\mathsf{Re}$. This notation will simplify the writing of the set of equations, as will be seen later on.

The Shields number θ is the ratio of bottom shear stress to the particle buoyant weight [Andreotti et al., 2013]. It is traditionally used in sediment transport problems to describe and quantify the transport threshold. It is generally admitted that above a certain threshold, usually called threshold for incipient motion or critical Shield stress (noted θ_{cr}) a granular medium starts moving under the erosive actions of viscous forces exerted by the fluid (water or air). This threshold is not universal and depends on many parameters like the hydrodynamic conditions, the slope, the physical properties of the grain among others. Moreover, the transport threshold is not unequivocally defined: generally transport is considered to occur when a 'significant' portion of the granular bed is entrained without any clear definition of significant. Moreover, the intermittent and stochastic nature of sediment transport further complicates a clear definition of transport threshold. Despite the obvious difficulties in the proper definition of the critical Shield stress, it still serves its purpose in sediment transport model to give a reasonable approximation on the threshold of erosion process. In the rest of the study $\theta_{cr} = 0.02$, as generally found in the literature [Julien, 2010].

The width-to-depth ratio β is the dimensionless number characterising the spatial extent in the transverse direction of the flow, or in other words the aspect ratio of the flow. It has been recognised both theoretically and experimentally as being the key parameter controlling the formation of free bars in rivers. Provided a given flow condition, sediment properties and that the dominant mode of sediment transport is bedload, bar forms above a certain threshold of β [Colombini et al., 1987, Tubino et al., 1999, Seminara, 2010]. In general braided rivers are found in nature for $\beta > 10$.

The relative sediment diameter (also called relative roughness) δ is the ratio between the grain size and the base flow depth. It measures the extent shallowness of the flow with respect to the granular material composing its bed. Deep flow tend to have low δ and conversely shallow flow tend to have large δ. Braided rivers, which are in general shallow and/or have large sediment with respect to the flow, tend to have high δ of the order of 10^{-1}–10^{-2}.

The bed slope S is by definition $\mathrm{d}z/\mathrm{d}x$, *i.e.* the change in altitude with changes in position. By definition S is dimensionless. Here it is expressed in function of Fr and of the Darcy-Weisbach friction factor f to emphasise its relation with the base state. It is also a convenient way to groupe together two dimensionless parameters into one.

The bed deposition number κ_η is a dimensionless version of the deposition rate κ and relates to the time it takes for a particle to settle down (alternatively called time of flight). It appears in the dimensionless Exner equation (5.65) and can be viewed as the parameter governing the rate of changes of the bed. In a way it directly relates to the bedform shape and dimension.

The activity deposition number κ_γ is a dimensionless version of γ and relates to the moving particles activity. It appears in the dimensionless particle activity equation (5.66).

The particle diffusion coefficient $\mathscr{D}$ the dimensionless expression of D_p and relates to the diffusion of particles in

the sediment transport process. To the best of our knowledge it has not been properly measured experimentally, it will be estimated by virtue of the Schmidt number Sc, the ratio between viscosity and diffusion. It will be introduced in more detail later on (see section 5.7).

5.5.3 Linearisations

Following the LST process (Figure 5.4), the governing equations (5.42)–(5.46) are linearised and perturbed. Every variable is expressed in the perturbed form

$$x = x_0 + \epsilon x_1 + \mathcal{O}(\epsilon^2) \tag{5.56}$$

where x is one of the variable between u, v, h, η and γ. The terms of order $\mathcal{O}(\epsilon^2)$ are neglected. The expansions write

$$u = u_0 + \epsilon u_1 + \mathcal{O}(\epsilon^2), \tag{5.57}$$
$$v = v_0 + \epsilon v_1 + \mathcal{O}(\epsilon^2), \tag{5.58}$$
$$h = h_0 + \epsilon h_1 + \mathcal{O}(\epsilon^2), \tag{5.59}$$
$$\eta = \eta_0 + \epsilon \eta_1 + \mathcal{O}(\epsilon^2), \tag{5.60}$$
$$\gamma = \gamma_0 + \epsilon \gamma_1 + \mathcal{O}(\epsilon^2), \tag{5.61}$$

with $u_0 = U_0/U_0 = 1$, $v_0 = 0$ and $h_0 = H_0/H_0 = 1$, $\eta_0 = 1$ and $\gamma_0 = \gamma_0/\gamma_0 = 1$. Recall that all variables and constants are dimensionless at this point. Replacing expansions (5.57)–(5.61) into equations (5.42)–(5.46), the set of linearised equations is obtained. It reads

$$\frac{\partial h_1}{\partial t} + \frac{\partial h_1}{\partial x} + \frac{\partial u_1}{\partial x} + \frac{\partial v_1}{\partial y} = 0, \tag{5.62}$$

$$\mathsf{Fr}^2 \left[\beta \frac{\partial (u_1 + h_1)}{\partial t} + 2\frac{\partial u_1}{\partial x} + \frac{\partial h_1}{\partial x} + \frac{\partial v_1}{\partial y} - \frac{\nu}{\beta} \left(\frac{\partial^2 u_1}{\partial x^2} + \frac{\partial^2 u_1}{\partial y^2} \right) \right] + \frac{\partial (h_1 + \eta_1)}{\partial x} = \beta S h_1 - \frac{\beta f_0 \mathsf{Fr}^2}{8} \left(2u_1 + \mathscr{C}_f h_1 \right), \tag{5.63}$$

$$\mathsf{Fr}^2 \left[\beta \frac{\partial (h_1 + v_1)}{\partial t} + \frac{\partial v_1}{\partial x} - \frac{\nu}{\beta} \left(\frac{\partial^2 v_1}{\partial x^2} + \frac{\partial^2 v_1}{\partial y^2} \right) \right] + \frac{\partial (h_1 + \eta_1)}{\partial y} = -\frac{\beta f_0 \mathsf{Fr}^2}{8} v_1, \tag{5.64}$$

$$\frac{\partial \eta_1}{\partial t} = \kappa_\eta \left(\gamma_1 - \gamma'_{ss}\right), \tag{5.65}$$

$$\frac{\partial \gamma_1}{\partial t} + \frac{\alpha}{\beta}\left(\frac{\partial (u_1+\gamma_1)}{\partial x} + \frac{\partial v_1}{\partial y}\right) - \frac{\mathscr{D}}{\beta^2}\left(\frac{\partial^2 \gamma_1}{\partial x^2} + \frac{\partial^2 \gamma_1}{\partial y^2}\right) = \kappa_\gamma \left(\gamma'_{ss} - \gamma_1\right), \tag{5.66}$$

where $\mathscr{C}_f$ is defined as

$$\mathscr{C}_f = \frac{1}{f_0}\left.\frac{\mathrm{d}f}{\mathrm{d}h}\right|_{h_0} \tag{5.67}$$

and γ'_{ss} is the linearisation of γ_{ss}. It reads

$$\gamma'_{ss} = 1 + \epsilon \frac{\theta_0}{\theta_0 - \theta_{cr}}(2u_1 + \mathscr{C}_f h_1) \tag{5.68}$$

The closure relations have been linearised and expressed in terms of the dependant variables of the problem and of the dimensionless parameters. They are linearised with a first order Taylor series expansion around the base state. A detailed computation of the linearisation of the closure relations is found on appendix C.1. At this point equations (5.62)–(5.68) have been expressed in function of the dependent variables of the problem $(u_1, v_1, h_1, \eta_1, \gamma_1)$ and of the dimensionless parameters. It is now possible to apply the Fourier transform to compute their normal mode expansion and to derive the eigenvalue problem.

5.6 Eigenvalue problem

5.6.1 Normal-mode expansion

As mentioned in section 5.5.1, the variables of the system of the linearised equations (5.62)–(5.66) are expanded in terms of their Fourier transform. The eigenvector thus writes

$$(u_1, v_1, h_1, \eta_1, \gamma_1) = \left(\bar{u}_1, \bar{v}_1, \bar{h}_1, \bar{\eta}_1, \bar{\gamma}_1\right) \mathrm{e}^{i(k_x x + k_y y - \omega t)} \tag{5.69}$$

where $\bar{u}_1$, $\bar{v}_1$, $\bar{h}_1$, $\bar{\eta}_1$, and $\bar{\gamma}_1$ are the complex amplitude of u_1, v_1, h_1, η_1 and γ_1 respectively, k_x and k_y are the real longitudinal and transverse wavenumber respectively. ω is the complex frequency. It is complex because the temporal stability of the perturbations is being studied, *i.e.* if they grow or decay in time and not in space. ω is

thus decomposed into a real and imaginary part, $\omega = \omega_r + i\omega_i$. k_x and k_y are defined as

$$k_x = \frac{2\pi\hat{H}_0}{\hat{\Lambda}_x}, \quad k_y = \frac{2\pi\hat{H}_0}{\hat{\Lambda}_y} \tag{5.70}$$

where $\hat{\Lambda}_x$ and $\hat{\Lambda}_y$ are the longitudinal and transverse wavelengths respectively. Note that for a given bar pattern, the transverse wavelength is related to the bedform that will ultimately develop. In particular the bar pattern is directly correlated to k_y. It will be presented in greater detail in section 5.7 and is of great importance when solving the dispersion relation to determine regions of stability and instability.

By expanding equations (5.62)–(5.66) in normal mode, a matrix equation is obtained. It reads in the general form

$$\mathbf{A}\mathbf{g} = \mathbf{0} \tag{5.71}$$

where $\mathbf{A}$ is the matrix equation and $\mathbf{g} = \left(\hat{u}_1, \hat{v}_1, \hat{h}_1, \hat{\eta}_1, \hat{\gamma}_1\right)$ is the vector of complex amplitudes of the dependent variables (the original unknowns of the system). The unknowns are now the wavenumbers k_x, k_y, the temporal frequency ω_r and the growth rate of the perturbation ω_i. k_x and k_y are the spatial dimensions of the bed perturbation that will ultimately develop, in the case of dunes for instance k_x corresponds to the wavenumber of the dune. The complete expression of $\mathbf{A}$ is presented in appendix C.2.

5.6.2 Numerical resolution of the dispersion relation

Recalling the definition of the normal mode expansion and decomposing ω into its real and complex part, any variable f can be written in the form

$$f = \bar{f}\mathrm{e}^{i(k_x x + k_y y - \omega t)} = \hat{f}\mathrm{e}^{i(k_x x + k_y y - \omega_r t)}\mathrm{e}^{\omega_i t}. \tag{5.72}$$

With this decomposition it appears clearly that ω_r is the temporal frequency of the bed perturbation and its sign determines the direction of propagation of the bed perturbation. On the other hand, ω_i is the growth rate of the amplitude $\bar{f}$ and its sign determine the growth or decay of $\bar{f}$, which is ultimately the amplitude of the bed perturbation. The longitudinal celerity of a given perturbation being $c = \omega_r/k_x$ and $k_x > 0$, it moves downstream if $\omega_r > 0$ (dunes for instance) and upstream if $\omega_r < 0$ (antidunes for instance). If $\omega_i > 0$, the amplitude $\bar{f}$ grows, the system is thus unstable and the bedform can develop. Conversely if $\omega_i < 0$, the amplitude $\bar{f}$ decays, the system is stable and no bedform can develop. The condition $\omega_i = 0$ serves to determine the neutral curve, *i.e.* the frontier between stability and instability. The Marginal Stability Curve (MSC) is the surface plot where ω_i is displayed. When plotted in a given parameter space, these marginal stability curves will synthesise the flow conditions for which bedforms can develop. They will be presented in section 5.7.

To obtain ω_r and ω_i and plot the MSC, the dispersion relation is solved numerically for a given set of parameters

$\{k_x, k_y, \mathsf{Fr}, \delta, \beta\}$. The numerical solution returns ω_r and ω_i in the parameter space $\{k_x, k_y, \mathsf{Fr}, \delta, \beta\}$. The choice of $\{k_x, k_y, \mathsf{Fr}, \delta, \beta\}$ is in principle free of constraints. Nevertheless, some range of values are more interesting than others. In particular one has to compare results of the linear stability analysis to experimental data on bedform development to assess the validity of the results. For instance if dunes are found in a specific range of k_x, δ and Fr, then the numerical resolution of the stability problem should yield $\omega_r > 0$ and $\omega_i > 0$ in this range of k_x, δ and Fr.

In practice, a range of two parameters is explored while fixing the other three in order to have MSC in a plane and to display it as a simple 2 dimensional plot. Which parameters are fixed and which parameters are varied depends on the bedform. For dunes and antidunes, the relevant parameters are the wavelength k_x and the Froude number Fr. For bars/alternate bars the relevant parameters are the longitudinal and transverse wavelengths k_x and k_y respectively. A more detailed presentation of experimental data on river bedforms is found on section 5.7 when the results of the morphodynamical model are presented in a much more detailed manner.

5.7 Results

5.7.1 Experimental observations

In this section I will present and discuss the main experimental observations on two and three-dimensional bedforms. I will introduce their main features in function of the dimensionless parameters that characterise them and determine their region of occurrence in the parameter space. To this end, several bedforms datasets from the literature are going to be used. For dunes and antidunes, the dataset of flume experiments by Guy et al. [1966] was used. Recking et al. [2009] provided a dataset of antidunes in both experimental study and field measurement, the same for Carling and Shvidchenko [2002], Cheng [2016] and Bradley and Venditti [2017] (both experimental and field studies for dunes).

For alternate bars and diagonal bars, the dataset of Colombini and Stocchino [2012] was used, referred to as JSM in their original paper, in reference to the collection of experiments from Jaeggi [1984], Sukegawa [1972], Muramoto and Fujita [1978]. In their investigation the authors made a clear distinction between alternate bars and diagonal bar, a distinction that is kept in this thesis even though it is not of particular importance. The dataset is complemented with a collection of alternate-bars experiments, namely Garcia and Niño [1993] and Lanzoni [2000]. Finally, the dataset is completed with Charru et al. [2013]'s as it is mentioned in Andreotti et al. [2012] (all the references of the corresponding work can be found in it).

Among all the parameters characterising a fluvial system over a loose bed, only a few dimensionless numbers are of practical relevance for the linear stability analysis. Recall the relevant ones when studying the development of bedforms, apart from the wavelengths:

$$\mathsf{Fr} = \frac{\hat{u}}{\sqrt{\hat{g}\hat{h}}}, \quad \delta = \frac{\hat{d}_s}{\hat{h}}, \quad \beta = \frac{\hat{B}}{\hat{h}}, \tag{5.73}$$

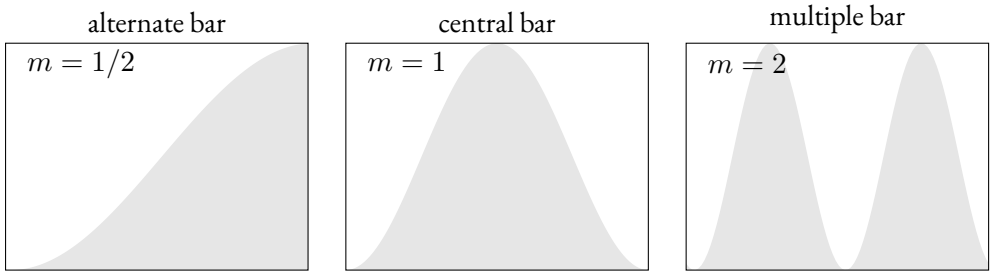

Figure 5.5: Bedforms in function of the transverse wavenumber for bar mode of order m. (a) alternate bars $\hat{\Lambda}_y = 4\hat{B}$; (b) central bars $\hat{\Lambda}_y = 2\hat{B}$; (c) for multiple bars $\hat{\Lambda}_y = \hat{B}$. The total width of each configuration is $\hat{W} = 2\hat{B}$.

where $\hat{B}$ is the half width of the river channel, $\hat{h}$ is the flow depth, $\hat{u}$ is the flow velocity, $\hat{g}$ is the gravitational acceleration and $\hat{d}_s$ is the sediment mean diameter. Recall here the definition of the longitudinal wavenumber and the transverse wavenumber from section 5.5.2

$$k_x = \frac{2\pi\hat{h}}{\hat{\Lambda}_x}, \quad k_y = \frac{2\pi\hat{h}}{\hat{\Lambda}_y} \tag{5.74}$$

where $\hat{\Lambda}_x$ and $\hat{\Lambda}_x$ are the longitudinal and transverse wavelengths respectively. Note that for a given bar pattern, the transverse wavelength is inversely proportional to β. For instance alternate bars have a transverse wavelength of twice the total channel width, *i.e.* $\hat{\Lambda}_y = 4\hat{B} = 4\hat{h}/\beta$ (see Figure 5.5). This means that, for alternate bars $k_y = 2\pi\hat{h}/4\hat{B} = \pi/2\beta$. Higher bar modes of order m have a wavelength $\hat{\Lambda}_{y,m} = 2B/m$ which means that the transverse wavenumber for bar mode of order m is $k_{y,m} = m\pi/\beta$. It reduces the number of fixed parameters when solving the dispersion relation numerically.

Figure 5.6 (a) presents bedforms in the $k_x - \mathsf{Fr}$ plane as have been commonly done in the literature (Charru et al. [2013] for instance). One readily observe the governing effect of Fr on the appearance of dunes and antidunes. Most of the experimental data on antidunes fall above the threshold $\mathsf{Fr} > 1$, even though a non negligible portion of antidunes are found at Fr close of below unity. In particular most field data of antindunes (the hollow green squares) are found for $\mathsf{Fr} < 1$. On the other hand, dunes display a more marked behaviour. Virtually all experimental data is found for $\mathsf{Fr} < 1$. This is even more pronounced for field data, where all the data is found for $\mathsf{Fr} < 0.251$. With respect to their wavelength (or wavenumber k_x), dunes and antidunes behave very similarly. Indeed, the bulk of the data is found in the region $0.5 - 2$, with a slight tendency for dunes to cover a broader range, especially for field dunes. Alternate bars and diagonal bars are less sensitive to Fr. Indeed, they are mostly found in the region $0.7 - 1.3$ quite indistinctively. This confirms the fact that the global controlling parameter for their occurrence is not Fr. A clear distinction between diagonal bars and alternate can be made through their longitudinal wavenumber k_x. Indeed, alternate bars have lower k_x than diagonal bars in general (up to one order of magnitude). k_x for diagonal bars is even closer to dunes and antidunes than to alternate bars to some extent. They have even been identified by some investigators as the transitional pattern between two-dimensional dunes and three-dimensional patterns through the decisive influence of the flow depth via Fr [Colombini and Stocchino, 2012]. However, such a distinction, although noteworthy of mention, is not of primary interest for

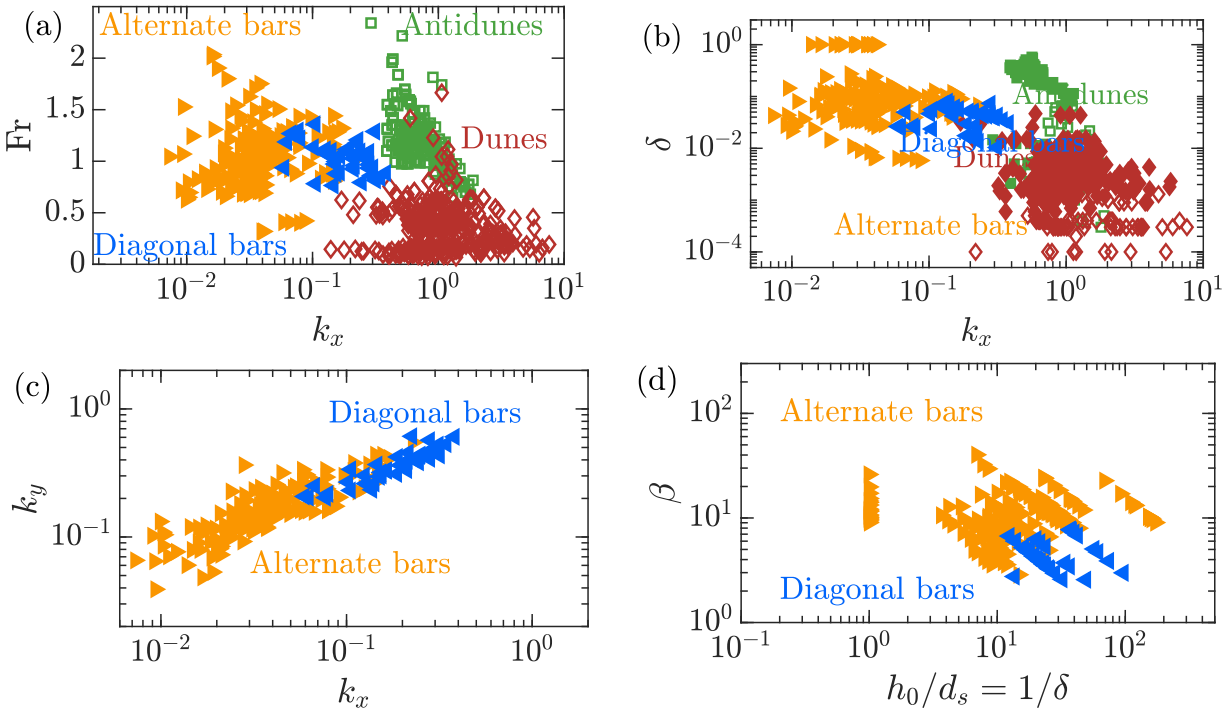

Figure 5.6: Bedform dataset from flume and field experiments. Plot (a) displays bedforms in the $k_x - \mathrm{Fr}$ plan; plot (b) displays bedforms in the $k_x - \delta$ plan; plot (c) displays bedforms in the $k_x - k_y$ plan; plot (d) displays bedforms in the $1/\delta - \beta$ plan. The data comes from the GSR and JSM dataset from Colombini and Stocchino [2012] (containing dunes, antidunes, alternate bars and multiple bars), Recking et al. [2009] for antidunes and Carling and Shvidchenko [2002], Cheng [2016] and Bradley and Venditti [2017] for dune experiments.

this work.

Figure 5.6 (b) shows the bedforms in the $k_x - \delta$ plane. The bulk of the dune dataset is found in the region $10^{-3} - 10^{-2}$. The majority of antidunes are also found in this region, except of a cluster of data which is found around 10^{-1}. This cluster correspond to experiments from the Recking et al. [2009] dataset, where the author investigated antidunes on steep slope. It is thus not very surprising to find higher values of δ, since on steep slopes the flow tend to be shallower, hence a higher relative roughness ratio. Alternate bars and diagonal bars behave similarly with respect to δ. They are found in the region $0.02 - 0.2$, with slightly lower δ for diagonal bars. The only notable exception is the Garcia and Niño [1993] dataset whose experimentally observed alternate bars are all found in the region $\delta = 1$. A substantial distinction between dunes and bars is thus δ which account for the fact that bars are found in shallow flows (low depth hence higher δ) or gravel bed rivers (high $\hat{d}_s$ hence higher δ). Of course, antidune on steep slopes are a notable exception to this global trend.

Figure 5.6 (c) shows the bedforms in the $k_x - k_y$ plane, thus discarding by definition dunes and antidunes. It is readily observed that alternate bars have lower k_x that diagonal bars. It is even true for the transverse wavenumber. In general diagonal bar have a higher k_y than alternate bar, in the most extreme cases up to an order of magnitude higher. This mean that they appear for lower values of the width-to-depth ratio β. Recall that for alternate and

diagonal bars $k_z = \pi/(2\beta)$. They are then consistently shorter than alternate bar and are found in relatively deeper flows.

Figure 5.6 (d) shows the bedforms in the $\delta - \beta$ plane, as was famously shown by Yalin and da Silva [2001].

5.7.2 Bars marginal stability curves

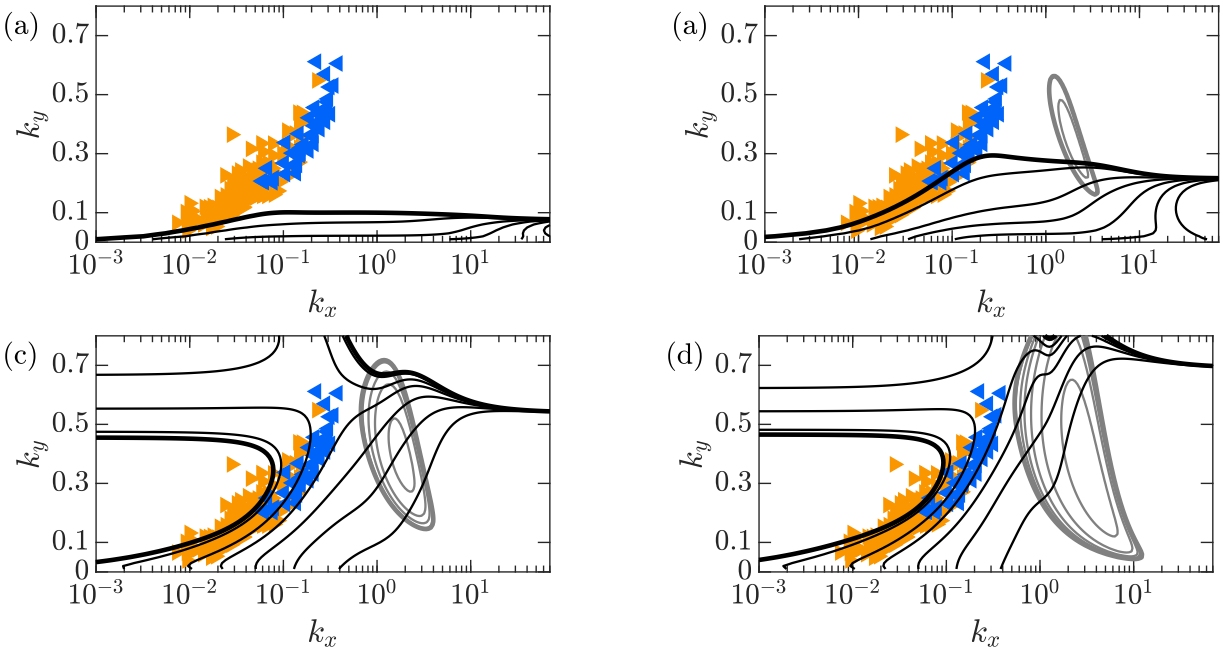

Figure 5.7: Marginal stability curve in the $k_x - k_y$ plane. The parameters are: (a) $\delta = 0.005$, $\mathsf{Fr} = 0.2272$; (b) $\delta = 0.0275$, $\mathsf{Fr} = 0.3992$; (c) $\delta = 0.203$, $\mathsf{Fr} = 0.7234$; (d) $\delta = 0.203$, $\mathsf{Fr} = 0.886$. The black lines correspond to the bar instability whereas the grey lines correspond to the antidune instability. The thick lines correspond to the neutral curve and the thin lines to growth rates of $\omega_i = 0.001,\ 0.005,\ 0.01,\ 0.02,\ 0.04,\ 0.08$

Figure 5.7 shows the marginal stability curve in the plane $k_x - k_y$ for different values of δ and Fr. Black line represent the growth rate of bars and grey lines represent the growth rate of antidunes (see section 5.8.1 for a thorough discussion). Increasing δ (plots (a), (b) and (c)) mainly affects the bar instability (black lines). Between plots (a) and (b) δ rises from 0.005 to 0.0275 and a very significant change is observed in the instability region, although it does no cover all the dataset on alternate and diagonal bars. When δ rises from 0.0275 to 0.203 the region of instability drastically increases and cover almost all of the experimental dataset. It appears that the instability region starts 'two-dimensional', in the sense that the maximum of the growth rates lies almost on the k_x axis (all the black lines are almost horizontal). It means that the fastest growing bedforms barely have a transverse direction component, they are almost purely two dimensional waves in the longitudinal direction. This behaviour is observed in Figure 5.6 (b), for a given k_x dunes are the bedforms that appear for the lowest values of δ. When δ increases three-dimensional bedforms such as alternate and diagonal bar start to appear. Moreover, when δ rises the maximum of the growth rate is translated toward lowest k_x. This is observed by the translation of the thin black lines towards the left in Figure 5.7 (a)–(b). This means that the fastest growing disturbances

have a diminishing wavenumber, a characteristic of bars more than of antidunes/dunes (see Figure 5.6 (a)–(d)). Therefore when δ increases the bedform becomes increasingly 'three-dimensional'. δ controls the transition from two-dimensional to three-dimensional bedform.

In Figure 5.7 (a) and (b) Fr is slightly increased with respect to the increase of delta. Indeed, it rises from $\mathsf{Fr} = 0.2272$ to $\mathsf{Fr} = 0.3732$, *i.e.* less than a twofold increase, whereas δ is increased from 0.005 to 0.02272 so almost a fivefold increase. Therefore the changes in the neutral curves are more likely to be attributed to δ than to Fr. Therefore Fr does not alter the bar instability region in a substantial manner. On the other hand increase in Fr explains the appearance of the antidune instability region (grey lines on plot (b)). Indeed, antidunes are found for high Fr ($\mathsf{Fr} > 0.7$) as shown in Figure 5.6 (a). However, variation in δ is much more substantial with respect to variation in Fr so it is not easy to clearly identify at this stage which one of the two parameters controls the onset of this instability. This point will be discussed in greater details in section 5.8.1. In Figure 5.7 (c)–(d) Fr is increased while δ is kept constant. The antidune instability region drastically widens. The maximum growth rate also increases with Fr (more thin grey lines on plot (d)), meaning that the antidune instability tends to grow faster than the bar instability, at least at the linear level. Moreover, the region of instability is found for k_x in the neighbourhood $1 - 10$, which is the characteristic longitudinal wavenumber for dunes and antidunes (see Figure 5.6 (a) and (b)). In addition on experimental and field studies antidunes are found in the upper flow regime, *i.e.* for Fr close to or higher than unity.

As an intermediate conclusion:

- the MSC is able to capture the region of formation of bars and alternate bars;
- δ controls the transition from two to three-dimensional bedforms, the higher δ the greater k_y (the transverse wavelength of the bedform);
- Fr does not alter significantly the bar instability region;
- Fr controls the dune/antidune instability, the higher Fr the greater the growth rate of the dune instability.

Bedforms celerity

Figure 5.8 shows the marginal stability curve of the antidune bedform in the plane $k_x - k_y$ for different values of δ and Fr and its corresponding celerity. The grey lines represent regions of positive growth rate (with the thicker line corresponding to the neutral curve at $\omega_i = 0$) and the colour plot represent the celerity of the corresponding perturbation. In all four plots $\omega_r < 0$ in the region where $\omega_i > 0$ (the region inside the grey thick lines). The bedform celerity being $c = \omega_r / k_x$ and $k_x > 0$, the bedforms migrate upstream. This is another of the characteristic features of antidunes in addition to high Fr and their characteristic scales, namely $k_x \sim O(10^0)$ and $\delta \sim 0.01$.

Figure 5.9 shows the marginal stability curve of the bar bedform in the plane $k_x - k_y$ for different values of δ and Fr and its corresponding celerity. The grey lines represent regions of positive growth rate (with the thicker line corresponding to $\omega_i = 0$) and the colour plot represent the celerity of the corresponding perturbation. In all four plots $\omega_r > 0$ in the region where $\omega_i > 0$ meaning that bars migrate downstream. This is a characteristic of

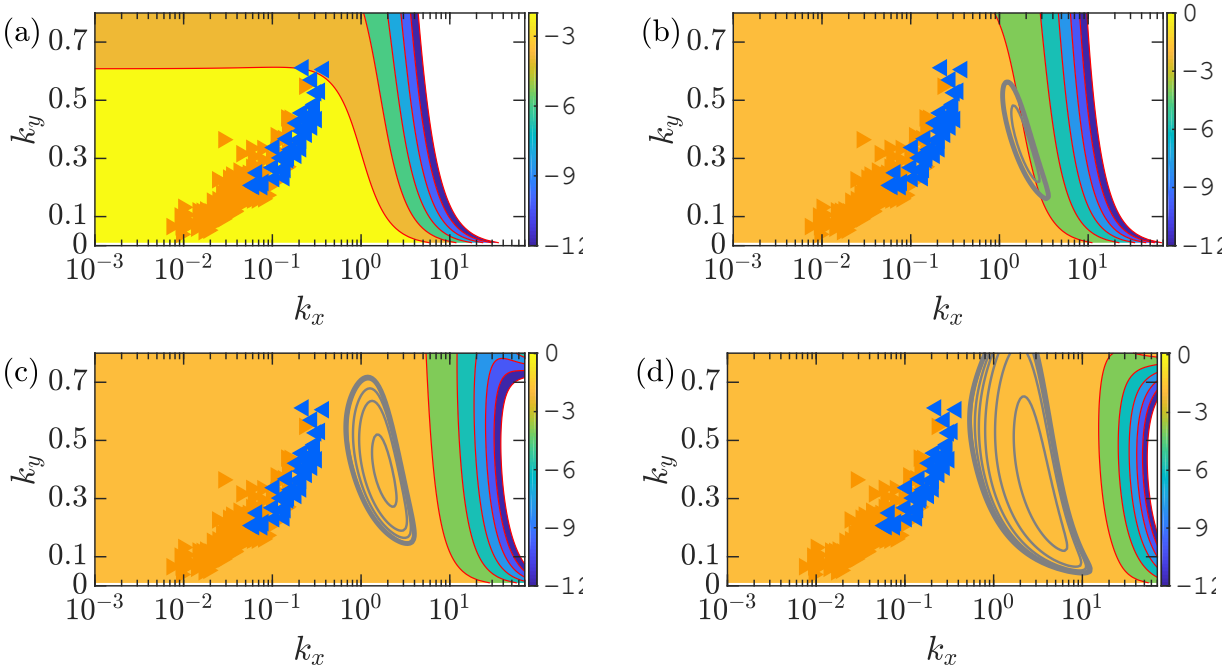

Figure 5.8: Marginal stability curve in the $k_x - k_y$ plane (solid grey lines) and the corresponding bedform celerity (in colour) for the antidune instability. The parameters are: (a) $\delta = 0.005$, $\mathsf{Fr} = 0.2272$; (b) $\delta = 0.0275$, $\mathsf{Fr} = 0.3992$; (c) $\delta = 0.203$, $\mathsf{Fr} = 0.7234$; (d) $\delta = 0.203$, $\mathsf{Fr} = 0.886$. The thick grey line correspond to the neutral curve and the thin grey lines to growth rates of $\omega_i = 0.001,\ 0.005,\ 0.01,\ 0.02,\ 0.04,\ 0.08$. The thin red lines correspond to contour line of the antidune celerity.

bars, which tend to migrate downstream. Specifically the fastest growing bars tend to have higher celerity, another characteristic feature of bars.

5.8 Discussion

5.8.1 Two-dimensional formulation

One of the objectives was to build a morphodynamical model that incorporates the development of both dunes/antidunes and bars. This model must incorporate the results obtained by [Bohorquez et al., 2019] on dunes. Their model was successful in capturing the development of dunes and antidunes with shallow-water equations coupled with the advection-diffusion bedload model. Their results should be recovered in the two-dimensional formulation of the present model. Two-dimensional formulation means that when computing the MSC there is no transverse wavelength in the perturbation, *i.e.* $k_y = 0$. All derivative with respect to y are discarded in the complex eigenvalue problem (see section 5.6). To compare both models, the same numeric values for the range of explored parameters in the computation of the MSC were used.

Figure 5.10 (a) shows a comparison of the MSC curves of the two models. In black lines is depicted Bohorquez

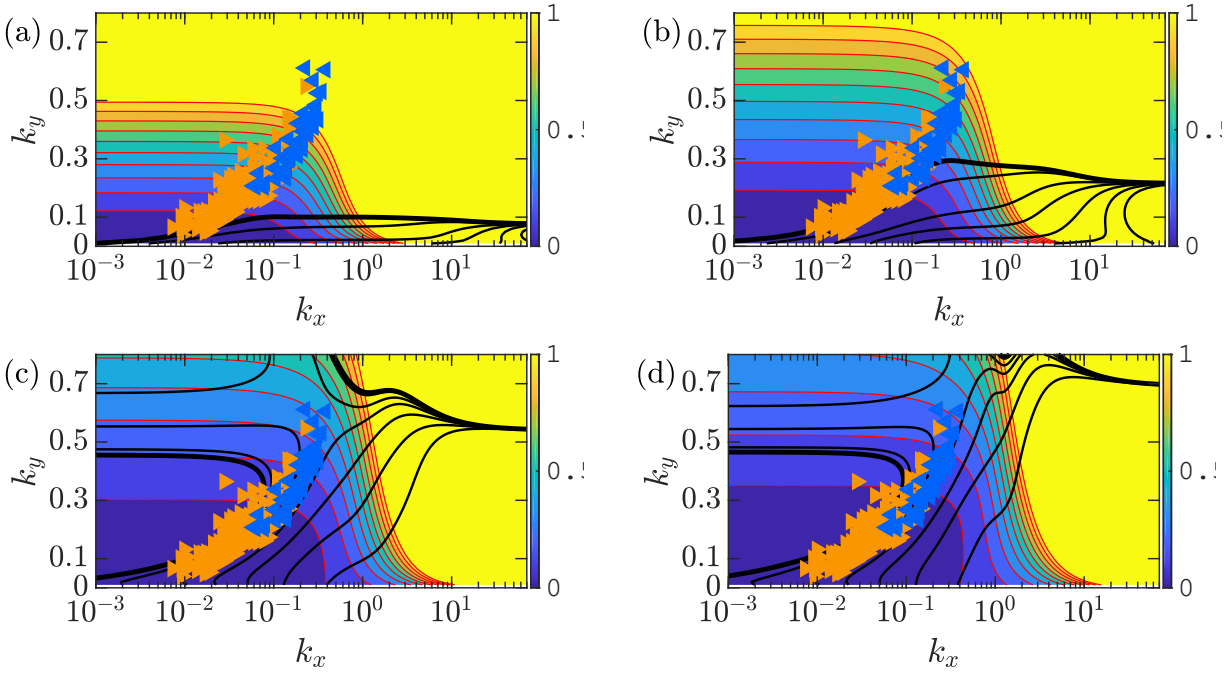

Figure 5.9: Marginal stability curve in the $k_x - k_y$ plane (solid black lines) and the corresponding bedform celerity (in colour) for the bar instability. The parameters are: (a) $\delta = 0.005$, $\mathsf{Fr} = 0.2272$; (b) $\delta = 0.0275$, $\mathsf{Fr} = 0.3992$; (c) $\delta = 0.203$, $\mathsf{Fr} = 0.7234$; (d) $\delta = 0.203$, $\mathsf{Fr} = 0.886$. The thick black line correspond to the neutral curve and the thin black lines to growth rates of $\omega_i = 0.001,\ 0.005,\ 0.01,\ 0.02,\ 0.04,\ 0.08$. The thin red lines correspond to contour line of the bar celerity.

et al. [2019]'s model with $\delta = 0.01$ (see Figure 6 (a) in Bohorquez et al. [2019]) and in grey lines is depicted our morphodynamical model with the same δ. In the antidunes regime (for $\mathsf{Fr} > 1$) the two curves almost exactly match each other. Dissimilarities arise for Fr close to or below unity, where the model fails to predict the second unstable region (the black lines that covers the dunes). It does partially cover it, although in a narrower range. In fact it includes the most unstable dunes regions (higher values of the growth rate of the lower unstable region in black). Interestingly, both model correctly predict that both dunes and antidunes should appear close to the maximum growth rate. This is coherent with the fact that $\delta = 0.01$ or lower is the region where dunes and antidunes are mostly found in the dataset (see Figure 5.7.1). One possible explanation for this discrepancy is the fact that the model does not incorporate a phase lag between the bottom shear stress and the bed elevation. This phase lag has been proven to be of critical importance in the development of dunes, but not so of antidunes. This might explain why the model successfully predicts the occurrence of antidunes but not quite so of dunes. Nonetheless, the region of occurrence of the most unstable dunes is accounted for, even if a clear distinction between dunes and antidunes is not possible.

Figure 5.10 (b) shows the influence of δ on the MSC. By increasing δ (and keeping all other parameters constant) the neutral curve is translated to the right, *i.e.* towards higher wavenumbers (or lower wavelengths). It means that the unstable bedforms, if they develop, are more likely to be ripples or any kind of bedform that scale with the grain size. Recall that increasing δ is equivalent to increasing the grain size or decreasing the flow depth (or

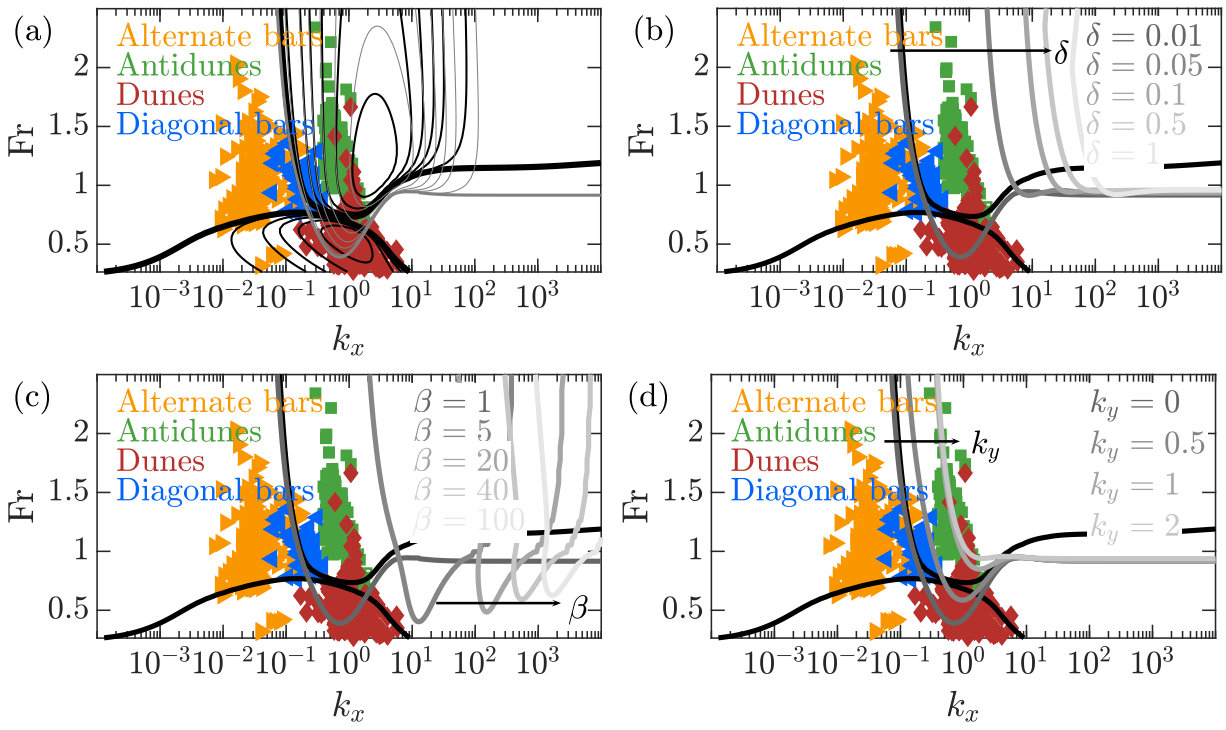

Figure 5.10: Comparison of the fully one-dimensional morphodynamical model of Bohorquez et al. [2019] (the reference curve) with the two-dimensional morphodynamical model. The stability curves for $\delta = 0.01$ are shown on the k_x–Fr plane (as in Figure 5.6 (a)). (a) The contour lines of constant growth rate are shown for the one-dimensional model of Bohorquez et al. [2019] (black lines) and for the two-dimensional model (gray lines), the thick lines correspond to the neutral curve and the thin lines to growth rates of $\omega_i = 0.001,\ 0.005,\ 0.01,\ 0.02,\ 0.04,\ 0.08$ for antidunes and one fourth of these values for dunes. (b) Neutral curves of the two-dimensional model for increasing values of δ, lighter grey lines correspond to higher δ, the black line correspond to the reference curve. (c) Neutral curves of the two-dimensional model for increasing values of β, lighter grey lines correspond to higher β, the black line correspond to the reference. (d) Neutral curves of the two-dimensional model for increasing values of k_y, lighter grey lines correspond to higher k_y, the black line correspond to the reference curve. In all four figures are displayed the dataset of bedforms, the same colour code as Figure 5.6 is used.

both), a configuration much more suitable for the appearance of ripples. Interestingly a threshold appears for $\mathrm{Fr} = 1$. Below 1 no bedforms grows, their development is confined to the so-called upper-regime. A clarification has to be made on the significance of large longitudinal wavenumbers. k_x is defined as $k_x = 2\pi\hat{h}/\hat{\Lambda}_x$, so large k_x (typically of order $O(10^1)$ and above) correspond to deep flows. In this case the shallow-water approximation is invalid and the results must be discarded, or at the very least taken with extreme caution.

Figure 5.10 (c) shows the influence of β on the stability curve. By increasing it (and keeping all other parameters constant) the neutral curve is again translated towards higher wavenumbers. Physically increasing β is equivalent to increasing the flow width or decreasing the flow depth (or both), again a configuration more suitable for the appearance of ripples (or bars for that matter). It is interesting to notice that this time the threshold $\mathrm{Fr} = 1$

does not appear. Indeed, the instability region exists for Fr above or below unity. Again in the two-dimensional formulation of the model high β is not a flow regime suited for the appearance of dunes/antidunes, and if they appear it is at the limit of validity of the model (deep flows).

Figure 5.10 (d) shows the influence of k_y on the stability curve. This time the translation towards high k_x is less pronounced and the neutral stability curve still grasp some of the antidunes from the dataset. Here I must stress the physical significance of k_y. It represent the transverse wavenumber of the bed perturbation and appear in the eigenvalue problem (see appendix B) anytime a partial derivative in y appears. Therefore $k_y = 1$ correspond to a complete sinusoidal perturbation along the channel width. In the two-dimensional formulation, increasing the transverse perturbation alter the shape of the instability region but not as significantly as increasing δ or β. It also slightly translates the neutral curve towards high k_x but not up to unphysical wavenumbers. In the two-dimensional formulation, the model is thus able to predict the formation of two-dimensional bedforms (mainly antidunes) even if a transverse perturbation is introduced ad hoc, so it confirms the robustness of the model.

5.8.2 Influence of diffusion

The equations that govern the evolution of the bed are the Exner equation (5.45) and the advection-diffusion equation (5.46). Three dimensionless parameters control these equations, namely $\mathscr{D}$, κ_η and κ_γ. They are the dimensionless counterparts of the particle diffusivity $\hat{D}_p$ (for $\mathscr{D}$) and of the deposition rate $\hat{\kappa}$ (for κ_η and κ_γ). To assess the influence of diffusion on the development of bedforms, the influence of these parameters on the MSC must be assessed. $\hat{D}_p$ and $\hat{\kappa}$ are expressed in function of the dimensionless parameters (see appendix C.1)

$$\hat{D}_p = \frac{\hat{\nu}}{\mathsf{Sc}}, \quad \hat{\sigma} = c_d \frac{\sqrt{s-1}}{\mathsf{Fr}\delta} \tag{5.75}$$

where Sc is the Schimdt number (the ratio of viscosity to diffusivity) and c_d is an empirical parameter [Lajeunesse et al., 2010]. Sc is chosen to be close to 1. This choice is made because there is no experimental study on particle diffusion that define a proper range of values for $\hat{D}_p$. Nonetheless, it is unlikely that this diffusivity is several order of magnitude lower or higher than water viscous effects. It is then convenient to define the diffusivity by setting the Schmidt number. A caveat has to be made: originally Sc is the ratio between a given fluid viscosity and its mass diffusivity, and so it characterize the relative strengths of its internal processes. In this case, the fluid viscosity is compared to the particle diffusivity, so strictly speaking two different physical processes are being compared. However, it can be argued that the particle diffusivity is the result of viscous effects of the fluid on the particles, hence particle diffusivity originates from the same physical process of water viscosity. By this line of reasoning $\hat{\nu} \sim \hat{D}_p$. Therefore the range $\mathsf{Sc} = 0.125, 0.25, 0.5, 1, 2$ is going to be explored, *i.e.* a diffusivity 8 times, 4 times, 2 times, equal and one half the strength of viscosity respectively.

c_d is a purely empirical parameter. It appear in the definition of the deposition rate, *i.e.* the typical time taken by a particle entrained by the flow to settle down. Lajeunesse et al. [2010] empirically determined its value as $c_d = 0.094 \pm 0.006$. Once the base flow is given, the deposition rate is entirely determined by the nature of the sediment s and by c_d. The range $c_d = 0.01, 0.05, 0.1, 0.5, 1$ is going to be explored.

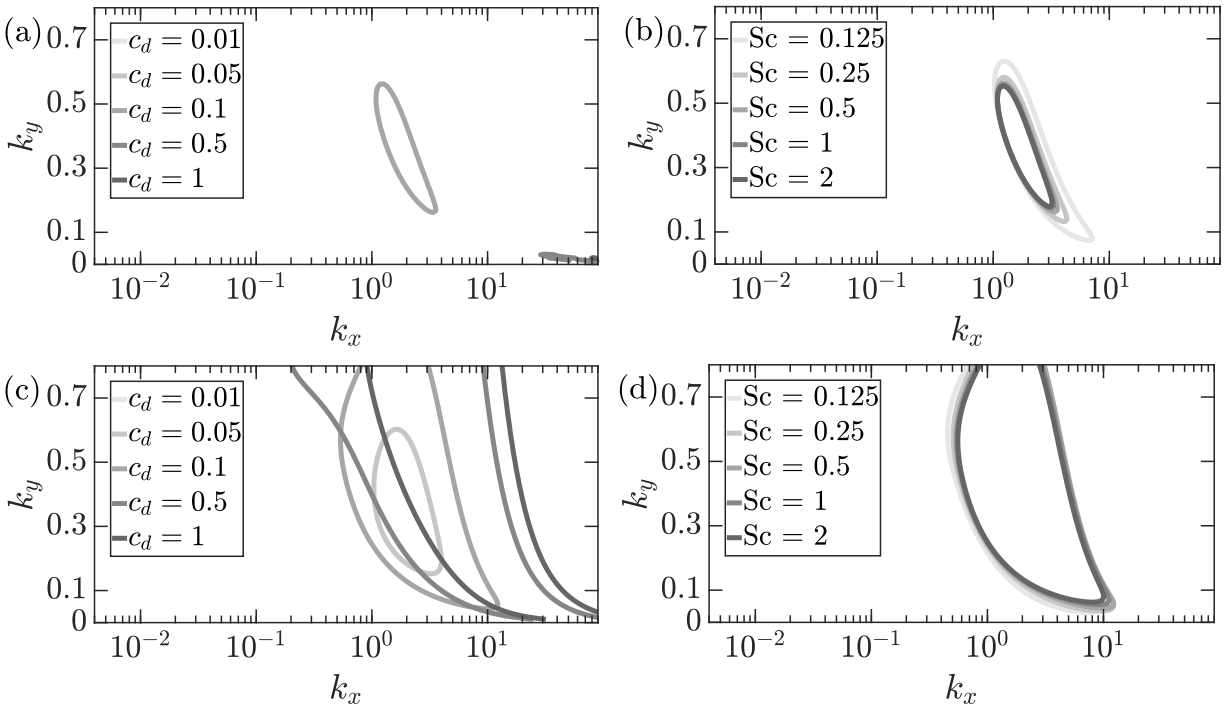

Figure 5.11: Marginal stability curve of the model in the $k_x - k_y$ plane for the antidune bedform with varying c_d (plots (a) and (c)) and Sc (plots (b) and (d)). The parameters of the base flow are: $\delta = 0.0275$, $\mathsf{Fr} = 0.3992$ for plots (a) and (b); $\delta = 0.203$, $\mathsf{Fr} = 0.886$ for plots (c) and (d). In plot (a) and (c) the Schmidt number is kept at $\mathsf{Sc} = 0.5$. In plot (b) and (d) c_d is kept at $c_d = 0.1$. The neutral curves are depicted in grey with lighter greys corresponding to lower values of the varied parameter.

Figure 5.11 shows the marginal stability curves for the antidune instability in the $k_x - k_y$ plane for different values of δ and Fr and for varying values of c_d and Sc. On plots (a) and (c) are shown the neutral curves for increasing values of c_d (in increasing shades of grey) for two different flow condition, $\delta = 0.0275$ and $\mathsf{Fr} = 0.399$ and $\delta = 0.203$ and $\mathsf{Fr} = 0.886$ respectively, the Schmidt number is fixed at $\mathsf{Sc} = 0.5$. The same flow conditions are used on plot (b) and (d), this time c_d is fixed at $c_d = 0.1$ and the Schmidt number is varied. In the lower regime (low Fr), the antidune instability only exists for $c_d \geq 0.1$, which is the experimentally determined value by Lajeunesse et al. [2010]. In spite of its existence, the instability region is extremely skewed and located on the horizontal axis for high k_x (on the bottom right of plot (a)). As mentioned earlier, these values of k_x are on the limits of validity of the shallow-water approximation. Moreover, in the lower regime antidunes are less likely to appear, which might explain why the instability region is smaller than the bar region and its growthrate is lower than the growthrate of the bar region (see section 5.7.2). In the higher regime, increasing values of c_d correspond to wider regions of the instability (plot (c)). This is probably due to the influence of c_d on the deposition rate. Indeed, both dimensionless deposition rates depends linearly on c_d (see equation (5.75)). Physically, the deposition rate is the timescale that a moving particle takes to settle back on the bed. Equivalently, it corresponds to the particle deposition length, *i.e.* the distance travelled by a particle before it settles back on the bed. This deposition length controls the size of alternate bars or rhomboid pattern [Devauchelle et al., 2010, Andreotti et al., 2012]. Intuitively, a higher deposition length is likely to induce larger bedforms. It is observed on plot (c), the higher c_d

the wider the instability region. With that being said, it is not self-evident that a wider instability region means a larger bedform. A wide instability region covers a range where large and small bedforms can develop (spanning over several order of magnitude of k_x), but the most unstable bedforms is not guaranteed to be influenced by this increase in the deposition rate. Further investigation is thus needed.

Variation of Sc does not seem to affect the instability in the same manner. Comparing plot (a) to (b) and (c) to (d), it is observed that diffusion seems to slightly alter the neutral curve, especially comparing with the effects c_d have on the neutral curves. It is even less pronounced in the higher regime (plot (d)) compared to the lower regime (plot (b)) even though in the higher regime antidunes are most likely to appear (and Indeed, the instability region is much wider). Lower values of Sc (that is higher relative influence of diffusion with respect to viscosity) correspond to wider instability regions (lighter grey curves on plot (b) and (d)). This results makes sense physically: a higher diffusion of particles is likely to increase their travelled distance, hence resulting in a wider instability region. In other words, it is very unlikely that diffusion, augmenting particle mobility, would not alter the instability region. Nevertheless, it does not seem to affect much the antidune instability, especially in the higher regime. A possible explanation might be the following: antidunes are bedforms that migrate upstream, whereas diffusion effects, unless they are particularly strong, are advected downstream by the flow. It might explain why in the antidune regime the diffusive effects of the particle activity are not 'felt' by the antidune. Keep in mind that it is a highly speculative explanation and further investigation must be done.

Figure 5.12 shows the marginal stability curves in the plane $k_x - k_y$ for different values of δ and Fr and for varying values of c_d and Sc for the bar instability. On plots (a) and (c) are shown the neutral curves for increasing values of c_d (in increasing shades of grey) for two different flow condition, $\delta = 0.0275$ and $\mathsf{Fr} = 0.399$ and $\delta = 0.203$ and $\mathsf{Fr} = 0.886$ respectively, the Schmidt number is fixed at $\mathsf{Sc} = 0.5$. The same flow conditions are used on plot (b) and (d), this time c_d is fixed at $c_d = 0.1$ and the Schmidt number is varied. In the lower regime, variations of c_d does not affect significantly the shape of the instability region. Apart from a slight peak around $k_x = 10^{-1}$ for $c_d = 0.01$, no significant changes in the instability region are observed. In the higher regime, changes in the instability region are much more pronounced. Increasing c_d has the effect of 'translating' the the instability region upwards (towards higher k_y). At this point, it is hard to determine the real influence of c_d on the bar instability. Compared to the antidune instability, where increasing c_d widens the instability region, here increasing c_d shifts the instability region. The physical significance of c_d being the same (that is controlling the deposition rate or equivalently the deposition length), it would be expected that its effects are rather similar, which does not seem to be the case here. Moreover, the effects of c_d are significantly different in the lower and the higher regime (a behaviour that is also found in the antidune instability).

Variation in Sc does not seem to affect the instability region in the same manner as variation in c_d (as in the antidune case). In the lower regime (plot (b)), Sc has virtually no effect on the MSC. In the higher regime, increasing Sc (that is decreasing the relative influence of diffusion) widens the instability region. Indeed, the horizontal lines are translated downwards. The opposite behaviour is observed when increasing c_d in the higher regime. A clear and intuitive explanation does not come to mind in this case and I could only speculate on its potential effects on the bar instability.

The exact effects of diffusion on the development of bedforms have not been investigated in this study, and unless a proper quantitative analysis is conducted the results presented here are only speculative. They give a qualitative

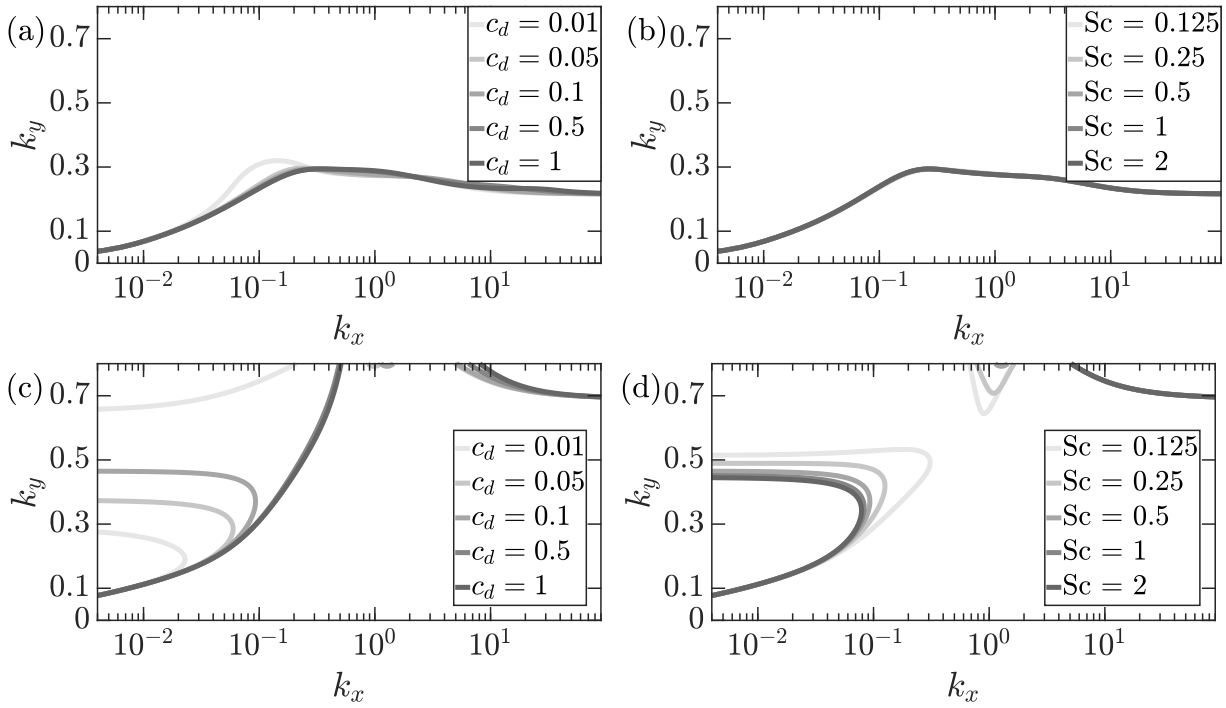

Figure 5.12: Marginal stability curve of the model in the $k_x - k_y$ plane for the bar bedform with varying c_d (plots (a) and (c)) and Sc (plots (b) and (d)). The parameters of the base flow are: (a) and (b) $\delta = 0.0275$, $\mathsf{Fr} = 0.3992$; (c) and (d) $\delta = 0.203$, $\mathsf{Fr} = 0.886$. In plot (a) and (c) the Schmidt number is kept at $\mathsf{Sc} = 0.5$. In plot (b) and (d) c_d is kept at $c_d = 0.1$. The neutral curves are depicted in grey with lighter greys corresponding to lower values of the varied parameter.

assessment of the influence of the advection-diffusion sediment transport model used in the morphodynamical model. To better assess and understand the influence of the advection-diffusion bedload model a proper numerical and/or analytical investigation is needed. Nonetheless, I can conclude that the morphodynamical model, with the presence of diffusion in the bedload transport formulation, is able to capture the development of two and three-dimensional bedforms. In particular, I showed that particle diffusivity plays a non-negligible role in the bedform development by modifying the bedforms instability regions. However, I was not able to relate the alterations of the marginal stability curves to the actual effects it has on the bedform development, besides some purely speculative hypothesis. I do argue, however, that diffusion combined with the particle deposition, the two mechanisms governing both the advection-diffusion model and the Exner equation, must be reckoned when investigation the development of bedforms, and further investigation down that road is needed.

5.8.3 Limitations

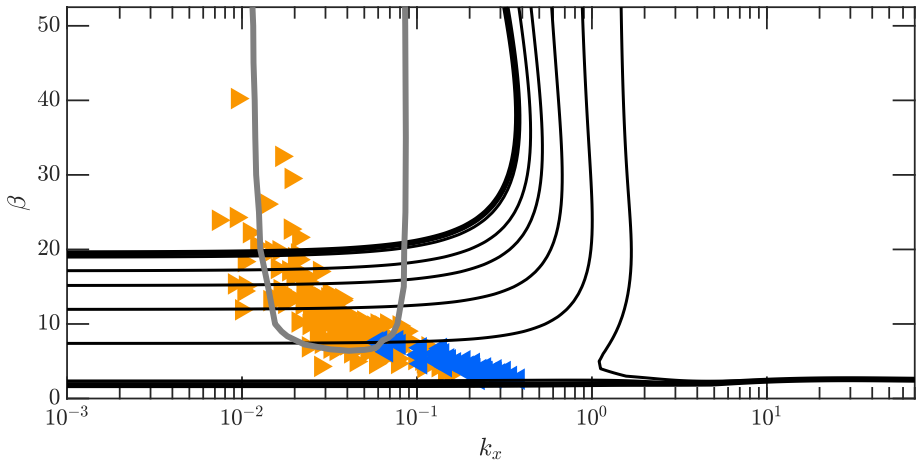

Figure 5.13: Marginal stability curve in the $k_x - \beta$ plane. In solid black lines is shown the marginal stability curve of the morphodynamical model; in solid gray lines is shown the marginal stability curve of Colombini et al. [1987].

I have identified two important limitations of the morphodynamical model: the inability to reproduce an accurate marginal stability curve of the bar bedform in the $k_x - \beta$ plane (like the one shown in Figure 5.7.1 in appendix A.1) and the inability to predict the development of dunes in the two-dimensional formulation. Let me expand on both issues:

- *Marginal stability curve:* in the first works on the development of bars, the authors obtained an U-shape marginal stability curve in the plane $k_x - \beta$ [Blondeaux and Seminara, 1985, Colombini et al., 1987]. The curve is depicted in grey in Figure 5.13. The model is able to predict an unstable region in the $k_x - \beta$ plane, however the shape is very different.

  For one thing, the unstable region is a prolonged horizontal stripe that overlaps in part with the U-shaped curve. Nonetheless, both curves actually contain most of the alternate bar experimental dataset.

  At the moment, I have not found a clear explanation as to this failure. It is a particularly important point

to correct, because β has been identified as the key controlling parameter of the onset of bars development (and therefore braiding). The encouraging part is that in spite of this failure (the shape of marginal stability curve), the morphodynamical model is able to grasp the lower bound of $\beta \sim 3$ at which diagonal bars occur.

– *Dune development:* in Figure 5.14, the dune instability region is not recovered. More precisely, it is found for Fr corresponding Shields numbers below θ_{cr}. From the definition of bedload transport, for these values of Fr there should be no sediment transport, hence no bedfrom development.

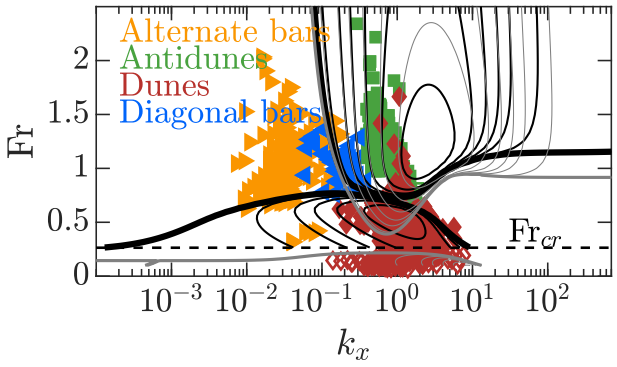

Figure 5.14: Marginal stability curve in the $k_x - \beta$ plane. In solid black lines is shown the marginal stability curve of the morphodynamical model; in solid gray lines is shown the marginal stability curve of Colombini et al. [1987].

5.9 Take home message

To conclude this chapter, I outline the following points:

– the morphodynamical model is able to capture the development of bars. Moreover, I showed that it is also able to predict the development of dunes and antidunes;

– I identified one of the key controlling parameter that governs the transition from two to three-dimensional bedforms, namely the relative grain diameter δ. This observation was successfully confronted with experimental results from the literature;

– I investigated qualitatively the influence of diffusion on the development of bed form. I showed that it affects the shape of the marginal stability curves of both bar and dunes instability.

6 Conclusion and perspectives

The main goal of this thesis was to study braided rivers from two different angles: from the angle of the braided network as a whole and from the angle of morphodynamics. Each part will be recapitulated separately.

Braided network dynamics

The evolution of braided networks was investigated using a laboratory-scale experiment. A flume was designed in which two experimental runs were conducted; the first run focusing on the development of braiding from a straight channel and the second focusing on the braided system at equilibrium. The Low Path method was used to extract the temporal evolution of the braided network from the topographic data Kleinhans et al. [2017]. A set of variables characterising the network was established (N_n, N_ℓ, L_ℓ/L), and they were found to depend on the flow conditions. With constant flow conditions, the network variables remained fairly constant, even in run one where the system evolved from a straight channel towards a fully braided river. Similar results were found in the literature [Bertoldi et al., 2009b], confirming the validity of our approach.

I subsequently developed our analysis based on identifying modes of the braided network from the network dataset [Hoffimann et al., 2019], a procedure called *modal analysis*. Surprisingly the braided network was found to evolve by constantly switching between modes. This result contrasted with the network variables, which remained constant in both runs. Finally, I used a Markov process to retrieve the probability of occurrence of the different modes.

The novelty of the approach followed in this thesis lies in the use of the Low Path method, firstly to obtain high-precision quantification of the braided system and subsequently to simulate the braided dynamics by applying the Low Path method within a stochastic framework. Both approaches addressed two specific current issues in the field, namely an appropriately rigorous definition and quantification of the braided network and a long-term predictions, in a statistical sense, of the network's evolution. To the best of my knowledge, this was one of the first investigation to tackle these issues jointly.

Morphodynamics

I developed a morphodynamic model based on coupling the shallow-water equations with Ancey et al. [2008]'s bedload transport model. The model's particularity lies in the introduction of a diffusive term into the bedload transport equation, which renders the model more complex than traditional ones Meyer-Peter and Müller [1948]. By applying linear stability theory to the model, the problem was solved numerically and I obtained marginal stability curves which predicted in which region of the parameter space bedforms would occur. Comparing these results with experimental data from the literature, these bedforms were identified as bars, dunes and antidunes.

The model is thus able to predict, within the same framework, the development of dunes and antidunes (two-dimensional bedforms) and bars (three-dimensional bedforms). To date, attempts to this using shallow-water equations had failed, and I believe the reason lies within the bedload equation. Using the microstructural bedload equation, which introduces diffusion into the process, made it possible to overcome the limitations of the shallow-water equation. Indeed, it was shown, albeit qualitatively, that diffusion had an impact on the marginal stability curves.

The morphodynamic model's novelty lies in the introduction of the diffusive term. It breaks the one-to-one relationship between flow conditions and bedload transport and seems to counterbalance the inherent limitations of the shallow-water equations. Coupling the microstructural bedload equation with the shallow-water equation is not new and, indeed has proven to work for the prediction of dunes and antidunes in a two-dimensional model [Bohorquez et al., 2019]. However, to the best of my knowledge, this is the first successful attempt to describe the development of three-dimensional bedforms (bars) within a three-dimensional model while at the same time describing the development of two-dimensional bedforms (dunes and antidunes).

In summary, this work emphasises the importance the bedload equation in morphodynamic models. Indeed, coupling the microstructural bedload model with the shallow-water equation allowed us to predict the development of both dunes and bars. Moreover, this also highlighted diffusion's effects on the overall process.

Perspectives

Three main perspectives were identified from my analysis of braided systems:

- *unsteady flow conditions:* Future investigations should address questions about the effects of unsteady flow conditions (water discharge, sediment supply, varying slope, etc.) on braided river networks;
- *generalisation of braided network's variables:* Our experimental runs were conducted for a single combination of water discharge, mean flume slope and median grain size. I suspect that general (*i.e.* dimensionless) empirical laws linking the network-related variables and physical variables (discharge, slope, etc.) may be found. This scaling might be useful to describe the relationship between network dynamics and flow conditions;
- *stochastic simulations:* There is a need for a complete stochastic framework simulating the evolution of braided rivers.

Two main perspectives were identified from the morphodynamic angle:

- *particle diffusion:* Even though the subject was only touched upon qualitatively, I strongly suspect that particle diffusion plays a key role in bedform development. Further studies, be they numerical or analytical, are needed to address this question;
- *numerical model:* A full numerical solution to the morphodynamical model is needed to comprehensively assess the model's validity via a comparison with benchmark tests, analytical and numerical solutions.

A Experimental setup and experimental methods

A.1 Experiments

A.1.1 Bedload influx

Once the water discharge is set (see section 2.2), there remains the issue to determine the appropriate sediment flux at the inlet so that it does not induce the system to erode (by under feeding) or to aggrade (by over feeding). To find the sediment transport rate that correspond to a given flow is an open problem in the literature, and the goal is not to tackle it in this preliminary study. Taking a more pragmatic approach, the sediment flux was estimated by means of the Recking formula Recking et al. [2009]. The author compiled an immense dataset of bedload measurement that also take into account the bedforms present; comparing several bedload transport formulae, he developed a formula that takes into account several parameters of the flow, the sediment properties etc. This formula was used to determine the sediment flux that correspond to the initial flow conditions. A graph with results of Recking's formula is shown in Figure A.1 below. In our case, for a water discharge of $Q = 2$ l/s, sediment of density $\varrho_s = 2650$ kg/m^3 and porosity $\zeta_b = 0.4$, we obtain a sediment flux of $q_{s,in} \approx 5$ g/s.

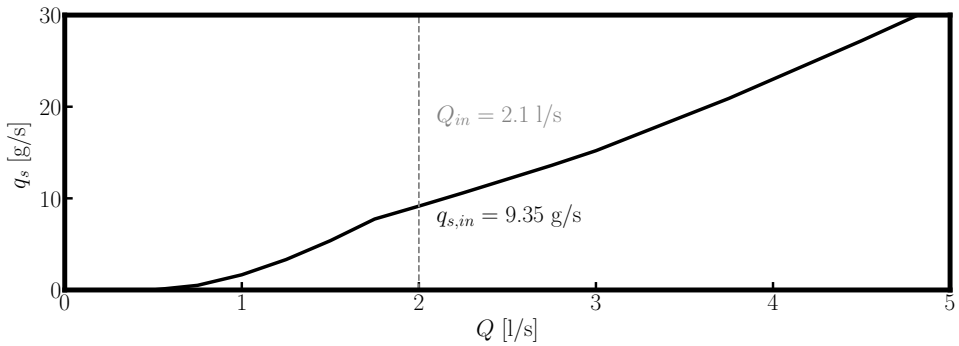

Figure A.1: Bedload Recking

The sediment flux $q_{s,in}$ will be used only for the first hours of the experiment (five hours). After this period, the

inlet sediment flux is equated with the outgoing flux averaged over the last hour. Mathematically it reads

$$\bar{q}_{in}(t + dt) = \bar{q}_{out}(t) \tag{A.1}$$

where $dt = 60$ min. The idea is to maintain a mass balance in the flume with periodic boundary conditions, periodic in the sense that what goes in equals to what goes out (with a delay of dt). To measure the outgoing sediment flux, sand is collected at the flume outlet in a basket and then weighted every dt. This procedure, in a sense, ensures that there is a mass balance of sediment and that, overall, the river bed is neither aggrading nor eroding.

A.1.2 Bed monitoring

The proper monitoring of the evolution of the river bed requires to scan it at regular time intervals Δt (not to be confused a priori with dt, the time interval used to averaged the sediment flux). This scanning provides a time-evolution of the river bed. However a question arises: what is the optimal time-scale to properly scan the bed topography? Some criteria have to be met to determine Δt: it has to be small enough to capture variations of the bed topography, so $\Delta t < \Delta t_{max}$; it does not have to be too small since morphological changes do not act with great speed. Continuous monitoring is therefore useless [Vesipa et al., 2017], meaning that there is a lower bound $\Delta t > \Delta t_{min}$. Both lower and upper bound for Δt have to be found.

The lower bound Δt_{min} does not impose any strong constraint on Δt. As mentioned earlier, fast monitoring of the river bed is not needed since the time-scale of morphological changes are quite high (of the order of 10–100 min). The real constraint on Δt comes from the upper bound Δt_{max}.

To properly study the evolution of the morphology, the data frequency of acquisition must be higher than the 'rate of change' of the morphology. In other words, if a bed perturbation migrates at a given velocity the bed monitoring must contain this migration. This migration speed must be estimated, or equivalently the characteristic time-scale of any morphological change, noted T_M. Exner equation (A.2) is used to estimate this time-scale. Bear in mind that the Exner equation corresponds to the mass conservation of the granular material bed, hence any changes in the morphology are controlled by it. In other words, it allows to estimates the time-scales of bed morphological evolutions. Here it is considered in its simplest form, that is the one-dimensional form:

$$(1 - \phi)\,\frac{\partial \eta}{\partial t} = -\frac{\partial q_s}{\partial x}. \tag{A.2}$$

with η the bed elevation and q_s the sediment flux in m^2/s. Choosing a proper scaling, it is possible to write equation (A.2) in dimensionless form. The following scaling is used

$$t = t^* T_M,\ x = x^* B,\ \eta = \eta^* E,\ q_s = Q_s/(\varrho_s B) \tag{A.3}$$

where T_M is the morphological time-scale, E is the flow depth (we suppose that the bedforms scale with the flow depth), B is the channel width, Q_s is the mass sediment discharge and ϱ_s is the sediment density. Manipulating equation (A.2), the characteristic time-scale of the Exner equation is expressed as

$$T = \frac{\varrho_s E B^2}{Q_s}. \tag{A.4}$$

Knowing $E,\ B,\ \varrho_s$ and Q_s (10^2 m, 2 m, 2650 kg/m^{3}and $5 \cdot 10^{-3}$ kg/s respectively), we obtain $T = 31\,800$ s or $T = 530$ min.

Since a braided system is being studied, a proper choice of characteristic lengths must be made, like the characteristic length of bars. Bars are the single most important morphological features of braided rivers. However, it is difficult to determine a priori their dimension. To bypass this difficulty, bar theory will be used to determine the dimension of the alternate bars that will develop in the initial straight channel [Blondeaux and Seminara, 1985, Colombini et al., 1987, Tubino et al., 1999]. Indeed, for a braided channel to emerge from the straight channel, bars have to develop first. Bar theory can predict the main characteristics of these bedforms, *i.e.* their wavelengths and migrating speed. The main result of the theory, the marginal stability curve of the system, is shown in Figure A.2. A small caveat has to be made. The bedforms that develop first are alternate bars, not exactly the same bars that will develop in the braided river. However, it is legitimate to suppose that braid bars will scale with the initial alternate bars. Moreover, it is the only quantitative information that we can use a priori to estimate Δt.

β and λ are dimensionless variables that represent the width-to-depth ratio and the alternate bar wavelength respectively. They are the main variables to characterize the flow and the bedform respectively. The hydraulic conditions (the green dashed line) of teh experimental setup can generate alternate bars within a range of $\lambda = 0.16$ to $\lambda = 0.78$, as seen on the marginal stability curve (Figure A.2). The wavelength of the most unstable mode (the lowest point of the dark line) is $\lambda = 0.4$. It is called the most unstable mode because it is the one that will develop for the lowest β value meaning that it is the first bedform to growth. Ultimately, it is the wavelength that dominates and is the only one that will be observed (see Figures A.3 and A.4). From λ, the dimensional wavelength L of the alternate bars is obtained:

$$\lambda = \frac{\pi 2B}{L} \Leftrightarrow L = \frac{\pi 2B}{\lambda} = 1.57\,\text{m}. \tag{A.5}$$

Using L instead of B as the length scale, the new characteristic time-scale of the Exner equation is computed. It yields $T_M = 298$ min. Physically, it means that $T_M = 300$ min represents the time that a perturbation will take to travel the length of bar, or in other words, the time-scale that it take for a bar to change. The topographic data have to be acquired at a period $\Delta t < T_M$ if its evolution is to be captured. The acquisition period was chosen $\Delta t = 60$ min, which is one fifth of the characteristic morphological time and the bedload averaging time as well. $\Delta t = 60$ min is thus considered short enough to capture the main morphological changes and large enough to avoid stopping the experiment too often since the data acquisition requires the experiment to be shut down. Moreover, it corresponds to the sampling time of $q_{s,in}$.

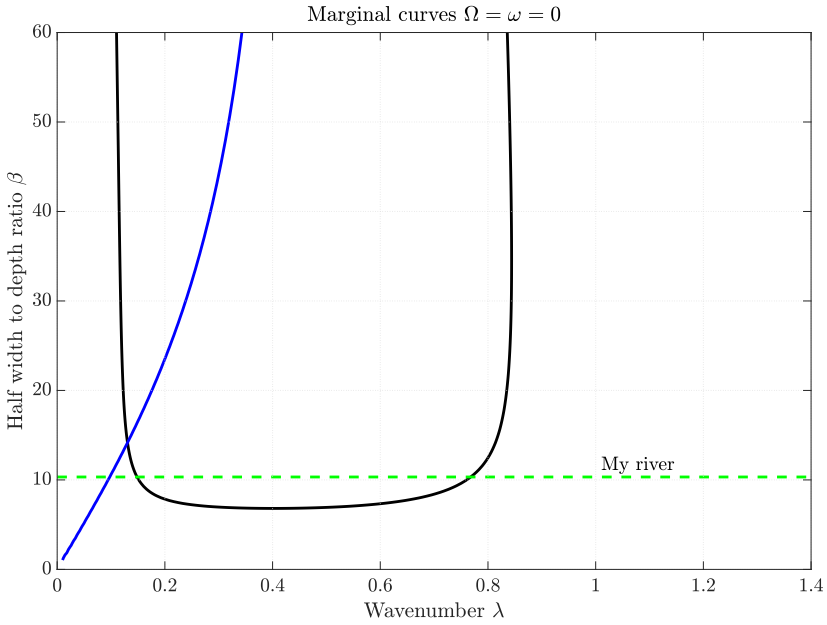

Figure A.2: Marginal stability curve of the initially straight channel for mode 1 (alternate bars). The dark line represents the neutral curve where instabilities do not grow nor decay. Below this curve, instabilities decays (the system is stable and bedforms do not develop) and above instabilities grows (the system is unstable and alternate bars do develop). The blue line represents the stationary mode (the bedforms that do not migrate). On the right of the curve, bedforms propagate downstream and on the left bedforms propagate upstream. The green dashed line represents the hydraulic conditions of the experimental.

As mentioned above, the bar theory allows to predict the formation of the most unstable bar. This is correct at the linear level when the perturbation are not significantly big but as they develop non-linear effects have to be taken into account and even their shape changes from purely sinusoidal perturbation to asymmetric bedforms. These non linear effects are one of the hypothesis that may explain the development of the braided pattern. Be that the case or not, the bar theory is the only analytical tool available to estimate Δt.

Figure A.3 shows the system at the beginning ($t = 0$ min) of the experiment and after alternates bars have developed at approximately $t = 30$ min (Figure A.3). The evolution from a straight initial channel to a straight channel with alternate bars is readily observed. The wavelength of the alternate bars is $L = 1.52$ m, which correspond to an error of 3 % with respect to the theory. Moreover, the alternate bar pattern is already being perturbed (right side of Figure A.4), a perturbation that will ultimately lead to the fully developed braided pattern.

Figure A.3: Intial development of alternate bars, $t = 0$ min

Figure A.4: Intial development of alternate bars, $t = 30$ min

A.2 Markov process' algorithm

A.2.1 Algorithm structure

The Markov chain was programmed in Python. The algorithm simulates the temporal evolution of modes of a braided river. This evolution is obtained from the modes' transition probabilities. The main steps are summarised in the following steps:

1. the simulation starts from the initial state, *i.e.* mode 0;
2. the next mode is computed via the transition probability matrix. Once obtained, it is stored in an array containing the previous mode (mode 0).
3. while the number of iterations i is below a given number N, mode $i + 1$ is computed and appended to the array containing the previous modes;
4. when $i = N$, the last mode is computed and stored. The algorithm stops and returns the array containing the simulated modes.

The algorithm's inputs are:

- the total number of modes n;
- the transition probability matrix of size $n \times n$ where each element p_{ij} correspond to the probability of witching from mode i to j;
- the total number of iterations N.

The algorithm's output is:

- the array of length N containing the simulated modes.

A schematic representation of the algorithm is shown in Figure A.5 below.

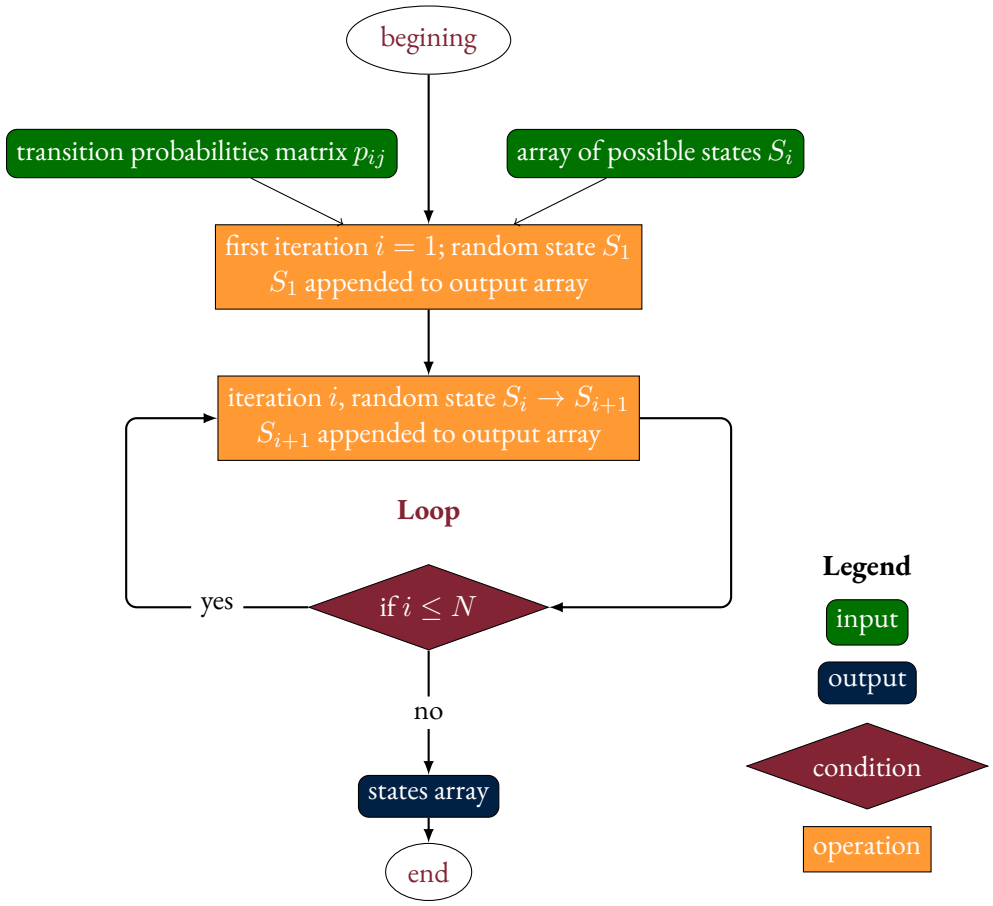

Figure A.5: Markov process' algorithm

A.2.2 Algorithm implementation

The Python code of the Marvov process is shown hereafter:

```
import os
import numpy as np

class MarkovChain(object):
def __init__(self, transition_matrix, states):
"""
Initialize the MarkovChain instance.

Parameters
----------
transition_matrix: 2-D array
A 2-D array representing the probabilities of change of
state in the Markov Chain.

states: 1-D array
An array representing the states of the Markov Chain. It
needs to be in the same order as transition_matrix.
"""
self.transition_matrix = np.atleast_2d(transition_matrix)
```

```
20 self.states = states
21 self.index_dict = {self.states[index]: index for index in
22 range(len(self.states))}
23 self.state_dict = {index: self.states[index] for index in
24 range(len(self.states))}
25
26 def next_state(self, current_state):
27 """
28 Returns the state of the random variable at the next time
29 instance.
30
31 Parameters
32 ----------
33 current_state: str
34 The current state of the system.
35 """
36 return np.random.choice(
37 self.states,
38 p=self.transition_matrix[self.index_dict[current_state], :]
39 )
40
41 def generate_states(self, current_state, no=10):
42 """
43 Generates the next states of the system.
44
45 Parameters
46 ----------
47 current_state: str
48 The state of the current random variable.
49
50 no: int
51 The number of future states to generate.
52 """
53 future_states = []
54 for i in range(no):
55 next_state = self.next_state(current_state)
56 future_states.append(next_state)
57 current_state = next_state
58 return future_states
```

A.3 Modified Hausdorff distance

The Hausdorff distance is a measure of the distance between two subsets of a metric space (V, d) (where d is the Euclidean distance). Let X and Y be two non-empty subsets of V, the Hausdorff distance is defined as

$$\delta_H(X, Y) = \max\left(\sup_{x \in X} \inf_{y \in Y} d(x, y), \sup_{y \in Y} \inf_{x \in X} d(x, y)\right), \tag{A.6}$$

whereinf and sup are the infimum and the supremum respectively. An example of both is shown in Figure A.6. By definition, the Hausdorff distance quantifies the closeness of the sets X and Y. By close is meant that every point of each set is located near some point of the other set. The first step is to determine the set of distances that contains the minimum distances of each points in a set with respect to the other set, that is $\inf_{y \in Y} d(x, y)$ for all x

in X. The Hausdorff distance is the maximum of this set, namely $\sup_{x \in X} \inf_{y \in Y} d(x, y)$. For instance, lets take the subset X in Figure A.6, the dotted line in the upper part of the Figure represents the minimum distance from the point x to the set Y (as shown by the circle arc that only intersects Y once). It is also the greater among all the distances from any point x belonging to X to the set Y. The same is true if the distance from the set Y to the set X is taken, as shown on the lower part of Figure A.6.

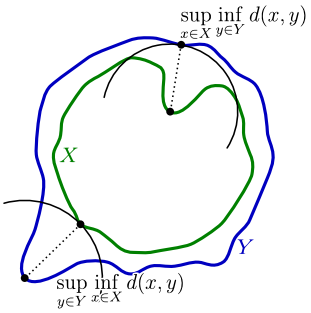

Figure A.6: Example of Hausdorff distance between a set X and a set Y. All the elements of the computation of δ_H, such as supremum and infimum are shown. This Figure comes from Wikipedia

In computer vision, the Hausdorff distance is often used in object matching algorithms. However, it is not the direct implementation of δ_H that is used but a modified version based on its definition. In the seminal work Dubuisson and Jain [1994], the authors compare the efficiency of 6×4 modifications of δ_H to quantify the differences between black and white images. They arrived to the conclusion that one of the modifications, the so-called modified Hausdorff distance, was the most efficient. Its definition is based on the distance of a point a to a set B noted $d(a, B)$, the distance between two sets A and B noted $d(A, B)$ and finally the modified Hausdorff distance noted δ_{mhd}. There are defined, respectively, as

$$d(a, B) = \min_{b \in B} \|a - b\|, \tag{A.7}$$

$$d(A, B) = \frac{1}{N_a} \sum_{a \in A}^{N_a} d(a, B), \tag{A.8}$$

$$\delta_{mhd} = \max(d(A, B), d(B, A)). \tag{A.9}$$

To define a proper distance measure between images, black and white images are used. Every black pixel of an image is then considered to be a point a of the set A. The coordinates (x_a, y_a) of a are in the space of pixels of the images, but are easily associated with an Euclidean space. Moreover, provided that the dimensions in meters of the pixel is known, it is even possible to express (x_a, y_a) in a metric space with distances measured in meters. With subsets A and B of the two images to be compared, the distance δ_{mhd} between them is properly defined.

To assess the robustness of δ_{mhd}, several numerical experiments were performed on synthetic images. Binary

images of dimension 32×32 or $n_x \times n_x$, were obtained by generating a random number of black points placed randomly,from a uniform distribution, on a grid. The images were then perturbed by three types of noise:

1. randomly adding a number N of black pixel placed randomly from a uniform distribution, let it be called noise 1;
2. randomly adding a number n of horizontal lines of length $l \leq 32$ placed randomly from a uniform distribution, let it be called noise 2;
3. randomly adding a number n of vertical lines of length $l \leq 32$ placed randomly from a uniform distribution, let it be called noise 3.

One last numerical experiment was performed increasing the image size and adding noise 1 to assess the variability of δ_{mhd} in function of the image size, *i.e.* the size of the sets A and B. This last noise is called noise 4. δ_{mhd} between the original image A and the noisy image A' was computed and normalized it by means of the maximum possible distance, which is the length of the diagonal of a square of dimension 32×32, hence $d_{max}(A, A') = 32\sqrt{2}$. This length, called auto-distance and noted $d(A, A')/d_{max}(A, A')$, measures the sensitivity of δ_{mhd} to noise. The higher $d(A, A')/d_{max}(A, A')$, the less precise δ_{mhd} to measure the similarity. The results are shown in Figure A.7.

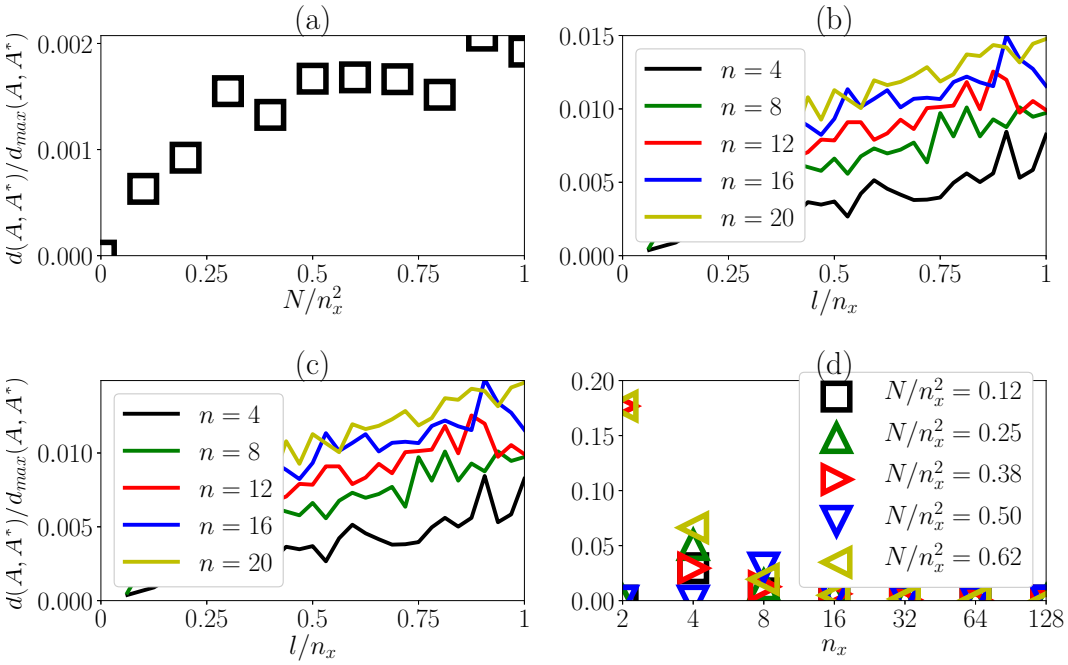

Figure A.7: Analysis of the sensitivity of δ_{mhd} to noise. Plot (a) refers to noise 1; plot (b) refers to noise 2; plot (c) refers to noise 3; plot (d) refers to noise 4.

On the graph (a) of Figure A.7, $d(A, A')/d_{max}(A, A')$ grows continuously from 0 (no noise) until reaching some sort of plateau close to $d(A, A')/d_{max}(A, A') = 0.0018$ for $N/n_x^2 \approx 0.5$. It finally reaches its maximum

of $d(A, A')/d_{max}(A, A') = 0.002$ for $N/n_x^2 = 1$ (total noise). Lets recall that N/n_x^2 is the ratio of added noise N over the total number of pixels of the image n_x^2. By definition, $N/n_x^2 \in [0, 1]$. The trend of Figure A.7 (a) suggests that δ_{mhd} is affected by a random noise up to a certain point where the measure seems to saturate and do not worsen significantly. The maximum measured error is of the order of 10^{-3}, a very low value. Therefore, δ_{mhd} is fairly insensitive to randomly added noise, especially if the noise ratio is significantly high.

On the graph (b) of Figure A.7, $d(A, A')/d_{max}(A, A')$ grows monotonously with noise 2, *i.e.* the length l of the added horizontal line. Adding more lines have the effect of adding more noise, thus increasing $d(A, A')/d_{max}(A, A')$. This increase is not linear, meaning that adding five times more lines did not increase $d(A, A')/d_{max}(A, A')$ by a factor five. No plateau seems to be observed with noise 2. The maximum measured error is of the order of 10^{-2}, a low value but an order of magnitude greater than the maximum value to pure random noise (noise 1). In conclusion, δ_{mhd} is sensitive to randomly added features, in this case horizontal lines. The distance error increase with the size of the added feature. The more feature the greater the error, but this increase is not linearly proportional.

Graph (c) of Figure A.7 have the exact same features of graph (b). It was expected. Indeed, noise 3 corresponds to adding randomly vertical lines to the image. By symmetry of the square (images are square-sized), adding a horizontal or a vertical lines is the same. Therefore, when computing distances between the noisy image and the original one, noise 3 have the exact same effect than noise 2.

On the graph (d) of Figure A.7 , $d(A, A')/d_{max}(A, A')$ decrease with increasing image size n_x. It means that the higher the image, in other words, the bigger the sets, the lower the error in δ_{mhd}. This means that for large set with a large number of elements, corresponding to large images with complex features, δ_{mhd} works best than in smaller sets with less elements. This result ensure the robustness and efficiency of δ_{mhd} for the identification of complex patterns such as a braided pattern.

As a final concluding remark, δ_{mhd} was shown to be a robust distance measure between two images. Since it is not sensitive to random perturbations, it means that it is very powerful and robust measure of very similar sets. Here it is used to measure the similarity between images (in which case δ_{mhd} is low) and to discriminate very dissimilar images (in which case δ_{mhd} is high). Lets recall that in the context of this thesis, δ_{mhd} will be used to identify 'modes' of the braided system. By mode are intend states of the system that are similar between them, similar in the sense of a low δ_{mhd}.

A.4 Frechet distance

The Fréchet distance measures the similarity between two curves in a metric space. By curve is intend a continuous mapping $f : [a, b] \to V$ where $a, b \in \mathbb{R}$, $a \leq b$ and (V, d) is a metric space with its measure d (the Euclidean distance). Given two curves $f : [a, b] \to V$ and $g : [a', b'] \to V$, their Fréchet distance is defined as

$$\delta_{Fr}(f, g) = \inf_{\alpha,\beta} \max_{t\in[0,1]} d\left(f(\alpha(t)), g(\beta(t))\right), \tag{A.10}$$

where α (respectively β) is an arbitrary continuous non-decreasing function defined from $[0, 1]$ to $[a, b]$ (respectively $[a', b']$).

The Fréchet distance is defined for continuous curves, but it is convenient to use it on discrete curves, typically the ones obtained from experimental data. It is possible to defined δ_{Fr} on discrete curves, called polygonal curves. The proper demonstration of the existence and validity of the discrete δ_{Fr} is presented in Eiter and Mannila [1994]. Here the main result is presented, namely the structure of the algorithm to compute δ_{Fr}.

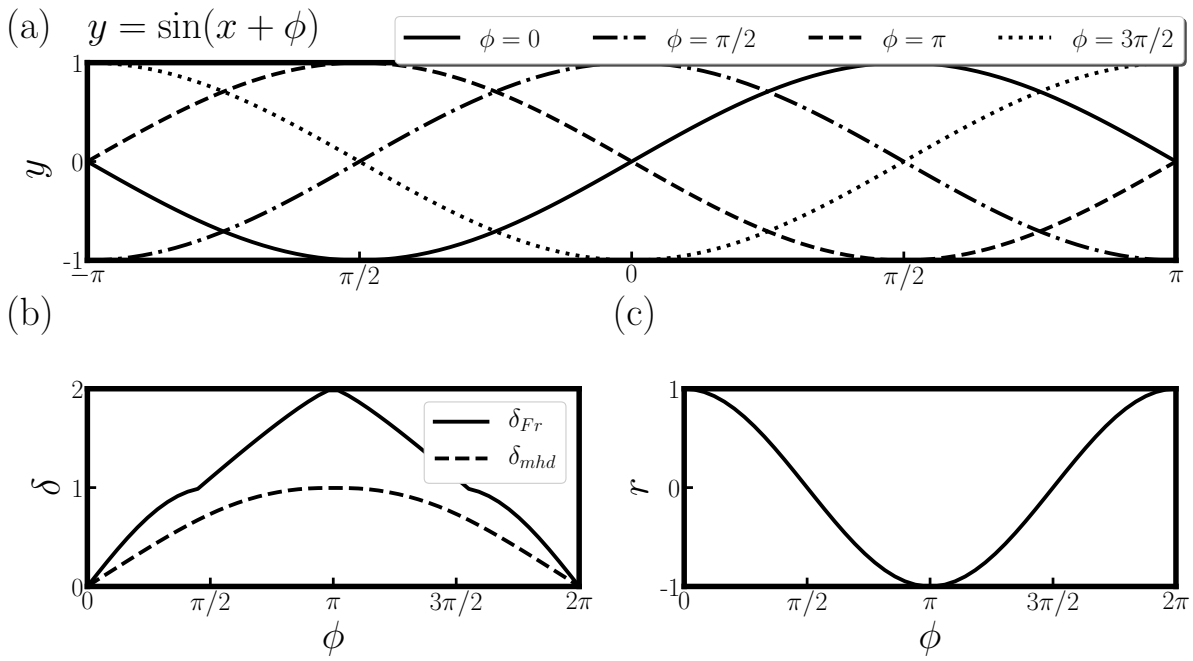

Figure A.8: δ_{Fr} and δ_{mhd} distances of two sinusoidal functions with a phase shift. Plot (a) shows four drawings of the sinusoidal function $y = \sin(x + \phi)$ with a phase shift of $\phi = 0, \pi/2, \pi, 3\pi/2$. Plot (b) shows the Fréchet distance δ_{Fr} and the Hausdorff distance δ_{mhd} in function of the phase shift ϕ. Plot (c) shows the Pearson's correlation coefficient r in function of the phase shift ϕ.

Figure A.8 shows a didactic example of the utilization of δ_{Fr}. The Fréchet distance and the Hausdorff distance of two sinusoidal functions (plot (b)) are computed in function of the phase shift ϕ between these two curves. The first observation is that δ_{Fr} and δ_{mhd} follow the same trend, they are minimum for $\phi = 0 \pmod{2\pi}$ (when the sinusoidal curves coincide) and they are maximum for $\phi = \pi$. The difference between both measures lies in their value, Fréchet's measure reaches 2 while Hasdorff reaches 1. This is due to the definition of δ_{Fr}. Indeed, recalling the definition from section 2.4.3, δ_{Fr} takes into account the direction taken by each curve. In the example of the two sinusoidal function, when the phase shift $\phi = \pi$ both curves are in phase opposition, meaning that on top of the difference of shape they are following opposite direction. Hence, their difference is 'doubled' in the Fréchet sense. δ_{Fr} thus captures an additional aspect than δ_{mhd} is not able to grasp. In a sense, they complement each other with δ_{mhd} quantifying the curves' shape similarity and δ_{Fr} quantifying the curves' trend similarity (in addition to their shape).

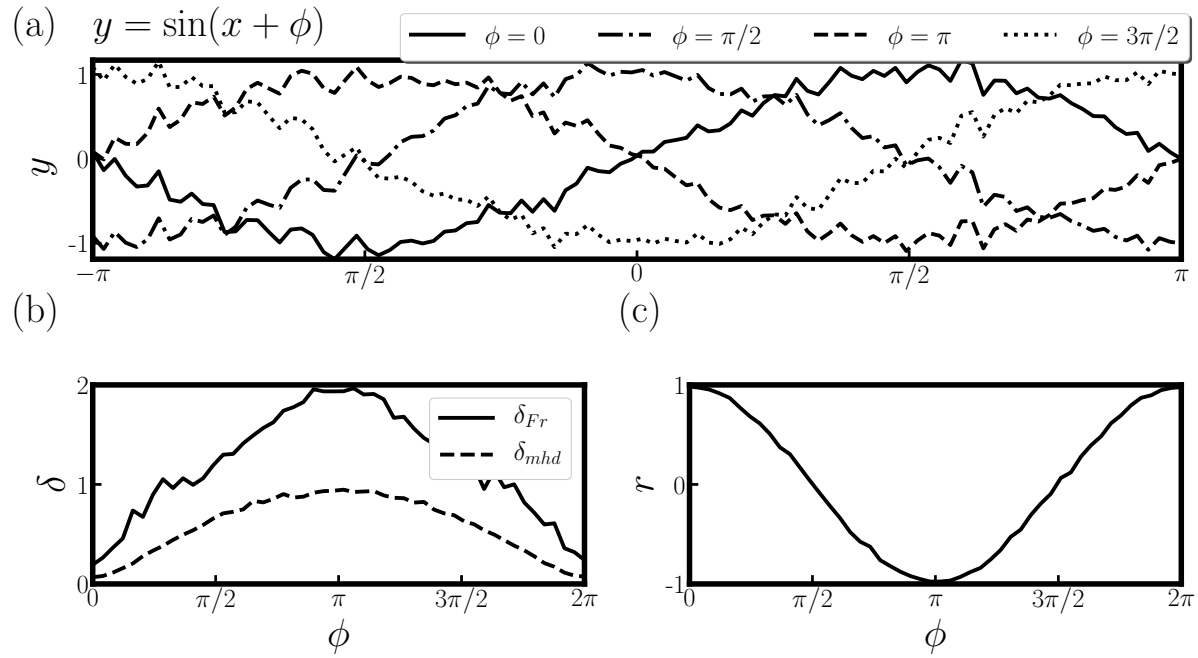

Figure A.9: δ_{Fr} and δ_{mhd} distances of two sinusoidal functions with a phase shift with added noise. Plot (a) shows four drawings of the sinusoidal function $y = \sin(x + \phi)$ with a phase shift of $\phi = 0, \pi/2, \pi, 3\pi/2$. Plot (b) shows the Fréchet distance δ_{Fr} and the Hausdorff distance δ_{mhd} in function of the phase shift ϕ. Plot (c) shows the Pearson's correlation coefficient r in function of the phase shift ϕ.

A.5 Bed morphological variables

A.5.1 Bed morphological variables

In a straight channel the concept of slope is easily conceivable, even in the presence of bedforms. It is possible to use the straightforward mathematical definition of slope, *i.e.* the variation of elevation with variation of space within a particular direction. Simply put, the longitudinal local slope is defined as $S = \mathrm{d}z/\mathrm{d}x$ (lateral slope is defined by differentiating in the transverse direction). The global slope is obtained by averaging over the whole bed elevation. In braided rivers, the notion of channel itself is problematical, since there are many of them. Defining a unique slope is already a problem. Moreover, there is always the debate whether to use the bed slope or the water surface slope (also called energy slope). Lacking information about the water level, the attention will be focused on the bed slope only. The average longitudinal slope will be used, simply called slope from now on. Mathematically, it reads (in discrete form)

$$s_x = \frac{1}{m * (n-1)} \sum_{i=1}^{m} \sum_{j=1}^{n-1} \frac{z(i, j+1) - z(i, j)}{dx} \tag{A.11}$$

where i and j are the coordinates in the lateral and longitudinal direction in the bed elevation matrix and dx is the

spatial discretization step in the longitudinal direction. As an average of all local slopes, s_x do not grasp any local effects that are actually an important part of a braided river. Recall that the bed elevation is detrended, meaning that it does not take into account the global inclination of the flume (1.5 %). For instance, when computing a negative slope, it has to be added to the 1.5 % inclination of the flume. s_x provides a good estimation of the overall state of a riverine system. It give an insight on the global erosional trend. Suppose that a system is undergoing intense erosion, it usually starts at the upstream and propagates downstream. This erosion will tend to lower the elevation of points located close to the upstream end, thus lowering the slope on average (recall that slope is simply $\mathrm{d}z/\mathrm{d}x$ and that erosion will tend to reduce $\mathrm{d}z$). The opposite is true for a system that is undergoing aggradation (deposition). Sediment will tend to accumulate at the upstream end thus increasing the overall slope. This principle, well know in the literature, is called the Lane balance principle, which states that when a river is undergoing erosion the global slope decreases and vice versa. In the analysis of results, the focus will be put on the trends of s_x rather than on its value per se.

To complete the analysis of the bed elevation, some basic statistics will be used: the average bed elevation z_m and its standard deviation σ_z. z_m is a good indicator of the overall regime of the bed. Indeed, an increasing z_m implies an aggrading bed on average while a decreasing z_m implies an eroding bed on average. σ_z gives an insight on how much the bed elevation varies in time. Garcia Lugo et al. [2015] have used the bed elevation empirical frequency distributions to distinguish between strongly confined channels (nearly straight channels) and fully braided channels. They demonstrated that confined channels show a low standard deviation while braided channels show higher variability. They were also interested on the skewness and kurtosis of the distribution, which is not of interest in this present work. The attention will be focused on variations of σ_z only as an indicator on the trends of braiding, with increasing σ_z indicating increasing braiding and vice-versa.

A.5.2 Bed Relief Index

The Bed Relief Index was initially developed by Hoey and Sutherland [1991] to study rivers undergoing different regimes, aggrading and/or eroding, and to specifically study the variability of a given cross-section. In their original study, they mentioned that it was in essence a measure of the standard deviation of each cross-section about the average bed elevation. It is defined as

$$B = \frac{1}{W} \sum_{j=1}^{m-1} \sqrt{\frac{(z(j) - \bar{z})^2 + (z(j+1) - \bar{z})^2}{2}} dy \tag{A.12}$$

where $z(j+1)$ and $z(j)$ are the elevation at a given position along the longitudinal direction, dy is the spatial discretization step in the transverse direction, m is the number of elements in the transverse direction and W is the river width. B is originally a dimensional variable, but for sake of generality it is rendered dimensionless with the river width, $B = B/W$. As mentioned, it was originally conceived to study a given cross-section. In the present case, it is used to compare two runs as a whole. Therefore, the averaged B is computed for all the cross sections of the topography.

To complete our study of the bed topography, B is slightly modified and extended to any cross-section in

the longitudinal direction (recall that it was originally defined for a cross-section in the transverse direction). Mathematically it reads

$$B_l = \frac{1}{L}\sum_{i=1}^{n-1}\sqrt{\frac{(z(i)-\bar{z})^2+(z(i+1)-\bar{z})^2}{2}}dx \tag{A.13}$$

where $z(i+1)$ and $z(i)$ are the elevation at a given position along the transverse direction, dy is the spatial discretization step in the longitudinal direction, n is the number of elements in the transverse direction and L is the river length. This definition of B_l give information on the variability of the elevation in the longitudinal direction around the the average elevation. In other words, it is a measure of the flatness of the bed in the longitudinal direction.

A.5.3 Morphologically Active Length

In a braided river not all channels are active, in the sense that they do not all convey sediment. Moreover, without information on the water level it is impossible to determine if a channel is abandoned (dry) from bed elevation only. To overcome this limitation, the concept of Morphologically Active Length is introduced. Since it is highly improbable that erosion exactly balance deposition in a channel that transport sediments, it is supposed that a channel is morphologically active if it undergoes erosional activity, be it erosion or deposition. By doing a simple difference between two consecutive bed elevations, it is possible to identify regions of erosional activity (when the difference is higher than a certain threshold). Mathematically it reads

$$\mathrm{diff}(z) = \begin{cases} |z(t+\Delta t)-z(t)| & \text{if} \quad |z(t+\Delta t)-z(t)| \geq \delta, \\ 0 \quad \text{if} \quad |z(t+\Delta t)-z(t)| < 0. \end{cases} \tag{A.14}$$

To compute L_{ma}, the process is the following: for every cross-section of $\mathrm{diff}(z)$, the total non-zero length $l_{nz,i}$ is measured (where the subscript $_i$ correspond to the cross-section i) and normalized with the cross-section length. The proportion of the cross-section which is morphologically active is then computed. L_{ma}, for a given bed elevation, gives the average over the whole topography. Mathematically it reads

$$L_{ma} = \frac{1}{n}\sum_{i=1}^{n}\frac{l_{nz,i}}{W} \tag{A.15}$$

where n is the number of cross-sections in the longitudinal direction and W is the width of the cross-sections (also the width of the bed elevation). L_{ma} is thus the average proportion of all the cross-sections that are morphologically actives, with 1 corresponding to activity everywhere along the cross-sections (fully active channel) and 0 to no activity. There is no correlation between L_{ma} and either erosion or aggradation, *i.e.* L_{ma} can be increasing for an eroding or aggrading system (and vice-versa).

A.5.4 Bed convexity

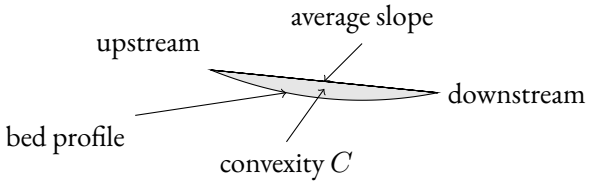

Figure A.10: Example of convex function adapted to a pseudo-parabolic river bed profile.

In mathematics, a function is convex if the line segment between any two points on the graph of the function lies above or on the graph. An example of a convex function is shown in Figure A.10. Making a parallel with a river bed profile, imagine the line defined by the elevation of both ends of the river (*i.e.* the average slope). If the bed profile lies everywhere below the average slope, then the river bed profile is convex. The interesting part does not lie in the convexity per se, but rather in its evolution. Imagine a river bed profile such as the one displayed in Figure A.10. If the river bed is generally eroding, then the elevation of the upstream point will decrease thus diminishing the overall convexity (the grey area). Conversely if the system is generally aggrading then the convexity will increase. Its evolution is an indicator of the general evolution of the river bed profile.

In the present case, the bed elevations are detrended, meaning that the bed slope cannot be used in the definition of C. z_m will be used instead. To compute C, the difference between the local elevation and z_m will be integrated over the entire length. Mathematically it reads

$$C = \int_{x_i}^{x_f} z - \bar{z} \, \mathrm{d}x \tag{A.16}$$

where x_i and x_f are the initial and final longitudinal position. It means that:

- when $C < 0$ the bed profile is below the average elevation, hence the profile is convex;
- when $C > 0$ the bed profile is above the average elevation, hence the profile is concave.

C is finally obtained by averaging over the whole bed elevation.

A.5.5 Area above average

The bed elevation data do not take into account the water level, meaning that there is no information on the morphological structures (their position, length, area etc.). However, one of their main characteristic is that they are mainly located above the water level. Assuming that water level elevation is on average close to z_m, then any point above z_m lies above water level. Any area above z_m, the so-called area above average A_a, is therefore supposed to be a good proxy of the morphological structure's area.

The attention will not be focused on the particular aspects of A_a, namely its length, shape, volume etc. The portion of the bed represented by A_a is going to be computed. In general, A_a tend to increase when a system is in general eroding. This is due to the fact that in this case a lot of erosion processes occur such as channel avulsion, pool deepening etc. All these phenomenon tend to leave a lot of area above the water level, hence a high value of A_a or an increasing A_a. The contrary is also true, when a system tend to aggrade A_a tends to decrease and to have low values.

A.5.6 Hydraulic power

The hydraulic power is a measure of the energy of a river system. It is defined as

$$\Omega = \varrho g Q S \tag{A.17}$$

where ϱ is the fluid density, g is the gravitational acceleration, Q is the water discharge and S is the bed slope. To compute it, the bed slope s_x will be used, meaning that Ω will have the same trends as s_x (all other variables being constants). In other words, for an eroding system Ω will decrease and vice-versa.

B Mathematical developments

B.1 Exner equation

Consider an infinitesimal volume of the solid phase $\mathrm{d}V$ of external surface $\mathrm{d}S$ and whose particle concentration is $c(\boldsymbol{x}, t)$. The particle concentration is expressed in number of particles per unit volume, meaning that every infinitesimal volume $\mathrm{d}V$ has an infinitesimal mass $\mathrm{d}m = c\mathrm{d}V$. It then follows that the total mass of a given material volume V is simply the sum of all particles contained in every infinitesimal volumes $\mathrm{d}V$, or to put it more correctly

$$m = \int_V c(\boldsymbol{x}, t)\, \mathrm{d}V. \tag{B.1}$$

In this section, the Exner equation will be derived from a mass balance of an infinitesimal portion of a river bed. By the mass conservation principle it follows that mass is constant over time, that is its temporal variation must be null. Consider an infinitesimal portion of a river bed of mass m. Applying the conservation of mass principle to m yields

$$\frac{\mathrm{d}m}{\mathrm{d}t} = \frac{\mathrm{d}}{\mathrm{d}t} \int_V c(\boldsymbol{x}, t)\, \mathrm{d}V = 0. \tag{B.2}$$

where V is the volume and c is the density of m. By virtue of the Reynolds transport theorem we obtain

$$\frac{\mathrm{d}}{\mathrm{d}t} \int_V c(\boldsymbol{x}, t)\, \mathrm{d}V = \int_V \frac{\partial c}{\partial t} + \boldsymbol{\nabla} \cdot (c\boldsymbol{v})\, \mathrm{d}V = 0 \tag{B.3}$$

where $\boldsymbol{\nabla} = (\partial/\partial x, \partial/\partial y)$ is the two-dimensional gradient operator and $\boldsymbol{v}$ is the velocity of the material surface surrounding m. Considering than this expression must hold true for any material volume V, it therefore writes as

$$\frac{\partial c}{\partial t} = -\nabla \cdot (c\boldsymbol{v}). \tag{B.4}$$

Some considerations have to be made. On a river bed, it is fair to assume that any changes in the mass of m act on the vertical direction since bed particles are either lifted upwards by the flow or deposited by gravity. In other words, the river bed erodes or aggrades, therefore the level of the river bed η can only evolve on the vertical direction. The term $\partial c/\partial t$ can be written, without any loss of generality as $\partial \eta/\partial t$, since any change in the mass m (or c equivalently) is ultimately captured by a change in the bed level η

On the right hand side term of equation B.4, $\boldsymbol{v}$ corresponds to the surface velocity of V, the volume of m. If m is considered at rest, then the velocity $\boldsymbol{v}$ corresponds to the velocity of the flux entering m through V. Therefore, $c\boldsymbol{v}$ may be assimilated in all generality to the mass flux entering V, which is by definition the bedload flux q_s.

Without any loss of generality, the mass balance of the river bed finally writes in the following form

$$(1 - \zeta_b)\frac{\partial \eta}{\partial t} = -\boldsymbol{\nabla} \cdot \boldsymbol{q_s} = D - E \tag{B.5}$$

with D and E the deposition and entrainment rates of particles from the bed respectively and ζ_b the bed porosity. This form (the first two terms of the equation) is commonly known as the Exner equation. The last term $D - E$ was added to highlight the fact that bedload transport can be viewed at the particle scale. At this scale, the gradient of q_s (the bedload flux) is nothing more than the difference between particles deposited on the bed (D) and particles entrained from the bed (E). Ultimately, the balance between deposited and entrained particles controls the temporal evolution of the bed level η, where η rises when more particles are deposited ($D > E$) and vice-versa.

B.2 Non dimensionalisation

The non-dimensionalizations of the morphodynamic equations is obtained with the scales presented in chapter 5. Lets recall these scales here:

$$(\hat{x}, \hat{y}) = \hat{B}(x, y), \tag{B.6}$$

$$\hat{t} = \frac{\hat{B}}{\hat{U}_0} t, \tag{B.7}$$

$$\hat{\boldsymbol{u}} = \hat{U}_0 \boldsymbol{u}, \tag{B.8}$$

$$(\hat{h}, \hat{\eta}) = \hat{H}_0 (h, \eta), \tag{B.9}$$

$$\hat{\gamma} = \hat{\gamma}_0 \gamma, \tag{B.10}$$

$$\hat{\gamma}_{ss} = \hat{\gamma}_0 \gamma_{ss}, \tag{B.11}$$

$$\hat{\boldsymbol{\tau}}_{\boldsymbol{b}} = \frac{\hat{\varrho} f}{8} \hat{U}_0^2 \boldsymbol{u} \left\| \boldsymbol{u} \right\|, \tag{B.12}$$

with the hat decoration standing for dimensional variables. As an example, lets present the non-dimensionalization of the mass conservation equation. It originally reads, in dimensional form:

$$\begin{aligned} &\frac{\partial \hat{h}}{\partial \hat{t}} + \boldsymbol{\nabla} \cdot (\hat{h} \bar{\hat{\boldsymbol{u}}}) = 0 \\ \Rightarrow &\frac{\partial \hat{h}}{\partial \hat{t}} + \frac{\partial \hat{h}\hat{u}}{\partial \hat{x}} + \frac{\partial \hat{h}\hat{v}}{\partial \hat{y}} = 0 \end{aligned} \tag{B.13}$$

Using the aforementioned scales, the equation writes

$$\begin{aligned} &\frac{\hat{H}_0 \hat{U}_0}{\hat{B}} \frac{\partial \hat{h}}{\partial \hat{t}} + \frac{\hat{H}_0 \hat{U}_0}{\hat{B}} \frac{\partial \hat{h}\hat{u}}{\partial \hat{x}} + \frac{\hat{H}_0 \hat{U}_0}{\hat{B}} \frac{\partial \hat{h}\hat{v}}{\partial \hat{y}} = 0 \\ \Rightarrow &\frac{\hat{H}_0 \hat{U}_0}{\hat{B}} \frac{\partial \hat{h}}{\partial \hat{t}} + \frac{\hat{H}_0 \hat{U}_0}{\hat{B}} \frac{\partial \hat{h}\hat{u}}{\partial \hat{x}} + \frac{\hat{H}_0 \hat{U}_0}{\hat{B}} \frac{\partial \hat{h}\hat{v}}{\partial \hat{y}} = 0 \\ &\Rightarrow \frac{\partial h}{\partial t} + \frac{\partial h}{\partial t} + \frac{\partial h}{\partial t} = 0. \end{aligned} \tag{B.14}$$

Using the same procedure, the set of equations of the morphological model are rendered dimensionless.

C Eigenvalue problem

C.1 Linearisations

The linearisation of the morphodynamic system is based on the perturbation of all the variables, namely u, v, h, η and γ and the Taylor expansion of the closure relations τ_b and γ_{ss}. The detailed linearisation of equation (5.43), *i.e.* the longitudinal momentum equation, and of the term γ_{ss} are presented here to show how the linearisation process works.

Recall the definition of equation (5.43)

$$\mathsf{Fr}^2\left[\beta\frac{\partial hu}{\partial t}+\frac{\partial hu^2}{\partial x}+\frac{\partial huv}{\partial y}-\frac{\nu}{\beta}\left(\frac{\partial}{\partial x}\left(h\frac{\partial u}{\partial x}\right)+\frac{\partial}{\partial y}\left(h\frac{\partial u}{\partial y}\right)\right)\right]+h\frac{\partial(h+\eta)}{\partial x}= \beta S_0 h-\frac{\beta f\mathsf{Fr}^2}{8}u\left|\boldsymbol{u}\right| \quad \text{(C.1)}$$

and the definitions of γ_{ss}

$$\gamma_{ss}=\frac{\gamma_{ss}}{\gamma_0}=\frac{\lambda_{ss}}{\kappa}\frac{\kappa}{\lambda_0}=\frac{\lambda_{ss}}{\lambda_0}=\begin{cases}\frac{\theta-\theta_{cr}}{\theta_0-\theta_{cr}} & \text{if} \quad \theta\geq\theta_{cr},\\ 0 \quad \text{if} \quad \theta<\theta_{cr}.\end{cases} \quad \text{(C.2)}$$

In both equations, the dependent variables are u, v, h and η. To linearise the equations, each of the variables are expanded in the following perturbed form

$$u = u_0 + \epsilon u_1 + \mathcal{O}(\epsilon^2), \tag{C.3}$$
$$v = v_0 + \epsilon v_1 + \mathcal{O}(\epsilon^2), \tag{C.4}$$
$$h = h_0 + \epsilon h_1 + \mathcal{O}(\epsilon^2), \tag{C.5}$$
$$\eta = \eta_0 + \epsilon \eta_1 + \mathcal{O}(\epsilon^2), \tag{C.6}$$
$$\gamma = \gamma_0 + \epsilon \gamma_1 + \mathcal{O}(\epsilon^2), \tag{C.7}$$

where x_0 is the variable (u, v, h, η or γ) evaluated at base state, x_1 is the first order perturbed variable and ϵ is a small order term. The linearisation simply consists in replacing every variables in equations (C.1) and (C.2) with their expansions, equations (C.3)–(C.7) and keeping the terms of order $\mathcal{O}(\epsilon^2)$. An example of such linearisation is shown for the second term in the left hand side of equation (C.1):

$$\frac{\partial hu^2}{\partial x} = \frac{\partial}{\partial x}\left((1+\epsilon h_1)(1+\epsilon u_1)(1+\epsilon u_1)\right) \tag{C.8}$$
$$= \frac{\partial}{\partial x}\left((1+\epsilon h_1)\left(1+2\epsilon u_1 + \mathcal{O}(\epsilon^2)\right)\right) \tag{C.9}$$
$$= \frac{\partial}{\partial x}\left(\left(1+2\epsilon u_1 + \epsilon h_1 + \mathcal{O}(\epsilon^2)\right)\right) \tag{C.10}$$
$$= \epsilon \frac{\partial (2u_1 + h_1)}{\partial x} + \mathcal{O}(\epsilon^2). \tag{C.11}$$

The procedure is repeated for every variable in equation (C.1).

The linearisation of closure relations follows the same principle. This time, however, a Taylor series expansion is used to express them in terms of the dependent variables of the problem. We will use the linearisation of γ_{ss} as a case in point.

From equation (C.2), we see that γ_{ss} depends on θ, θ_0 and θ_{cr}, with θ being the Shields stress, θ_0 the Shield stress evaluated at base state and θ_{cr} the critical Shield stress. Recall the definition of θ:

$$\theta = \frac{\mathsf{Fr}^2 f}{8(s-1)\delta}(u^2+v^2), \quad \frac{1}{\sqrt{f}} = -2\log\left(\frac{\delta}{3.71h}\right). \tag{C.12}$$

θ is thus a function of u, v and h while f is a function of h only (δ and Fr being constant dimensionless numbers). The Taylor expansion of γ_{ss} will then be expressed in function of these three variables, namely u, v and h. The first order Taylor expansion around the base state of γ_{ss}, noted γ'_{ss}, thus writes

$$\gamma'_{ss} = \gamma_{ss}|_0 + \epsilon u_1 \left.\frac{\partial \gamma_{ss}}{\partial \theta}\right|_0 \cdot \left.\frac{\partial \theta}{\partial u}\right|_0 + \epsilon v_1 \left.\frac{\partial \gamma_{ss}}{\partial \theta}\right|_0 \cdot \left.\frac{\partial \theta}{\partial v}\right|_0 + \epsilon h_1 \left.\frac{\partial \gamma_{ss}}{\partial \theta}\right|_0 \cdot \left.\frac{\partial \theta}{\partial h}\right|_0 \tag{C.13}$$

where by $|_0$ is intended $|_{u_0,v_0,h_0}$, *i.e.* evaluation of the function at base state. Recall that the base state variables are $u_0 = 1$, $v_0 = 0$ and $h_0 = 1$.

The first term on the right hand side of equation (C.13) writes

$$\gamma_{ss}|_0 = \frac{\theta_0 - \theta_{cr}}{\theta_0 - \theta_{cr}} = 1. \tag{C.14}$$

The second term on the right hand side of equation (C.13) writes

$$\epsilon u_1 \left.\frac{\partial \gamma_{ss}}{\partial \theta}\right|_0 \cdot \left.\frac{\partial \theta}{\partial u}\right|_0 = \frac{\epsilon u_1}{\theta_0 - \theta_{cr}} \frac{\partial}{\partial u} \left(\frac{\mathsf{Fr}^2 f}{8(s-1)\delta}(u^2 + v^2) \right)\Bigg|_0 = \frac{\epsilon u_1}{\theta_0 - \theta_{cr}} \left(\frac{\mathsf{Fr}^2 f}{8(s-1)\delta} 2u \right)\Bigg|_0 = \frac{2\epsilon u_1 \theta_0}{\theta_0 - \theta_{cr}}. \tag{C.15}$$

The third term on the right hand side of equation (C.13) writes

$$\epsilon v_1 \left.\frac{\partial \gamma_{ss}}{\partial \theta}\right|_0 \cdot \left.\frac{\partial \theta}{\partial v}\right|_0 = \frac{\epsilon v_1}{\theta_0 - \theta_{cr}} \frac{\partial}{\partial v} \left(\frac{\mathsf{Fr}^2 f}{8(s-1)\delta}(u^2 + v^2) \right)\Bigg|_0 = \frac{\epsilon u_1}{\theta_0 - \theta_{cr}} \left(\frac{\mathsf{Fr}^2 f}{8(s-1)\delta} 2v \right)\Bigg|_0 = 0 \tag{C.16}$$

The fourth term on the right hand side of equation (C.13) writes

$$\begin{aligned} \epsilon h_1 \left.\frac{\partial \gamma_{ss}}{\partial \theta}\right|_0 \cdot \left.\frac{\partial \theta}{\partial h}\right|_0 = \frac{\epsilon h_1}{\theta_0 - \theta_{cr}} \left.\frac{\partial \theta}{\partial f}\right|_0 \left.\frac{\partial f}{\partial h}\right|_0 = \frac{\epsilon h_1}{\theta_0 - \theta_{cr}} \left(\frac{\mathsf{Fr}^2}{8(s-1)\delta} \right)\Bigg|_0 \left.\frac{\mathrm{d}f}{\mathrm{d}h}\right|_0 = \\ \frac{\epsilon h_1}{\theta_0 - \theta_{cr}} \left(\frac{\mathsf{Fr}_0^2}{8(s-1)\delta} \right) \frac{f_0}{f_0} \left.\frac{\mathrm{d}f}{\mathrm{d}h}\right|_0 = \frac{\epsilon h_1 \theta_0}{\theta_0 - \theta_{cr}} \mathscr{C}_f \end{aligned} \tag{C.17}$$

with $\mathscr{C}_f$ is defined as

$$\mathscr{C}_f = \frac{1}{f_0} \left.\frac{\mathrm{d}f}{\mathrm{d}h}\right|_{h_0} \tag{C.18}$$

The linearisation of γ_{ss} ultimately writes

$$\gamma'_{ss} = 1 + \epsilon \frac{\theta_0}{\theta_0 - \theta_{cr}} (2u_1 + \mathscr{C}_f h_1). \tag{C.19}$$

Applying the perturbation expansion to every terms of equation (C.1) and using the Taylor expansion to expand

the term $\beta f \mathsf{Fr} u \left|\boldsymbol{u}\right| / 8$, equation (C.1) finally writes, in its linearised form

$$\mathsf{Fr}^2 \left[\beta \frac{\partial (u_1 + h_1)}{\partial t} + 2\frac{\partial u_1}{\partial x} + \frac{\partial h_1}{\partial x} + \frac{\partial v_1}{\partial y} - \frac{\nu}{\beta}\left(\frac{\partial^2 u_1}{\partial x^2} + \frac{\partial^2 u_1}{\partial y^2}\right)\right] + \frac{\partial (h_1 + \eta_1)}{\partial x} = \beta S h_1 - \frac{\beta f_0 \mathsf{Fr}^2}{8}\left(2u_1 + \mathscr{C}_f h_1\right). \quad \text{(C.20)}$$

The same process is applied to all the remaining equations of the morphodynamic model to ultimately obtain the linearised equations.

C.2 Eigenvalue problem

As mentioned in Chapter 5, the variables of the system of the linearised equations (5.62)–(5.66) are expanded in terms of their Fourier transform. The eigenvector thus writes

$$(u_1, v_1, h_1, \eta_1, \gamma_1) = \left(\bar{u}_1, \bar{v}_1, \bar{h}_1, \bar{\eta}_1, \bar{\gamma}_1\right) \mathrm{e}^{i(k_x x + k_y y - \omega t)} \quad \text{(C.21)}$$

where $\bar{u}_1$, $\bar{v}_1$, $\bar{h}_1$, $\bar{\eta}_1$, and $\bar{\gamma}_1$ are the complex amplitude of u_1, v_1, h_1, η_1 and γ_1 respectively, k_x and k_y are the real longitudinal and transverse wavenumber respectively. To illustrate the process, we expand the linearised Exner equation in terms of the Fourier modes. The linearised Exner equation originally writes

$$\frac{\partial \eta_1}{\partial t} = \kappa_\eta \left(\gamma_1 - \gamma'_{ss}\right), \quad \text{(C.22)}$$

Replacing the variables with their Fourier modes, even in the linearised closure relation γ'_{ss}, we obtain

$$\begin{aligned} \frac{\partial}{\partial t}\left(\bar{\eta}_1 \mathrm{e}^{i(k_x x + k_y y - \omega t)}\right) &= \kappa_\eta \left(\bar{\gamma}_1 \mathrm{e}^{i(k_x x + k_y y - \omega t)} - \frac{\theta_0}{\theta_0 - \theta_{cr}}\left(2\bar{u}_1 + \mathscr{C}_f \bar{h}_1\right) \mathrm{e}^{i(k_x x + k_y y - \omega t)}\right) \\ \Rightarrow -i\omega \bar{\eta}_1 \cancel{\mathrm{e}^{i(k_x x + k_y y - \omega t)}} &= \kappa_\eta \left(\bar{\gamma}_1 - \frac{\theta_0}{\theta_0 - \theta_{cr}}\left(2\bar{u}_1 + \mathscr{C}_f \bar{h}_1\right)\right) \cancel{\mathrm{e}^{i(k_x x + k_y y - \omega t)}} \\ \Rightarrow -i\omega \bar{\eta}_1 &= \kappa_\eta \left(\bar{\gamma}_1 - \frac{\theta_0}{\theta_0 - \theta_{cr}}\left(2\bar{u}_1 + \mathscr{C}_f \bar{h}_1\right)\right). \end{aligned} \quad \text{(C.23)}$$

The differential equation (C.22) is thus transformed into an algebraic equations whose unknowns are now the amplitudes of the Fourier transforms, namely $\bar{u}_1$, $\bar{h}_1$ and $\bar{\eta}_1$. Expanding all the equations in terms of their Fourier modes, the differential system of equation is transformed into a system of algebraic equations that can be written

in the following matrix form $\mathbf{Ag} = \mathbf{0}$ with $\mathbf{g} = \left(\bar{u}_1, \bar{v}_1, \bar{h}_1, \bar{\eta}_1, \bar{\gamma}_1\right)$. $\mathbf{A}$ is decomposed as

$$\mathbf{A} = -i\omega\mathbf{A_1} + ik_x\mathbf{A_2} + ik_y\mathbf{A_3} - k_x^2\mathbf{A_4} - k_y^2\mathbf{A_5} + \mathbf{A_6} \tag{C.24}$$

The terms are separated for clarity. The first matrix contains the first order temporal derivative terms, hence the prefactor $-i\omega$. The second matrix contains the first order spatial derivative terms in the longitudinal direction, hence the prefactor ik_x. Matrices $\mathbf{A_3}$, $\mathbf{A_4}$ and $\mathbf{A_5}$ contain the terms of the first order spatial derivative in the transverse direction, the second order spatial derivative in the longitudinal direction and the second order spatial derivative in the transverse direction respectively. Matrix $\mathbf{A_6}$ contains the remaining terms pertaining to the closure relations and the advection-diffusion equation. The matrices write

$$\begin{aligned}
&-i\omega\begin{pmatrix} 0 & 0 & 1 & 0 & 0 \\ \beta\mathsf{Fr}^2 & 0 & 0 & 0 & 0 \\ 0 & \beta\mathsf{Fr}^2 & 0 & 0 & 0 \\ 0 & 0 & 0 & 1 & 0 \\ 0 & 0 & 0 & 0 & 1 \end{pmatrix} + ik_x\begin{pmatrix} 1 & 0 & 1 & 0 & 0 \\ (2-\beta)\mathsf{Fr}^2 & 0 & (1-\beta)\mathsf{Fr}^2 & 1 & 0 \\ -\beta\mathsf{Fr}^2 & \mathsf{Fr}^2 & -\beta\mathsf{Fr}^2 & 0 & 0 \\ 0 & 0 & 0 & 0 & 0 \\ \frac{\alpha}{\beta} & 0 & 0 & 0 & \frac{\alpha}{\beta} \end{pmatrix} \\
&+ ik_y\begin{pmatrix} 0 & 1 & 0 & 0 & 0 \\ 0 & (1-\beta)\mathsf{Fr}^2 & 0 & 0 & 0 \\ 0 & -\beta\mathsf{Fr}^2 & 1 & 1 & 0 \\ 0 & 0 & 0 & 0 & 0 \\ 0 & \frac{\alpha}{\beta} & 0 & 0 & 0 \end{pmatrix} - k_x^2\begin{pmatrix} 0 & 0 & 0 & 0 & 0 \\ \frac{-\nu\mathsf{Fr}^2}{\beta} & 0 & 0 & 0 & 0 \\ 0 & \frac{-\nu\mathsf{Fr}^2}{\beta} & 0 & 0 & 0 \\ 0 & 0 & 0 & 0 & 0 \\ 0 & 0 & 0 & 0 & \frac{\mathscr{D}}{\beta} \end{pmatrix} \\
&- k_y^2\begin{pmatrix} 0 & 0 & 0 & 0 & 0 \\ \frac{-\nu\mathsf{Fr}^2}{\beta} & 0 & 0 & 0 & 0 \\ 0 & \frac{-\nu\mathsf{Fr}^2}{\beta} & 0 & 0 & 0 \\ 0 & 0 & 0 & 0 & 0 \\ 0 & 0 & 0 & 0 & \frac{\mathscr{D}}{\beta} \end{pmatrix} + \begin{pmatrix} 0 & 0 & 0 & 0 & 0 \\ 2\beta S_0 & 0 & \beta S_0 f'\mathscr{C}_f & 0 & 0 \\ 0 & 0 & \beta S_0 & 0 & 0 \\ \kappa_\gamma\gamma'_{ss}\frac{\partial\theta}{\partial u} & 0 & \kappa_\gamma\gamma'_{ss}\frac{\partial\theta}{\partial h} & 0 & -\kappa_\gamma \\ -\kappa_\eta\gamma'_{ss}\frac{\partial\theta}{\partial u} & 0 & -\kappa_\eta\gamma'_{ss}\frac{\partial\theta}{\partial h} & 0 & \kappa_\eta \end{pmatrix} = 0.
\end{aligned} \tag{C.25}$$

The problem is solved when computing the determinant of $\det \mathbf{A} = 0$.

C.3 Matematica notebook for the resolution

```
(*Usethisexpressiontoclearallthevariablesfrommemory.Before,
thereweresevaralonesthatwerenotcleanwhenrunningseveraltimesthescript*)
ClearAll["Global*"]
```

$$A = -I\omega \begin{pmatrix} 0 & 0 & 1 & 0 & 0 \\ \beta\mathrm{w}\mathrm{Fr}^2 & 0 & 0 & 0 & 0 \\ 0 & \beta\mathrm{w}\mathrm{Fr}^2 & 0 & 0 & 0 \\ 0 & 0 & 0 & 1 & 0 \\ 0 & 0 & 0 & 0 & 1 \end{pmatrix} + I\mathrm{kad} \begin{pmatrix} 1 & 0 & 1 & 0 & 0 \\ (2-\beta\mathrm{w})\mathrm{Fr}^2 & 0 & (1-\beta\mathrm{w})\mathrm{Fr}^2+1 & 1 & 0 \\ -\beta\mathrm{w}\mathrm{Fr}^2 & \mathrm{Fr}^2 & -\beta\mathrm{w}\mathrm{Fr}^2 & 0 & 0 \\ 0 & 0 & 0 & 0 & 0 \\ \frac{\beta}{\beta\mathrm{w}} & 0 & 0 & 0 & \frac{\beta}{\beta\mathrm{w}} \end{pmatrix} + I\mathrm{ky} \begin{pmatrix} 0 & & & & \\ & & & & \\ & & & & \\ & & & & \\ & & & & \end{pmatrix}$$

$$\mathrm{kad}^2 \begin{pmatrix} 0 & 0 & 0 & 0 & 0 \\ \frac{-\nu\mathrm{ad}\mathrm{Fr}^2}{\beta\mathrm{w}} & 0 & 0 & 0 & 0 \\ 0 & \frac{-\nu\mathrm{ad}\mathrm{Fr}^2}{\beta\mathrm{w}} & 0 & 0 & 0 \\ 0 & 0 & 0 & 0 & 0 \\ 0 & 0 & 0 & 0 & \frac{\mathrm{Du}}{\beta\mathrm{w}} \end{pmatrix} - \mathrm{ky}^2 \begin{pmatrix} 0 & 0 & 0 & 0 & 0 \\ \frac{-\nu\mathrm{ad}\mathrm{Fr}^2}{\beta\mathrm{w}} & 0 & 0 & 0 & 0 \\ 0 & \frac{-\nu\mathrm{ad}\mathrm{Fr}^2}{\beta\mathrm{w}} & 0 & 0 & 0 \\ 0 & 0 & 0 & 0 & 0 \\ 0 & 0 & 0 & 0 & \frac{\mathrm{Du}}{\beta\mathrm{w}} \end{pmatrix} +$$

$$\begin{pmatrix} 0 & 0 & 0 & 0 & 0 \\ 2\beta\mathrm{wS0} & 0 & \frac{\beta\mathrm{wS0dfdh}}{f} & 0 & 0 \\ 0 & \beta\mathrm{wS0} & 0 & 0 & 0 \\ \mathrm{keD}\phi\mathrm{eq02Sh0} & 0 & \mathrm{keD}\phi\mathrm{eq0Sh0}\frac{\mathrm{dfdh}}{f} & 0 & -\mathrm{ke} \\ -\kappa\mathrm{adD}\phi\mathrm{eq02Sh0} & 0 & -\kappa\mathrm{adD}\phi\mathrm{eq0Sh0}\frac{\mathrm{dfdh}}{f} & 0 & \kappa\mathrm{ad} \end{pmatrix};$$

```
disprel = Numerator[Together[Det[A]]]//Simplify;

ζb = 0.4;
ke = 2Cdfπ Fr / (6(1 - ζb)√(s - 1)√δ2) (1 - ucr^2);
S0 = f Fr^2 / 8;
κad = CdSqrt[s - 1]/(FrSqrt[δ2]);
friccion[d2_]:=1 / (-2Log10 [d2/3.71])^2 ;
f = friccion[δ2];
dfdh = -δ2friccion'[δ2];
```

$\beta = 1;$

$s = 2.65;$

$\mathrm{Cd} = 0.1;$

$\mathrm{Sc} = 0.5;$

$\mathrm{Shcr} = 0.02;$

$\mathrm{Sh0} = f\ \mathrm{Fr}^2 / \left(8(s-1)\delta 2\right);$

$\mathrm{ucr} = \sqrt{\mathrm{Shcr}/\mathrm{Sh0}};$

$\mathrm{D}\phi\mathrm{eq0} = 1/(\mathrm{Sh0} - \mathrm{Shcr});$

$\nu\mathrm{ad} = \nu\mathrm{t}\sqrt{f/8};$

$\nu\mathrm{t} = 1;$

$\mathrm{Du} = \nu\mathrm{ad}/\mathrm{Sc};$

$\mathrm{ak} = -3;$

$\mathrm{bk} = 2;$

$\mathrm{aky} = 0.01;$

$\mathrm{bky} = 1;$

$\mathrm{pkadlog} = 0.025;$

$\mathrm{pky} = 0.01;$

$\mathrm{kad} = 10^{\mathrm{kadlog}};$

$\delta 2 = 0.1;$

$\mathrm{Fr} = 0.875;$

$\beta\mathrm{w} = \frac{\pi}{2\mathrm{ky}};$

$\mathrm{totalsol} = \mathrm{Table}[\{\mathrm{kadlog}, \mathrm{ky}, \mathrm{NSolve}[\mathrm{disprel} == 0, \omega]\}, \{\mathrm{kadlog}, \mathrm{ak}, \mathrm{bk}, \mathrm{pkadlog}\}, \{\mathrm{ky}, \mathrm{aky}, \mathrm{bky}, \mathrm{pky}\}];$

$\mathrm{xx} = \{\};$

$\mathrm{yy} = \{\};$

$x = \mathrm{Table}[\mathrm{ky}, \{\mathrm{ky}, \mathrm{aky}, \mathrm{bky}, \mathrm{pky}\}];$

$y = \mathrm{Table}[\mathrm{kadlog}, \{\mathrm{kadlog}, \mathrm{ak}, \mathrm{bk}, \mathrm{pkadlog}\}];$

```
growthrate = {};
celerity = {};
beta = {};
z1 = {};
z2 = {};
z3 = {};
z4 = {};
z5 = {};
c1 = {};
c2 = {};
c3 = {};
c4 = {};
c5 = {};
m = Dimensions[totalsol][[1]];
n = Dimensions[totalsol][[2]];
For[i = 1, i ≤ m, i++,
{For[j = 1, j ≤ n, j++,
{sol = totalsol[[i]][[j]][[3]];
nsol = Length[sol];
solsim = Range[nsol]; solsre = Range[nsol];
For[k = 1, k ≤ nsol, k++, {
solsim[[k]] = Im[sol[[k]][[1]][[2]]];
solsre[[k]] = Re[sol[[k]][[1]][[2]]];
}
];
AppendTo[growthrate, Max[solsim]];
AppendTo[celerity, solsre[[Ordering[solsim, -1][[1]]]]];
```

```
AppendTo[xx, totalsol[[i]][[j]][[1]]];
AppendTo[yy, totalsol[[i]][[j]][[2]]];
AppendTo[z1, Im[sol[[1]][[1]][[2]]]];
AppendTo[z2, Im[sol[[2]][[1]][[2]]]];
AppendTo[z3, Im[sol[[3]][[1]][[2]]]];
AppendTo[z4, Im[sol[[4]][[1]][[2]]]];
AppendTo[z5, Im[sol[[5]][[1]][[2]]]];
AppendTo[c1, Re[sol[[1]][[1]][[2]]]];
AppendTo[c2, Re[sol[[2]][[1]][[2]]]];
AppendTo[c3, Re[sol[[3]][[1]][[2]]]];
AppendTo[c4, Re[sol[[4]][[1]][[2]]]];
AppendTo[c5, Re[sol[[5]][[1]][[2]]]];

}
]
}
];



dir = "X:\\Papa\\linear_stability_analysis\\jaen\\2019_10_10\\mathematica-msc-kx-ky\\test";
SetDirectory[dir];
Export["growthrate.mat", growthrate];
Export["celerity.mat", celerity];
Export["xx.mat", xx];
Export["yy.mat", yy];
Export["x.mat", x];
Export["y.mat", y];
```

```
Export["z1.mat", z1];
Export["z2.mat", z2];
Export["z3.mat", z3];
Export["z4.mat", z4];
Export["z5.mat", z5];
Export["c1.mat", c1];
Export["c2.mat", c2];
Export["c3.mat", c3];
Export["c4.mat", c4];
Export["c5.mat", c5];
Export["pky.mat", pky];
Export["pkadlog.mat", pkadlog];
```

Bibliography

A. Abramian, O. Devauchelle, and E. Lajeunesse. Streamwise streaks induced by bedload diffusion. *Journal of Fluid Mechanics*, 863:601—-619, 2019. doi: 10.1017/jfm.2018.1024.

R. Albert and A.-L. Barabási. Statistical mechanics of complex networks. *Rev. Mod. Phys.*, 74:47–97, Jan 2002. doi: 10.1103/RevModPhys.74.47. URL http://link.aps.org/doi/10.1103/RevModPhys.74.47.

C. Ancey. Stochastic modeling in sediment dynamics: Exner equation for planar bed incipient bed load transport conditions. *Journal of Geophysical Research: Earth Surface*, 115(F2):n/a–n/a, 2010. doi: 10.1029/2009JF001260. URL http://dx.doi.org/10.1029/2009JF001260.

C. Ancey. Bedload transport: a walk between randomness and determinism 1. State of the Art. *Journal of Hydraulic Research*, 2020a.

C. Ancey. Bedload transport: a walk between randomness and determinism 2. Challenges and prospects. *Journal of Hydraulic Research*, 2020b.

C. Ancey and J. Heyman. A microstructural approach to bed load transport: mean behaviour and fluctuations of particle transport rates. *Journal of Fluid Mechanics*, 744:129–168, 4 2014. doi: 10.1017/jfm.2014.74. URL http://journals.cambridge.org/article_S0022112014000743.

C. Ancey, F. Bigillon, P. Frey, J. Lanier, and R. Ducret. Saltating motion of a bead in a rapid water stream. *Phys. Rev. E*, 66, Sep 2002. doi: 10.1103/PhysRevE.66.036306. URL https://link.aps.org/doi/10.1103/PhysRevE.66.036306.

C. Ancey, A. C. Davison, T. Böhm, M. Jodeau, and P. Frey. Entrainment and motion of coarse particles in a shallow water stream down a steep slope. *Journal of Fluid Mechanics*, 595:83–114, 1 2008. doi: 10.1017/S0022112007008774. URL http://journals.cambridge.org/article_S0022112007008774.

C. Ancey, P. Bohorquez, and J. Heyman. Stochastic interpretation of the advection-diffusion equation and its relevance to bed load transport. *Journal of Geophysical Research: Earth Surface*, 120(12):2529–2551, 2015. doi: 10.1002/2014JF003421. URL https://agupubs.onlinelibrary.wiley.com/doi/abs/10.1002/2014JF003421.

B. Andreotti, P. Claudin, O. Devauchelle, O. Durán, and A. Fourrière. Bedforms in a turbulent stream: ripples, chevrons and antidunes. *Journal of Fluid Mechanics*, 690:94–128, 1 2012. doi: 10.1017/jfm.2011.386. URL http://journals.cambridge.org/article_S0022112011003867.

B. Andreotti, Y. Forterre, and O. Pouliquen. *Granular media: between fluid and solid*. Cambridge University Press, 2013.

P. Ashmore. 9.17 Morphology and Dynamics of Braided Rivers. In John F. Shroder, editor, *Treatise on Geomorphology*, pages 289–312. Academic Press, 2013. doi: https://doi.org/10.1016/B978-0-12-374739-6.00242-6.

P. E. Ashmore. Bed load transport in braided gravel-bed stream models. *Earth Surface Processes and Landforms*, 13(8):677–695, 1988. doi: 10.1002/esp.3290130803. URL http://dx.doi.org/10.1002/esp.3290130803.

P. E. Ashmore. How do gravel-bed rivers braid? *Canadian Journal of Earth Sciences*, 28(3):326–341, 1991a. doi: 10.1139/e91-030. URL http://dx.doi.org/10.1139/e91-030.

P. E. Ashmore. Channel morphology and bed load pulses in braided, gravel-bed streams. *Geografiska Annaler. Series A, Physical Geography*, 73(1):37–52, 1991b. URL http://www.jstor.org/stable/521212.

Peter E. Ashmore. Laboratory modelling of gravel braided stream morphology. *Earth Surface Processes and Landforms*, 7(3):201–225, 1982. doi: 10.1002/esp.3290070301. URL http://dx.doi.org/10.1002/esp.3290070301.

P. J. Ashmworth, J. L. Best, and M. A. Jones. The relationship between channel avulsion, flow occupancy and aggradation in braided rivers: insights from an experimental model. *Sedimentology*, 54(3):497–513, 2007. doi: 10.1111/j.1365-3091.2006.00845.x. URL http://dx.doi.org/10.1111/j.1365-3091.2006.00845.x.

R. Bagnold. The flow of cohesionless grains in fluids. *Philosophical Transactions of the Royal Society of London, Series A, Mathematical and Physical Sciences*, 1956.

N. J. Balmforth and A. Provenzale. Patterns of dirt. In *Geomorphological Fluid Mechanics*, Lecture notes in physics. Springer, Berlin, 2001. ISBN 3-540-42968-9.

N. J. Balmforth and A. Vakil. Cyclic steps and roll waves in shallow water flow over an erodible bed. *Journal of Fluid Mechanics*, 695:35–62, 2012. doi: 10.1017/jfm.2011.555.

G. I. Barenblatt. *Scaling*. Cambridge Texts in Applied Mathematics (34). Cambridge University Press, Cambridge, 10 2003. doi: 10.1017/CBO9780511814921. URL https://www.cambridge.org/core/books/scaling/E08325F4C8A14AAD4742E39FE5D0A6B3.

B. Belletti, S. Dufour, and H. Piégay. What is the Relative Effect of Space and Time to Explain the Braided River Width and Island Patterns at a Regional Scale? *River Research and Applications*, 31(1):1–15, 2015. doi: 10.1002/rra.2714. URL https://onlinelibrary.wiley.com/doi/abs/10.1002/rra.2714.

W. Bertoldi. Life of a bifurcation in a gravel-bed braided river. *Earth Surface Processes and Landforms*, 37(12): 1327–1336, 2012. doi: 10.1002/esp.3279.

W. Bertoldi and M. Tubino. Bed and bank evolution of bifurcating channels. *Water Resources Research*, 41(7): n/a–n/a, 2005. doi: 10.1029/2004WR003333. URL http://dx.doi.org/10.1029/2004WR003333.

W. Bertoldi and M. Tubino. River bifurcations: Experimental observations on equilibrium configurations. *Water Resources Research*, 43(10), 2007. doi: 10.1029/2007WR005907.

W. Bertoldi, P. Ashmore, and M. Tubino. A method for estimating the mean bed load flux in braided rivers. *Geomorphology*, 103(3):330–340, 2009a. doi: http://dx.doi.org/10.1016/j.geomorph.2008.06.014. URL http://www.sciencedirect.com/science/article/pii/S0169555X08002936.

W. Bertoldi, L. Zanoni, and M. Tubino. Planform dynamics of braided streams. *Earth Surface Processes and Landforms*, 34(4):547–557, 2009b. doi: 10.1002/esp.1755. URL http://dx.doi.org/10.1002/esp.1755.

P. Blondeaux and G. Seminara. A unified bar–bend theory of river meanders. *Journal of Fluid Mechanics*, 157:449–470, 8 1985. doi: 10.1017/S0022112085002440. URL http://journals.cambridge.org/article_S0022112085002440.

P. Blondeaux, M. M. Colombini, G. Seminara, and G. Vittori. *Introduction to Morphodynamicsof Sedimentary Patterns*. Genova University Press, 2017. ISBN 978-88-97752-99-8.

P. Bohorquez and C. Ancey. Stochastic-deterministic modeling of bed load transport in shallow water flow over erodible slope: Linear stability analysis and numerical simulation. *Advances in Water Resources*, 83:36–54, 2015. doi: http://dx.doi.org/10.1016/j.advwatres.2015.05.016. URL http://www.sciencedirect.com/science/article/pii/S0309170815001104.

P. Bohorquez and C. Ancey. Particle diffusion in non-equilibrium bedload transport simulations. *Applied Mathematical Modelling*, 40(17):7474–7492, 2016. doi: https://doi.org/10.1016/j.apm.2016.03.044. URL http://www.sciencedirect.com/science/article/pii/S0307904X16301925.

P. Bohorquez, P. Cañada-Pereira, P.J. Jimenez-Ruiz, and J.D. del Moral-Erencia. The fascination of a shallow-water theory for the formation of megaflood-scale dunes and antidunes. *Earth-Science Reviews*, 193:91–108, 2019. doi: https://doi.org/10.1016/j.earscirev.2019.03.021. URL http://www.sciencedirect.com/science/article/pii/S0012825218306846.

M. Bolla Pittaluga, R. Repetto, and M. Tubino. Channel bifurcation in braided rivers: Equilibrium configurations and stability. *Water Ressources Research*, 39(3), 2003. doi: 10.1029/2001WR001112.

R. W. Bradley and J. G. Venditti. Reevaluating dune scaling relations. *Earth-Science Reviews*, 165:356–376, 2017. doi: https://doi.org/10.1016/j.earscirev.2016.11.004. URL http://www.sciencedirect.com/science/article/pii/S0012825216301295.

R. A. Callander. Instability and river channels. *Journal of Fluid Mechanics*, 36:465–480, 5 1969. doi: 10.1017/S0022112069001765. URL http://journals.cambridge.org/article_S0022112069001765.

J. Canny. A Computational Approach to Edge Detection. *IEEE Transactions on Pattern Analysis and Machine Intelligence*, PAMI-8(6):679–698, 1986. doi: 10.1109/TPAMI.1986.4767851.

Z. Cao, P. Hu, K. Hu, G. Pender, and Q. Liu. Modelling roll waves with shallow water equations and turbulent closure. *Journal of Hydraulic Research*, 53(2):161–177, 2015. doi: 10.1080/00221686.2014.950350. URL https://doi.org/10.1080/00221686.2014.950350.

P. A. Carling and A. B. Shvidchenko. A consideration of the dune:antidune transition in fine gravel. *Sedimentology*, 49(6):1269–1282, 2002. doi: 10.1046/j.1365-3091.2002.00496.x. URL https://onlinelibrary.wiley.com/doi/abs/10.1046/j.1365-3091.2002.00496.x.

F. Charru, H. Mouilleron, and O. Eiff. Erosion and deposition of particles on a bed sheared by a viscous flow. *Journal of Fluid Mechanics*, 519:55––80, 2004. doi: 10.1017/S0022112004001028.

F. Charru, B. Andreotti, and P. Claudin. Sand ripples and dunes. *Annual Review of Fluid Mechanics*, 45(1):469–493, 2013. doi: 10.1146/annurev-fluid-011212-140806. URL https://doi.org/10.1146/annurev-fluid-011212-140806.

N.-S. Cheng. Comparison of sediment-pickup rates over plane bed and dunes. *Journal of Hydraulic Engineering*, 142(12):04016057, 2016. doi: 10.1061/(ASCE)HY.1943-7900.0001204. URL https://ascelibrary.org/doi/abs/10.1061/%28ASCE%29HY.1943-7900.0001204.

G. Cimini, T. Squartini, and F. Saracco. The statistical physics of real-world networks. *Nature Review of Physics*, 1:58–71, 2019. doi: 10.1038/s42254-018-0002-6. URL https://doi.org/10.1038/s42254-018-0002-6.

M. Colombini and G. Parker. Longitudinal streaks. *Journal of Fluid Mechanics*, 304:161–183, 1995. doi: 10.1017/S0022112095004381.

M. Colombini and A. Stocchino. Three-dimensional river bed forms. *Journal of Fluid Mechanics*, 695:63—-80, 2012. doi: 10.1017/jfm.2011.556. URL https://doi.org/10.1017/jfm.2011.556.

M. Colombini, G. Seminara, and M. Tubino. Finite-amplitude alternate bars. *Journal of Fluid Mechanics*, 181: 213—-232, 1987. doi: 10.1017/S0022112087002064.

G. Connor-Streich, A. J. Henshaw, J. Brasington, W. Bertoldi, and G. L. Harvey. Let's get connected: A new graph theory-based approach and toolbox for understanding braided river morphodynamics. *WIREs Water*, 5(5):e1296, 2018. doi: 10.1002/wat2.1296. URL https://onlinelibrary.wiley.com/doi/abs/10.1002/wat2.1296.

T.R. Davies and A. Lee. Physical hydraulic modelling of width reduction and bed level change in braided rivers. *Journal of Hydrology (New Zealand)*, 27(2):113 – 127, 1988.

O. Devauchelle, L. Malverti, É. Lajeunesse, P.-Y. Lagrée, C. Josserand, and K.-D. Nguyen Thu-Lam. Stability of bedforms in laminar flows with free surface: from bars to ripples. *Journal of Fluid Mechanics*, 642:329––348, 2010. doi: 10.1017/S0022112009991790.

S. Dey. *Fluvial Hydrodynamics*. GeoPlanet: Earth and Planetary Sciences. Springer, 1 edition, 2014. doi: 10.1007/978-3-642-19062-9.

Blaise Dhont and Christophe Ancey. Are Bedload Transport Pulses in Gravel Bed Rivers Created by Bar Migration or Sediment Waves? *Geophysical Research Letters*, 45(11):5501–5508, 2018. doi: 10.1029/2018GL077792. URL https://agupubs.onlinelibrary.wiley.com/doi/abs/10.1029/2018GL077792.

P. du Boys. Le rhône et les rivières à lit affouillable - Étude du régime du rhône et de l'action exercée par les eaux sur un lit à fond de graviers indéfiniment affouillable. *Annales des Ponts et Chaussées*, 49:141–95, 1879.

M.-P. Dubuisson and A. K. Jain. A modified hausdorff distance for object matching. In *Proceedings of 12th International Conference on Pattern Recognition*, volume 1, pages 566–568, Oct 1994. doi: 10.1109/ICPR.1994.576361.

Simon Dufour and Hervé Piégay. From the myth of a lost paradise to targeted river restoration: forget natural references and focus on human benefits. *River Research and Applications*, 25(5):568–581, 2009. doi: 10.1002/rra.1239.

R. Egozi and P. E. Ashmore. Defining and measuring braiding intensity. *Earth Surface Processes and Landforms*, 33(14):2121–2138, 2008. doi: 10.1002/esp.1658. URL http://dx.doi.org/10.1002/esp.1658.

R. Egozi and P. E. Ashmore. Experimental analysis of braided channel pattern response to increased discharge. *Journal of Geophysical Research: Earth Surface*, 114(F2):n/a–n/a, 2009. doi: 10.1029/2008JF001099. URL http://dx.doi.org/10.1029/2008JF001099.

H. A. Einstein. *The bed-load function for sediment transportation in open channel flows*. US Department of Agriculture, 1950.

T Eiter and H Mannila. Computing discrete fréchet distance. techreport CD-TR 94/64, Technische Universität Wien, April 1994.

Frank Engelund and Ove Skovgaard. On the origin of meandering and braiding in alluvial streams. *Journal of Fluid Mechanics*, 57:289–302, 2 1973. doi: 10.1017/S0022112073001163.

M. Ester, H.-P. Kriegel, J. Sander, and X. Xu. A Density-Based Algorithm for Discovering Clusters in Large Spatial Databases with Noise. In AAAI Press, editor, *Proceedings of the 2nd International Conference on Knowledge Discovery and Data Mining*, pages 226–231, 1996.

E. Foufoula-Georgiou and V. Sapozhnikov. Scale invariances in the morphology and evolution of braided rivers. *Mathematical Geology*, 33(3):273–291, 2001. doi: 10.1023/A:1007682005786. URL https://doi.org/10.1023/A:1007682005786.

D. J. Furbish, P. K. Haff, J. C. Roseberry, and M. W. Schmeeckle. A probabilistic description of the bed load sediment flux: 1. theory. *Journal of Geophysical Research: Earth Surface*, 117(F3):n/a–n/a, 2012a. doi: 10.1029/2012JF002352.

D. J. Furbish, J. C. Roseberry, and M. W. Schmeeckle. A probabilistic description of the bed load sediment flux: 3. the particle velocity distribution and the diffusive flux. *Journal of Geophysical Research: Earth Surface*, 117 (F3), 2012b. doi: 10.1029/2012JF002355.

P. A. Gagniuc. *Markov Chains: From Theory to Implementation and Experimentation*. Wiley, July 2017. ISBN 1119387558. URL https://www.xarg.org/ref/a/1119387558/.

M. Garcia and Y. Niño. Dynamics of sediment bars in straight and meandering channels: Experiments on the resonance phenomenom. *Journal of Hydraulic Research*, 31(6):739–762, 1993. doi: 10.1080/00221689309498815. URL https://doi.org/10.1080/00221689309498815.

G. A. Garcia Lugo, W. Bertoldi, A. J. Henshaw, and A. M. Gurnell. The effect of lateral confinement on gravel bed river morphology. *Water Resources Research*, 51(9):7145–7158, 2015. doi: 10.1002/2015WR017081. URL http://dx.doi.org/10.1002/2015WR017081.

C. W. Gardiner. *Handbook of Stochastic Methods: For Physics, Chemistry and Natural Sciences (Springer Series in Synergetics)*. Springer, January 1985. ISBN 3540616349. URL https://www.xarg.org/ref/a/3540616349/.

D. Germanoski and M. D. Harvey. Asynchronous terrace development in degrading braided channels. *Physical Geography*, 14(1):16–38, 1993. doi: 10.1080/02723646.1993.10642465. URL http://www.tandfonline.com/doi/abs/10.1080/02723646.1993.10642465.

D. Germanoski and S. A. Schumm. Changes in braided river morphology resulting from aggradation and degradation. *The Journal of Geology*, 101(4):451–466, 1993. URL http://www.jstor.org/stable/30068799.

B. Gomez. Bedload transport. *Earth-Science Reviews*, 31(2):89–32, 1991. doi: https://doi.org/10.1016/0012-8252(91)90017-A.

B. Gomez and M. Church. An assessment of bed load sediment transport formulae for gravel bed rivers. *Water Resources Research*, 25(6):1161–1186, 1989. doi: 10.1029/WR025i006p01161. URL http://dx.doi.org/10.1029/WR025i006p01161.

M. H. Gradowczyk. Wave propagation and boundary instability in erodible-bed channels. *Journal of Fluid Mechanics*, 33(1):93—-112, 1968. doi: 10.1017/S0022112068002387.

W. H. Graf. *Hydraulics of Sediment Transport*. Water Ressources Publications, Littleton, 1984.

É. Guazzelli, J. F. Morris, and S. Pic. *A Physical Introduction to Suspension Dynamics*. Cambridge Texts in Applied Mathematics. Cambridge University Press, 2011. doi: 10.1017/CBO9780511894671.

A. Gurnell, N. Surian, and L. Zanoni. Multi-thread river channels: A perspective on changing European alpine river systems. *Aquatic Sciences*, 71:253, 2009. doi: 10.1007/s00027-009-9186-2.

H. P. Guy, D. B. Simons, and E. V. Richardson. Summary of alluvial channel data from flume experiments, 1956-61. Professional paper, US Geological Survey, 1966. URL http://pubs.er.usgs.gov/publication/pp462I.

F. Harary. *Graph Theory*. Addison-Wesley Publishing COmpany, 1969.

T. Heckmann, W. Schwanghart, and J. D. Phillips. Graph theory-recent developments of its application in geomorphology. *Geomorphology*, 243:130–146, 2015. doi: http://dx.doi.org/10.1016/j.geomorph.2014.12.024. URL http://www.sciencedirect.com/science/article/pii/S0169555X1400628X.

M. Hiatt, W. Sonke, E. A. Addink, W. M. van Dijk, M. van Kreveld, T. Ophelders, K. Verbeek, J. Vlaming, B. Speckmann, and M. G. Kleinhans. Geometry and Topology of Estuary and Braided River Channel Networks Automatically Extracted From Topographic Data. *Journal of Geophysical Research: Earth Surface*, 125(1):e2019JF005206, 2020. doi: 10.1029/2019JF005206.

T. B. Hoey. Sediment dispersion and duration of storage in a model braided river. *Journal of hydrology. New Zealand*, 35(2):213–237, 1996.

T. B. Hoey and A. J. Sutherland. Channel morphology and bedload pulses in braided rivers: a laboratory study. *Earth Surface Processes and Landforms*, 16(5):447–462, 1991. ISSN 1096-9837. doi: 10.1002/esp.3290160506. URL http://dx.doi.org/10.1002/esp.3290160506.

J. Hoffimann, A. Bufe, and J. Caers. Morphodynamic Analysis and Statistical Synthesis of Geomorphic Data: Application to a Flume Experiment. *Journal of Geophysical Research: Earth Surface*, 124(11):2561–2578, 2019. doi: 10.1029/2019JF005245. URL https://agupubs.onlinelibrary.wiley.com/doi/abs/10.1029/2019JF005245.

A. D. Howard, M. E. Keetch, and C. L. Vincent. Topological and geometrical properties of braided streams. *Water Resources Research*, 6(6):1674–1688, 1970. doi: 10.1029/WR006i006p01674.

S. Ikeda. Prediction of alternate bar wavelength and height. *Journal of Hydraulic Engineering*, 110(4):371–386, 1984.

M. N. R. Jaeggi. Formation and effects of alternate bars. *Journal of Hydraulic Engineering-ASCE*, 110(2):142–156, 1984.

P. Y. Julien. *Erosion and Sedimentation*. Cambridge University Press, second edition edition, 2010. ISBN 978-0-511-71294-4.

M. P. Juniper, A. Hanifi, and V. Theofilis. Modal Stability Theory: Lecture notes from the FLOW-NORDITA Summer School on Advanced Instability Methods for Complex Flows, Stockholm, Sweden, 2013. *Applied Mechanics Reviews*, 66(2), 03 2014. doi: 10.1115/1.4026604. URL https://doi.org/10.1115/1.4026604.

M. Kleinhans, M. van Kreveld, T. Ophelders, W.e Sonk, B. Speckmann, and K. Verbeek. Computing Representative Networks for Braided Rivers. In Boris Aronov and Matthew J. Katz, editors, *33rd International Symposium on Computational Geometry (SoCG 2017)*, volume 77 of *Leibniz International Proceedings in Informatics (LIPIcs)*, pages 48:1–48:16. Schloss Dagstuhl–Leibniz-Zentrum fuer Informatik, 2017. ISBN 978-3-95977-038-5. doi: 10.4230/LIPIcs.SoCG.2017.48. URL http://drops.dagstuhl.de/opus/volltexte/2017/7220.

M. G. Kleinhans. Sorting out river channel patterns. *Progress in Physical Geography*, 34(3):287–326, 2010. doi: 10.1177/0309133310365300.

M. G. Kleinhans and J. H. van den Berg. River channel and bar patterns explained and predicted by an empirical and a physics-based method. *Earth Surface Processes and Landforms*, 36(6):721–738, 2011. doi: 10.1002/esp.2090. URL http://dx.doi.org/10.1002/esp.2090.

M. G. Kleinhans, R. I. Ferguson, S. N. Lane, and R. J. Hardy. Splitting rivers at their seams: bifurcations and avulsion. *Earth Surface Processes and Landforms*, 38(1):47–61, 2013. doi: 10.1002/esp.3268. URL http://dx.doi.org/10.1002/esp.3268.

E. Lajeunesse, L. Malverti, and F. Charru. Bed load transport in turbulent flow at the grain scale: Experiments and modeling. *Journal of Geophysical Research: Earth Surface*, 115(F4):n/a–n/a, 2010. doi: 10.1029/2009JF001628. URL http://dx.doi.org/10.1029/2009JF001628.

S. Lanzoni. Experiments on bar formation in a straight flume: 1. uniform sediment. *Water Resources Research*, 36(11):3337–3349, 2000. doi: 10.1029/2000WR900160. URL http://dx.doi.org/10.1029/2000WR900160.

Pauline Leduc. *Étude expérimentale de la dynamique sédimentaire des rivières en tresses*. PhD thesis, Irstea Grenoble, 2013.

M. Lehotský, M. Rusnák, A. Kidová, and J. Dudžák. Multitemporal assessment of coarse sediment connectivity along a braided-wandering river. *Land Degradation & Development*, 29(4):1249–1261, 2018. doi: 10.1002/ldr.2870.

G. Mariethoz and J. Caers. *Multiple-point geostatistics: stochastic modeling with training images*. John Wiley & Sons, Ltd, 2015. ISBN 978-1-118-66275-5.

G. Mariethoz, P. Renard, and J. Straubhaar. The direct sampling method to perform multiple-point geostatistical simulations. *Water Resources Research*, 46(11), 2010. doi: 10.1029/2008WR007621.

W. A. Marra, M. G. Kleinhans, and E. A. Addink. Network concepts to describe channel importance and change in multichannel systems: test results for the jamuna river, bangladesh. *Earth Surface Processes and Landforms*, 39(6):766–778, 2014. doi: 10.1002/esp.3482.

E. Meyer-Peter and R. Müller. Formulas for Bed-Load transport. In IAHR, editor, *IAHR 2nd meeting*, pages 39–64, Stockholm, Sweden, 1948.

M. P. Mosley. RESPONSE OF BRAIDED RIVERS TO CHANGING DISCHARGE. *Journal of Hydrology (New Zealand)*, 22(1):18–67, 1983. URL http://www.jstor.org/stable/43944509.

F. Métivier and P. Meunier. Input and output mass flux correlations in an experimental braided stream. implications on the dynamics of bed load transport. *Journal of Hydrology*, 271(14):22–38, 2003. doi: http://dx.doi.org/10.1016/S0022-1694(02)00312-8. URL http://www.sciencedirect.com/science/article/pii/S0022169402003128.

F. Métivier, E. Lajeunesse, and O. Devauchelle. Laboratory rivers: Lacey's law, threshold theory, and channel stability. *Earth Surface Dynamics*, 5(1):187–198, 2017. doi: 10.5194/esurf-5-187-2017.

Y. Muramoto and Y. Fujita. The classification of meso-scale river bed configuration and the criterion of its formation. In *Proceedings of 22nd Japanese Conference on Hydraulics, Japan*, pages 275–282, 1978.

D. J. Needham and J. H. Merkin. On roll waves down an open inclined channel. *PROC. R. SOC. - A*, 394(1807 , Aug. 8, 1984):259–278, 1984.

M. E. J. Newman. The structure and function of complex networks. *SIAM Review*, 45(2):167–256, 2003. doi: 10.1137/S003614450342480.

M. E. J. Newman. *Networks: An Introduction*. Oxford University Press, 2010. ISBN 97S-0-19-920665-0.

C. Paola. Modelling stream braiding over a range of scales. *New Zealand Hydrological Society*, 2001.

C. Paola and V. R. Voller. A generalized exner equation for sediment mass balance. *Journal of Geophysical Research: Earth Surface*, 110(F4), 2005. doi: 10.1029/2004JF000274.

G. Parker. On the cause and characteristic scales of meandering and braiding in rivers. *Journal of Fluid Mechanics*, 76:457–480, 1976. doi: 10.1017/S0022112076000748. URL http://journals.cambridge.org/article_S0022112076000748.

J. D. Phillips, W. Schwanghart, and T. Heckmann. Graph theory in the geosciences. *Earth-Science Reviews*, 143: 147–160, 2015. doi: http://dx.doi.org/10.1016/j.earscirev.2015.02.002. URL http://www.sciencedirect.com/science/article/pii/S0012825215000239.

G. Pirot, J. Straubhaar, and P. Renard. Simulation of braided river elevation model time series with multiple-point statistics. *Geomorphology*, 214:148 – 156, 2014. doi: https://doi.org/10.1016/j.geomorph.2014.01.022.

B. S. Pryor, T. Lisle, D. S. Montoya, and S. Hilton. Transport and storage of bed material in a gravel-bed channel during episodes of aggradation and degradation: a field and flume study. *Earth Surface Processes and Landforms*, 36(15):2028–2041, 2011. doi: 10.1002/esp.2224. URL https://onlinelibrary.wiley.com/doi/abs/10.1002/esp.2224.

A. Recking. Influence of sediment supply on mountain streams bedload transport. *Geomorphology*, 175–176: 139–150, 2012. ISSN 0169-555X. doi: 10.1016/j.geomorph.2012.07.005. URL http://www.sciencedirect.com/science/article/pii/S0169555X12003297.

A. Recking. An analysis of nonlinearity effects on bed load transport prediction. *Journal of Geophysical Research: Earth Surface*, 118(3):1264–1281, 2013. doi: 10.1002/jgrf.20090.

A. Recking, V. Bacchi, M. Naim, and P. Frey. Antidunes on steep slopes. *Journal of Geophysical Research*, 114 (F4), 2009. doi: 10.1029/2008JF001216. URL https://agupubs.onlinelibrary.wiley.com/doi/abs/10.1029/2008JF001216.

M. Redolfi, M. Tubino, W. Bertoldi, and J. Brasington. Analysis of reach-scale elevation distribution in braided rivers: Definition of a new morphologic indicator and estimation of mean quantities. *Water Resources Research*, 52(8):5951–5970, 2016. doi: 10.1002/2015WR017918. URL http://dx.doi.org/10.1002/2015WR017918.

A. J. Reynolds. Waves on the erodible bed of an open channel. *Journal of Fluid Mechanics*, 22(1):113—-133, 1965. doi: 10.1017/S0022112065000630.

C. Scheidt, A. M. Fernandes, C. Paola, and J. Caers. Quantifying natural delta variability using a multiple-point geostatistics prior uncertainty model. *Journal of Geophysical Research: Earth Surface*, 121(10):1800–1818, 2016. doi: 10.1002/2016JF003922. URL https://agupubs.onlinelibrary.wiley.com/doi/abs/10.1002/2016JF003922.

E. Schubert, J. Sander, M. Ester, H. P. Kriegel, and X. Xu. DBSCAN revisited, revisited: Why and how you should (still) use DBSCAN. *ACM Trans. Database Syst.*, 42(3), July 2017. doi: 10.1145/3068335. URL https://doi.org/10.1145/3068335.

G. Seizilles, O. Devauchelle, E. Lajeunesse, and F. Métivier. Width of laminar laboratory rivers. *Phys. Rev. E*, 87: 052204, 2013. doi: 10.1103/PhysRevE.87.052204.

G. Seizilles, E. Lajeunesse, O. Devauchelle, and M. Bak. Cross-stream diffusion in bedload transport. *Physics of Fluids*, 26(1):013302, 2014. doi: 10.1063/1.4861001. URL https://doi.org/10.1063/1.4861001.

G. Seminara. Fluvial sedimentary patterns. *Annual Review of Fluid Mechanics*, 42:43–66, 2010. ISSN 0066-4189. doi: 10.1146/annurev-fluid-121108-145612.

C. A. Shannon. A mathematical theory of communication. *The Bell System Technical Journal*, 27(3):379–423, 1948.

A. Shields. Application of similarity principles and turbulence research to bed-load movement. Technical report, California Institute of Technology, Pasadena, CA, 1936.

N. Snavely, S. M. Seitz, and R. Szeliski. Modeling the World from Internet Photo Collections. *International Journal of Computer Vision*, 80(2):189–210, 2008. doi: 10.1007/s11263-007-0107-3. URL https://doi.org/10.1007/s11263-007-0107-3.

Steven H. Strogatz. Exploring complex networks. *Nature*, 410(6825):268–276, 2001. ISSN 0028-0836. doi: 10.1038/35065725. URL http://dx.doi.org/10.1038/35065725.

N. Sukegawa. Criterion for alternate bars formation in experimental flumes. *Proceedings of the Japan Society of Civil Engineers*, 1972(207):47–50, 1972. doi: 10.2208/jscej1969.1972.207_47.

K. Tockner, A. Paetzold, U. Karaus, C. Claret, and J. Zettel. *Ecology of Braided Rivers*, pages 339–359. John Wiley & Sons, Ltd, 2009. ISBN 9781444304374. doi: 10.1002/9781444304374.ch17.

M. Tubino. Growth of alternate bars in unsteady flow. *Water Resources Research*, 27(1):37–52, 1991. doi: 10.1029/90WR01699. URL http://dx.doi.org/10.1029/90WR01699.

M. Tubino, R. Repetto, and G. Zolezzi. Free bars in rivers. *Journal of Hydraulic Research*, 37(6):759–775, 1999. doi: 10.1080/00221689909498510. URL http://dx.doi.org/10.1080/00221689909498510.

L. Turnbull, M.-T. Hütt, A. A. Ioannides, S. Kininmonth, R. Poeppl, K. Tockner, L. J. Bracken, S. Keesstra, L. Liu, R. Masselink, and A. J. Parsons. Connectivity and complex systems: learning from a multi-disciplinary perspective. *Applied Network Science*, 3:11, 2018. doi: 10.1007/s41109-018-0067-2.

R. Vesipa, C. Camporeale, and L. Ridolfi. A shallow-water theory of river bedforms in supercritical conditions. *Physics of Fluids*, 24(9):094104, 2012. doi: 10.1063/1.4753943. URL https://doi.org/10.1063/1.4753943.

R. Vesipa, C. Camporeale, and L. Ridolfi. Effect of sampling time in the laboratory investigation of braided rivers. *Water Resources Research*, 53(6):5184–5197, 2017. doi: 10.1002/2017WR020474. URL http://dx.doi.org/10.1002/2017WR020474.

J. Warburton. Active braidplain width, bed load transport and channel morphology in a model braided. *Journal of Hydrology (NZ)*, 35(2):259–285, 1996.

J. Warburton and T. Davies. Variability of bedload transport and channel morphology in a braided river hydraulic model. *Earth Surface Processes and Landforms*, 19(5):403–421, 1994. doi: 10.1002/esp.3290190503. URL http://dx.doi.org/10.1002/esp.3290190503.

E. K. Webb. Simulation of braided channel topology and topography. *Water Resources Research*, 31(10):2603–2611, 1995. doi: 10.1029/95WR01952.

E. Wohl, P. L. Angermeier, B. Bledsoe, G. M. Kondolf, L. MacDonnell, D.d M. Merritt, M. A. Palmer, N. L. Poff, and D. Tarboton. River restoration. *Water Resources Research*, 41(10), 2005. doi: 10.1029/2005WR003985.

E. Wohl, F. J. Magilligan, and S. L. Rathburn. Introduction to the special issue: Connectivity in Geomorphology. *Geomorphology*, 277:1–5, 2017. doi: https://doi.org/10.1016/j.geomorph.2016.11.005.

E. Wohl, G. Brierley, D. Cadol, T. J. Coulthard, T. Covino, K. A. Fryirs, G. Grant, R. G. Hilton, S. N. Lane, F. J. Magilligan, K. M. Meitzen, P. Passalacqua, R. E. Poeppl, S. L. Rathburn, and L. S. Sklar. Connectivity as an emergent property of geomorphic systems. *Earth Surface Processes and Landforms*, 44(1):4–26, 2019. doi: 10.1002/esp.4434.

M. Wong and G. Parker. Reanalysis and Correction of Bed-Load Relation of Meyer-Peter and Müller Using Their Own Database. *Journal of Hydraulic Engineering*, 132(11):1159–1168, 2006. doi: 10.1061/(ASCE)0733-9429(2006)132:11(1159).

W. Wu. *Computational River Dynamics*. Taylor & Francis, 2007. ISBN 978-0-203-93848-5.

M. S. Yalin. *Theory of Hydraulic Models*. The Macmillan Press Ltd, 1971. ISBN 978-1-349-00247-4. doi: 10.1007/978-1-349-00245-0.

M. S. Yalin. *Mechanics of sediment transport*. Pergamon Press, 1972. URL https://books.google.fr/books?id=v_71WLXLH-UC.

M. S. Yalin and A. M. F. da Silva. *Fluvial Processes*. IAHR Monograph, Delft, 2001.

W. J. Young and T. R. H. Davies. Bedload transport processes in a braided gravel-bed river model. *Earth Surface Processes and Landforms*, 16(6):499–511, 1991. doi: 10.1002/esp.3290160603. URL http://dx.doi.org/10.1002/esp.3290160603.

W. J. Young and J. Warburton. Principles and practice of hydraulic modelling of braided gravel-bed rivers. *Journal of Hydrology New Zealand*, 35:175–198, 1996.

Daniel V. **Papa**

Mechanical Engineer and PhD in Fluid Mechanics

Avenue du 14 avril 18, 1020 Renens, Switzerland

(+41) 79 660 09 97 | danielvito.papazang@protonmail.com

Education

Swiss Federal Institute of Technology — *Lausanne, Switzerland*

PhD in Fluid Mechanics — *Jul. 2015 – Oct. 2020*

- Study of the morphodynamics (hydraulics) of braided rivers.

Swiss Federal Institute of Technology — *Lausanne, Switzerland*

M.S. in Mechanical Engineering — *Feb. 2012 – Feb. 2014*

- Master with a specialization in aero and hydrodynamics.

Swiss Federal Institute of Technology — *Lausanne, Switzerland*

B.S. in Mechanical Engineering — *Sep. 2008 – Feb. 2012*

- Bachelor with general engineering courses.

Experience

Ponera Group — *Lausanne*

IoT Solutions — *Jul. 2020 – Today*

- Developed MVP for Operations Facilitation Tool: calculate modules needed, show operator procedure for assembly and disassembly, organization of empty modules during reverse logistic process.
- Develop analytics tool for Ponera Sales team, quickly estimate Savings, ROI, and CO2 potentials for specific logistic flows.
- Active participation in the connectivity tools strategy, and further implementation.

Swiss Federal Institute of Technology (EPFL) — *Lausanne*

PhD candidate — *Jul. 2015 – Today*

- Scientific investigation on braided rivers morphodynamics (fluid mechanics and sediment transport processes).
- Publication of scientific articles in peer-reviewed journals.
- Participation at internation scientific conferences.
- Supervision of Master students' projects.
- Teaching assistantship of several courses at various level (Bachelor and Master).

Endosense (now St. Jude Medical) — *Geneva*

Intern — *Jun. 2013 – Agu. 2013*

- Developed and optimized an optical fiber cutting and installation process.
- Translated important processes and document in Spanish for outsourcing purposes.

Ecole des Techniques et des Métiers de Lausanne (ETML) — *Lausanne*

Intern — *Jun. 2010 – Jul. 2010*

- Internship in technical machinery handling.

Swiss Federal Institute of Technology (EPFL) — *Lausanne*

Student assistant — *Sept. 2009 – Feb. 2014*

- Student teaching assistant for a wide range of courses, amongs them: Physics, Informatics, Mathematics (calculus, algebra, geometry)

Scientific publications

Shallow-water morphodynamic model for the formation of two and three-dimensional bedforms — *Journal of Hydraulic Resarch*

Article — *In preparation*

- In preparation to be submitted

Analysis of braided rivers network's temporal evolution: an experimental study — *Earth Surface Processes and Landforms*

Article — *In preparation*

- In preparation to be submitted

153

Braided rivers networks dynamics: analyzing topographic data from a large flume experiment — *European Geophysical Union (EGU)*

Conference Talk — *May. 2020*

- Oral presentation

Evolution of braided rivers morphodynamical indices: data insight from experiments — *European Geophysical Union (EGU)*

Conference Poster — *Apr. 2018*

High-speed camera recording of bedload transport from large scale braided rivers experiments — *River Coastal and Estuarine Morphodynamics (RCEM)*

Conference Poster — *Sept. 2017*

Influence of hyporheic flows on the incipient motion threshold — *European Geophysical Union (EGU)*

Conference Poster — *Apr. 2017*

Bedload transport fluctuations in large flume experiments with alternate bars. — *American Geophysical Union (AGU)*

Conference Poster — *Submitted Dec. 2015*

Skills

Engineering Software	Abaqus CAE, ANSYS Fluent, Autocad, CATIA v5
Front-end	Joomla, HTML5
Programming	Python, LaTeX, Matlab, C++
Languages	French (C2), Spanish(C2), English(C1), Italian(C1), German (A2)

Extracurricular Activity

ArchiTango — *Lausanne*

President — *Septs. 2016 – Today*

- President of the tango association promoting dancing on and off campus for students and university collaborators.
- Responsible of the organization of conferences linking tango music (and music in general) with science (fundamental sciences as well as social and medical sciences).
- Formerly webmaster of the association.

Music

- Piano playing as a recreational activity. Two years in the conservatory in Belgium at the age of 12 to 14 years old.
- Active tango dancing since three years.
- Formerly part of a tango orchestra.

Dance

- Tango dancing since four years.

Football Player — *Lausanne*

Racing Club Lausanne — *Jan. 2015 – Today*

- Football player of the Racing Club Lausanne

ESN Lausanne — *Lausanne*

Member — *Sept. 2009 – Feb. 2014*

- Member of the ESN (Erasmus Student Network) association, an association devoted to promote the integration of Erasmus students in Switzerland by means of cultural activities.
- Responsible of the organization of sport events as well as cultural events.

154